High throughput computing for high mobility p-type transparent conducting materials

Viet-Anh Ha
Institute of Condensed Matter and Nanosciences
Université catholique de Louvain

Members of the jury:

Prof. Geoffroy Hautier (UCL), supervisor
Prof. Gian-Marco Rignanese (UCL), supervisor
Prof. Bernard Nysten (UCL), chairperson
Prof. Xavier Gonze (UCL), secretary
Prof. Yaroslav Filinchuk (UCL)
Dr. Damien Lenoble (LIST, Luxembourg)
Dr. Geoffrey Pourtois (IMEC, Leuven, Belgium)

A thesis submitted for the degree of
Doctor of Philosophy

Louvain-la-Neuve, 2019

Share your knowledge.

It is a way to achieve immortality.

- Dalai Lama XIV

Acknowledgements

First of all, I would like to express my deep gratitude to my supervisors, Profs. Geoffroy Hautier and Gian-Marco Rignanese, for giving me a chance to be their PhD student. I will never forget how they meticulously taught me from basic lessons about Density Functional Theory (DFT) since the first days I worked in MODELLING laboratory (UCL) to more critical and complicated calculations and skills for doing research in computational materials science. In more than four years, they helped me to answer many scientific questions, guided me how to do research, make critical-thinking and disseminate scientific knowledge, *etc.* I also would thank Prof. Xavier Gonze for introducing Prof. Geoffroy Hautier to me when I tried to contact you and show my desire to learn and work on DFT. To be honest, I ever thought that it would be difficult for me to receive a reply from a prestigious professor like you but I was wrong.

During the time working in MODELLING laboratory, I was constantly supported by many colleagues of mine: David Waroquiers, Anna Miglio, Francesco Ricci, Yudong Yu, Matteo Giantomassi, Michel van Setten, Guido Petretto, Guillaume Brunin, Wei Chen, Henrique Miranda, Diana Dahliah, Benoit van Troeye, Yanick Gillet, Sriram Ramkumar, Viet-Hung Nguyen,... Without the support from these generous and kind persons, I could not rush my projects and finish my PhD on time. Our relationships have been cultivated not only through science but also many extra-activities, *e.g.*

football - the most favourite sport of mine. I will remember the football matches I played with some of you which brought so much fun and joy to me. To be immersed in the terrific atmosphere of the biggest football tournaments such as UEFA Euro 2016 and World Cup 2018 with Belgium (the best) beer and fries (in the world) was my stunning experience.

To complete this dissertation, I was mainly funded through a grant from the FRIA/FNRS and partly subsidized by UCL in the last six months of my PhD. I cannot say how much I appreciate these important financial supports. I also acknowledge access to various computational resources: the Tier-1 supercomputer of the Fédération Wallonie-Bruxelles funded by the Walloon Region (grant agreement N^0 1117545), and all the facitilies provided by the Université catholique de Louvain (CISM/UCL) and by the Consortium des Équipements de Calcul Intensif en Fédération Wallonie Bruxelles (CÉCI).

In the last words, I would say many thanks to my wife, my son, my parents and my siblings whom have been always encouraging me very much. I truly appreciate all the help from Vietnamese friends living and working in Ottignies-Louvain-la-Neuve like brothers Trong-Viet Ho, Ngoc-Diep Ho, Viet-Hoang Tran, Long-Hung Nguyen... and sisters Thuy-Hang Hoang, Ai-Vi Tran, Thanh-Loan Ngo, Thu-Thao Le, My-Anh Nguyen, Kim-Minh Nguyen,... These friends are incredibly helpful and it is so hard for me to describe their generosity. They aided my family and myself remarkably in daily life since the first days I came to Belgium. Without doubt, the period of time I have lived and worked in Louvain-la-Neuve is an unforgettable chapter in my life.

Abstract

In this thesis, we investigate transparent conducting materials (TCMs) which are the need of many modern technologies and devices. These are semiconductors which can combine both high visible transparency and electrical conductivity/mobility. While n-type TCMs (oxides) have been utilized in many applications such as solar-cells, touch screens *etc.*, their counterpart, p-type TCMs, is performing poorly in carrier mobility. This impedes the development of many modern technologies such as transparent solar cells. We, therefore, target on design of high mobility p-type TCMs. Using DFT in combination with other computational methods, we suggest new practical design principles for high mobility p-TCMs, particularly oxides. We hope that these principles can accelerate progress in this field, especially in the era of computational materials sciences nowadays. Moreover, we also extend our vision by exploring non-oxide zone instead of being bound to the traditional space of oxides. We set up high throughput computing framework based on DFT and beyond DFT methods such as hybrid functional, GW, electron-phonon (el-ph) interaction, semi-classical transport. Starting from a large database of (> 34000) crystalline structures, we implement a series of computations for non-oxide compounds and sort out some materials showing positive potentiality (searching for "a needle in a haystack"). In final, several candidates including BP, CaTe and Li_3Sb are identified as promising p-type TCMs. These binary compounds exhibit p-type dopability, low hole effective mass (high hole

mobility) and high transparency in thin-film samples. Our results might inspire future works and convince researchers in the community that "there is still plenty of room" for high mobility p-type TCMs in non-oxide space.

Contents

List of Figures

List of Tables

Chapter 1

Introduction

In this chapter, the basic background and concept of transparent conducting materials will be briefly introduced. Why do these materials achieve a great interest of active researchers? What types of applications are they needed for? We will review the state-of-the-art progress in both investigations and applications in this field. We also raise the controversial questions and challenging problems and then present our main motivations and purposes for this thesis.

1.1 Transparent conducting materials

The world is presently confronting and dealing with different major problems such as climate change, environmental contamination, inequity, food and water security, growth of economic prosperity in a stagnation,... We are, therefore, in a race for a new scientific and technological revolution to find solutions for many of these critical and hard issues. The main purpose is to develop novel technologies which manoeuvre the society into more advantageous manufacturing methods with many innovations such as higher productivity, more automation, lower cost and energy consumption... In particular, electronic industries are focusing on design and fabrication of new (generations of) devices with innovative features and higher efficiency. The fundamental base for the development of this field is definitely novel materials with novel and exceptional properties.

TCMs is a clear-cut example. These materials are semiconductors with a rare combination of different properties including high mobility, visible transparency and dopability (n- or p-type). Fig. 1.1 sketches these properties in association with electronic band structures. From the view of electronic band structure, this combination seems to be somehow rare and contradictory. To be high transparency, these materials must show wide optical band gap, normally at least 3.0 eV. However, this might lead to more difficulties in doping them with n/p-type or both and therefore in making them highly conductive. For instance, to facilitate n-type doping, materials should show conduction band minimum (CBM) far from vacuum level (large electron affinities). On other hand, materials whose valence band maximum (VBM) are close to the vacuum level (low ionization energy) can be easier to dope with p-type [1]. Because of these principles, large band-gap semiconductors/insulators have less possibility to be doped with n/p-type or both (extremely difficult). In fact, only some materials satisfy this rare combination are called TCMs and utilized for many devices such as low-emissivity coatings, flat-panel displays, thin-film solar cells, transparent transistors, *et cetera* [2, 3].

Historically, the first TCMs, n-type CdO and p-type CuI, were reported in 1907 by German physicist Karl Baedeker [4]. In his paper [5], metals (Cd, Cu,...) were coated by sputtering on glass substrates and then oxidized in air and iodized at elevated temperature of iodine vapor, respectively. Until 40 years later, H. A. McMaster, an American inventor, reported another compound, SnO_2 film, formed by evaporating tin chloride crystal ($SnCl_2$) with water on a glass substrate [6]. The author proposed to use this transparent conductive film for coating and melting ice attached on plane windows at high attitude. The following patents also reported n-type SnO_2 film doped with other dopants such as Sb [7] or F [8]. Conductive film of In_2O_3 was reported in two independent patents [9, 10] the first time in 1947, followed by two other researches showing Sn-doped In_2O_3 is n-type transparent conductor [11, 12]. Nowadays, In_2O_3 becomes the most important n-type TCM in the

market. For later decades, very many other n-type TCMs have been discovered but the most interesting one among these is ZnO [13, 14]. There are several textbooks [15, 16] presenting and reviewing state-of-the-art progress and applications of ZnO, which shows how much this material is interesting. More updated information about n-type TCMs can be seen in a recent topical review paper [17]. Unlike n-type TCMs which were developed rapidly in both number of candidates and quality of processing after the first one CdO was discovered [4, 5], p-type TCMs experienced an amazing stagnation in design and fabrication. 90 years after CuI was identified as the first promising p-type TCMs [4, 5], $CuAlO_2$ had been explored by Kawazoe and his co-workers [18] as the next candidate. This was a significant breakthrough because it brought out a design principle for p-type TCMs based on hybridization between d-orbitals of metals and p-orbitals of anions in valence bands. Inspired by this rule, a series of Cu^{+1}-based p-type oxides have been designed [19] such as $CuAlO_2$ [18, 20], $CuCrO_2$ [21, 22], $CuInO_2$ [23, 24, 25], $CuScO_2$ [26], $CuYO_2$ [27], $CuGaO_2$ [28] and $SrCu_2O_2$ [29, 30]. There were other researches extending to other chalcogen-based compounds like LaCuOS [31, 32], $LaCuOS_{1-x}Se_x$ [33], BaCuChF (Ch=S,Se,Te) [34, 35, 36] and $Sr_3Cu_2Sc_2O_5S_2$ [37]. In addition, other cations such as M = Co, Rh and Ir (ZnM_2O_4) [38] and Cr (Cr_2O_3, Cr_2MnO_4, $LaCrO_3$) [39, 40, 41, 42] were also used to design novel materials. However, these compounds have the same drawback: low hole mobility of around 1 cm^2/Vs. Recently, some researches go beyond the traditional rule by using post-transition metals such as Sn, B and Bi and obtain higher performance p-type TCMs including SnO [43, 44, 45], B_6O [46], and Ba_2BiTaO_6 [47].

So far, some oxides such as In_2O_3, ZnO, SnO_2, Ga_2O_3, PbO, PbO_2 are the best n-type TCMs which have been used as transparent electrodes in many devices including smartphones, tablets and tablet PCs (personal computers), notebooks, all-in-one PCs, monitors, TV (television) displays, electronic paper, OLED (organic light-emitting diode) lighting, flexible electronics, OPV (organic photovoltaics), gas sensor... [48, 49]

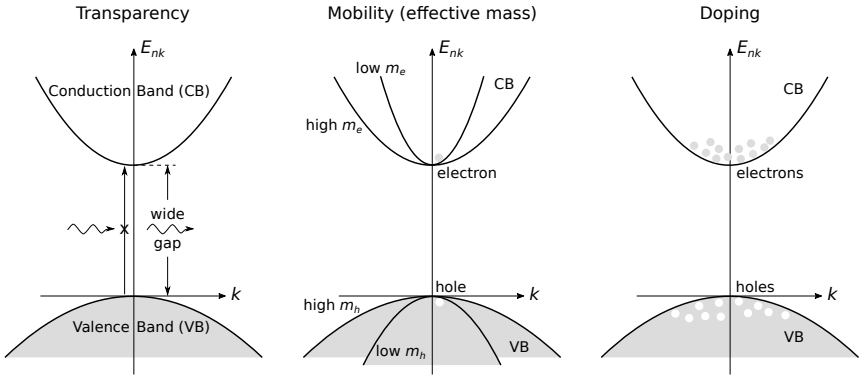

Figure 1.1: The fundamental properties of TCMs in association with their electronic band structures.

Fig. 1.2, for instance, presents a structure of solar cell using tin-doped indium oxide (ITO) film working as a transparent electrode. In principle, this structure includes an intrinsic material layer sandwiched between thin n-type and p-type layers. The electron-hole pairs are mainly generated in the intrinsic layer through photon-absorption process. The electrons and holes are separated to the n- and p-type terminals with enhancement by space-charge electric field, respectively, which forms a potential bias between two terminals. To extract a voltage, we need to utilize electrodes in contact with the n-type and p-type layers. From the logical implication, metals are the best choices because of their electrical conductivity, however, they reflect visible light significantly because of plasma resonance effect [50]. This prevents light from outside going into the active layer. The solution for this problem is to use a transparent electrode such as ITO thin film. In principle, because of its wide optical gap, ITO allows visible light to go through and then reach the active layer. This film can also be highly doped, therefore, exhibits high conductivity and can work as an electrode. More details about operation of solar cell can be found in Ref. [51].

Another example of current application of n-type TCMs, a so-called electronic paper (e-paper), is presented in Fig. 1.3. The fundamental elements are millions of microcapsules with diameters in the range of

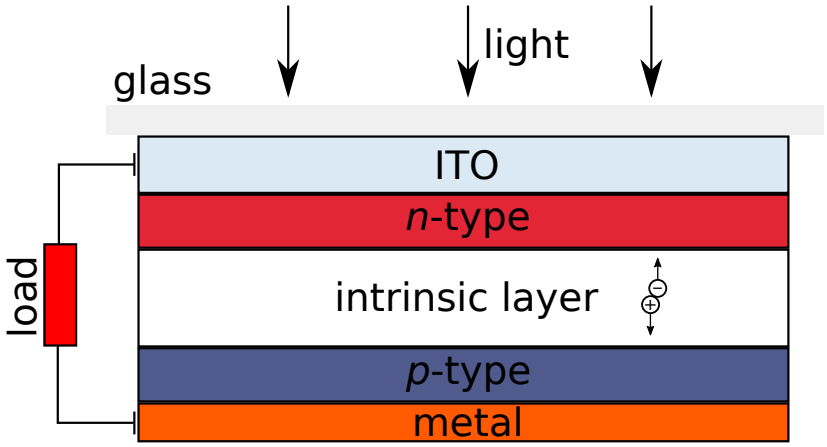

Figure 1.2: The structure of a *p-i-n* organic solar cell using ITO film as a transparent electrode at the front contact. The *n*- and *p*-type layers are heavily doped.

30-300 μm [52]. These microcapsules contain clear liquid and dispersive pigment micro-particles (white and black). These white and black micro-particles are positively and negatively charged respectively. The white micro-particles are regularly rutile TiO_2 with average diameters of 0.5 μm because they exhibit high reflectivity. Each microcapsule is controlled by a metal electrode on the backplane by switching voltage through electronic circuits. On the frontplane, the microcapsules are contacted with a TCM film, *e.g.* ITO. When a positive (negative) voltage is applied into a microcapsule, the white (black) micro-particles are pulled to frontplane while the black (white) ones are attracted to and located at the backplane. By controlling the voltages of matrix of metal electrodes, we can create specific white and black regions on the frontplane. The TCM film allows light to shine through itself and reach to the top of microcapsules. Consequently, viewers from the frontplane can distinguish the contrast between white and black regions. In addition, TCM film is conductive and therefore, charged inductively creating positive and negative charged regions. Even if the voltages applied into matrix of metals electrodes are off, the white and black regions still remain. The operational combination of microcapsule and metal electrode

is a pixel of display. E-paper possesses much advantages in comparison with liquid crystal displays (LCDs). First, this has paper-like readability with wider viewing angle because its high contrast is based on a reflective mechanism. Second, power consumption is much less than LCDs display. The voltage is only applied in charging process and the value of bias voltage is also much smaller, around 4-5 V (as seen in current ePaper Adapter Datasheets). Third, the structure of e-paper is thinner and lighter. We can see e-paper is more widely used in Amazon kindle or electronic price tags in supermarkets. More details about this sort of device can be seen in Ref. [48].

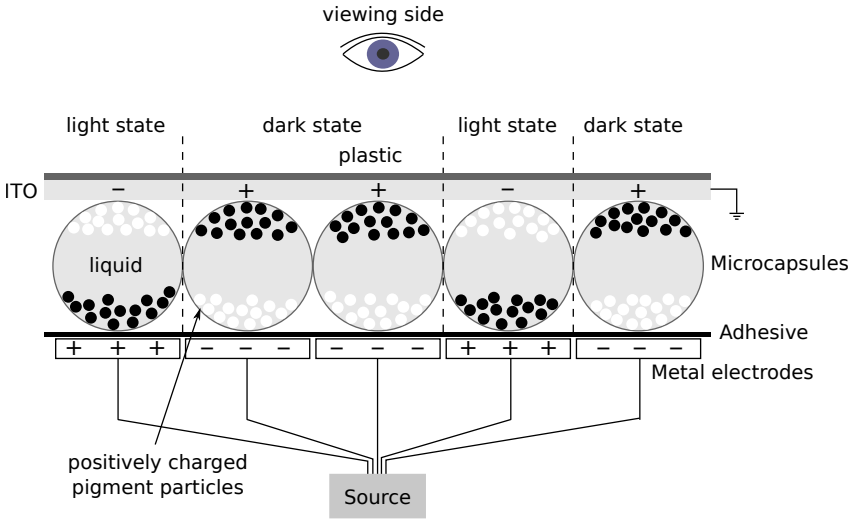

Figure 1.3: Schematic cross-section view of the electronic paper.

Because the demand for energy and energy saving or usage of smart and modern devices keeps increased yearly, the transparent conductive film market has growth with incredible rate in years. The value of this market is forecasted to reach to $5.86 billion by 2020 [53]. The most widely used TCM film in technologies is ITO with approximately 90% of revenue. In general, the best n-type TCMs have been investigated comprehensively and used in many commercial applications [16, 54, 48, 49, 55]. People are fairly satisfied with the best n-type TCMs because

they meet all necessary requirements for applications such as high mobility/conductivity, high transparency and high electron-doping concentration, $\sim 10^{21}$ cm^{-3}. The current researches on n-type TCMs, therefore, mainly focus on improvement of processing and synthesis to obtain higher quality films with lower price [17, 16, 54, 48, 49, 55]. For instance, ITO is currently the most popular n-type TCM but In is not an abundant-earth element leading to expensive ITO-used products. Researchers, therefore, proposed ternary or quaternary oxides in which In is partly replaced by other more abundant elements such as Zn, Ga [56, 57, 58, 59, 60, 61]. Another way is to fabricate n-type TCMs in amorphous phases to lower expenditure, which is considered through both experimental [62, 63, 2, 64, 65] and theoretical [66, 67, 68] works. On the other hand, p-type TCMs do not have a boost in both fundamental researches and applications. As mentioned above, the current p-type TCMs are falling behind their counterparts, n-type TCMs, in terms of carrier mobility. In experiment, mobility of carriers depends significantly on method of manufacture and morphologies of samples (single crystal, polycrystalline, amorphous or thin-film). In Tab. 1.1, we collect experimental data for most of current p-TCMs including proccessing methods, dopants, concentration of holes and hole mobility. It is interesting to see that, the highest hole mobility p-TCM is a non-oxide compound, γ-CuI. It has cubic space group and has been rather well-studied [69]. The optical band gap is experimentally confirmed of about 3-3.1 eV [70, 71, 69, 72, 73]. A record of its hole mobility is obtained with 43.9 cm^2/Vs for γ-CuI crystalline structure at low concentration of hole 4.3×10^{16} cm^{-3} [71]. This material can be unintentionally p-doped because Cu vacancies activate as an acceptor located about 26 meV above VBM [73]. Recently, several studies tried to develop applications based on CuI such as organic solar cell [74], "transparent p-CuI/n-ZnO heterojunction diodes" [75] and hole-transport channel in photoelectrocatalytic applications [76]. On the other hand, most of oxide p-TCMs are less impressive in terms of hole mobility. The hole mobility in transition-metal-based (mostly Cu) p-type TCMs cannot be

over 10 cm^2/Vs. Exceptionally, novel p-type TCMs based-on Sn^{2+} or Bi^{3+} which was reported recently show a breakthrough in hole mobility. B_6O is another compound computationally identified to show low hole effective mass [46] but there has not been many experimental studies to measure its hole mobility. The only one we have known [77] reported a very low hole mobility of 0.1-1 cm^2/Vs. This might be explained as a low crystalline quality mentioned in the article. These preliminary achievements are significant, however, still not good enough in comparison with the best current n-type TCMs. To demonstrate the large gap in mobility between the current n- and p-type TCMs, we also reviewed many experimental works and presented their data in electron mobility (see Tab. 1.2) for n-type TCMs. Most of them exhibit electron mobility at the order of 100 cm^2/Vs.

Table 1.1: The current p-type TCMs, fabrication methods (abbreviations of some methods are at the bottom of this table), sorts of dopants used, hole-carrier concentrations C (in unit cm^{-3}) and mobilities μ (in unit cm^2/Vs). These values are extracted from experimental measurements (as cited references) at room temperature. The values of mobility depend on morphologies of fabricated samples such as single crystal, polycrystalline, amorphous, thin-film,...

p-TCMs	Processing	Dopants	C (cm^{-3})	μ (cm^2/Vs)
γ-CuI	I vapor	Undoped	1-26 $\times 10^{19}$	1.6-5.0 [5, 69]
	I vapor	Undoped	1.3-8.1 $\times 10^{18}$	6-11.1 [70]
	HTM	Undoped	4.3×10^{16}	43.9 [71]
	I vapor	Undoped	5×10^{18}	6 [75]
	VEM	Undoped	1.3-3 $\times 10^{19}$	1.4-20.6 [72]
	†	Undoped	0.1-8.9 $\times 10^{19}$	2.4-9 [73]
$CuAlO_2$	PLD	Undoped	1.3×10^{17}	10.4 [18]
	PLD	Undoped	2.7×10^{19}	0.1 [20]
	Sputtering	N	2.6×10^{17}	1.2 [78]
	Melting	Undoped	-	3^{ab}; 0.1^{c} [79]
$CuCrO_2$	Sputtering	Mg	-	~ 0.1 [21]
	Sputtering	Undoped	4.8×10^{17}	~ 11.2 [80]
	Sputtering	N	1.4×10^{20}	0.8 [81]
	Sputtering	Undoped	4.2×10^{18}	0.3 [82]
	Sputtering	Mg	1.2×10^{21}	0.2 [83]

Continued on next page

Continuation of Table 1.1

p-TCMs	Processing	Dopants	C (cm^{-3})	μ (cm^2/Vs)
Cr_2O_3	SPT	Mg & N	$\sim 10^{19}$	~ 0.1 [39]
	EBE	Mg	-	$\sim 10^{-4}$ [84]
Cr_2MnO_4	SPT	Li	$> 10^{17}$	< 1 [41]
$LaCrO_3$	Epitaxy	Sr	7.5×10^{21}	0.04 [42]
Cu_2O	AALD	Undoped	$\sim 10^{16}$	5.3 [85]
$CuInO_2$	Sputtering	Intrinsic	1.6×10^{19}	0.2 [86]
$CuScO_2$	HTSSR	Undoped	0.5×10^{20}	0.05 [87]
	HTSSR	Mg	4.5×10^{20}	0.03 [87]
	PLD	Mg	3.5×10^{17}	0.09 [88]
	PLD	O & Mg	8.5×10^{17}	0.26 [89]
$CuYO_2$	Sputtering	Ca	$\sim 10^{19}$	~ 1 [90]
	HTSSR	Undoped	0.26×10^{19}	0.04 [87]
	HTSSR	Ca	3.3×10^{19}	0.05 [87]
$CuGaO_2$	PLD	Undoped	1.7×10^{18}	0.23 [28]
	PLD	Undoped	5×10^{17}	0.2 [91]
	sol-gel SC	Mg	3×10^{16}	2 [92]
	sol-gel SC	Zn	3.5×10^{16}	2.3 [92]
$SrCu_2O_2$	PLD	K	6.1×10^{17}	0.46 [29]
	PLD	Ca	1.3×10^{17}	3.8 [93]
	PLD	Undoped	4×10^{16}	6.7 [94]
$ZnRh_2O_4$	HTSSR	Undoped	$\sim 10^{21}$	0.1 [95]
$ZnCo_2O_4$	Sputtering	Undoped	2.8×10^{20}	> 0.2 [96]
LaCuOS	R-SPE	Undoped	10^{19}	0.5 [97]
	R-SPE	Se	$\sim 10^{19}$	~ 1 [98]
	R-SPE	Undoped	$< 10^{19}$	0.5 [99]
LaCuOSe	R-SPE	Undoped	2×10^{19}	8 [98]
	R-SPE	Mg	2.2×10^{20}	4 [98]
BiCuOSe	PLD	Ca	5×10^{20}	4 [34]
BaCuSeF	PLD	Undoped	1.7×10^{18}	1.6 [34]
BaCuTeF	PLD	Undoped	1.3×10^{20}	8 [34]
Cu_3TaS_4	PLD	Undoped	5-7 $\times 10^{19}$	0.2-0.4 [34]
SnO	PLD	Undoped	2.5×10^{17}	2.4 [43]
	PLD	Undoped	2-9 $\times 10^{17}$	0.4-0.6 [44]
	Sputtering	Undoped	$\sim 10^{18}$	4.8 [100]
	EBE	Y & Sb	10^{17}-10^{19}	0.1-2.6 [101]
	PLD	Undoped	$\sim 4.9 \times 10^{19}$	2.1 [102]
	PLD	Undoped	2.5×10^{17}	2.4 [103]
	Sputtering	Undoped	2.2×10^{17}	18.7 [104]
B_6O	HTSSR	Undoped	10^{17}	0.1-1 [77]

Continued on next page

Continuation of Table 1.1

p-TCMs	Processing	Dopants	C (cm^{-3})	μ (cm^2/Vs)
Ba_2BiTaO_6	PLD	K	10^{14}	30 [47]

HTM: Hydrothermal method
VEM: Vacuum evaporation method
†: Chemical reaction of polycrystalline Cu_3N with solid/vapor phase of iodine
PLD: Pulsed laser deposition
EBE: Electron beam evaporation
SPT: Spray Pyrolysis Technique
AALD: Atmospheric atomic layer deposition
^{ab}: ab-plane; ^{c}: c-plane
HTSSR: High temperature solid state reaction
sol-gel SC: sol-gel spin coating
R-SPE: Reactive solid phase epitaxy

In many applications mentioned above, the use of n-type TCMs meets the needed requirements. Why high mobility p-type TCMs are still an important issue? The answer is that p-type TCMs are irreplaceable parts of some devices, for example, transparent electronics or optoelectronics. We will provide two examples in the following paragraphs.

Table 1.2: The current n-type TCMs, fabrication methods (abbreviations of some methods are at the bottom of this table), sorts of dopants used, electron-carrier concentrations C (in unit cm^{-3}) and mobilities μ (in unit cm^2/Vs). These values are extracted from experimental measurements (as cited references) at room temperature. The values of mobility depend on morphologies of fabricated samples such as single crystal, polycrystalline, amorphous, thin-film,...

n-TCMs	Processing	Dopants	C (cm^{-3})	μ (cm^2/Vs)
CdO	MOCVD	In	-	$\sim$ 200 [105]
	VPT	Undoped	$\sim 0.94 \times 10^{18}$	$\sim$ 330 [106]
	PLD	Sn	4.74×10^{20}	609 [107]
	MOCVD	Undoped	2.23×10^{20}	307 [108]
	VEM	Sm	2.57×10^{20}	43.3 [109]
SnO_2	CVD	Sb	8.5×10^{15}	260 [110]
	CVD	Sb	8.6×10^{16}	240 [110]

Continued on next page

Continuation of Table 1.1

n-TCMs	Processing	Dopants	C (cm^{-3})	μ (cm^2/Vs)
	CVD	Sb	2.2×10^{18}	150 [110]
	PLD	Ta	2.7×10^{20}	83 [111]
	PLD	Sb	$\sim 10^{19}$	~ 40 [112]
ZnO	VPT	Undoped	6×10^{16}	205 [113]
	a	b	10^{15}-10^{20}	50-230 [2, 49]
	PLD	Undoped	3×10^{16}	155 [114]
	Sputtering	Al	3.6×10^{20}	41.3 [115]
	Sputtering	Al	8×10^{20}	17 [116, 117]
In_2O_3	PVD	-	3-9 $\times 10^{17}$	160 [118]
	ST	Sn	0.1-6 $\times 10^{20}$	30-70 [12]
	Sputtering	Undoped	10^{17}-10^{20}	< 10 [119]
	VEM	Undoped	$> 3.5 \times 10^{19}$	25-60 [120]
	VEM	Undoped	4.69×10^{20}	74 [121]
	EBE	Sn	0.46-8.6 $\times 10^{20}$	43-79 [122]
	Flux	Sn	1.6×10^{20}	100 [123]
	Sputtering	Sn	6×10^{20}	~ 25 [124]
	TRE	Mo	2.5-3.5 $\times 10^{20}$	80-130 [125]
	PLD	Mo	1.9×10^{20}	95 [126]
	Sputtering	H	1.4-1.8 $\times 10^{20}$	98-130 [127]
	Sputtering	H	1.5×10^{20}	140 [128]
	Sputtering	Sn	10^{21}	40 [129]
Ga_2O_3	Verneuil	Undoped	10^{18}	80 [130]
	FZM	Undoped	1.2-5.2 $\times 10^{18}$	2.6-46 [131]
	EFG	Undoped	10^{17}	153 [132]
	-	Undoped	8×10^{16}	~ 150 [133]
$BaSnO_3$	HTSSR	La	8×10^{19}	320 [134]
	PLD	La	4.4×10^{20}	70 [134]
	HTSSR	La	8-10 $\times 10^{19}$	103 [135]
	PLD	La	$\sim 3 \times 10^{20}$	> 75 [136]
	MBE	La	-	150 [137]
$ZnSnO_3$	Sputtering	Undoped	$\sim 8 \times 10^{19}$	~ 20 [138]
	Sputtering	Undoped	$\sim 2 \times 10^{19}$	~ 25 [139]
	Sputtering	Undoped	$> 2 \times 10^{19}$	< 25 [140]
$InGaZnO_4$	Sputtering	Undoped	1.2×10^{20}	24 [141]
	Sputtering	Undoped	$\sim 10^{16}$	35 [142]
	PLD	Undoped	$\sim 10^{20}$	15 [143]
	Sputtering	Undoped	$\sim 6 \times 10^{19}$	> 20 [144]
$Zn_2In_2O_5$	Sputtering	Undoped	5×10^{20}	~ 30 [145]
	Sputtering	Undoped	5.42×10^{20}	16.2 [146]

Continued on next page

Continuation of Table 1.1

n-TCMs	Processing	Dopants	C (cm^{-3})	μ (cm^2/Vs)
MOCVD: Metalorganic chemical vapor deposition				
VPT: Vapor phase transport				
a: Reviewed from many papers				
b: Reviewed from many papers				
PLD: Pulsed laser deposition				
VEM: Vacuum evaporation method				
CVD: Chemical vapor deposition				
PVD: Physical vapor deposition				
ST: Spray technique				
EBE: e-beam evaporation				
TRE: Thermal reactive evaporation				
FZM: Floating zone method				
EFG: Edge-defined film-fed growth				
HTSSR: High temperature solid state reaction				
MBE: Molecular beam epitaxy				

Fig. 1.4 shows schematically structure of transparent solar cell. This device has been an interesting topic in the renewable energy. Nowadays most of office buildings in big cities are constructed by glasses. As a consequence, these buildings have to equip air conditioners to keep them cool and comfortable. Basically, nearly a half of energy of solar spectrum lies in infrared electromagnetic waves. The heating effect in glass-buildings is, in fact, caused by infrared radiation. Thus, the problem is that how we can prevent this drawback but still keep buildings to be illuminated. Transparent solar cell is an ideal solution [147, 148, 149, 150, 151, 152]. This type of device when attached to glass-walls can absorb infrared light to generate electricity but still allow a part of visible light to transmit through. As shown in Fig. 1.4, the back-contact is now a p-type TCM layer instead of a metallic one as in the traditional solar cells (see Fig. 1.2). The incident solar photons come to and go through the front-contact, ITO, will interact with a thick absorber layer which is n-type doped and generate electron-hole pairs. The absorber layer

should exhibit weak optical absorption in visible region and strong absorption in infrared region, for instance, chloroaluminum phthalocyanine [153]. As a result, most of the visible light can be transmitted through the thin p-type region and TCM layer. We can see that the high mobility p-type TCM layer in this case plays an important role. This layer operates as a transparent electrode as it can simultaneously conduct holes and allow the visible light to get through. In principle, it needs to show a high electrical conductivity. From Drude's theory [154], the conductivity is proportional to the carrier density and mobility as $\sigma = en\mu$ (e is the elementary charge). We, therefore, can enhance the conductivity by controlling n or μ. However, because of the plasmonic effect, we cannot dope the p-type TCM electrode too heavily as this can lead to a visible light reflection. Because of this limit in doping not only high conductivity but more specifically, high mobility materials are needed. It is worth noting that the choice of TCM for PV application also depends on other factors such as workfunction, band alignment, processing, cost,...

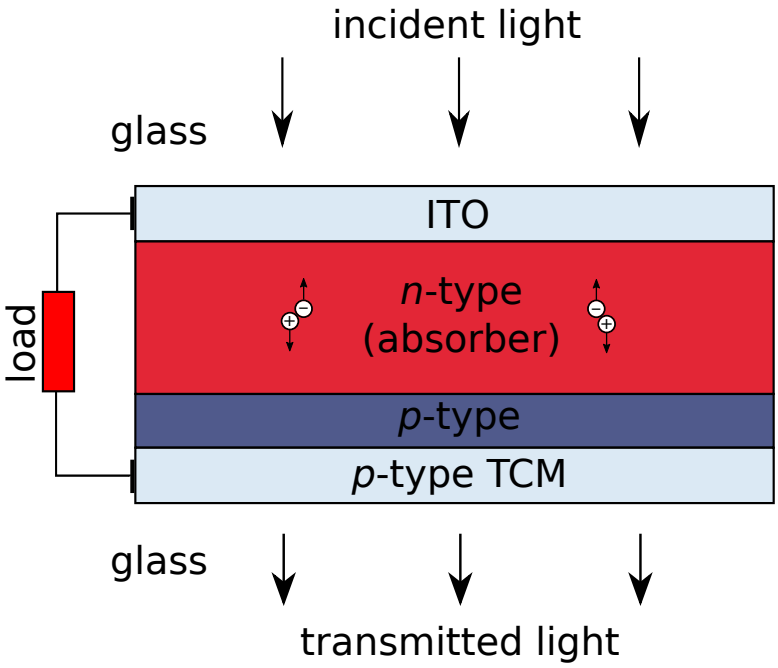

Figure 1.4: Schematic cross-section view of the transparent solar cell.

Another promising technology, in which p-TCMs are fundamental materials, is transparent electronics. In this case, we need to fabricate transparent transistors used in many electronic circuits. The two most important devices in transparent electronics are thin-film transistor (TFT) and metal-oxide-semiconductor field-effect transistor (MOSFET). Fig. 1.5 shows structure of transparent thin-film transistor (TTFT). The materials used for fabrication of channel are fundamental. This channel can be n-type or p-type doped. The conducting property of it is controlled by potential applied into gate electrode (G). For example, if the channel is n-type, a negative potential applied to G can deplete concentrations of carriers (electrons) in the region around the contacting surface between insulator layer and conducting channel. This decreases the conductivity of channel and therefore lowers the instensity of electric current from source electrode to drain electrode. So far, fabrication of n-type channel has obtained a tremendous success [3, 64] because the best n-type TCMs show high mobility that satisfies the fast response requirement for transistor applications. Among several best n-type TCMs, ZnO and multi-component Ga_2O_3-In_2O_3-ZnO (GIZO) are the most used compounds (in about 75 % researches). On the opposite, p-type TCMs are far left behind in this field. The reason is that the limitation in hole mobility cannot help TTFTs with p-channel to achieve high performance as their counter parts. However, there have been many researches trying to use the current p-type TCMs to manufacture p-channel TTFTs, for instance, SnO [43, 100, 44, 155]. With SnO, other researchers even went further to fabricate complementary metal oxide semiconductors (CMOS) structures which are key elements in microelectronic circuits [156, 157]. The heterostructure of transparent p-n junctions such as p-$SrCu_2O_2$/n-ZnO [158] and p-$ZnRh_2O_4$/n-ZnO [159] were also reported. Another research combined SnO and Cu_2O as p-type channel [160].

The two examples mentioned above are demonstration of the potential and importance of p-type TCMs. We can see that discovery of novel candidates with higher hole mobility is very critical. If successfully de-

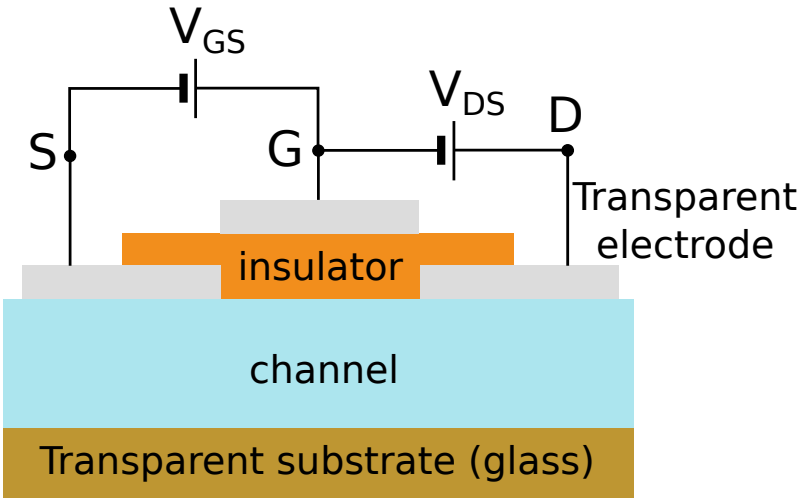

Figure 1.5: Schematic cross-section view of the transparent thin-film transistor. S, G and D stand for source, gate and drain electrodes respectively.

signed or discovered, these materials can open the new era of transparent electronics.

1.2 How to accelerate the design of novel *p*-type TCMs?

As mentioned above, most of current p-type TCMs exhibit very low hole mobilities leading to a blockage in development of many modern devices. Findings of underlying mechanisms those drive hole mobility are very important to speed up design of novel p-TCMs. From the simple Drude's transport model, mobilities of carriers μ are managed by their effective mass m and scattering time τ through the expression $\mu = e\tau/m$ (e is elementary charge). The effective mass directly associates to the electronic band structures of materials. Fig. 1.6 presents simply the electronic band structures and density of states (DOS) of current n-TCMs and p-TCMs. From the chemical view, the conduction band minimum (CBM) of the current n-type TCMs is mainly composed of two s-orbitals of metal (M) and oxygen. S-orbital, in fact, is less localized and non-direction-

dependent (spherical symmetry). As a result, the overlap between these s-orbitals are frequently significant, leading to strong chemical hybridization and therefore, very dispersive conduction bands (very low electron effective masses). This tendency was verified through a large set of very low electron effective mass oxides in a recent high throughput (HT) computing [161]. In different circumstances, most of current p-type TCMs have valence bands based on d-orbitals of metals and p-orbitals of oxygen or other anions such as sulfur, selenium or tellurium. The valence bands are commonly created by hybridization M-d/Ch-p (Ch = O, S, Se, Te). This type of bonding shows weaker interactions because d-orbitals are very localized and direction-dependent. It depends on specific p-TCMs, in some cases, there are also (nearly) non-bonding states of M-d or Ch-p or both of them standing in valence bands. All these factors result in very flat valence bands (high hole effective masses) at valence band maximum (VBM).

For scattering rate τ, it *de facto* depends on different scattering mechanisms. Carriers can be scattered by phonons, ionized and neutral impurities, grain boundaries, *et cetera*. While the former is an intrinsic factor and cannot be avoided, the later ones can be improved through processing of purity and microstructure. The scattering rate of a given electronic state with phonons depends not only on el-ph scattering matrix but also on the electronic DOS around that (more details will be discussed in Chp. 4). It is worth noting that electronic DOS around CBM or VBM directly relates to dispersion of electronic bands and therefore, the effective mass. Therefore, effective mass is a critical quantity because it roughly impacts twice the carrier mobility. For el-ph scattering matrix, its strength depends on how the self-consistent potential of system changes against vibrations of atoms in the lattice. To our best knowledge, there is no research investigating this aspect (statistically) systematically to be able to elucidate it and propose some general rules. Recently, when investigating some systems, we have seen that in the strong polarized materials (*e.g.* materials with ionic bondings),

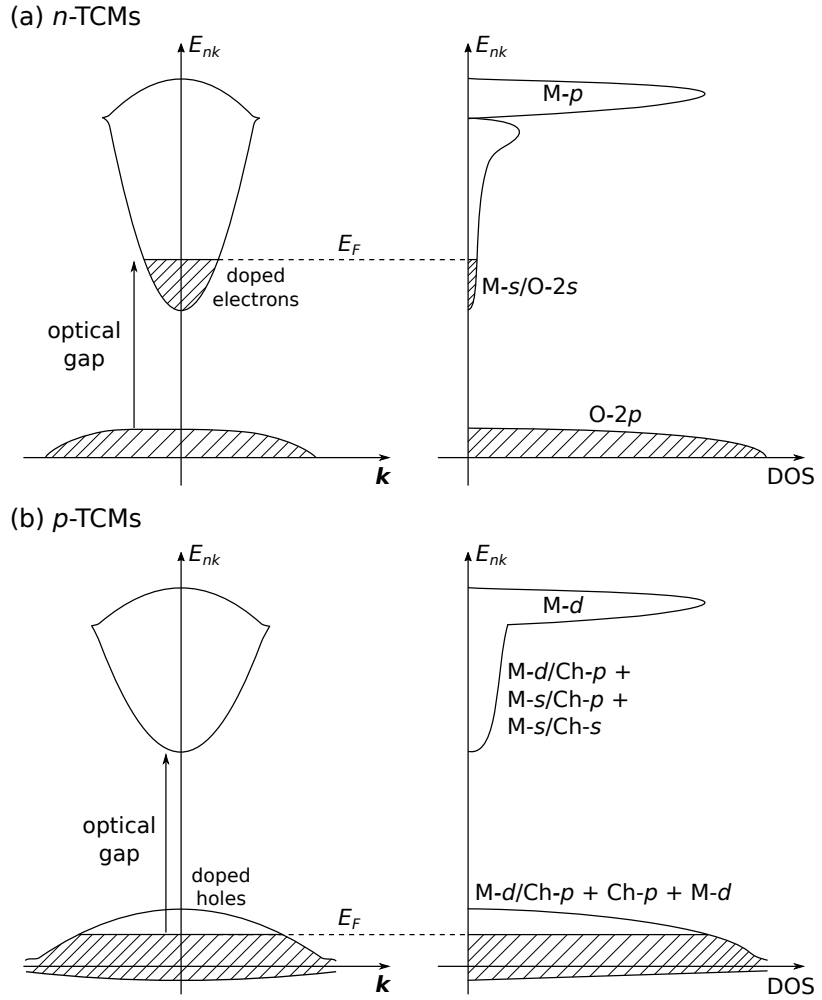

Figure 1.6: Schematic electronic band structures (left) and density of states (right) of typical current (a) n-TCMs and (b) p-TCMs. M = metals and Ch = O, S, Se, Te.

carriers scatter with phonons stronger. This might be meaningful for HT approach/computational design as the polarization can be roughly associated with electronegativity of elements in materials.

The understanding of fundamental principles is necessary to accelerate the discovery and design of novel materials with requisite properties. These more general rules will guide both experimentalists and theorists to target on smaller groups of compounds instead of trying to test one

by one in larger space. This not only strengthens probability of finding promising candidates but also reduces a large amount of money and time spending on researches. In 2003, Zunger generalized seven rules for "practical doping principles" for wide-bandgap semiconductor through his computational studies [1]. This has constantly motivated many researches considering doping properties of different fields including TCMs [162, 163], photovoltaics [164, 165], thermoelectrics [166, 167],... More recently, considering how cations influence the hole effective mass of oxides, Hautier *et al.* [45] performed a HT computing using database of thousands of binary and ternary oxides available in Inorganic Crystal Structure Database (ICSD) [168]. This work identified unconventional low hole effective mass *p*-TCMs whose valence bands are formed by *s*-orbitals of cations and *p*-orbitals of oxygens. The key difference here is the new set of cations including Sn^{2+}, Pb^{2+}, Sb^{3+} [45] and Bi^{3+} [47] which have active lone-pair *s*-electrons in some conditions. When these cations exist in several specific oxides, their *s*-character lone-pairs will be activated and hybridize with O-2*p* leading to curvy top of valence bands [169] (low hole effective mass). The authors not only found a consistence with an exceptional low hole effective mass *p*-type TCM, SnO, observed previously but also extended more generally to a larger set of promising cations.

To be aware of the important roles of critical criteria for the design of novel materials, in this thesis we continue to investigate and supplement other rules for the design of *p*-type TCMs. In addition, we will also go beyond traditional consideration when implementing HT search for non-oxide materials in order to find out other exceptional high hole mobility *p*-TCMs. To help readers, we will briefly discuss the definition of 'effective mass'. This is one of the most important physical quantities used to describe electrical transport characteristics in semiconductors/insulators. In Chp. 4 of this thesis, we employ band theory and Boltzmann's formalism to simulate the electrical transport, however, the basic theory for polaronic transport will be shortly mentioned for a discrimination. The

explanation for HT computing will be showed in the following section as well.

1.3 Basic concepts of effective mass, polaronic transport and high throughput computing

Effective mass: In solid-state physics, transport properties or optoelectronic properties are driven by characteristics of electronic band structures around energy extrema in the Brillouin zone (BZ) of reciprocal space. Deriving from the concept of wave packet in quantum mechanics (first used to describe the motion of free quantum particle), the 'group velocity' of electron is also defined for electron in a given quantum state in the crystal [50, 154]

$$\mathbf{v} = \frac{d\omega}{d\mathbf{k}} = \frac{1}{\hbar}\frac{d\epsilon_{n\mathbf{k}}}{d\mathbf{k}}, \tag{1.1}$$

where $\mathbf{v}$ is the group velocity (from now on, the bold symbols in equations represent for vector quantities), ω is the angular frequency, $\mathbf{k}$ is the wave vector, $\hbar$ is the reduced Planck's constant, and $\epsilon_{n\mathbf{k}}$ is the band energy of band n^{th} at wave vector $\mathbf{k}$. It is supposed that the electron (in crystal) moves under the action of an external field. In the context of classical mechanics, we have

$$\begin{aligned} \mathbf{F} &= \frac{d\mathbf{p}}{dt} = \hbar\frac{d\mathbf{k}}{dt} \\ \mathbf{F} &= m^*\mathbf{a} = m^*\frac{d\mathbf{v}}{dt}, \end{aligned} \tag{1.2}$$

where $\mathbf{F}$, m^* and $\mathbf{a}$ are the force applied on electron, its 'effective mass' and acceleration, respectively. Since from (1.1),

$$\mathbf{a} = \frac{d\mathbf{v}}{dt} = \frac{1}{\hbar}\frac{d}{dt}\frac{d\epsilon}{d\mathbf{k}} = \frac{1}{\hbar}\frac{d^2\epsilon}{dk^2}\frac{d\mathbf{k}}{dt} = \frac{1}{\hbar^2}\frac{d^2\epsilon}{dk^2}\mathbf{F}, \tag{1.3}$$

we, therefore, can define the effective mass as

$$\frac{1}{m^*} = \frac{1}{\hbar^2}\frac{d^2\epsilon}{dk^2}. \tag{1.4}$$

To take into account the anisotropic properties of $\epsilon_{n\mathbf{k}}$, the effective mass is regularly written in a tensor,

$$\left(\frac{1}{m^*}\right)_{\alpha\beta} = \frac{1}{\hbar^2}\frac{\partial^2\epsilon_{n\mathbf{k}}}{\partial k_\alpha \partial k_\beta}, \tag{1.5}$$

where α and β are Cartesian coordinates. This is known as quadratic representation (approximation) of effective mass and widely used in solid-state physics. However, this definition is typically broken down when band energies are degenerate at extrema in the BZ. This was theoretically foreseen by Luttinger and Kohn [170]. In fact, the electrical transport properties can be contributed by different bands and pockets. Thus, it is more reasonable to define an average effective mass which takes into account these complexities by integrating over the BZ. Deriving from semi-classical Boltzmann transport theory (more details will be presented in section B.7 of Apd. B), we have the conductivity tensor with constant relaxation time approximation

$$\sigma_{\alpha\beta} = e^2\tau\sum_n \int \mathbf{v}_\alpha(n,\mathbf{k})\mathbf{v}_\beta(n,\mathbf{k})\frac{\partial f(\epsilon_{n\mathbf{k}},\mu,T)}{\partial\epsilon_{n\mathbf{k}}}d\mathbf{k}, \tag{1.6}$$

where e is the elementary charge, τ is the relaxation time and $f(\epsilon_{n\mathbf{k}},\mu,T)$ is Fermi-Dirac distribution at given temperature T and Fermi level μ (corresponding to a given concentration of carrier). It is worth noting that Boltzmann transport theory is restrictively applied for the systems in which carriers are nearly-free. If the carriers are "trapped" in lattice points because of strong el-ph interaction (small polarons) [171], *e.g.* Sr-doped $LaCrO_3$ [42], polaronic transport theory is used to describe their transport characteristics. In this thesis, we utilize Boltzmann framework (see section B.7 of Apd. B) to simulate the transport phenomenon for several materials in Chp. 4, however, the polaronic transport theory will be briefly introduced as well.

In the context of Drude's model, the relation between conductivity, effective mass and concentration of carriers n is

$$\frac{\sigma_{\alpha\beta}}{\tau} = \frac{ne^2}{m^*}. \tag{1.7}$$

From (1.6) and (1.7), we can define an average effective mass tensor

$$\frac{1}{\overline{m}_{\alpha\beta}} = \frac{\sigma_{\alpha\beta}}{ne^2\tau} = \frac{\sum\limits_{n}\int \mathbf{v}_{\alpha}(n,\mathbf{k})\mathbf{v}_{\beta}(n,\mathbf{k})\frac{\partial f(\epsilon_{n\mathbf{k}},\mu,T)}{\partial \epsilon_{n\mathbf{k}}}d\mathbf{k}}{\sum\limits_{n}\int f(\epsilon_{n\mathbf{k}},\mu,T)d\mathbf{k}}. \tag{1.8}$$

Here, we will compute the average effective mass defined in (1.8) using finite difference estimation of (DFT) electronic band structure. However, this approach requires a dense **k**-mesh for the numerical convergence, thus, it might be more costly. An interpolation method for the electronic band structures was developed and implemented in Boltztrap code [172], which helps to improve the convergence. This interpolation, in fact, is Fourier transform of band energies in the real (crystal) space

$$\begin{aligned} \widetilde{\epsilon}_{n\mathbf{k}} &= \sum_{\mathbf{R}} C_{n\mathbf{R}} S_{\mathbf{R}}(\mathbf{k}), \\ S_{\mathbf{R}}(\mathbf{k}) &= \frac{1}{N}\sum_{\{\wedge\}} e^{i\mathbf{k}.\wedge\mathbf{R}}, \end{aligned} \tag{1.9}$$

where $\mathbf{R}$ is the real lattice vector, $\{\wedge\}$ is N rotation symmetries of the crystal, $S_{\mathbf{R}}(\mathbf{k})$ is called star functions which represent all symmetric characters of the crystal. The coefficients $C_{n\mathbf{R}}$ are defined from the initial DFT electronic band structure on a fairly dense **k**-mesh (see section 2 of Ref. [172] for more details). When the analytical form of band energy is defined as (1.9), the integration in (1.8) will be implemented on a much denser **k**-mesh leading to a faster convergence. Recently, the numerical noise of finite difference method has been eliminated by using density functional perturbation theory (DFPT) framework [173]. Moreover, the limitation of effective mass defined in (1.5) due to degenerate band energies has been taken into account in another research [174]. In this work, Mecholsky and co-workers redefined the concept of the effective mass. The authors argued that the degeneracy should be better to describe by using a dimensionless "angular effective mass surface" $f(\theta,\phi)$, with θ and ϕ being spherical angles. This effective mass is defined in the proximity of a given **k**. By using this concept, several effects of the band energy surface such as "band warping", "fluted energy surfaces", or "corrugated

energy surfaces" are also fully described.

Polaronic transport: In Fig. 1.7, when an electron moves in the crystal, its Coulomb attraction and repulsion with positive and negative ions can cause the distortion in the lattice [50, 171]. The displacements of the lattice points can be, in theory, described as phonon exciations [171]. The combination of electron and phonons induced is seen as a new quasi-particle of a so-called *polaron*. The polaron term was first proposed by Landau in 1933 to to describe the motion of an electron in a dielectric crystal [175]. This effect is significantly large in ionic materials (*e.g.* KCl, KBr,...) because of strong Coulomb interactions between electron and ions. In contrary, it is weak in covalent compounds as the electric polarization becomes smaller.

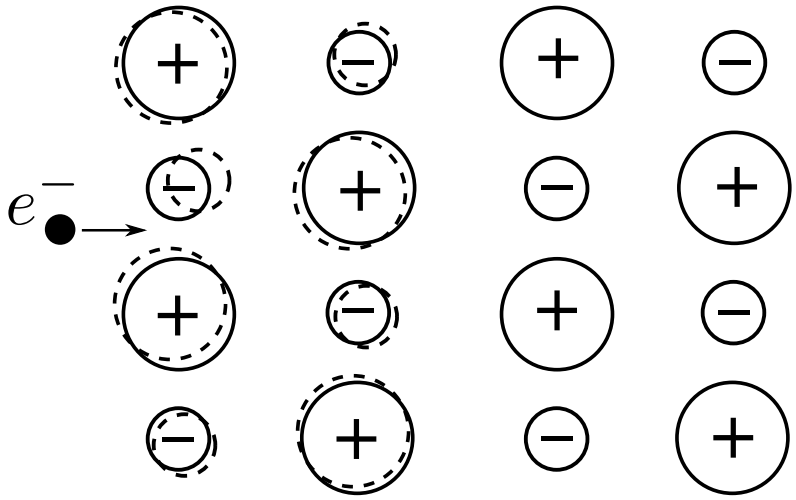

Figure 1.7: An electron moving in a ionic crystal, which can lead to the lattice distortion.

By definition, ones often name these two problems as small and large polarons. If we define an effective size of a polaron as l_p, the large polaron means $l_p > d$ (interatomic distance) and indicates weak el-ph interactions. The electron/hole moves in the crystal with a slight increase of its effective mass and thus, Boltzmann transport framework

(mentioned above) with band theory describes thoroughly the transport process. On the other hand, if the el-ph coupling is strong, we have a small polaron with $l_p \leq d$. In some materials, *e.g.* Sr-doped $LaCrO_3$ [42], the el-ph coupling can be so strong that an electron is "self-trapped" in a single ion. The term "self-trapped" is used in the physical sense that the motion of electron causes lattice distortion and then consequently binds itself to an ion. In this case, the electron/hole can only jump from site to site by thermally activated hopping. The activated mobility in hopping transport can be expressed as [176]

$$\mu = \frac{ea^2\omega_{LO}}{6k_BT} exp\Big(\frac{-E_a}{k_BT}\Big), \tag{1.10}$$

where e is the elementary charge, a is the hopping distance, ω_{LO} is the longitudinal optical phonon frequency, k_B is Boltzmann's constant, T is the temperature and E_a is energy barrier between two sites. The formula (1.10) is derived from an assumption in which the electron mainly couples to LO phonons (Fröhlich model).

High throughput computing: This concept was suggested by computer science community. By definition, "throughput" term refers to a side effect of how much time spending on a task since the time it is submitted until completed. Thus, "high throughput computing" (HT) describes the use of computing resources in a long period of time (for example, a month) to complete many computational tasks. In HT computing, people interest more in how many jobs can be done in a long time instead of how fast the computation is. This differs from the concept of "high performance computing" (HPC) which means completing a job in much less time. To do this, parallel or distributed computing is regularly used.

In our case, HT computing is applied for materials science. We perform many (thousands) tasks corresponding to many (thousands) materials for a particular property. Because the calculation using DFT takes relatively much time (depending on primitive cell of materials), we also

employ HPC using supercomputers. More details about our HT strategy will be presented in section 4.2 of Chp. 4. In contents, this thesis will be organized as follows,

Chapter 1: As mentioned above, this part presented basic concepts, properties and also reviewed the state-of-the-art literature of TCMs including materials processing, applications, materials design, challenging issues, several basic definitions...

Chapter 2: In this chapter, we will consider another criterion for design of high performance TCMs so called "second gap". We will clarify how this factor influences the optical properties of TCMs.

Chapter 3: Another criterion for the design of low hole effective mass Sn^{2+}-based oxides will be pointed out thanks to analyzing geometry structures and local environments between tin and oxygen.

Chapter 4: We will carry on HT computing for non-oxide compounds and see how obtained unconventional candidates outperform the best current *p*-type TCMs in terms of mobility.

Chapter 5: We summarize what we have done and discuss more future perspectives. The benefit of using computational tools to solve problems in materials science and remaining challenges can be mentioned.

Appendices: The computational method mainly used in computations of this thesis is DFT which has become dominant, standard and well-known in computational materials sciences nowadays. There are many textbooks writing systematically and clearly on all aspects of DFT from fundamental theorems, local density approximation (LDA) and general gradient approximation (GGA) for exchange-correlation functionals, pseudopotentials to numerical solution algorithms [177]. As the main contents of this thesis focus on materials sciences, instead of rewriting everything in very detailed chapters, we will organize DFT and relevant theories and methods in the appendices. In each chapter, we will briefly present computational methods to help readers in following information. All the necessary references for more details will be provided.

Chapter 2

Second gap and additional optical absorption in doped-TCMs

TCMs are required to have large enough band gaps (ideally > 3 eV) to ensure their high transparency. In addition, high dopability with n- or p-type of these materials is also another crucial criterion, which intensifies their conductivity. However, the high carrier concentrations present in TCMs lead to possibilities for additional optical transitions from the occupied conduction-bands to the higher empty states above in n-type materials or from the lower occupied valence-bands to the unoccupied states at top of valence band in p-type TCMs. The "second gap" formed by these transitions, therefore, might limit the transparency. A wide second gap (> 3 eV) has been sometimes proposed as a design criteria for high performance TCMs. In this chapter, we will study the influence of the "second gap" on the optical absorption using *ab initio* computations for several well-known n- and p-type TCMs. Specifically, we demonstrate that most known n-type TCMs do not suffer from second gap absorption significantly in the visible range even in the very high doping electron concentration (10^{21} cm^{-3}) regime. On the contrary, the current p-type TCMs partially loose their visible transmission at high doping hole concentrations (10^{21} cm^{-3}) due to second gap effects. We

link this dissimilarity to the different chemistries involved in n- versus typical p-type TCMs. Quantitatively, we show that "second gap" leads to only a moderate loss of transmission (even in p-type TCMs) and suggest that a wide "second gap", while beneficial, should not be considered as a stringent criteria for a working TCMs. The results which will be presented in this chapter are already published in Appl. Phys. Lett. **108**, 201902 (2016).

2.1 Introduction

The properties of importance for TCMs such as transparency, mobility and high dopability can be related to their fundamental electronic structures [178, 179, 46]. This has led to an important body of computationally or chemically driven searches for good TCMs candidates [45, 161, 180, 181, 18, 43, 44, 182, 183, 184]. Those studies have highlighted a series of straightforward design criteria, or necessary properties for a TCM: a large band gap (ideally > 3 eV), a low effective mass (of electrons for n-type and holes for p-type), and a high dopability [1, 185, 163]. To achieve substantial conductivity, TCMs must present high carrier concentrations up to the order of 10^{21} (cm^{-3}). The additional electrons or holes inserted into the conduction band (CB) (for n-type TCMs) or the valence band (VB) (for p-type TCMs) can lead to new optical transitions. When interacting with incident photons, the electrons at the bottom of CB of n-type TCMs can absorb photons and undergo transitions to higher states as illustrated in the left panel of Fig. 2.1. In a similar way, in p-type TCMs (right side of Fig. 2.1), the occupied electrons in lower states can transition up and recombine with the holes at the top of VB. Such second gap transitions, might affect significantly the transparency of TCMs, and therefore appear as another key criteria for the design of transparent conductors. This issue was considered as an important problem [19] but to our best knowledge, there has been no research assessing how quantitatively it can decrease the transparency of

TCM materials.

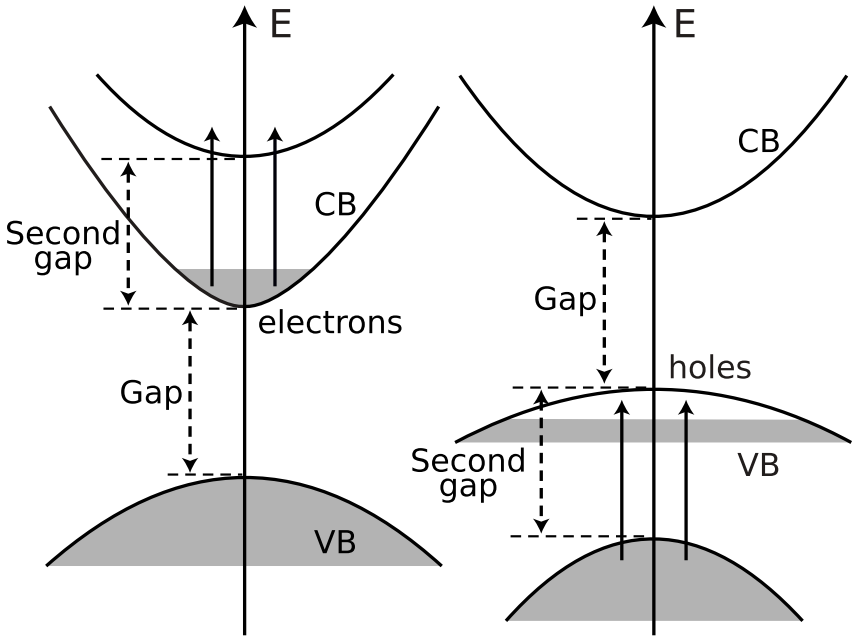

Figure 2.1: New transitions in highly doped TCMs. On the left panel, n-TCMs, electronic transitions come from the bottom of CB to higher energy states. On the right panel, p-TCMs, electronic transitions come from lower energy states to the top of VB.

In this research, we will quantitatively investigate the influence of "second gap" transitions on the transparency of TCMs. The absorption coefficient is computed for different doping concentrations in many well-known n-type: ZnO, In_2O_3, SnO_2 and $BaSnO_3$ and p-type transparent conducting oxides (TCOs): $CuAlO_2$, SnO, LaCuOS and $ZnRh_2O_4$. We show that, at large doping concentrations, the transparency can be lowered by second gap transitions and provide a quantitative estimate of the magnitude of this effect through a so-called visible transmittance quantity (will be defined in section 2.2 below). We also point out a fundamental dissimilarity in second gap effect in different p-type TCOs compared to n-type TCOs. We relate this fundamental contrast to the different types of chemistry present in n- and p-type TCOs. Chemical interactions between atoms will be analyzed clearly.

2.2 Computational methods

Response functions are fundamental physical quantities in condensed matter physics. These functions represent the response of a many-body system to an external field (*e.g.* electromagnetics, strain,...) and connection with different experimental measurements. Dielectric function ϵ is one of the most important quantities. In fact, some optical quantities such as absorption, reflectance,... can be computed through this function. Therefore, in this research, the computation of ϵ depending on doping (electron or hole) concentrations is the main work. The expression of dielectric function ϵ for periodic solid-state systems were done by Adler [186] and Wiser [187] since 1960s. Then the calculations for macroscopic static dielectric constant using DFT were also performed [188, 189]. At present, these calculations are developed in many DFT codes. Here, the Vienna *Ab initio* Simulation Package (VASP) was used [190, 191]. In the approach of VASP [192], the local field effect is included in random phase approximation (RPA). The formulas and relevant quantities are rewritten as follows. The imaginary part of the frequency-dependent dielectric tensor is given by

$$\begin{aligned}\varepsilon^{(2)}_{\alpha\beta}(\omega) = \frac{4\pi^2 e^2}{\Omega} \lim_{q\to 0} \frac{1}{q^2} \sum_{n,n',\mathbf{k}} 2w_{\mathbf{k}} \delta(\epsilon_{n\mathbf{k}} - \epsilon_{n'\mathbf{k}} - \omega)[f(\epsilon_{n'\mathbf{k}}) - f(\epsilon_{n\mathbf{k}})] \\ \times \langle u_{n\mathbf{k}+\mathbf{q}_\alpha} | u_{n'\mathbf{k}} \rangle \langle u_{n\mathbf{k}+\mathbf{q}_\beta} | u_{n'\mathbf{k}} \rangle^*,\end{aligned} \tag{2.1}$$

where α and β refer to the three space directions, ω is the photon energy, e is the elementary charge, Ω is the volume of the cell, q is the incident photon wave vector, $w_{\mathbf{k}}$ are the weights of the different $\mathbf{k}$-points in the irreducible Brillouin zone (IBZ), $\epsilon_{n\mathbf{k}}$ is the energy of n^{th} eigenenergy at $\mathbf{k}$-point, $|u_{n\mathbf{k}}\rangle$ are the Bloch wave functions, and

$$f(\epsilon) = \left(1 + e^{(\epsilon - E_f)/k_B T}\right)^{-1} \tag{2.2}$$

is Fermi-Dirac distribution at the temperature T. Here, E_f is the Fermi level, and k_B is the Boltzmann constant. The real part of the dielectric tensor can be found through the Kramers-Kronig relation:

$$\varepsilon^{(1)}_{\alpha\beta}(\omega) = 1 + \frac{2}{\pi} \mathcal{P} \int_0^\infty \frac{\varepsilon^{(2)}_{\alpha\beta}(\omega')\omega'}{\omega'^2 - \omega^2} d\omega', \tag{2.3}$$

where $\mathcal{P}$ denotes the Cauchy principal value [193].

We introduce the effect of doping by changing the Fermi level so as to reach a certain carrier concentration using the following formulas

$$\begin{aligned} n &= \int_{CBM}^{\infty} f(E) g(E) dE, \\ p &= \int_{-\infty}^{VBM} [1 - f(E)] g(E) dE, \end{aligned} \tag{2.4}$$

where E is the energy, $f(E)$ is the Fermi-Dirac distribution as defined in equation (2.2), and $g(E)$ is the density of state (DOS).

We adopt the rigid band approximation which assumes that the doping does not modify the band structure and only plays a role in the Fermi level. The (dipole) matrix elements

$$\lim_{q\to 0}\frac{1}{q^2}\langle u_{n\mathbf{k}+\mathbf{e}_\alpha q}|u_{n'\mathbf{k}}\rangle\langle u_{n\mathbf{k}+\mathbf{e}_\beta q}|u_{n'\mathbf{k}}\rangle^* \tag{2.5}$$

are determined from the DFT calculations. The dielectric tensor is computed for various Fermi levels at 300 K using equations (2.1) and (2.3). Our implementation relies on computations of the matrix elements with VASP [190, 191] and post-processing including the carrier concentration dependence using the python-based pymatgen code [194].

The optical absorption coefficient is derived from the dielectric tensor as follows [195]:

$$\alpha(\omega) = \frac{2\omega k(\omega)}{c}, \tag{2.6}$$

where c is the speed of light and $k(\omega)$ is the extinction coefficient defined by:

$$k(\omega) = \sqrt{\frac{\sqrt{\varepsilon_1^2(\omega)+\varepsilon_2^2(\omega)}-\varepsilon_1(\omega)}{2}}. \tag{2.7}$$

In this formula, $\varepsilon_1(\omega)$ and $\varepsilon_2(\omega)$ are determined as the average of the three diagonal components of the dielectric tensors $\varepsilon^{(1)}_{\alpha\beta}(\omega)$ and $\varepsilon^{(2)}_{\alpha\beta}(\omega)$, respectively.

We should note that similar computations have been performed recently on various perovskites to also obtain the dependence of carrier concentrations dependence of optical absorption but taking into account the specific dopant specie in a virtual crystal approximation framework [196, 197]. Our approach does not model the type of dopant inserted as we only assumes a rigid band approach and doping setting a given Fermi level (and carrier concentration). Neither does our approach take into account indirect transitions (involving phonons) as well as the increase in reflectivity due to plasmons present in highly doped semiconductors. Here, the hybrid exchange-correlation functional Heyd-Scuseria-Ernzherof (HSE) [198, 199] is utilized to correct the band gaps of materials. More details about DFT, HSE functional are presented in Apd. A and the definition of dielectric function is presented in section B.1 of Apd. B.

In order to provide a quantitative estimate of the effect of the "second gap" transitions, we compute the visible transmittance, which is defined as the fraction of energy in the visible range passing through a thin film of given thickness. It is obtained by the following formula

$$T_V = \frac{\int_{1.8}^{3.2} e^{-\alpha d} I(\omega) d\omega}{\int_{1.8}^{3.2} I(\omega) d\omega}, \tag{2.8}$$

where α and d are the absorption coefficient and the thickness of the thin film, respectively, and $I(\omega)$ is the distribution of the radiation spectrum with ω is photon energy. The energy range of visible photons is chosen from 1.8 to 3.2 eV. Here, we assume that the incident light is perpendicular to the surface of the thin film. As a side note, the reflection of incident light caused by the plasmonic

effect is neglected here as we simply clarify the effect of "second-gap". We also assume a uniform radiation distribution within the visible range from 1.8 to 3.2 eV (simplify solar spectrum distribution).

We have selected a series of well-known representative n-type and p-type TCMs, in particular oxides, covering a diverse range of chemistries. We have considered In_2O_3, ZnO, SnO_2 and $BaSnO_3$ as n-type and $CuAlO_2$, LaCuOS, $ZnRh_2O_4$ and SnO as p-type TCMs. The crystal structures of these materials are shown in Fig. 2.2 and Fig. 2.3.

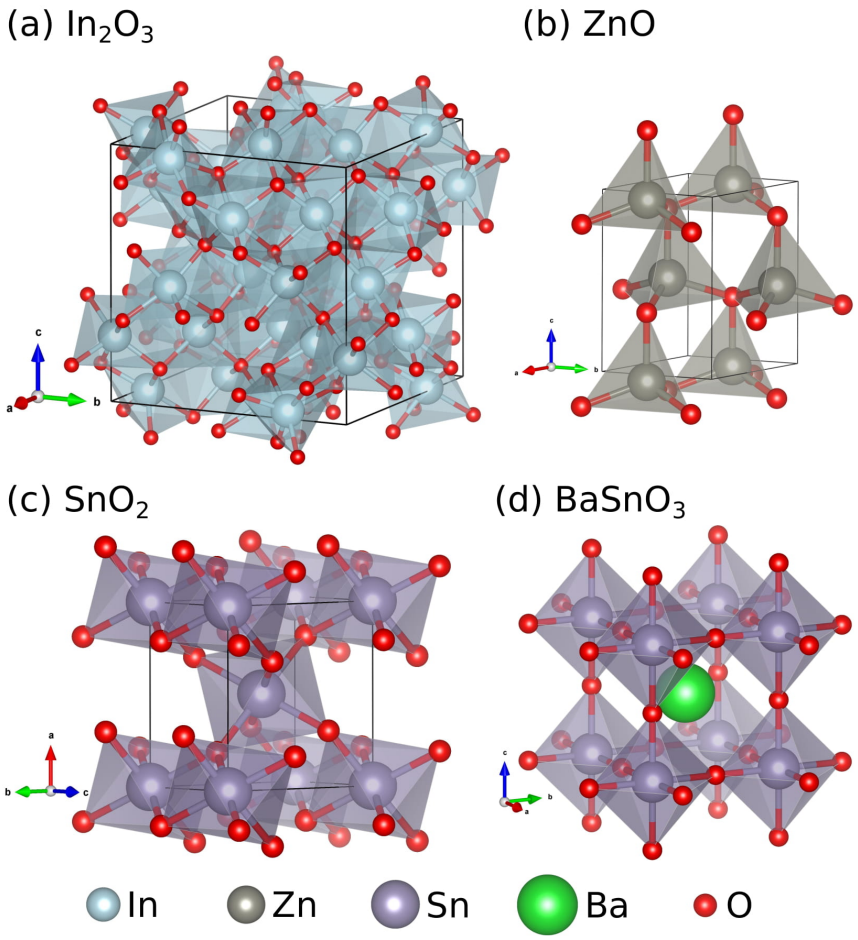

Figure 2.2: Crystal structures of n-type TCMs. The conventional cells with local environments.

The HSE functional is known to better capture the electronic structure and especially the band gap of semiconductors and insulators [198, 199]. Following previous works, we use different fractions of exact-exchange a for materials in order to obtain band gaps reproducing the experimental data: a=25 % for In_2O_3 [200, 181, 201], $BaSnO_3$ [202], $CuAlO_2$ [203, 180], and $ZnRh_2O_4$ [204];

a=32 % for SnO_2 [205] and SnO [206]; and a=37.5 % for ZnO [207]. For LaCuOS, we are not aware of any previous HSE studies. So, we adopt a value of a=25 % which leads to a good agreement with experimental data [31]. The Tab. 2.1 provides their chemical formula, their space group (Spg), their identification number (MP-id) in the Materials Project (MP) [208, 209] database in which all the details about their structures can be found, the type of doping considered, the fraction of exact exchange a used in the HSE calculations, their computed direct band gap E_{dg}^{HSE}, and as well as their reported experimental direct band gap E_{dg}^{exp}. The chosen values for the parameter a guarantee a fair consistence between E_{dg}^{HSE} and E_{dg}^{exp}. It is worth noting that while the fraction of exact exchanges chosen here can moderately correct band gaps, they do not ensure that band widths (relating to width of "second gap") in both valence and conduction bands are treated accurately [210]. This issue was also systematically investigated using state-of-the-art perturbative GW corrections (G_0W_0) for a series of materials including Si, Ge, SiO_2, ZnO, SnO, SnO_2, CaS, CaO, MgO and LiF [211]. This formalism produces results being consistent very well with experiments for Si, Ge, SiO_2, MgO and LiF but worst for the remaining systems. The basic idea of GW formalism and its implementation will be presented in section B.5 of Apd. B.

Table 2.1: Formula, space group (Spg), MP [208, 209] identification number MP-id, type of doping (n or p-type), fraction of exact exchange a, computed direct band gap E_{dg}^{HSE}, and experimental direct band gap E_{dg}^{exp} (in unit eV) for all TCMs studied in this work.

Formula	Spg	MP-id	Type	a (%)	E_{dg}^{HSE} (eV)	E_{dg}^{exp} (eV)
In_2O_3	$Ia3$	22598	n	25	2.65	2.9 [200]
ZnO	$P6_3mc$	2133	n	37.5	3.19	3.3 [212]
SnO_2	$P4_2/mnm$	856	n	32	3.62	3.5 [213]
$BaSnO_3$	$Pm\bar{3}m$	3163	n	25	2.91	3.1 [214]
$CuAlO_2$	$R\bar{3}m$	3748	p	25	3.42	3.47 [79]
SnO	$P4/nmm$	2097	p	32	2.89	2.8 [43]
LaCuOS	$P4/nmm$	6088	p	25	2.95	3.1 [31]
$ZnRh_2O_4$	$Fd\bar{3}m$	5146	p	25	2.84	2.74 [38]

To understand how chemistries drive band structure's dispersion and the width of "second gap", we analyze chemical bonding for all considered materials. Our analysis of the orbital hybridization and band structure character for the TCM candidates is based on projected DFT band structures computed with VASP [190, 191] within the Projector Augmented Wave (PAW) method [215].

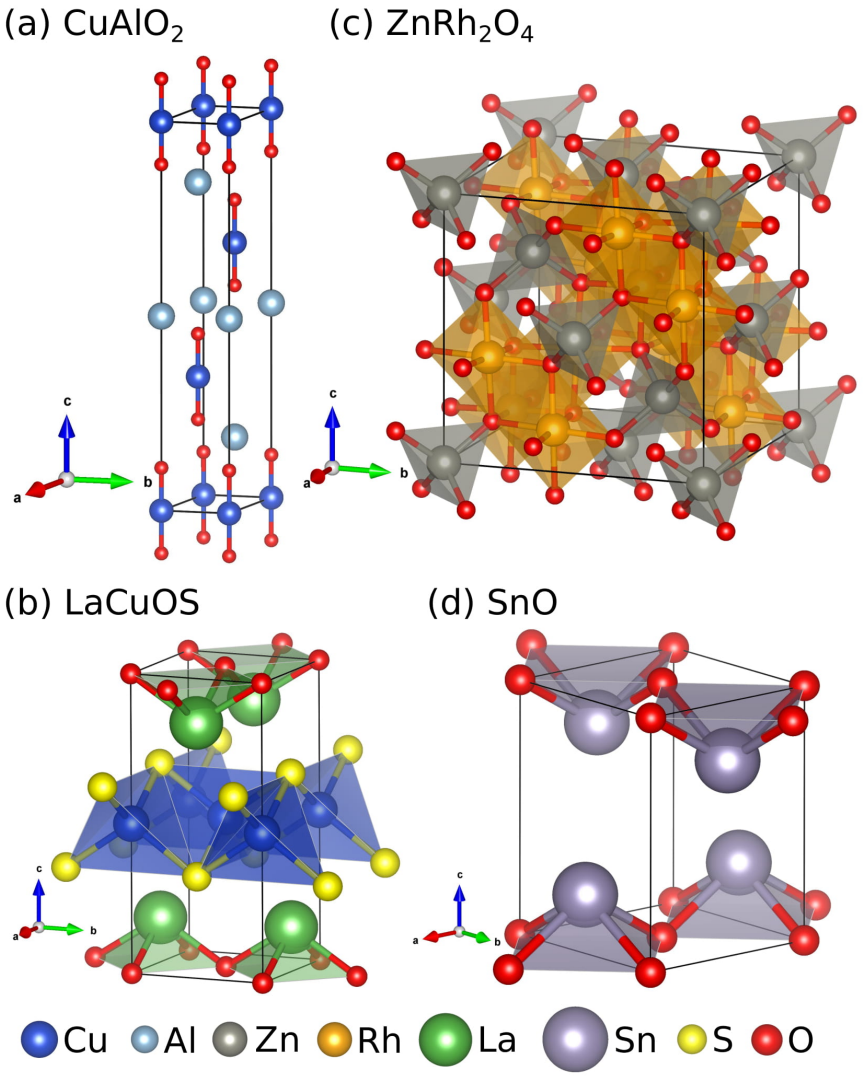

Figure 2.3: Crystal structures of p-type TCMs. The conventional cells with local environments.

We combine both standard atomic projected band structures and Crystal Orbital Hamilton Populations (COHP) analysis [216]. The COHP are computed using the Lobster package [217, 218]. The set of basis functions is chosen to guarantee a small total charge spilling (ideally < 1 %). More details about theory of COHP and implementation can be seen in section B.2 of Apd. B.

2.3 Results and discussions

The computed absorption coefficients at different carrier concentrations (C= 10^{18}-10^{21} cm^{-3}) of the selected n-type materials (In_2O_3, ZnO, SnO_2, and $BaSnO_3$) are reported in Fig. 2.4 (on the left side) together with the corresponding band structures (all computations are performed with HSE functional). Interestingly, increase of the carrier concentration does not lead to any absorption in the visible range. Indeed, the "second gap" above the CB is quite large, typically around 4 eV, and cannot lead to contributions in the visible range. In fact, for the highest carrier concentrations ($C \geq 10^{20}$ cm^{-3}), the optical gap for these n-type TCMs is even widened due to the Moss-Burnstein effect [219]. This behavior was clearly confirmed in different experimental measurements for Sn-doped In_2O_3 [220, 221], F-doped SnO_2 [222], Al-doped ZnO [223], La-doped $BaSnO_3$ [214], Sb-doped $BaSnO_3$ [224],...

Similarly, the left side of Fig. 2.5 shows the absorption for the selected p-type materials ($CuAlO_2$, LaCuOS, $ZnRh_2O_4$ and SnO). Significant absorption appears at low energy as the hole concentration increases. The effect is particularly large for the highest hole concentrations ($C \geq 10^{20}$ cm^{-3}). $ZnRh_2O_4$, $CuAlO_2$ and LaCuOS all show second gap transitions at energies lower than 3 eV. As indicated in their band structures (left side of Fig. 2.5) by red arrows, the width of second gaps of these materials are in ($CuAlO_2$ and LaCuOS) or below ($ZnRh_2O_4$) range of visible light. Because we neglected the effects of plasmons as well as of defects (as a results of chemical doping in reality), it is difficult to directly compare our results for the "second gap" transitions with the available experimental measurements. However, the decrease of transmittance with respect to doping were commonly observed in different transition-metal-based p-type TCMs, particularly $CuAlO_2$ [18, 78, 225, 79], LaCuOS [31]... Among the selected p-type materials, only SnO does not present a strong degradation of its transparency when the carrier concentration is increased. Indeed, the band structure of SnO shows a large second gap of about 4 eV as the case of n-type ones. The Moss-Burnstein effect in these p-type materials is small or negligible. Indeed, the tops of CB are flat (see Fig. 2.5) leading to high DOS. Thus, Fermi levels slightly move downwards to CB when we increase the doping concentrations (even at very high doping regime (10^{21} cm^{-1}).

The difference between n- and p-type TCMs is striking. The n-type materials tend to have large second gap transitions that do not affect transparency when doped. In contrast, most p-type TCMs show significant absorption in the visible range due to second gap transitions with the notable exception of SnO. A quantitative estimate of the effect of the second gap on the transparency is provided by the visible transmittance of a typical thin-film. Fig. 2.6 plots the transmittance for a 100-nm film depending on the carrier concentration (computed by equation 2.8). The blue and red lines correspond to n-type and p-type materials. As expected from the computed absorption coefficients, n-type TCMs do not show any degradation of their visible transmittance when the carrier concentration increases. In contrast, the transmittance of p-type TCMs is significantly degraded. This is the case for $CuAlO_2$ and LaCuOS. The lower band gap of $ZnRh_2O_4$ induces a degradation in the transmission

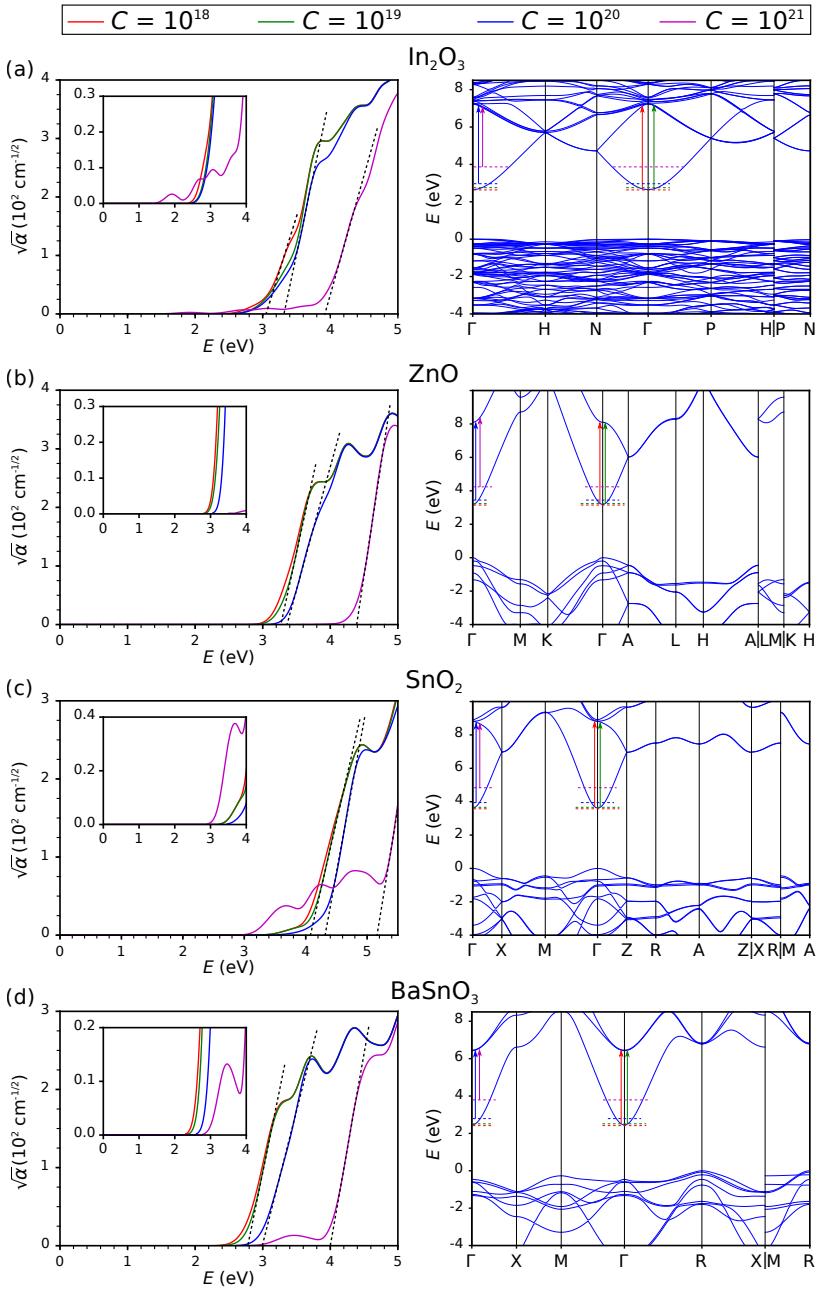

Figure 2.4: Square root of absorption coefficients (left) of selected n-type TCOs at different doping levels. The dash lines (left) indicate the optical gaps corresponding to different doping levels. The band structures (right) with the dash color lines showing different Fermi levels and the color arrows indicating the second gaps.

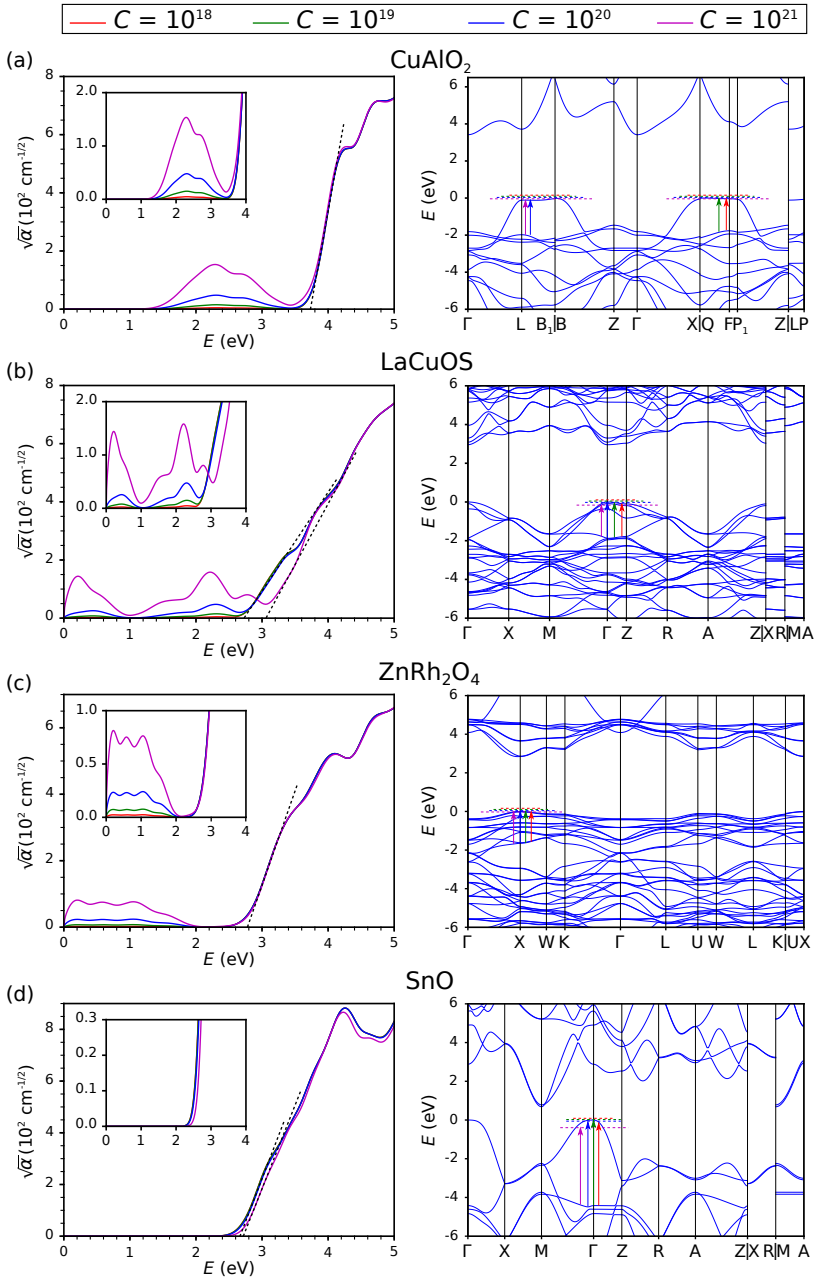

Figure 2.5: Square root of absorption coefficients (left) of selected p-type TCOs at different doping levels. The dash lines (left) indicate the optical gaps corresponding to different doping levels. The band structures (right) with the dash color lines showing different Fermi levels and the color arrows indicating the second gaps.

with doping but only in an energy window lower than the visible light. In fact, the effect of second gap absorption in the near infrared range in $ZnRh_2O_4$ might be decreased because of plasmon reflection which is out of examination in this study. Finally, SnO shows a slight improvement in transparency due to its large second gap combined with a small Moss-Burnstein effect. We would like to emphasize that our analysis only takes into account direct inter-band transitions. Including also indirect transitions [226] would be significantly more computationally expensive. Moreover, we do not consider the loss of transmission due to the possible contribution of plasma reflectivity when carrier concentration is increased [2, 178]. This explains why the visible transmittance of n-type materials shown in Fig. 2.6 approaches 100 %, which cannot happen in reality. Nevertheless, our study points out to lower second gap transitions as one of the reasons explaining why many p-type TCMs show a less favorable trade-off between transparency and carrier concentration than n-type materials do [42].

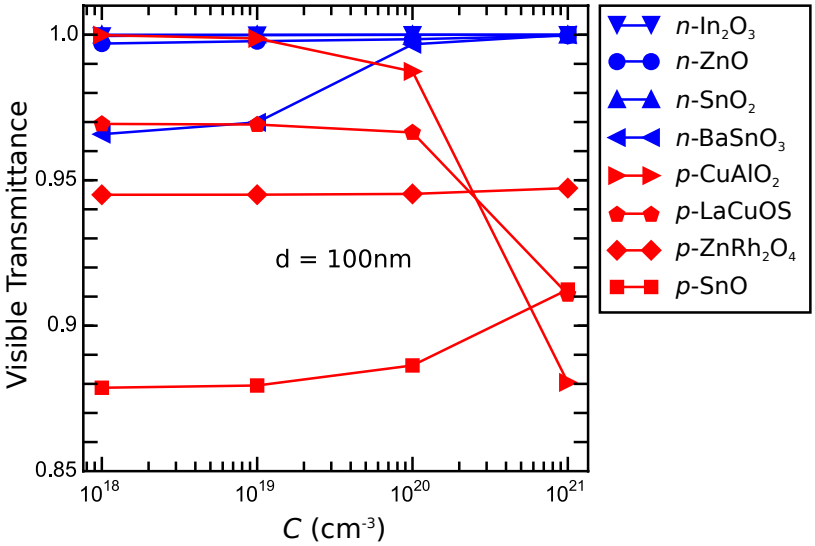

Figure 2.6: Visible transmittance through a 100 nm-film for the eight selected TCMs versus the carrier concentration C. The transmittance is estimated by integrating over the whole visible range as equation 2.8.

We give a quantitative estimate of the effect of the second gap transitions (see Fig. 2.6). For a 100-nm film, the observable loss of transparency with carrier concentration reached 10 % at most (20 % for a 200-nm film) and for the highest carrier concentrations (10^{20} cm^{-3} to 10^{21} cm^{-3}). Therefore, a small second gap has a more moderate effect on transparency than the principal band gap. This comes from the smaller amount of carriers available in the small energy window corresponding to the second gap. This suggests that, while beneficial, a high second gap should not be considered a necessary condition for obtaining a working TCM.

The dissimilitude between n- and p-type TCMs can be traced back to

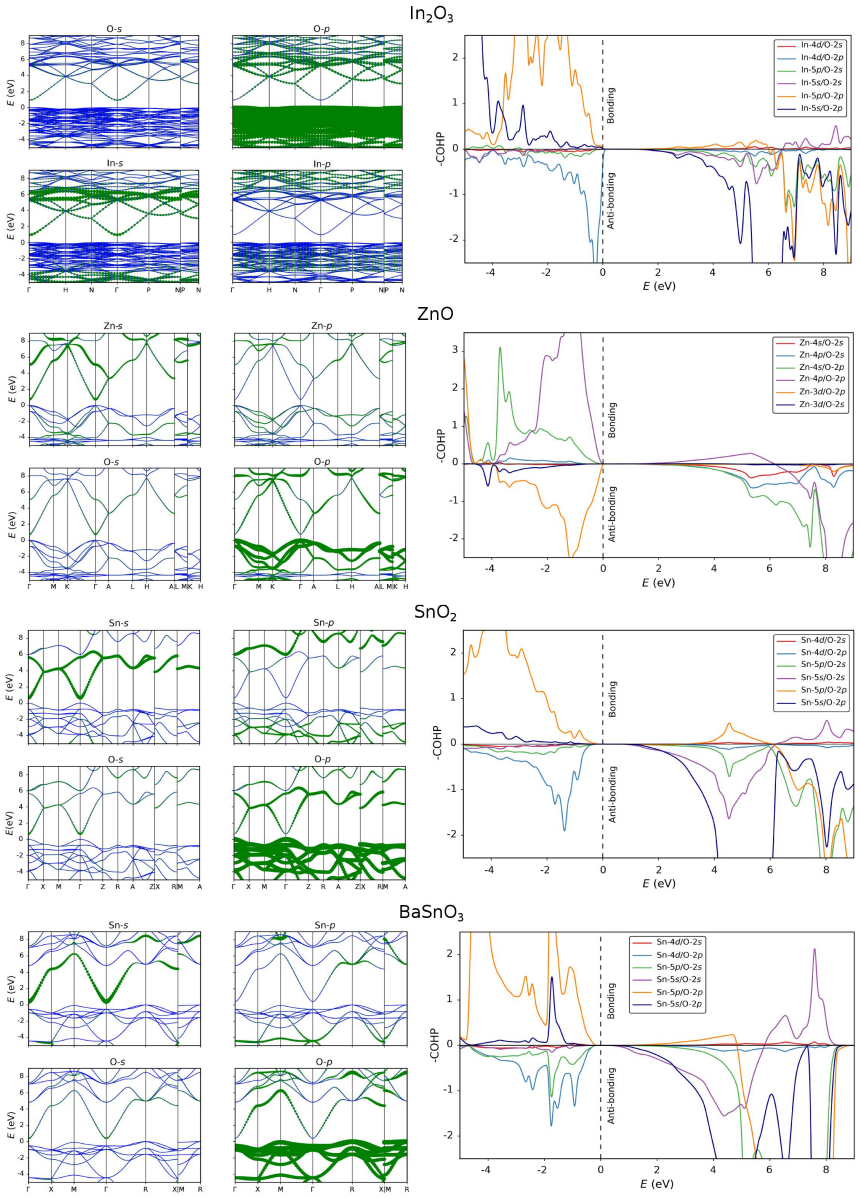

Figure 2.7: The DFT projected band structures (left) and COHP projections (right) of n-type TCMs.

the materials chemistry. To analyze chemical interactions, we combine both projected band structure and COHP projection. Fig. 2.7 present results for n-type TCMs. The projected band structures show contributions of different atomic orbitals to specific bands while COHP can give us information about the overlap between different pairs of orbitals. In general, we see that the

bottom of n-type TCMs' CB is composed of s-p hybridization. The same calculations were performed for p-type TCMs and the results are shown in Fig. 2.8. It is difficult to interpret fully all complicated chemical interactions from the projected band structure and the COHP projection. We, therefore, simplify problem by focusing on the main characters around CBM and VBM.

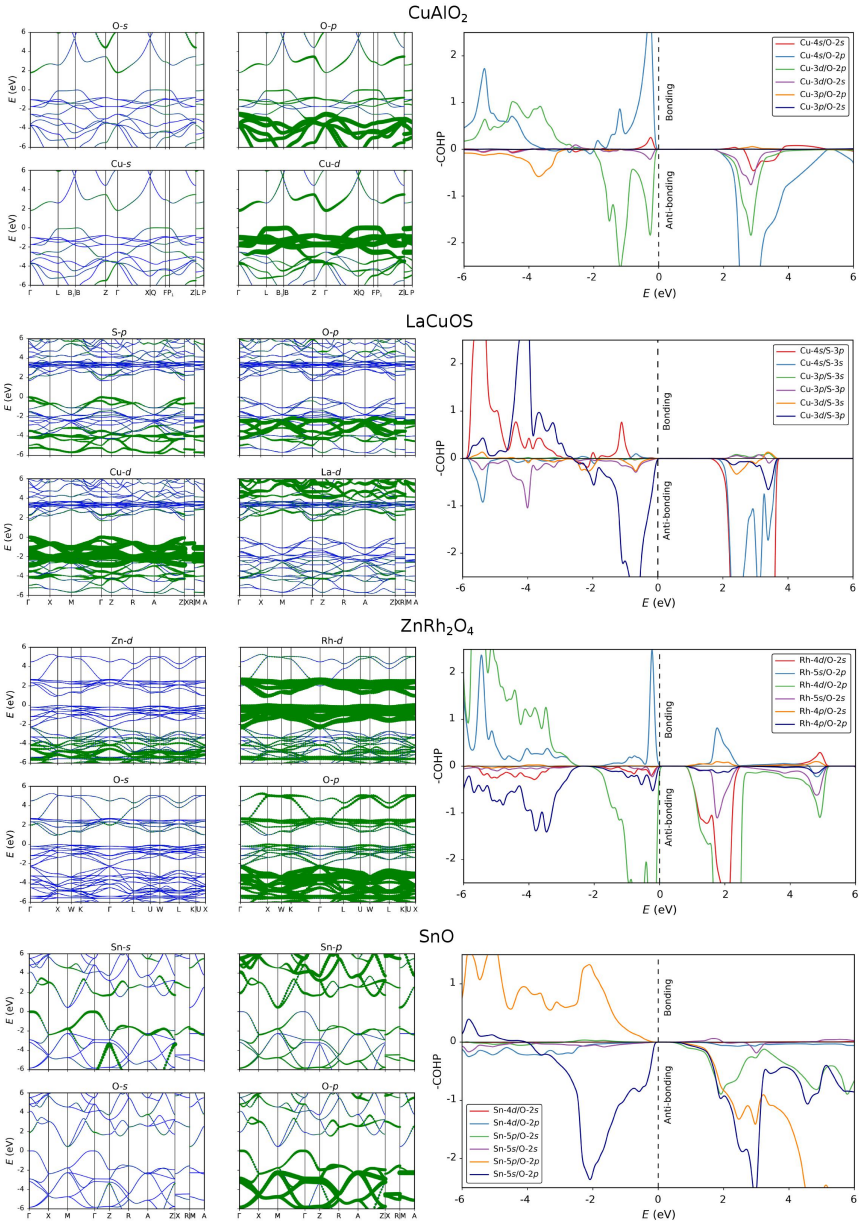

Figure 2.8: The DFT projected band structures (left) and COHP projections (right) of p-type TCMs.

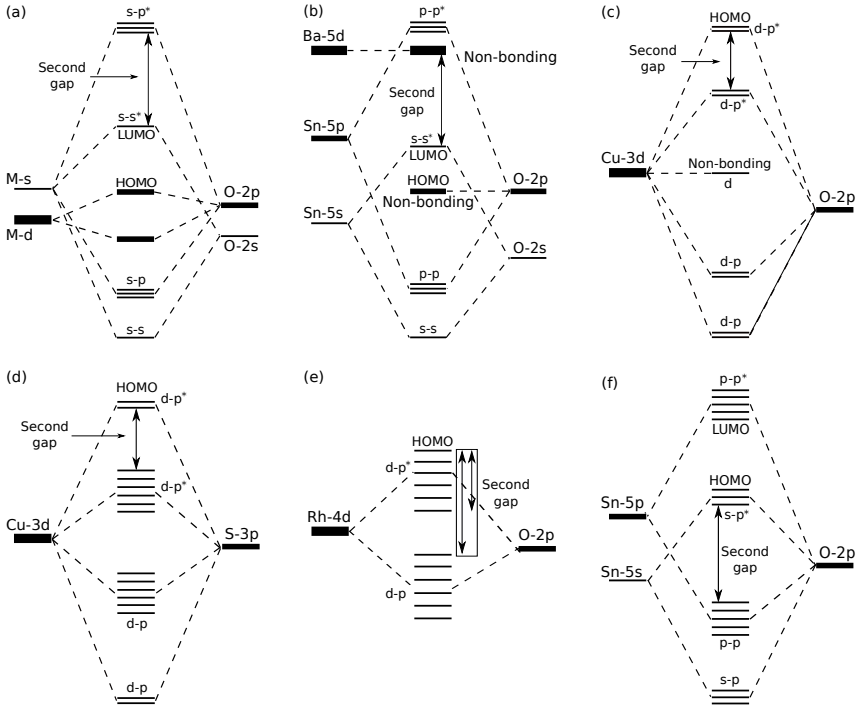

Figure 2.9: The chemical origin of the second gap in TCMs can be revealed by molecular orbital diagrams at particular **k**-points of the Brillouin zone (BZ): (a) the Γ point in In_2O_3, ZnO, and SnO_2; (b) the Γ point in $BaSnO_3$; (c) the X point in $CuAlO_2$; (d) the Γ point in LaCuOS; (e) the X point in $ZnRh_2O_4$; and (f) the Γ point in SnO. Bonding and anti-bonding orbitals are distinguished by marking the latter with a star. For the sake of clarity, irrelevant orbitals are not indicated.

Fig. 2.9 shows simplified molecular orbital diagrams for the studied TCMs. In n-type oxides (panel a), the second gap is formed by M-s/O-s and M-s/O-p anti-bonding states (with M=In, Sn or Zn) which have a large difference in energy. $BaSnO_3$ (panel b) is slightly different with the presence of a Ba-d non-bonding states but also provides a wide second gap. The p-type TCMs on the other hand (panels c to f) show more complex orbital diagrams. The materials based on transition metals (TM) have a valence band maximum (VBM) formed by TM-d/O-p or TM-d/S-p anti-bonding states (with TM=Cu or Rh). The second gap is formed between the VBM and other TM-d/O-p, or TM-d/S-p states that are very close in energy to this VBM. This leads to small second gap transitions that can be in the visible range. In contrast, SnO presents a very different character for its VBM (Sn-s/O-p) and no hybridized d-states. Hence, it shows a much larger second gap which is due to the larger hybridization of Sn-s/O-p states compared to d states to O-p. This indicates that the lower hole effective mass obtained by M-s/O-p hybridization is not only beneficial for the mobility of this compound but also for its second gap transitions. Our

analysis points out to an intrinsic limit to transition d-metal-based compared to s-metal-based p-type TCMs as they not only lead to higher effective masses but also present larger limitations in terms of second gap absorption. The fundamental gap of SnO is rather narrow. We will discuss this more clearly from the point of view of local environment and chemical bonding in Chp. 3.

2.4 Conclusions

In summary, we used *ab initio* calculations combined with the rigid band approximation to study the effect of heavy doping on optical absorption through "second gap" transitions. We studied a series of common n-type and p-type TCMs. A very different behavior is observed between n- and p-type materials. The n-type TCMs show high second gap transitions and do not lose transparency when highly doped. On the contrary, most p-type materials have second gap transitions lower than 3 eV which lead to a degradation of their transparency when doped. We relate the asymmetry in behavior between n- and p-type materials to their chemistry. The lower second gap present in transition metal-based p-type TCMs comes from the small energy differences between metal-d/O-p hybridized states. Our results on SnO, one of the rare non-transition metal-based p-type TCMs, indicates that using p-type TCMs relying on the hybridization of O-p with metal s-states lead naturally to higher second gap transitions that are less detrimental to transparency. In Chp. 3, we will illustrate that the presence of s-orbital in VB also plays an important role in design of low hole-effective-mass p-type TCMs. Our work also quantitatively estimates the effect of these second gap transitions and demonstrates that, while it is beneficial to select materials with a high second gap (> 3 eV ideally), the magnitude of the effect should not lead to making it a strict requirement for design of TCMs.

Chapter 3

Structural design principles for low hole effective mass *s*-based *p*-type TCOs

The design of materials with targeted functionalities is envisioned as an inevitable part in the new industrial revolution. In traditional approach, the design process generally includes experimental and theoretical studies of given materials. One often considers three factors including atomic identities, composition and structure to design novel compounds. This is called "direct design" and can be done within each compound or in a HT mode. It is always better to have an "inverse design" in which the targeted properties will be used as constraint conditions. To do this, fundamental principles (rules) that regulate desired properties play an important role and must be generally studied and explored. These are known as "design principles" or in more extensively, people envision and try to map the so-called Materials Genome Initiative. More details can be found in the Ref. [227].

As reviewed in Chp. 1, although researchers have used different anions such as O, S, Se, Te,... to design *p*-TCMs, oxides are still the most popular group. The understanding of the relationship between chemistry, structure and properties is a very important part of materials science. Indeed, when these factors are more clearly understood, the design of new materials can be performed more efficiently (inverse design). In this chapter, we will focus on finding the relationship between crystal structure and hole effective mass for Sn^{2+}-based oxides. While typical oxides have flat oxygen-based valence bands, Sn^{2+} oxides are known to be able to possess Sn-s/O-p mixture in their valence bands and thus low hole effective mass [45]. However, not all Sn^{2+} oxides exhibit low hole effective mass pointing at the importance of structural factors. Here, we analyze the electronic structure and chemical bonding of three *p*-type TCOs candidates: SnO and the two $K_2Sn_2O_3$ polymorphs. We rationalize their differences in hole effective mass by their Sn−O−Sn angles. As valence band dispersion is governed by Sn-s/O-p overlap, Sn−O−Sn angles near 180°

maximize the later and minimize the hole effective mass. We show that this principle is generalizable to a larger set of Sn^{2+} oxides. Our work leads to a simple structural design principle for the development of high-mobility *p*-type oxides based on not only Sn^{2+} but also other reduced main group cations, *e.g.* Pb^{2+}. The results which will be presented in this chapter are already published in J. Mater. Chem. C **5**, 5772 (2017).

3.1 Introduction

The commercially available TCMs are *de facto* *n*-type while their *p*-type counterparts are lagging behind because of their poor materials properties [2, 17, 19]. One of the main issues with currently known *p*-type TCMs is their lower carrier mobility in comparison with the best performing *n*-type oxides. The absence of high mobility *p*-type TCMs prevents the development of many technologies including transparent electronics [64]. Hence, the discovery, design and development of novel *p*-type TCMs is a very active field in materials sciences [19].

One can chemically rationalize the poor hole mobility of typical oxides by their very flat valence bands with O-*p* character which leads to large hole effective masses [228]. The use of certain transition metals cations such as Cu^{1+} can mitigate this problem as their *d*-orbitals hybridize with the O-*p* orbitals lowering the hole effective mass [18, 29, 30, 23, 25]. However, while the works on Cu-based materials lead to significant progress in the field, *p*-type transparent conducting oxides (TCOs) still perform poorly compared to *n*-type oxides especially in terms of mobility. One should also mention the recent demonstration of high *p*-type conductivities in highly doped Cr-based oxides (*e.g.* Cr_2O_3, $LaCrO_3$, $CuCrO_2$) [42, 39, 229]. However, the transport mechanism in these materials is polaronic leading to very low mobilities and excluding their use in various applications such as transparent transistors.

An alternative way of inducing curvature in the valence band is to use reduced main group cations with the (n-1)d^{10}ns^2 electronic configuration (Sn^{2+}, Pb^{2+}, Sb^{3+}, Bi^{3+}...). Recently, we performed a computationally-driven HT search to identify several high-mobility *p*-type TCO candidates. This large-scale study highlighted the potential of *s*-orbital-based *p*-type TCOs [45, 47]. Quantitatively, the diffuse *s*-orbital of the (n-1)d^{10}ns^2 cations overlaps more significantly with the O-*p* orbitals than the localized *d*-orbitals of the transition metals. This leads to much lower hole effective masses for oxides based on reduced main group cations ($m_h \simeq$ 0.2-0.3 m_o with m_o being the free electron mass) than for traditional Cu-based chemistries ($m_h \simeq 2$ m_o). This finding is in-line with the experimental interest in *s*-orbital-based *p*-type TCOs, more particularly in SnO [43, 44, 230]. It has also motivated further computational studies of Sn^{2+} compounds [231, 232]. While the presence of reduced main group cations such as Sn^{2+} can lead to very low hole effective masses, our HT search demonstrated that this is not a sufficient requirement. Indeed, a significant fraction of oxides containing reduced main group cations does not exhibit low hole effective masses. Among the 50 known Sn^{2+} oxides present in the ICSD [168], only a handful materials ($K_2Sn_2O_3$ and $Rb_2Sn_2O_3$ in different

polymorphs) show exceptionally low hole effective masses. This demonstrates that not only the chemistry components (*i.e.* the presence of certain cations) but also the crystalline structures play an important role in determining the hole effective masses.

In this chapter, we precisely investigate the structural factors leading to low hole effective masses in oxides containing cations with electron configuration (n-1)d^{10}ns^2. We focus on Sn^{2+} oxides and analyze the electronic structure and the character of the valence band for SnO as well as for two $K_2Sn_2O_3$ phases. We rationalize the much lower hole effective mass present in the $K_2Sn_2O_3$ phases in comparison with SnO in terms of their very different Sn−O−Sn angles. Angles close to 180° maximize the overlap between the Sn-s and O-p orbitals and lead to lower hole effective masses. We demonstrate the generality of this simple principle on a larger set of known Sn^{2+} oxides. Our analysis leads to a new design principle for high mobility p-type TCOs requiring Sn−O−Sn angles as close as possible to 180°.

3.2 Computational details

To clarify how the local environment of Sn−O impacts on hole effective mass (m_h), we perform analyses for a series of known Sn-based oxides available in ICSD [168] by utilizing database from MP [208, 209]. It is worth of noting that characterizing electronic band structure can help to explore various properties of materials such as transport, optical absorption, chemistry of bonding, *etc.* All computations have been performed within DFT using the GGA exchange-correlation (XC) functional [233, 234] in its Perdew-Burke-Ernzerhof (PBE) version [235]. We used the VASP package [190, 191] and PAW method [215]. The (average) effective mass tensors were computed using the approach outlined in our previous works [45, 161] and using the Boltztrap code [172]. Details about the definition and calculating procedure were already presented in section 1.3 of Chp. 1. The hole effective mass (m_h) is a symmetrical tensorial property:

$$\mathbf{m_h^T} = \begin{pmatrix} m_{11} & m_{12} & m_{13} \\ m_{12} & m_{22} & m_{23} \\ m_{13} & m_{23} & m_{33} \end{pmatrix}. \tag{3.1}$$

This symmetrical second-rank tensor has three real eigenvalues and associated principal directions (eigenvectors). In the following, we will report these three eigenvalues in order to compare the different materials. For linking transport property to geometric configuration of Sn−O networks we need to compute m_h in a given direction $\vec{d}\,(m_h^d)$. We employ the quadratic representation (ellipsoid) for the effective mass and therefore, can calculate m_h^d as the formula below

$$m_h^d = m_1 a_1^2 + m_2 a_2^2 + m_3 a_3^2, \tag{3.2}$$

where m_1, m_2, m_3 are three principal values of m_h^T in (3.1) and a_1, a_2, a_3 are three cosine values of angles between $\vec{d}$ and three corresponding eigenvectors of m_h^T in (3.1). More details about (3.2) can be found in the textbook [236].

The creation of the input files and the processing of the output files are performed using the Pymatgen code [194]. The band structures are obtained along high-symmetry lines following the conventions introduced in Ref. [237]. The Crystal Orbital Overlap Population (COOP) [216] analysis are performed using the Lobster package [217, 218]. All the visualizations of the crystal structures and of the charge densities are obtained using VESTA [238]. More information about DFT and COOP can be found in Apd. A and section B.2 of Apd. B, respectively.

3.3 Results

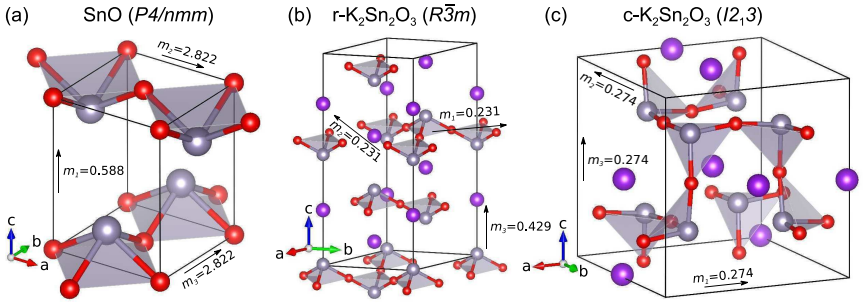

Figure 3.1: The conventional cells of (a) SnO with space group $P4/nmm$, (b) r-$K_2Sn_2O_3$, and (c) c-$K_2Sn_2O_3$. The oxygen, tin, and potassium atoms are respectively colored in red, gray and violet. The three principal values of hole effective mass tensor (m_1, m_2, m_3) and their corresponding principal directions are reported in the crystals.

The most investigated s-orbital-based p-type transparent conducting oxide (TCO) is currently tin monoxide (SnO). It has been widely studied experimentally [43, 44, 239] and computationally [206, 230, 240]. Its tetragonal (P4/nmm) unit cell is shown in Fig. 3.1 (a). It consists of layers of square out-of-plane coordinated Sn^{2+} sharing O^{2-} vertices.

Fig. 3.2 shows the DFT band structure of SnO along high-symmetry lines of the Brillouin zone (BZ). Due to its tetragonal symmetry, SnO shows only two hole effective mass eigenvalues: one along the Γ-Z direction of 0.59 m_o and another one of 2.8 m_o in the plane perpendicular to the former direction (for instance, along the Γ-X direction). These directions correspond respectively to inter-layer and intra-layer transport (see Fig. 3.1 (a)). It is remarkable that the low-effective-mass (high-mobility) direction is the one perpendicular to the layers. This is in agreement with the higher mobilities measured in c-axis oriented SnO samples [241].

To relate the effective mass to the electronic structure of SnO, we analyzed the character of the valence band using atomic projected band structures, the partial charge densities, and the COOP analysis. In Fig. 3.2 (a), the color scheme for the band structure indicates the Sn or O character of the different bands. The valence band shows Sn and O characters as expected with Sn^{2+}

cations. The Sn and O characters of the valence band are also observed in the partial charge density isosurface plot at the valence band maximum (VBM) (see Fig. 3.2 (b)).

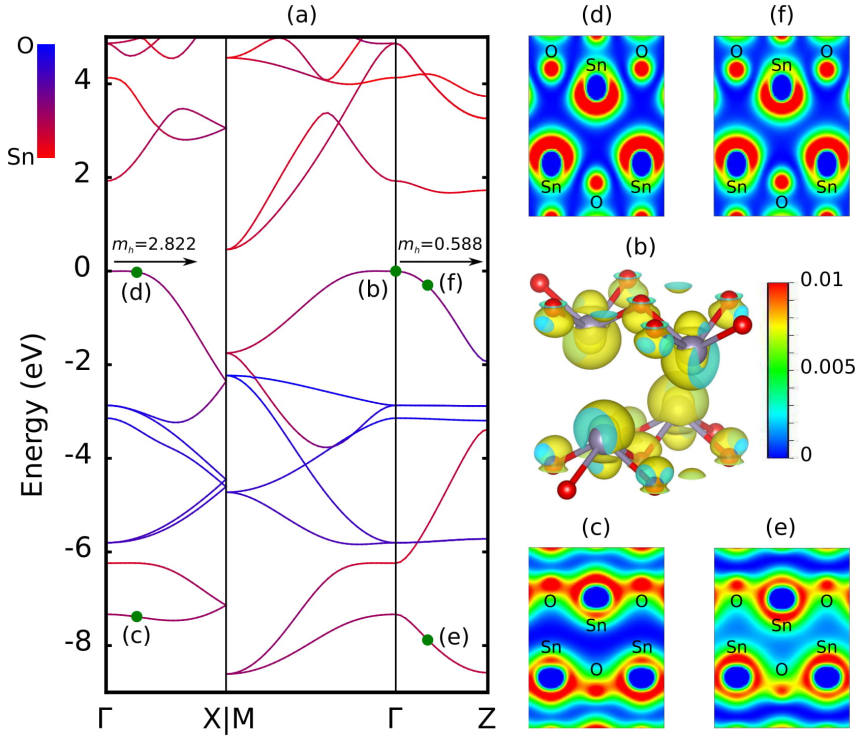

Figure 3.2: (a) DFT band structure of SnO, (b) partial charge density at the valence band maximum, and (c)-(f) partial charge density cuts in the (101) plane of the conventional cell (Fig. 3.1 (a)) for two different valence bands at two specific k-points (as indicated in panel (a)). In panel (b), the isosurface corresponds to 0.009 (bohr^{-3}). In panels (c)-(f), the partial charge densities are represented using a color scale ranging from 0 to 0.01 bohr^{-3}.

In addition, we carried a COOP analysis (see Fig. 3.3). The COOP indicates an anti-bonding Sn-O and Sn-Sn characters for the valence band. Linear combination of atomic orbitals (LCAO) theory applied to solids relates the effective mass to the orbital overlap. Larger overlaps lead to lower effective masses [161, 242]. Following the previous analysis, the hole effective mass in SnO is driven by Sn-Sn and Sn-O overlap. Information about the directional dependence of the overlap can be obtained by observing the partial charge densities of the valence band in the two directions. Plane-cuts of the partial charge densities of the valence band (anti-bonding) but also at the corresponding bonding part of the band structure are shown in Fig. 3.2. Fig. 3.2 (c) and (d) correspond respectively to the plane-cuts for the bonding and anti-bonding partial charge densities in the Γ-X, intra-layer direction. The orbital interaction which is easier to visualize in the bonding state is mainly between

Sn and O. On the other hand, Fig. 3.2 (e) and (f) correspond respectively to the plane-cuts for the bonding and anti-bonding partial charge densities in the Γ-Z, inter-layer direction. Here, the bonding state shows weaker Sn-O interaction and a stronger Sn-Sn overlap. The anisotropic transport in SnO is then easily explained by intra-layer orbital interaction due to Sn-O overlap while inter-layer transport is due to the Sn-Sn orbital interaction [243].

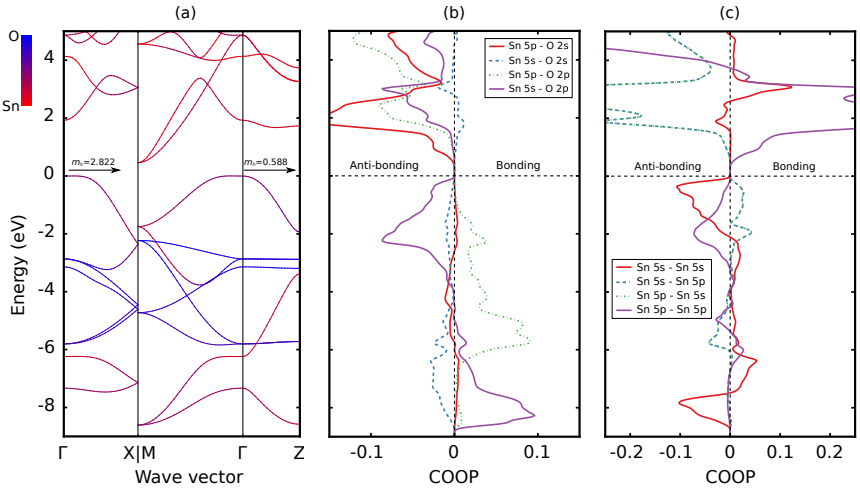

Figure 3.3: The projected band structure of SnO on Sn (red colors) and O (blue colors) atoms (a) and the projected COOP for Sn-O (b) and Sn-Sn (c) interactions.

Among the lowest hole effective mass materials identified by our previous HT study [45] are two Sn^{2+} polymorphs of $K_2Sn_2O_3$: a rhombohedral form (r-$K_2Sn_2O_3$) with space group $R\bar{3}m$ and a cubic one (c-$K_2Sn_2O_3$) with space group $I2_13$. The synthesis of these two compounds had been reported in the literature but without experimental optoelectronic characterization [244, 245]. The computed hole effective masses of the $K_2Sn_2O_3$ phases are around 0.2 to 0.4 m_o and close to the electron effective masses in traditional n-type TCOs (*i.e.* 0.1 to 0.2 m_o) [161]. The presence of Sn^{2+} in these oxides is at the origin of its exceptional low hole effective mass as Sn-s orbitals mix with O-p orbitals to lead to a dispersive valence band. However, it has been unclear why the $K_2Sn_2O_3$ phases outperform significantly SnO.

The structure of r-$K_2Sn_2O_3$ in its conventional hexagonal unit cell is reported in Fig. 3.1 (b). Similarly to SnO, r-$K_2Sn_2O_3$ forms a layered structure. The Sn−O−Sn network is here composed of out-of-plane triangular Sn^{2+} sharing O^{2-} vertices. Fig. 3.4 shows the DFT band structure of r-$K_2Sn_2O_3$ along high-symmetry lines. Due to the rhombohedral symmetry, the hole effective mass tensor exhibits only two eigenvalues. The eigenvalues corresponding to intra-layer transport (Γ-X direction for instance) are extremely low at 0.23 m_o while the inter-layer hole effective mass (Γ-Z direction) is higher but still competitive at 0.43 m_o. Similarly to SnO, the atomic projections used for coloring the DFT band structure in Fig. 3.4 (a) indicate the Sn and O mixture at the

valence band. Additionally, the Sn and O characters at the valence band are also observed in the partial charge density isosurface plot at the VBM (see Fig. 3.4 (b)).

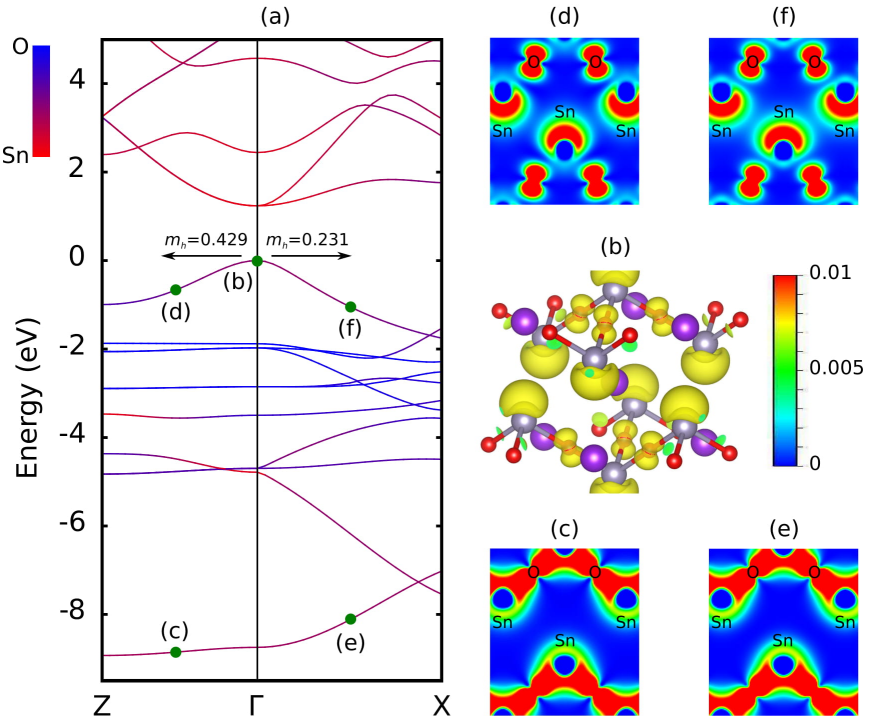

Figure 3.4: (a) DFT band structure of r-$K_2Sn_2O_3$, (b) partial charge density at the valence band maximum, and (c)-(f) partial charge density cuts in the $(1\bar{1}2)$ plane of the conventional cell (Fig. 3.1 (b)) for two different valence bands at two specific k-points (as indicated in panel (a)). In panel (b), the isosurface corresponds to 0.012 (bohr^{-3}). In panels (c)-(f), the partial charge densities are represented using a color scale ranging from 0 to 0.01 bohr^{-3}.

Furthermore, the COOP analysis suggests that the valence band originates from an anti-bonding Sn-O interaction with an important bonding Sn-Sn interaction (see Fig. 3.5). The directional dependence of the partial charge densities can also be observed in Fig. 3.4 (c)-(f). The bonding states corresponding to the anti-bonding Sn-O states at the valence band are observed in Fig. 3.4 (c) and (e). The mainly bonding character of Sn-Sn is observed in Fig. 3.4 (d) and (f). r-$K_2Sn_2O_3$ behaves differently than SnO which shows a more pronounced difference between the overlap in the intra-layer and inter-layer directions. Nevertheless, the analysis of both oxides leads to the same conclusion that Sn-Sn and Sn-O overlap drives the valence band curvature and the hole effective mass.

In r-$K_2Sn_2O_3$, the intra-layer hole transport is easier than the inter-layer hole transport. The inter-layer transport is similar to SnO with values of 0.43 and 0.59 m_o. On the other hand, the intra-layer hole effective mass is

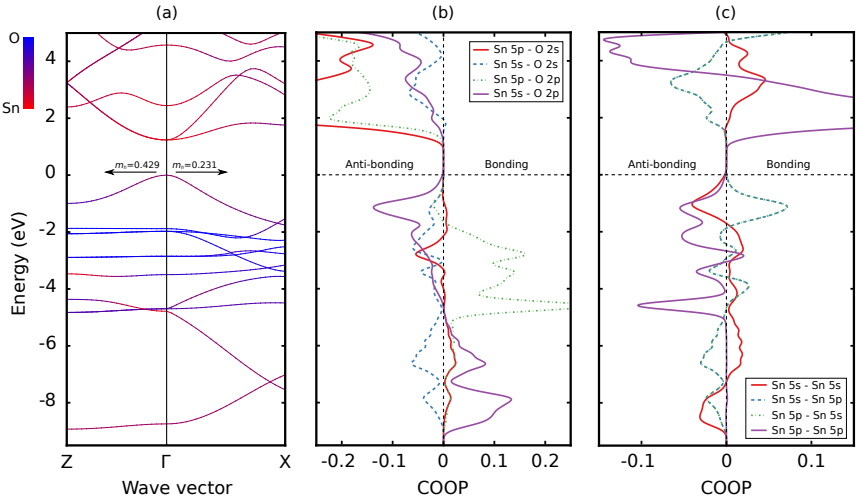

Figure 3.5: The projected band structure of $K_2Sn_2O_3$-$R\bar{3}m$ on Sn (red colors) and O (blue colors) atoms (a) and the projected COOP for Sn-O (b) and Sn-Sn (c) interactions.

much smaller (0.23 m_o) than for SnO (2.82 m_o). The lower effective mass should be the result of stronger orbital overlap between Sn and O. This stronger overlap can naturally be rationalized in terms of the very different Sn−O−Sn angle between r-$K_2Sn_2O_3$ and SnO. In the case of SnO, the Sn−O−Sn angles are around 118° leading to a smaller Sn-s/p to O-p overlap than that of r-$K_2Sn_2O_3$ which shows 180° Sn−O−Sn angles maximizing s-p overlap. Fig. 3.6 schematically illustrates how the Sn−O−Sn angle sets the magnitude of Sn-s/O-p overlap. It is worth noting that from r-$K_2Sn_2O_3$ to SnO, we also observe a narrowness of DFT band gap (roughly from 1.2 to 0.5 eV). This can be explained as the Sn-Sn interaction between Sn-O layers in SnO. The CBM of SnO is mainly contributed by Sn-p character (see Fig. 2.8 in Chp. 2). The projected COOP shown in Fig. 3.5 (c) proves that the CBM is contributed by Sn-5p/Sn-5p bonding and Sn-5p/O-2s anti-bonding. We can see that while Sn-Sn interaction can help to lower the hole effective mass (0.59 m_o), it can also reduce the band gap leading to a detrimental effect on the transparency of Sn^{2+} oxides. Despite having a small fundamental gap, SnO is still considered as a good TCM because it has a wide direct gap of around 2.8 eV [43]. On other hand, $K_2Sn_2O_3$ has a wider fundamental gap about 2.3 eV but unfortunately it is a direct semiconductor and could not be applied for TCM applications.

The other existing polymorph of $K_2Sn_2O_3$ is cubic (c-$K_2Sn_2O_3$) with space group $I2_13$. It also shows extremely low hole effective masses. The crystal structure of c-$K_2Sn_2O_3$ in its conventional cell is reported in Fig. 3.1 (c). Similarly to the rhombohedral phase, the Sn^{2+} cations sit in triangular out-of-plane local environments. These triangular environments share vertices similarly to the rhombohedral phase but do not form a layered structure. Instead, a three-dimensional Sn−O−Sn network is formed. Due to the cubic symmetry, the

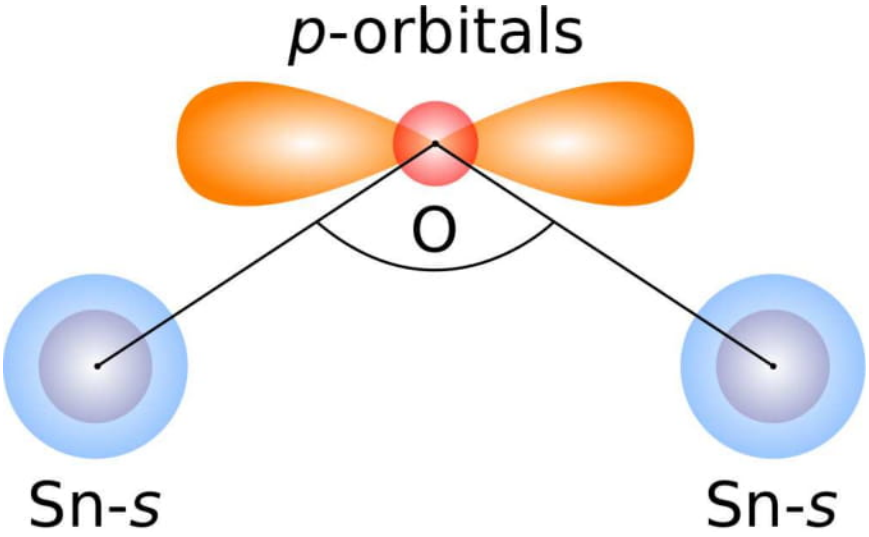

Figure 3.6: The angle Sn−O−Sn influences the overlap between Sn-s and O-p orbitals.

tensor is isotropic. The unique hole effective mass is very low (0.27 m_o). The DFT band structure of c-$K_2Sn_2O_3$ is shown in Fig. 3.7 (a) along with the atomic projections. The valence band is also composed of Sn and O characters as visualized in the partial charged density isosurface at the VBM (Fig. 3.7 (b)).

In contrast with the layered SnO and r-$K_2Sn_2O_3$, the COOP analysis indicates negligible Sn-Sn overlap and only Sn-O mixture at valence band (see Fig. 3.8). Plane-cuts of the partial charge densities along two of the crystallographic directions (see pairs of panels (c)/(d) and (e)/(f) of Fig. 3.7) at the anti-bonding valence state and corresponding bonding state clearly show the Sn-O overlap. Similarly to the intra-layer transport in the rhombohedral phase, the very low hole effective mass emerges here from the large overlap between Sn and O-p orbitals due to the a near 180° Sn−O−Sn angle.

Our study on SnO and the two polymorphs of $K_2Sn_2O_3$ shows that the hole effective masses in tin oxide materials are set by Sn-Sn as well as Sn-O overlap. The Sn-O overlap (and therefore the effective masses) will depend strongly on the Sn−O−Sn angle (see Fig. 3.6). The maximum overlap is obtained when the angle is at 180° and the Sn−O−Sn is linear. This rationalizes the much lower effective mass obtained for c-$K_2Sn_2O_3$ and intra-layer r-$K_2Sn_2O_3$, compared to intra-layer SnO. To further test how general the importance of the Sn−O−Sn angle in driving hole effective mass of Sn^{2+} oxides, we took into account all the available Sn^{2+} oxides present in the ICSD [168] (around 50 compounds). The low number of compounds is an indication of the challenges in the synthesis of Sn^{2+} oxides but also points out to the high potential for the discovery of novel Sn^{2+} oxides. As we only focus on the link between effective mass and Sn-O overlap, we exclude oxides which had an important contribution from other

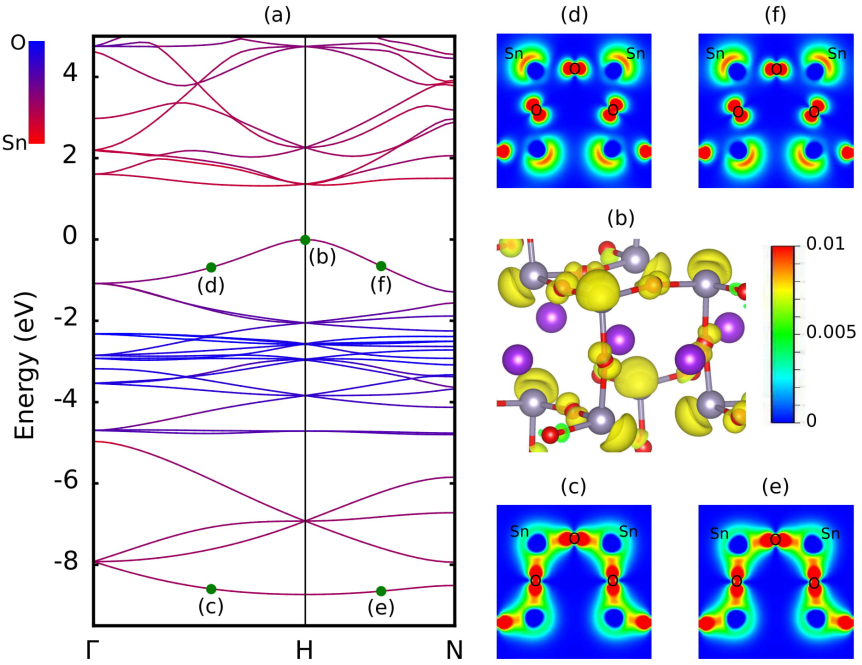

Figure 3.7: (a) DFT band structure of c-$K_2Sn_2O_3$, (b) partial charge density at the valence band maximum, and (c)-(f) partial charge density cuts in the (010) plane of the conventional cell (Fig. 3.1 (c)) for two different valence bands at two specific k-points (as indicated in panel (a)). In panel (b), the isosurface corresponds to 0.009 (bohr^{-3}). In panels (c)-(f), the partial charge densities are represented using a color scale ranging from 0 to 0.01 bohr^{-3}.

elements than Sn or O at the VBM. We also excluded oxides with isolated Sn-O groups that are not linked together (*e.g.* $NaSn_4(PO_4)_3$, $Na_2Sn(CO_2)_4$, $SnSO_4$). More details about the excluded Sn-based oxides can be seen in Tab. C.2 of Apd. C. In this table, we list reasons of which these oxides were eliminated. We notice that none of these excluded oxides presents very low hole effective masses. This leaves us within 18 Sn^{2+} oxides for which we can relate the hole effective mass with respect to the average Sn−O−Sn angle in a given direction. In these selected compounds, Sn−O network exists in at least one direction and the VBM must have a partial contribution of Sn-*s*. The information on all the Sn^{2+} oxides chosen for the verification of our model is provided in Tab. 3.1 and extensively (including quantitative contributions of Sn-*s*, O-*p*, Sn-*s*,... to the VBM) in Tab. C.1 of Apd. C.

Fig. 3.9 shows the relation between the hole effective mass and the average Sn−O−Sn angle along given directions of the selected Sn^{2+} oxides. The directions in which Sn−O networks are developed are chosen to calculate hole effective masses as equation 3.2. Although there is a slight scattering of data points, we can still observe the expected general trend with the lowest hole effective masses being achieved for angles close to 180°. Angles lower than 120°

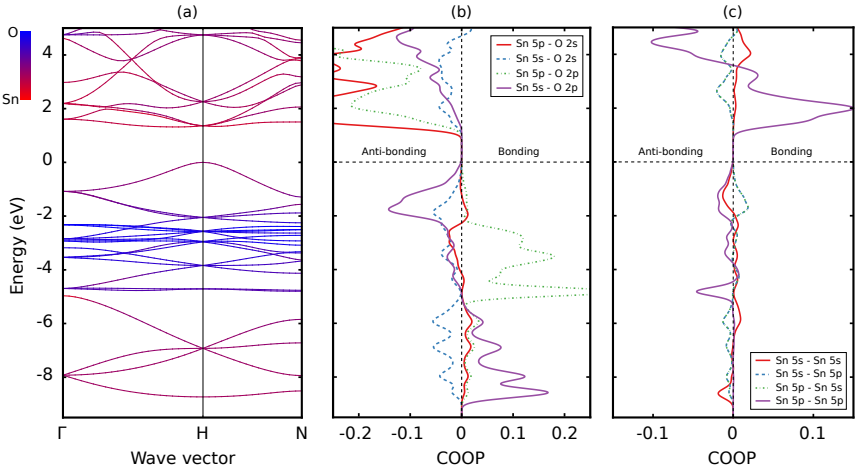

Figure 3.8: The projected band structure of $K_2Sn_2O_3$-$I2_13$ on Sn (red colors) and O (blue colors) atoms (a) and the projected COOP for Sn-O (b) and Sn-Sn (c) interactions.

only lead to very large effective masses and poor hole mobility (*e.g.* $Ta_2Sn_2O_7$). While the lowest hole effective masses are obtained for angles close to 180° in the $K_2Sn_2O_3$ and the isostructural $Rb_2Sn_2O_3$ phase, we notice that angles higher than 120° can lead to already competitive hole effective masses. There is also a gap of hole effective mass in a range of Sn−O−Sn angles from 135° to 175°. As we are currently limited in the number of Sn^{2+} oxides, it is difficult to interpret this behavior.

Table 3.1: Formula, space group (Spg), inorganic crystal structure data base [168] identification number (ICSD-id), three principal hole effective masses m_1, m_2 and m_3 (in unit m_o-free electron mass), average Sn−O−Sn angle $\measuredangle_a$ (in unit °) and average Sn−O distance d_a (in unit Å) for all materials matching with our model.

Formula	Spg	ICSD-id	m_1	m_2	m_3	$\measuredangle_a$	d_a
$K_2Sn_2O_3$	$R\bar{3}m$	2216	0.231	0.231	0.429	180	2.07
$K_2Sn_2O_3$	$I2_13$	40463	0.274	0.274	0.274	167.6	2.09
$Rb_2Sn_2O_3$	$R\bar{3}m$	24816	0.265	0.265	0.369	180	2.1
Rb_2SnO_2	$P2_12_12_1$	24805	1.797	2.227	2.489	131.1	2.12
SnO	$Pmn2_1$	20624	0.557	0.624	7.852	115.6	2.16
SnO	$P4/nmm$	60619	0.588	2.822	2.822	118.0	2.26
$Nb_2Sn_2O_7$	$Fd\bar{3}m$	163817	4.744	4.744	4.744	98.3	2.65
Nb_2SnO_6	$C2/c$	163815	0.425	2.126	5.634	104.0	2.3
$Sn_3(PO_4)_2$	$P2_1/c$	966	0.995	1.997	3.155	110.1	2.31
$Sn_4P_2O_9$	$P2_1/c$	418459	2.433	2.631	5.772	107.6	2.12

Continued on next page

Table 3.1 – continued from previous page

Formula	Spg	ICSD-id	m_1	m_2	m_3	$\measuredangle_a$	d_a
$SnWO_4$	$Pnna$	2147	1.034	2.231	2.417	101.4	2.3
$Ta_2Sn_2O_7$	$Fd\bar{3}m$	163818	6.921	6.921	6.921	98.0	2.66
Ta_2SnO_6	Cc	54078	1.222	3.498	5.094	103.1	2.28
$TiSn_2O_4$	$P4_2/mbc$	163230	0.962	0.962	1.427	126.2	2.12
$BaSn_2H_2O_4$	$P2_1$	37115	1.471	2.274	5.256	116.5	2.09
$SnPHO_4$	$P2_1/c$	658	0.959	1.088	4.524	109.2	2.39
$Cs_2Sn_2O_3$	$Pnma$	24392	2.675	3.575	9.537	123	2.1
$Sn(CO_2)_2$	$C2/c$	150101	0.766	10.214	12.231	113.6	2.63

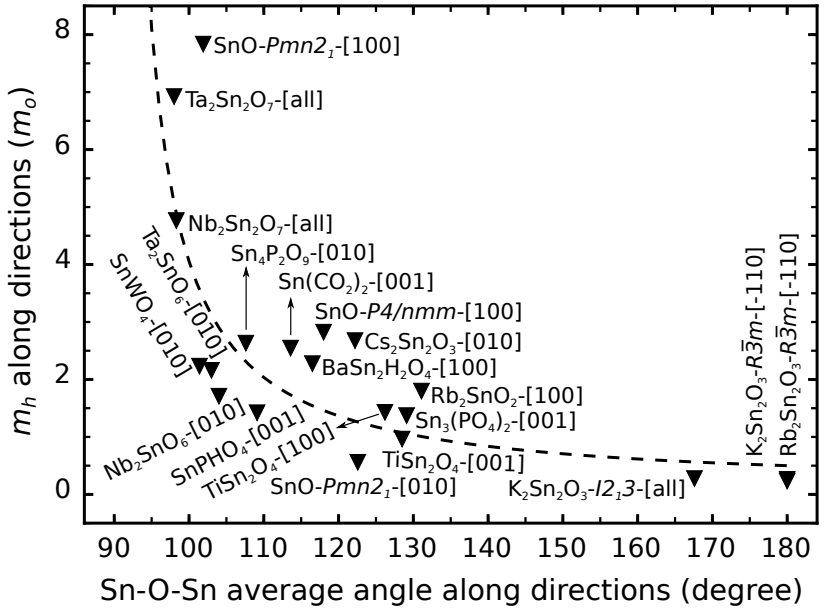

Figure 3.9: The hole effective masses (m_h) as a function of the average Sn−O−Sn angle along different directions for various Sn-based oxides. For each data point (down arrow triangle), the chemical formula and the direction are explicitly indicated. The dash curve simply indicates the trend of hole effective masses.

3.4 Discussions

We have linked the hole effective mass to the chemical bonding in the three Sn^{2+} compounds SnO, r-$K_2Sn_2O_3$ and c-$K_2Sn_2O_3$. Our analysis outlines the importance of the Sn−O−Sn angle in leading to extremely low hole effective masses. Indeed, the Sn-O overlap which drives the curvature of the valence band in

these Sn^{2+} oxides is maximized for Sn−O−Sn angles close to 180°. Our work leads to simple design principles for achieving low hole effective masses in Sn^{2+} containing oxides. Obviously, the VBM should have only Sn and O-p characters as the presence of other (non (n-1)d^{10}ns^2) cations in the VBM character would be detrimental to transport. This is the reason for high hole effective masses in oxides such as $SnMo_5O_8$ or $VSnPO_5$ (see Table C.1 of Apd. C). When only Sn^{2+} is present in the valence band, two types of overlap can be observed Sn-Sn and Sn-O. If a good hole transport is achieved in all directions (as it is favored for materials used in polycrystalline films), at least one crystalline direction will be influenced by the Sn-O overlap. For this (or these) direction(s), which depend(s) on the Sn-O overlap, the Sn−O−Sn angles should be as close as possible to 180° to maximize the overlap between Sn-s and O-p orbitals.

These design principles explain why many Sn^{2+} compounds do not show low hole effective masses despite of the favorable Sn^{2+} chemistry. It also rationalizes why the $K_2Sn_2O_3$ phases are among the lowest hole effective mass oxides reported so far. The potassium atomic levels are low in energy leading to a valence band of Sn and O characters. In addition, the optimal arrangement of Sn^{2+} out-of-plane triangular environment in the $K_2Sn_2O_3$ phases leads to Sn−O−Sn angles close to 180°. The cubic $K_2Sn_2O_3$ is especially fascinating as it provides isotropic transport in a fully three-dimensional Sn−O−Sn network with Sn−O−Sn angles close to the optimal value. While we focused here on Sn^{2+} compounds, our design criteria should be extendable to other (n-1)d^{10}ns^2 chemistries such as Pb^{2+}, Bi^{3+}, Sb^{3+}... In fact, the isostructural cubic phase of $K_2Pb_2O_3$ also exhibits very a low hole effective mass.

The best n-type TCOs are based on chemistries related to the reduced main group cations leading to s-orbital-based p-type TCOs. Indeed, compounds containing (n-1)d^{10}ns^0 cations such as Sn^{4+} (SnO_2), In^{3+} (In_2O_3), Sb^{5+} ($ZnSb_2O_6$), Zn^{2+} (ZnO), Ga^{3+} (Ga_2O_3) show a large overlap with O orbitals as well but in the conduction band [17]. It is therefore natural to wonder if it is also required to have linear metal-oxygen-metal (M-O-M) networks in order to lower the electron effective masses. The two situations are however slightly different. Previous studies have shown that the conduction band minimum of n-type TCOs shows a significant oxygen-s component [161, 246]. No O-s character is present in the valence band of the p-type TCOs based on reduced main group cations and only the strongly directional p orbitals are at play. The O-s character present at the bottom of conduction band of n-type TCOs should result in electron effective masses less sensitive to the oxygen local environment and to the crystal structure in general. This could explain why cations leading to high performance n-type TCOs in the binaries lead to low electron effective mass oxides even in alternate polymorphs or in ternaries. This is also in line with the common explanation of the good mobility in n-type amorphous TCOs based on non-directional metal oxygen orbital interactions [247]. Interestingly, our finding hints at larger difficulties in making s-orbital-based high mobility p-type amorphous oxides. However, recent studies have shown that percolating lone-pair Sn-Sn interactions could be sufficient to provide good electronic transport in Sn^{2+} amorphous TCOs in three dimensions [248]. Further investigation of the relatively less explored

field of *p*-type amorphous *s*-orbital-based TCOs could clarify this discussion.

Finally, we would like to notice that it is challenging to find the appropriate crystal structures following our design principle based on the reduced main group cations. Three dimensional linear M-O-M chains are easily formed using centrosymmetric coordination environments (octahedron and tetrahedron). For instance, this is the case in perovskites ABO_3 [249]. However, reduced main group cations such as Sn^{2+}, Pb^{2+} and Bi^{3+} are lone-pair active and tend to form non-centrosymmetric environments [169]. For instance, Sn^{2+}-based oxides mainly show square out-of-plane, triangular out-of-plane and see-saw coordination environments [250]. The combination of such distorted environments in order to form three-dimensional networks with linearly coordinated oxygen is possible as demonstrated with the $K_2Sn_2O_3$ phases. It is, however, achieved in relatively rare crystal structures.

3.5 Conclusions

A very high hole mobility can be achieved in *p*-type TCOs based on reduced main group cations (Sn^{2+}, Bi^{3+}, Pb^{2+},...). However, the appropriate chemistry alone does not guarantee low hole effective masses. It is thus important to identify the structural factors that influence the hole effective masses. We addressed this question using Sn^{2+} as a typical reduced main group cation. By performing an extensive analysis of the bonding and the electronic structure for three Sn^{2+} oxides proposed as *p*-type TCOs (SnO, r-$K_2Sn_2O_3$, and c-$K_2Sn_2O_3$), we have identified the Sn−O−Sn angle to be an essential structural factor governing the hole effective masses in Sn^{2+} oxides. Indeed, the Sn-O overlap which drives the curvature of the valence band in these oxides is maximized for Sn−O−Sn angles close to 180°. Not only can the important hole effective mass differences between SnO and $K_2Sn_2O_3$ be rationalized in terms of the Sn−O−Sn bond angle, but the relation between this angle and the hole effective mass also holds for other Sn^{2+} oxides. Our work leads to a series of design principles for high mobility *s*-orbital-based *p*-type TCOs. In addition to the presence of a reduced cation from the main group controlling the character of the valence band, a network of metal-oxygen bonds with angles as large as possible (ideally close to 180°) is necessary. We hope that these new design principles will facilitate and motivate future experimental and computational search for novel *s*-orbital-based *p*-type oxides.

Chapter 4

High throughput screening for high mobility *p*-type TCMs, exploring non-oxide space

The finding of high-mobility *p*-type TCMs is very important as these materials are needed for many applications such as transparent solar cells, transparent devices, *etc.* (see Chp. 1). Until now, oxides have been conventionally considered as a promising chemical space to dig out novel *p*-type TCMs but the enhancement in hole mobility has not been significantly achieved. On the other hand, many other non-oxide compounds also show very low hole effective mass and might perform better than traditional *p*-type TCMs (oxides) in terms of mobility. In this chapter, we present a HT computing (relying on density functional theory) for a large dataset of more than 30.000 compounds and identify BP, CaTe and Li_3Sb as very good candidates for high-mobility *p*-type TCMs. These materials are indirect band gap semiconductors with band gaps smaller than 3.0 eV but show high transparency in thin-film form because of their weak phonon-assisted optical transitions. The *p*-type doping tendencies are verified through defect calculations. We also computed el-ph interactions and obtained scattering rate used as a part of inputs for solving Boltzmann transport equation (BTE). The results which will be presented in this chapter are already published in Chem. Mater. **29**, 2568 (2017) and Phys. Rev. Materials **3**, 034601 (2019).

4.1 Introduction

In the past decades, people have put a lot of effort into design of novel *p*-type TCMs with purpose of high hole mobility. After the breakthrough with $CuAlO_2$ in 1997 [18], many transition-metal-based novel *p*-type TCMs were

discovered (see Tab. 1.1). However, these materials still exhibit very low hole mobilities and cannot compare with the best n-type TCMs (SnO_2, In_2O_3, ZnO). Acceleration in exploring novel high-mobility p-type TCMs is, therefore, very needed. In fact, an exploration using only experimental syntheses is very time-consuming and high expenditure as the number of compounds chemical space is rather large. On the other hand, many of the relevant properties (*e.g.* carriers' effective masses, optical absorption, electronic mobility, dopability,...) can be nowadays evaluated by first-principles calculations. This advantage gives a possibility to accelerate the design process by computationally searching new TCM compounds using developed electronic structure methods such as DFT and many-body perturbation theory in the GW framework (see section B.5 of Apd. B). In fact, HT *ab initio* computing is emerging as a very powerful tool to dig out materials for many applications including TCMs. For instance, several HT computations targeting on oxides have recently identified novel p-type TCMs such as $K_2Sn_2O_3$ and Ba_2BiTaO_6 [45, 47]. The analysis of a large dataset of thousands oxides in these researches confirmed that p-type oxides have inherently higher effective masses than n-type oxides. This rationalized the current gap in mobility between the best p-type and n-type oxides. The presence of oxygen p-orbitals in the valence band of most oxides is responsible for this properties. These works also found out that oxides containing reduced main group elements like Sn^{2+}, Sb^{3+}, Bi^{3+}... might likely exhibit low hole effective mass (high mobility).

The inherent difficulty in developing high hole mobility oxides justifies a movement towards non-oxide TCM chemistries including fluorides [251], sulfides [252, 253], oxianions [31], or germanides [183]. By data mining of a large computational data set, we demonstrate that non-oxide materials show lower hole effective masses and therefore can potentially give higher hole mobility. Fig. 4.1 (a) compares hole effective mass of four different classes of materials including oxides, sulfides, nitrides and phosphides. We can see that effective masses of non-oxide compounds distribute mainly in low range from 0 to 5 m_o (m_o is the mass of free electron) while oxides show effective masses in a wider range. This is a clue for us to step out of oxide-space and find out low hole effective mass p-type TCMs. Nonetheless, Fig. 4.1 (b) also points out that non-oxide materials exhibit smaller gaps which can be detrimental to their transparencies. Here, we propose a strategy to overcome this obstacle by exploiting indirect band gaps leading to weak indirect optical transitions. The indirect optical absorption is regularly weak because this sort of absorption is three-particle interaction process and the probability for it to happen is small as a requirement of momentum-conservation. As shown in Fig. 4.2, if the material works in thin-film form, the magnitude of absorption only starts being powerful thanks to vertical transitions corresponding to minimum direct gap. We emphasize that this mechanism is completely similar with the way in which one of the best current p-type TCMs, SnO [230], is working. In this chapter, the direct gap will be considered as an important factor. We will search among thousands of non-oxide materials to identify what compounds in less usual materials such as phosphides, nitrides or sulfides can work as high performance p-type TCMs. Here, we combine different methods such as DFT, hybrid func-

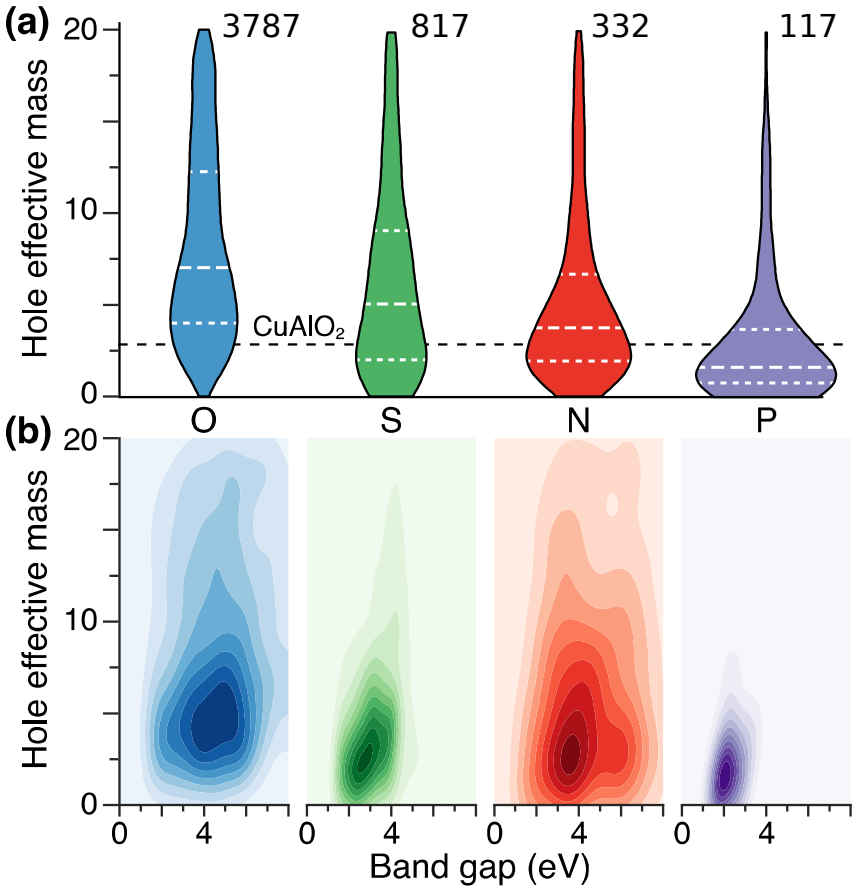

Figure 4.1: (a) Violin plot of the hole effective mass for four chemistries: oxides (O), sulfides (S), nitrides (N), and phosphides (P). The dashed white lines indicate median and quartiles. The hole effective mass of the typical p-type TCM $CuAlO_2$ is also indicated. (b) Hole effective mass vs empirically corrected DFT band gap for the four different chemistries. All masses are scaled relative to the mass of free electron (m_o). The number of investigated compounds is indicated at the top for each chemistry.

tionals, GW and el-ph coupling computations. We identify that BP, CaTe and Li_3Sb would be of great interest as high mobility p-type TCMs. The details of HT screening will be presented in the next section. More information of DFT and hybrid functionals can be seen in Apd. A while that of GW and el-ph coupling is presented in section B.5 and B.6 of Apd. B, respectively.

4.2 High throughput computing approach

Recently, thanks to development of DFT and supercomputers, HT computing has been applied into materials science. It was proved that HT computing

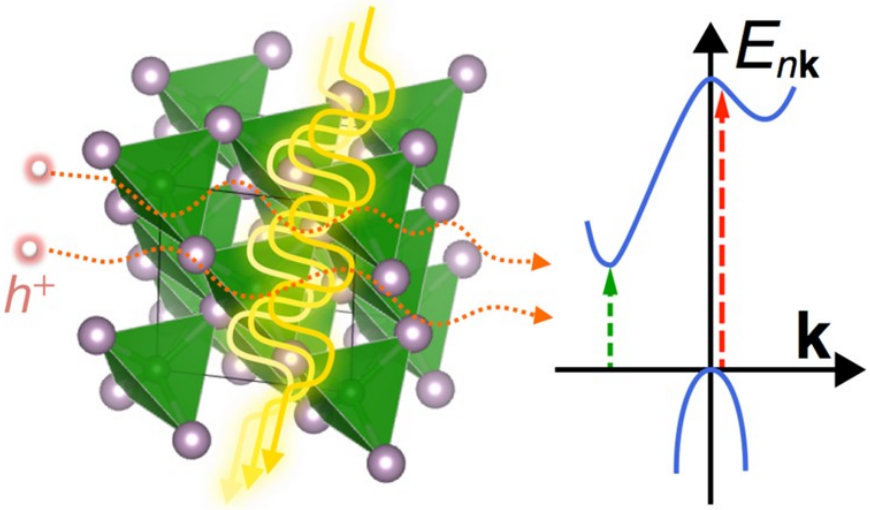

Figure 4.2: The optical absorption in indirect band gap semiconductors. If the indirect optical absorption is weak, the onset of absorption can be seen as it starts at the minimum direct gap.

is an useful approach to uncover and design novel materials satisfying specific requirements. Fig. 4.3 shows a funnel-like tier representing ideas of HT computing approach utilized in this chapter for high mobility p-type TCMs. Basically, we need to start with a big database of crystalline structures. Here, our work is in association with the MP [208, 209] which mainly uses crystalline structures from the ICSD [168] and then relaxes and calculates different relevant properties such as band structure, density, elasticity, *et cetera*. It depends on materials needed for specific applied purposes, a series of necessary properties need to be computed and we, therefore, can quantitatively assess performance of materials. An appropriate tier which includes different calculations corresponding to different properties must be set up. To minimize the cost and maximize the efficiency of the computations, we have to arrange a series of computed properties in the order of which the calculation time and difficulty of methods increase through each step (represented as a layer in the funnel in Fig. 4.3). After each step, the number of compounds remaining decrease because a number of compounds not satisfying the criterion (set up for the corresponding computed property) will be ruled out of consideration.

In our strategy for p-type TCMs, we put effective mass, stability (estimated from phase diagram), band gap (low accuracy-computed by DFT) at top of the HT funnel as these are cheap calculations and easy to do for thousands of compounds. The band gap (high accuracy-computed by HSE functional, GW), defects and mobility are located at the bottom because they are very costly and only doable for a small number of materials (around a dozen or less). After operating a series of computations, we hopefully can obtain some promising candidates in the end. The stability of each compound is assessed through a phase diagram which represents thermodynamic phase equilibria of different

multielement systems composed of elements in that compound. Thermodynamic base and construction of phase diagram will be specifically presented in section B.3 of Apd. B. In this appendix, we also present methodology of GW (section B.5) and *ab initio* el-ph interaction (section B.6) in combination with Boltzmann's transport framework (section B.7) used for calculations of band structure with higher accuracy and carrier mobility, respectively.

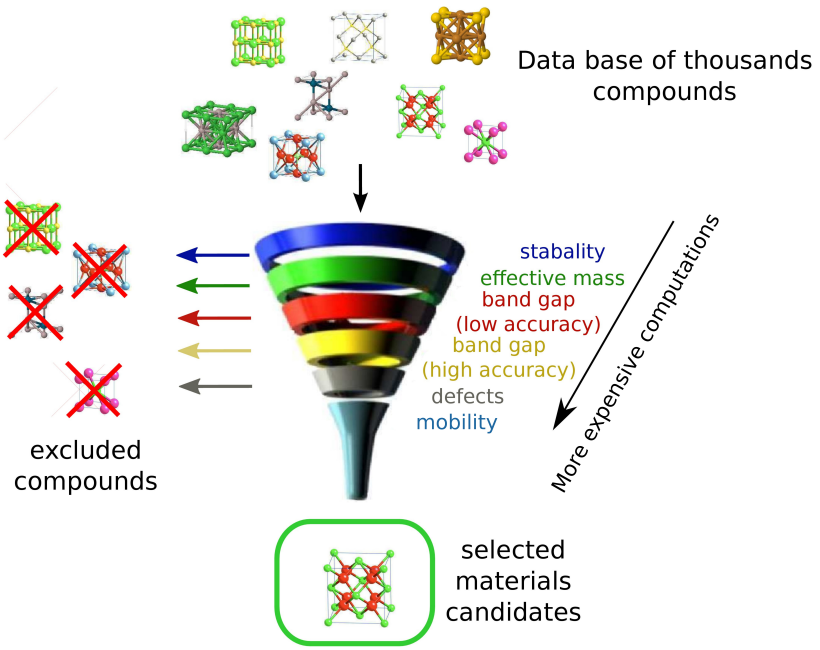

Figure 4.3: The screening strategy of HT computing, in particular for p-type TCMs. After each step, materials which do not satisfy a given criterion will be removed. The further calculations are considered, the more expensive computational methods are employed.

4.3 Computational methods in short

All the considered materials originate from the ICSD [168]. Their relaxed crystal structures and electronic band structures were obtained from the MP database [208, 209]. These rely on DFT high throughput computations which were performed with VASP [190, 191] using the PBE exchange-correlation (XC) functional [254] within the PAW method [215] (see Apd. A).

Fig. 4.4 schematically shows the first four steps in our HT implementation. One of the first calculation is electronic band structure on uniform $\boldsymbol{k}$-mesh in BZ using GGA-PBE functional. Then we use the electronic band structures as inputs for BoltzTrap package [172] (based on Boltzmann transport theory

framework) computing (average) effective masses (see section 1.3 of Chp. 1 for definition). In HT mode, our calculations were set up to run automatically using the Fireworks workflow [255] and pymatgen [194] packages. All the raw effective mass data is freely available in a separate paper which covers around 48,000 inorganic materials [256]. Regarding the effective masses, in the quadratic form, they are represented by a second rank tensor. Because most TCMs are usually used as polycrystalline films, materials with isotropic or close to isotropic transport are easier to use in practical applications. Therefore, for the screening, we focus on the three principal values of this tensor and sort the materials based on the highest of the three principal hole effective masses. We only pick compounds showing hole effective mass $< 1.0\ m_o$ (m_o - mass of free electrons). A rough estimation of band gap is also done here and we filter materials with $E_g > 0.5$ eV.

The next selection criteria for TCMs is their stability. Here, it is assessed by the energy above hull E_{hull} estimated from thermodynamic phase diagrams (computed by DFT at temmperature 0 K and pressure 0 atm) which are already in the MP database [208, 209]. For a compound stable at 0K, $E_{\text{hull}} = 0$ meV/atom, and the stability decreases as E_{hull} increases. We set criterion $E_{\text{hull}} < 24$ meV/atom. This threshold corresponds to the typical standard deviation of computational errors (compared with experiment) of DFT formation-energies [257]. This criteria might be too stringent, thus, many metastable materials (with a higher E_{hull} of around 100 meV/atom) might be excluded after this step. The metastable materials, in fact, can be stabilized in some specific processing conditions (*e.g.* on proper substrates). However, in order to reduce computational cost (in the following steps) and focus on the most stable compounds, it is rational to choose $E_{\text{hull}} < 24$ meV/atom. There are about 320 materials passing through this step. In the next step, band structures along symmetry lines are computed with GGA-PBE functionals. We will screen out candidates exhibiting $E_g^d < 1.5$ eV and continue to perform more accurate calculations for remaining ones since GGA-PBE is known to systematically underestimate the band gap. The more accurate fundamental and direct band gaps are calculated for about a hundred materials using the HSE hybrid XC functional [198, 199] and adopting the same computational parameters as for the PBE calculations. All results of a hundred compounds can be seen in Tab. C.3 of Apd. C. We only choose materials with direct band gap ≥ 2.8 eV for further consideration and calculations such as GW, defects, mobility (with taking into account scattering with phonons)... More information will be presented and discussed in Tab. 4.1 of section 4.4.

As the computational cost becomes more and more expensive in the later steps, only very promising materials will be considered further. In this chapter, we chose three binary compounds including BP, CaTe and Li_3Sb as the most potential candidates. More details about analysis and reasons for this selection will be mentioned and analyzed more in section 4.4. G_0W_0 calculations were performed with ABINIT [258, 259, 260, 261] for these in order to validate band gap and direct gap obtained with HSE previously and therefore we can judge their transparent properties. In these calculations, optimized norm-conserving (NC) pseudopotentials including semi-core electrons were used which were gen-

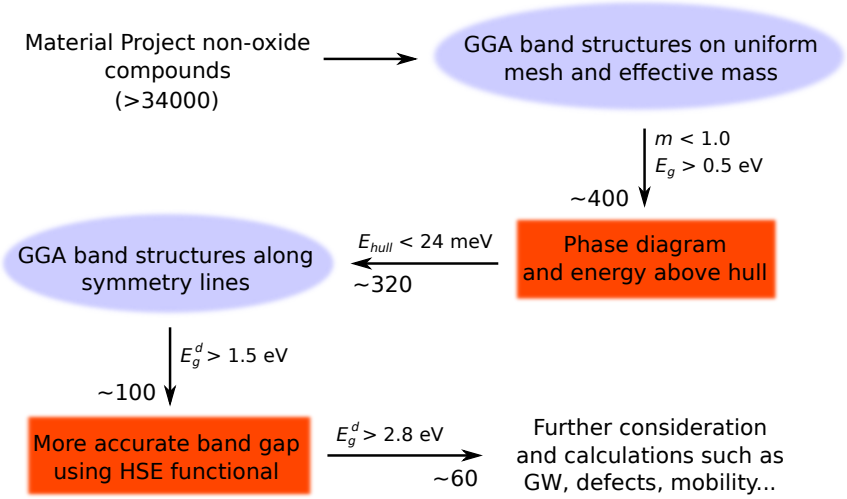

Figure 4.4: The first four steps in HT screening and corresponding criteria. The number of remaining compounds going through the filters are marked at the tips of arrows.

erated with ONCVPSP [262, 263]. The kinetic cut-off energy for the wavefunctions were set to 44, 51 and 52 Ha for BP, CaTe and Li_3Sb respectively, as recommended in the PseudoDojo table [263]. The convergence of these calculations with respect to the kinetic energy cut-off E_c for the dielectric function and the number of bands N_b was tested using automatic GW workflows [264] based on the pymatgen [194] and AbiPy packages [265, 261]. With BP, the convergence of the gap at the Γ point (with a truncation error smaller than 0.01 eV) was easily obtained for $E_c = 10$ Ha and $N_b = 90$. For CaTe, the same convergence was harder to achieve with $E_c = 12$ Ha and $N_b = 480$. In the case of Li_3Sb, the convergence is significantly faster: using $E_c = 10$ Ha and $N_b = 240$ guarantee a truncation error smaller than 0.01 eV. More details about the convergence tests are available in the Apd. C. For the calculations of the screening and the quasi-particle self-energy, $10 \times 10 \times 10$ **k**-point mesh were used for CaTe while $8 \times 8 \times 8$ **k**-point meshes were applied for both BP and Li_3Sb. After that, the band structures could be interpolated from these **k**-point meshes using AbiPy [265, 261].

The intrinsic (or native) point defects consist of vacancies, self-interstitials and antisites (cations on sites of anions, for example). The extrinsic point defects (impurities or dopants) are substitutional and interstitial foreign atoms. Indeed, charged defects in semiconductors can generate free electrons or holes. The intrinsic or extrinsic doping of a material can be assessed by computing defect formation energies as functions of the Fermi level. In this work, the point defect computations were performed using the supercell technique [266] adopting $3 \times 3 \times 3$ supercells of the primitive cells. We calculated the defect formation energies first using the PBE XC functional but also with the more

accurate HSE hybrid functional for Li_3Sb and CaTe [198, 199]. The HSE functional was proved to capture better not only the energy but also the band gap [267]. Here, the screening length and fraction of exact exchange were set to the common values of 0.2 Å and 25 % respectively. The kinetic energy cut-off for the wavefunctions was set to 19.1 Ha (520 eV) and the relaxations are stopped when the change in total energy between two ionic relaxation-steps is smaller than 3.67×10^{-4} Ha (0.01 eV). The formation energy of defect D in charged state q can be written as [268, 269]

$$\begin{aligned} E_f[D^q] = E[D^q] + E_{corr}[D^q] - E[bulk] - \Sigma_i n_i \mu_i \\ + q(\epsilon_{\mathrm{VBM}} + \Delta v + \Delta \epsilon_F), \end{aligned} \tag{4.1}$$

where $E[D^q]$ and $E[bulk]$ are the total energies of the supercell with a defect D in the charge state q and without any defects, respectively; n_i is the number of atoms of type i removed ($n_i < 0$) or added ($n_i > 0$); and, μ_i is the corresponding chemical potential. ϵ_{VBM} is the energy of the valence band maximum (VBM), and $\Delta\epsilon_F$ is the Fermi level referenced to ϵ_{VBM}. The correction terms $E_{corr}[D^q]$ and Δv are introduced to take care of the spurious image-charge interactions and the potential alignment for charged defects, respectively. The defect states with the charge q were corrected using the extended Freysoldt's (Kumagai's) scheme [270, 271]. All defects computations were performed using the PyCDT package [272]. More computational details about the defect calculation can be found in section B.4 of Apd. B.

The mobility depends on the effective mass m^* through $\mu = e\tau/m^*$ where the relaxation time τ (inverse of the scattering rate) depends on different scattering mechanisms. Carriers can be scattered by phonons, ionized and neutral impurities, grain boundaries,... In this work, we only took into account the scattering of electrons by phonons which is likely to be an important component of scattering and is an intrinsic mechanism, difficult to control through purity and microstructure. The carriers scattering by phonons can be computed theoretically if the el-ph matrix elements are known. In principle, one can employ DFPT to obtain all the el-ph matrix elements from first principles. However, converging the relevant physical properties (such as the scattering rate of electrons by phonons) often requires very dense **k**-point and **q**-point meshes for electrons and phonons respectively leading to a considerable increase of computational time. The recently developed interpolation techniques based on Wannier functions offer a very practical and efficient solution to overcome this obstacle. In this work, we used the EPW code [273, 274] interfaced with Quantum ESPRESSO [275, 276] to calculate the relaxation-time $\tau_{n\mathbf{k}}$ (n and $\mathbf{k}$ are band index and wave vector of a Bloch's state, respectively). More details on the theory and the implementation can be found in Ref. [274]. The $\tau_{n,\mathbf{k}}$ were interpolated on a dense $40 \times 40 \times 40$ mesh for both **k**-points (for electrons) and **q**-points (for phonons) starting from the DFPT values on a $6 \times 6 \times 6$ mesh. The latter (together with the structural relaxation, self-consistent, non self-consistent calculations which are needed to run EPW) were obtained using Quantum ESPRESSO with NC pseudopotentials and very stringent parameters for convergence, *e.g.* high cut-off energy of 40 Ha. These $\tau_{n,\mathbf{k}}$ are then used as an input to compute the carrier mobility by solving the BTE by means of

the BoltzTrap package [172]. In the latter calculations, the DFT band energies (computed on a finite number of **k**-points) are interpolated using star functions (see section 1.3 of Chp. 1). Here, we have implemented another interpolation for the relaxation time in BoltzTrap in order to obtain the same very dense **k**-point grid as the one used for band energies. The physical principle for this implementation is that the symmetries of the quasi-particle energies are the same as those of band energies [277] ($\tau_{n,\mathbf{k}}$ due to the interaction with phonons can be calculated from the imaginary part of the el-ph self-energy). More details about el-ph coupling can be seen in section B.6 of Apd. B. We would like to emphasize that the el-ph coupling and the following transport simulation are done for bulk materials. In fact, when samples are fabricated in specific conditions (temperature, substrates,...), this can be influenced by impurities, grain, interface,...

As mentioned in section 4.1, when stepping out of oxide-space, we can possibly find much lower hole-effective-mass candidates but can face with lower transparency as well (band gaps might be shrunk). We will, therefore, target on indirect band gap materials with large direct gap (> 3.0 eV) so that they still can preserve their transparency when working in thin-film form. The physical insight is that in the energy range from indirect band gap to direct gap, the phonon-assisted optical transitions are regularly weak. To validate this tendency, we will carry phonon-assisted optical absorption if necessary. EPW code [273, 274] is also used to implement this task. *Ab initio* computation for indirect optical absorption was done the first time for Silicon in Ref. [278] and the authors obtained an excellent agreement with experiment. More information can be found in section B.6 of Apd. B.

4.4 Results

4.4.1 Preliminary views and analyses

Tab. 4.1 shows a selection of 63 materials with a direct band gap ≥ 2.8 eV after performing first four steps as shown in Fig. 4.4. The materials are sorted in decreasing order as a function of the computed direct band gap. Among the materials at the top of the list, SiC is a well-known wide band gap semiconductor. This material exhibits polymorphism (*e.g.* cubic: 3C, rhombohedral: 15R, hexagonal: 6H, 4H, 2H) [279] and can be doped with both *n*- and *p*-type [280, 281, 282, 283]. A high hole mobility of 40 cm^2/Vs was obtained for the cubic phase [284]. The indirect optical absorption of cubic phase is very weak at room temperature with a coefficient of 10^3 cm^{-1} at 3.1 eV [285]. We suggest that SiC can be considered as a good *p*-type TCM. The main disadvantage of this compound is the difficulty of hole doping. Most known impurities such as Al, B, Ga and Sc create deep doping-levels leading to rather low concentrations of holes which were typically measured to be lower than 10^{18} cm^{-3} [284] and is suitable for transistor applications.

Next comes a series of beryllium based compounds (BeS, BeSe, $BeCN_2$, Be_2C and BeTe). While their computed performance in terms of band gap and hole effective masses are very attractive, the toxicity of beryllium lowers their

interest for technological applications. Likewise, the many lead-based halide perovskites ($CsPbCl_3$, $RbPbF_3$, and $CsPbF_3$) and Li_2GePbS_4 also present toxicity issues. It is interesting however to see these halide perovskites being of great interest as solar absorbers when they are made in chemistries showing smaller gaps [286, 287]. Toxicity is also an issue with the series of arsenides, *e.g.* AlAs. These arsenides are also very analogous to the phosphides such as BP and AlP. Some of the materials in the list contain rare-earth elements which might present some cost issues. We consider that further assessment of all these materials in terms of dopability and mobility is not a priority. Therefore, in the penultimate column of Tab. 4.1, the absence of toxic or rare-earth elements is verified, as indicated by a checkmark.

Continuing to explore the list of materials, many hydrides appear to be of interest with low hole effective mass and large direct band gaps for LiH, $BaLiH_3$ and CsH. Unfortunately, our subsequent defect computations indicate that these hydrides have low-lying hole-killing defects especially the hydrogen vacancy making unlikely their efficient p-type doping (see Apd. C). A few sulfides are also identified by our screening: ZnS and $ZnAl_2S_4$. ZnS has been indeed recently studied as a good performance p-type TCM [253]. $ZnAl_2S_4$, on the other hand, is less studied but our defect computation indicates that it is very unlikely to be p-type dopable because Zn-Al anti-site defects form easily and act as hole-killers. Al_2CdS_4 is likely to present the same issues. The defect formation energies computed by DFT for $ZnAl_2S_4$ are given in the Apd. C. Among the different materials in the table, three promising candidates including BP, Li_3Sb and CaTe also attracted our attention. The following parts are dedicated to the further computations that were performed for these compounds.

Table 4.1: Formula, space group (Spg), Materials Project identification number (MP-id) [208, 209], fundamental E_g and direct gaps E_g^d computed by HSE functional (in eV), energy above hull E_{hull} (in meV/atom), principal components m_1, m_2 and m_3 of the hole effective mass tensor (in atomic units), verification of the absence of toxic/rare-earth (T/RE) elements (Be, As, Cd, Yb, Hg, Pb and Th) and of the p-type dopability (when computed here or obtained from the existing literature) for the selected compounds (see text). The materials are sorted as a function of the direct band gap in decreasing order.

Formula	Spg	MP-id	E_g^d	E_g	E_{hull}	m_1	m_2	m_3	T/RE	p-type
BeS	$F\bar{4}3m$	422	6.89	4.05	0.0	0.65	0.65	0.65	×	-
$KMgH_3$	$Pm\bar{3}m$	23737	5.76	3.58	0.0	0.75	0.75	0.75	✓	-
SiC	$F\bar{4}3m$	8062	5.75	2.25	0.7	0.58	0.58	0.58	✓	✓ [†]
BeSe	$F\bar{4}3m$	1541	5.27	3.36	0.0	0.55	0.55	0.55	×	-
$BeCN_2$	$I\bar{4}2d$	15703	5.21	5.21	0.0	0.75	0.75	0.78	×	-
$RbPbF_3$	Cc	674508	5.20	4.84	0.0	0.71	0.83	0.95	×	-
MgS	$Fm\bar{3}m$	1315	4.95	3.84	0.0	0.98	0.98	0.98	✓	-
$RbHgF_3$	$Pm\bar{3}m$	7482	4.90	2.11	0.0	0.93	0.93	0.93	×	-

Continued on next page

Table 4.1 – continued from previous page

Formula	Spg	MP-id	E_g^d	E_g	E_{hull}	m_1	m_2	m_3	T/RE	p-type
AgCl	$Fm\bar{3}m$	22922	4.81	2.28	0.0	0.83	0.83	0.83	✓	-
$CsHgF_3$	$Pm\bar{3}m$	561947	4.59	2.20	0.0	0.89	0.89	0.89	×	-
Be_2C	$Fm\bar{3}m$	1569	4.56	1.63	0.0	0.37	0.37	0.37	×	-
$SrMgH_4$	$Cmc2_1$	643009	4.52	3.78	0.0	0.84	0.90	0.95	✓	-
Li_2Se	$Fm\bar{3}m$	2286	4.36	3.70	0.0	0.95	0.95	0.95	✓	-
BP	$F\bar{4}3m$	1479	4.35	2.26	0.0	0.34	0.34	0.34	✓	✓ [228]
CaS	$Fm\bar{3}m$	1672	4.28	3.34	0.0	0.88	0.88	0.88	✓	-
$LiCa_4B_3N_6$	$Im\bar{3}m$	6799	4.25	3.38	0.0	0.86	0.86	0.86	✓	-
$BaSrI_4$	$R\bar{3}m$	754852	4.22	4.22	21.8	0.73	0.73	0.80	✓	-
$LiSr_4B_3N_6$	$Im\bar{3}m$	9723	4.18	3.22	0.0	0.89	0.89	0.89	✓	-
$NaSr_4B_3N_6$	$Im\bar{3}m$	10811	4.08	3.14	0.0	0.92	0.92	0.92	✓	-
K_2LiAlH_6	$Fm\bar{3}m$	24411	4.04	3.70	9.1	0.65	0.65	0.65	✓	-
BeTe	$F\bar{4}3m$	252	4.04	2.45	0.0	0.42	0.42	0.42	×	-
Ba_3SrI_8	$I4/mmm$	756235	4.02	4.02	7.5	0.70	0.81	0.81	✓	-
CaSe	$Fm\bar{3}m$	1415	4.01	2.95	0.0	0.77	0.77	0.77	✓	-
LiH	$Fm\bar{3}m$	23703	3.97	3.97	0.0	0.46	0.46	0.46	✓	×
AlP	$F\bar{4}3m$	1550	3.90	2.50	0.0	0.56	0.56	0.56	✓	×
YbS	$Fm\bar{3}m$	1820	3.76	2.96	0.0	0.76	0.76	0.76	×	-
Na_2LiAlH_6	$Fm\bar{3}m$	644092	3.75	3.75	3.9	0.66	0.66	0.66	✓	-
SrSe	$Fm\bar{3}m$	2758	3.68	3.03	0.0	0.83	0.83	0.83	✓	-
$BaLiH_3$	$Pm\bar{3}m$	23818	3.62	3.26	0.0	0.36	0.36	0.36	✓	×
$CsPbF_3$	$Pm\bar{3}m$	5811	3.59	3.59	4.6	0.39	0.39	0.39	×	-
Cs_3ZnH_5	$I4/mcm$	643702	3.58	3.58	0.0	0.69	0.93	0.93	✓	-
Al_2CdS_4	$Fd\bar{3}m$	9993	3.56	3.55	20.0	0.78	0.78	0.78	×	-
K_2LiAlH_6	$R\bar{3}m$	23774	3.52	3.52	0.0	0.68	0.84	0.84	✓	-
$BaMgH_4$	$Cmcm$	643718	3.51	3.26	4.8	0.48	0.55	0.70	✓	-
CaTe	$Fm\bar{3}m$	1519	3.50	2.18	0.0	0.60	0.60	0.60	✓	✓
Cs_3MgH_5	$P4/ncc$	23947	3.49	3.49	0.3	0.88	0.93	0.93	✓	-
Cs_3MgH_5	$I4/mcm$	643895	3.49	3.49	0.0	0.83	0.94	0.94	✓	-
YbSe	$Fm\bar{3}m$	286	3.48	2.43	0.0	0.67	0.67	0.67	×	-
ZnS	$F\bar{4}3m$	10695	3.46	3.46	0.0	0.81	0.81	0.81	✓	✓ [253]
$TaCu_3S_4$	$P\bar{4}3m$	10748	3.46	2.95	0.0	0.98	0.98	0.98	✓	-
Al_2ZnS_4	$Fd\bar{3}m$	4842	3.46	3.43	0.0	0.66	0.66	0.66	✓	×
Li_2ThN_2	$P\bar{3}m1$	27487	3.46	3.33	0.0	0.85	0.95	0.95	×	-
$Mg_2B_{24}C$	$P\bar{4}n2$	568556	3.42	3.41	0.0	0.77	0.93	0.93	✓	-
Li_2GePbS_4	$I\bar{4}2m$	19896	3.33	3.20	0.0	0.61	0.61	0.98	×	-
Cs_3H_5Pd	$P4/mbm$	643006	3.32	3.09	0.0	0.79	0.83	0.83	✓	-
SrTe	$Fm\bar{3}m$	1958	3.24	2.39	0.0	0.67	0.67	0.67	✓	×
MgTe	$F\bar{4}3m$	13033	3.24	3.24	0.9	0.95	0.95	0.95	✓	-
$CsTaN_2$	$I\bar{4}2d$	34293	3.22	3.22	0.0	0.71	0.71	0.92	✓	-
Cs_3MnH_5	$I4/mcm$	643706	3.21	3.18	0.0	0.82	0.96	0.96	✓	-
LiMgP	$F\bar{4}3m$	36111	3.18	2.00	0.0	0.65	0.65	0.65	✓	-
BaS	$Fm\bar{3}m$	1500	3.17	3.02	0.0	0.85	0.85	0.85	✓	-
$LiAlTe_2$	$I\bar{4}2d$	4586	3.11	3.11	0.0	0.52	0.83	0.83	✓	-

Continued on next page

Table 4.1 – continued from previous page

Formula	Spg	MP-id	E_g^d	E_g	E_{hull}	m_1	m_2	m_3	T/RE	p-type
YbTe	$Fm\bar{3}m$	1779	3.09	1.76	0.0	0.54	0.54	0.54	×	-
Li_3Sb	$Fm\bar{3}m$	2074	3.06	1.15	0.0	0.24	0.24	0.24	✓	✓
$SrAl_2Te_4$	$I422$	37091	3.06	2.66	0.0	0.42	0.79	0.80	✓	-
$TaCu_3Te_4$	$P\bar{4}3m$	9295	3.05	2.50	0.0	0.63	0.63	0.63	✓	-
$CsPbCl_3$	$Amm2$	675524	2.99	2.99	0.0	0.30	0.32	0.33	×	-
$TaCu_3Se_4$	$P\bar{4}3m$	4081	2.98	2.43	0.0	0.82	0.82	0.82	✓	-
BaSe	$Fm\bar{3}m$	1253	2.95	2.59	0.0	0.76	0.76	0.76	✓	-
KAg_2PS_4	$I\bar{4}2m$	12532	2.87	2.53	0.0	0.67	0.82	0.82	✓	-
AlAs	$F\bar{4}3m$	2172	2.84	2.12	0.0	0.50	0.50	0.50	×	-
$LiErS_2$	$I4_1/amd$	35591	2.80	2.80	10.4	0.62	0.99	0.99	✓	-
GaN	$F\bar{4}3m$	830	2.80	2.80	5.2	0.94	0.94	0.94	✓	-

† [280, 281, 282, 283]

4.4.2 Boron monophosphide

Fig. 4.5 presents the conventional cell of BP. Each B atom is surrounded by four P atoms in tetrahedral corner-sharing local environments. This is a cubic system with high symmetry, which leads to an isotropic effective mass tensor as shown in Tab. 4.1.

Fig. 4.6 shows the band structure of BP computed by DFT and G_0W_0. It is worth noting that the G_0W_0 along symmetry lines in Fig. 4.6 was interpolated from G_0W_0 band structure on uniform $\boldsymbol{k}$-mesh of $8 \times 8 \times 8$ using Abipy package [265, 261]. The interpolation method uses the star functions as basis sets (see section 1.3 of Chp. 1). We can see that the band structure is degenerated at VBM, thus, the warping effect is clearly seen here. The effective mass shown in Tab. 4.1 apparently does not describe this effect. The G_0W_0 fundamental gap is about 1.97 eV with VBM locating at Γ-point and CBM locating close to X-point on $\Gamma - X$ line. This is consistent with experimental values (vary in range from 1.9 to 2.1 eV) measured by different methods such as optical absorption, electro-luminescence and X-ray spectroscopy [288, 289, 290, 291, 292, 293]. The direct gap is located at Γ-point and has a value of 4.25 eV. The G_0W_0 direct gap is large so that we expect such a large direct band gap to lead to transparency in the visible region. This was validated through experimental reports [294, 290, 291]. In Fig. 4.7 we show indirect optical absorption coefficient calculated with EPW [273, 274]. The experimental data [290, 291] were extracted and plotted as well. Our calculated result underestimates indirect optical absorption. This indicates that the el-ph in BP might be underestimated or the theoretical framework used for the indirect absorption calculation [295] does not produce fairly good result as the temperature-dependence effect of electronic band structure is neglected. Additionally, it is worth noting that the experimental data [290, 291] referred here is rather old. In general, it shows quite weak absorption in the visible range with the average intensity about 2.5×10^3 cm^{-1}. Using the visible transmittance defined in equation (2.8) of

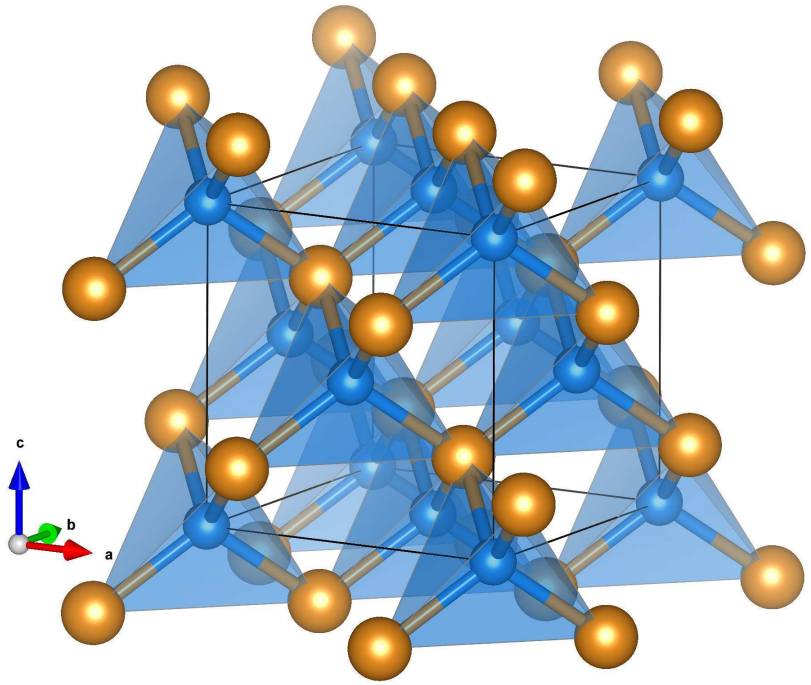

Figure 4.5: The conventional cell of BP with tetrahedral local environments around B atoms (blue).

Chp. 2, we can roughly estimate the loss of transmittance caused by indirect absorption (the plasmon effect is not taken into account). For 100-nm BP film, only a few percent of visible light energy is lost.

In order to check p-type dopability, we implemented defect calculations using supercell technique as mentioned in section 4.3. The chemical potential of defects (see equation (4.1)) is estimated from thermodynamic phase diagram (see section B.3 of Apd. B) in limit conditions. The chemical potentials are chosen in conditions which lead to the most favorable p-type doping tendency for this material. We first tried with intrinsic point defects and the results is shown in Fig. 4.8 (a). We can see that we cannot dope BP with hole by using intrinsic defects as positive charged states of anti-site defect P_B exhibit low formation energy close to VBM and therefore, actively work to release electrons. This totally compensates for holes generated by anti-site defect B_P or vacancy V_B. We continue to investigate extrinsic defects with some dopants such as Si, C, Mg, Be. Fig. 4.8 (b) show that extrinsic defects lower formation energy in comparison with intrinsic ones. Among many these defects, substitutions Be_B and Si_P are the most energetically favorable for p-doping. Defect formation energy of these around VBM is low enough to defeat intrinsic hole killer, P_B. Moreover, it is interesting to see that Si_B and C_B can be good electron generators as well. It is not surprising that our strategy identifies materials with a small fundamental band gap but large direct gap can lead to bipolar

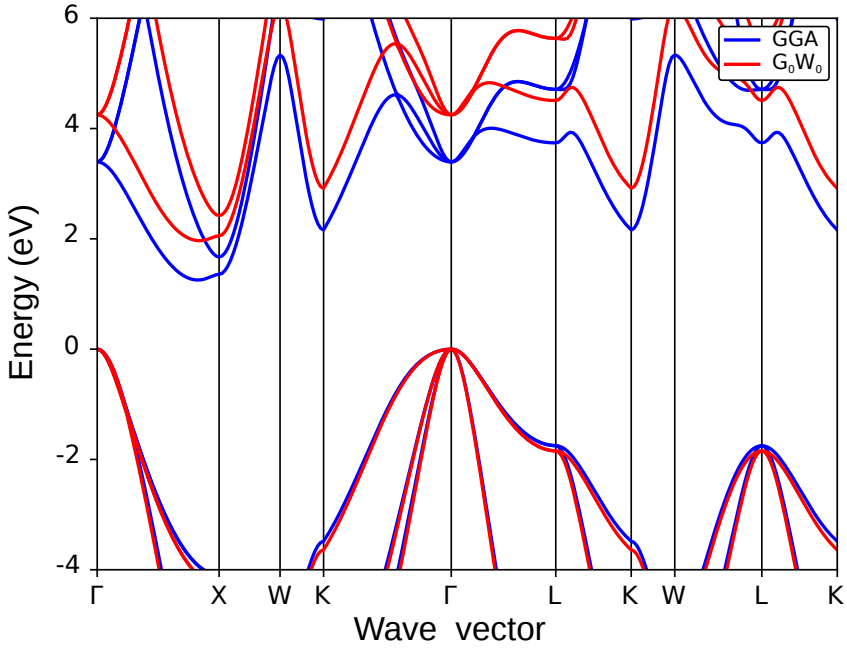

Figure 4.6: The band structure of BP computed by DFT (blue) and G_0W_0 (red).

doping. BP, therefore, can be doped with both n- and p-types and might be a ambipolar transparent materials similar to SnO [206, 230]. In fact, this was validated through many experimental researches [296, 297, 298, 299, 300, 301].

Our last calculation focuses on an estimate of hole mobility. BP shows very low hole effective mass 0.35 m_o within DFT. Indeed, BP has threefold degeneracy at VBM (Γ point), therefore, the transport of holes occurs in three bands with some lighter and some heavier. Our definition of effective mass takes into account the competition among these three bands and give an average value that is representative of the transport which will happen in the different bands. More details about formulas and calculation techniques is written in section 1.3 of Chp. 1. This should be kept in mind when comparing our results to other studies which sometimes only focus on one band when several competing bands are present [302, 303]. It is worth noting that the effective masses might be changed in the GW band structures, which is not assessed in this work. Here, we still use the DFT band structures for the transport calculations. As seen in Fig. 4.10, the top of valence band is mainly composed of p-orbital characters of B and P. We will compute el-ph scattering and use this to solve semi-classical BTE. Fig. 4.9 shows phonon dispersions (fat bands) and projected DOS of phonons for BP using the PBE functional. The fat bands represent qualitatively characteristics of the vibrational modes, including what type of atom participates in the phonon modes at a given energy, their direction and amplitude. The absence of modes with imaginary frequencies proves that these

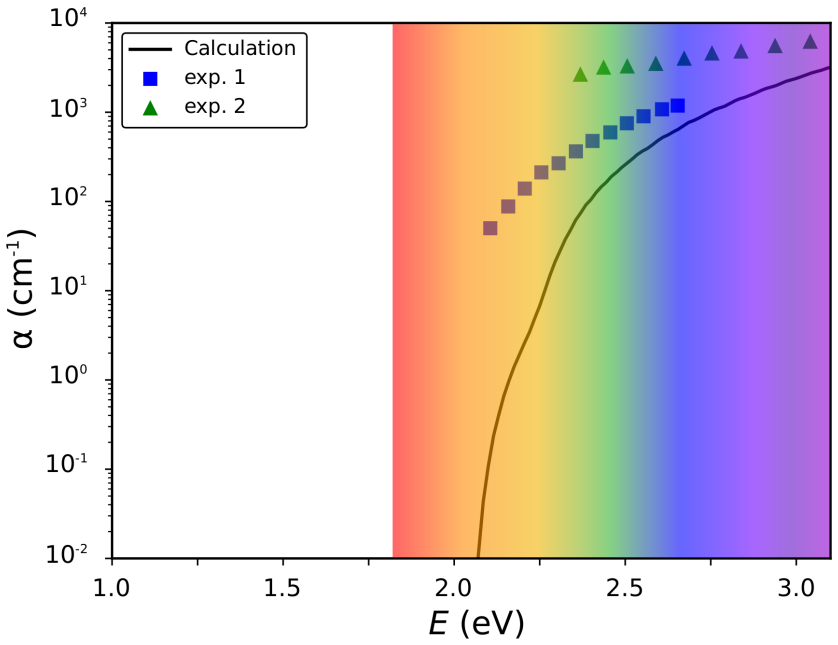

Figure 4.7: Indirect absorption coefficient as a function of photon energy calculated at 300 K. The DFT band structure was used and applied a scissor shift to fit with G_0W_0 band gap. The experimental data from Refs. [290] (exp. 1) and [291] (exp. 2) is also reproduced for comparison.

materials are dynamically stable at 0 K. The lighter B atoms mainly contribute to the optical modes at high frequencies (3 modes) while the heavier element P atoms play an important role in the three acoustic modes at low frequencies.

The effective mass is an important factor driving carrier mobility but not the only one. Scattering rate or relaxation time also affects the mobility. There are several mechanisms which can influence relaxation time as mentioned in 4.3. Phonon scattering is the most intrinsic factor as it is not affected by purity and microstructure. The evaluation of relaxation time from phonon scattering can be performed *ab initio* using el-ph coupling matrices obtained from DFPT phonon computations. We can then interpolate el-ph coupling matrices and the relaxation time $\tau_{n\mathbf{k}}$ on a dense $\boldsymbol{k}$-point grid using EPW as mentioned in section 4.3. Fig. 4.10 (a) shows the DFT band structure and the scattering rates (inverse of $\tau_{n\mathbf{k}}$) at 300 K for different electronic states. The radii of the red dots account for the intensity of the scattering rate of the corresponding electronic state. We also present the projected and total DOS (Fig. 4.10 (b)) and the corresponding relaxation time and scattering rate (Fig. 4.10 (c)) as functions of energy (see section B.6 of Apd. B for computational details). In general, the scattering rates are proportional to the DOS, implying that the relaxation time becomes smaller in regions of high DOS. The Fermi level in doped BP can be located above or below the VBM, depending on the number

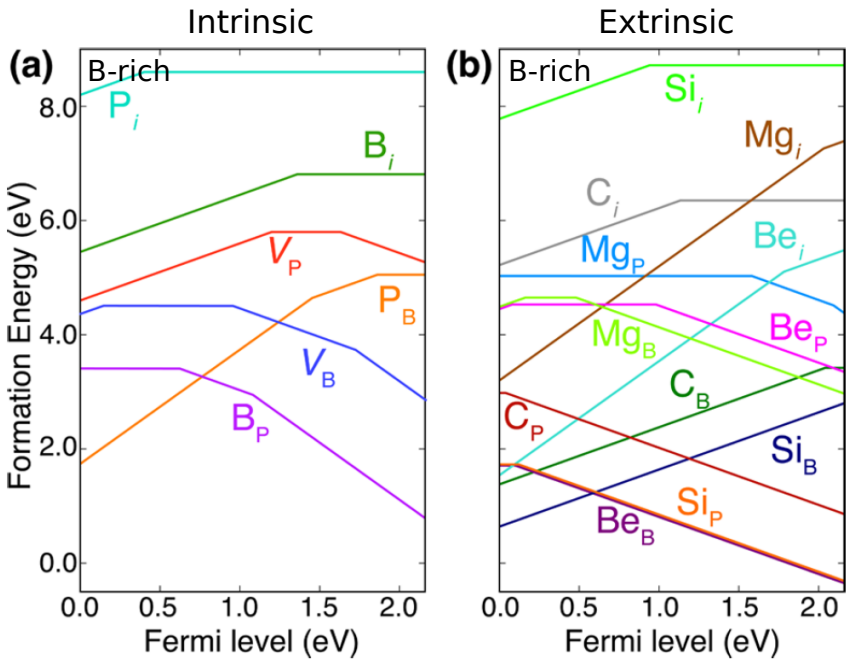

Figure 4.8: (a) Intrinsic defect formation energy with respect to Fermi level for BP in boron-rich region. X_Y indicates X on an Y's site, V presents for vacancy and the subscript i stands for interstials. (b) Extrinsic defect formation energy vs Fermi level for BP in boron-rich region.

of holes and the DOS around this valley. In this work, at the doping hole concentration of 10^{18} cm^{-3}, the Fermi level is 90.5 meV above the VBM while it is located 273.2 meV below the VBM for very high doping concentrations of 10^{21} cm^{-3}. The transport of holes takes place in the pocket around the Γ-point and is contributed by there bands. Around the Γ-point, we can see that the scattering is very weak (see Fig. 4.10 (a)) leading to high relaxation times around the VBM (see Fig. 4.10 (c)). This can be understood because BP is a weakly polarized material, leading to a small Born effective charge [304, 305] and therefore weak long-range el-ph interactions [306].

Fig. 4.11 shows the hole mobilities as a function of hole concentrations at 300 and 400 K for BP. The mobilities decrease with hole concentration because at the higher carrier concentrations the Fermi level shifts deeper below the VBM and the carriers at the Fermi surface occupy electronic states with higher scattering rates (see Fig. 4.10 (c)). It is also lower at the higher temperature of 400 K because of the increase of scattering with phonons. The value of the hole mobility obtained at room temperature is high at around 900 cm^2/Vs at a doping concentration of 10^{18} cm^{-3}. This is consistent with the very weak scattering shown in Fig. 4.10. However, the calculated hole mobility is still too high in comparison with experimental measurements as shown in Tab. 4.2. We attribute this difference to the fact that we only take into account scattering

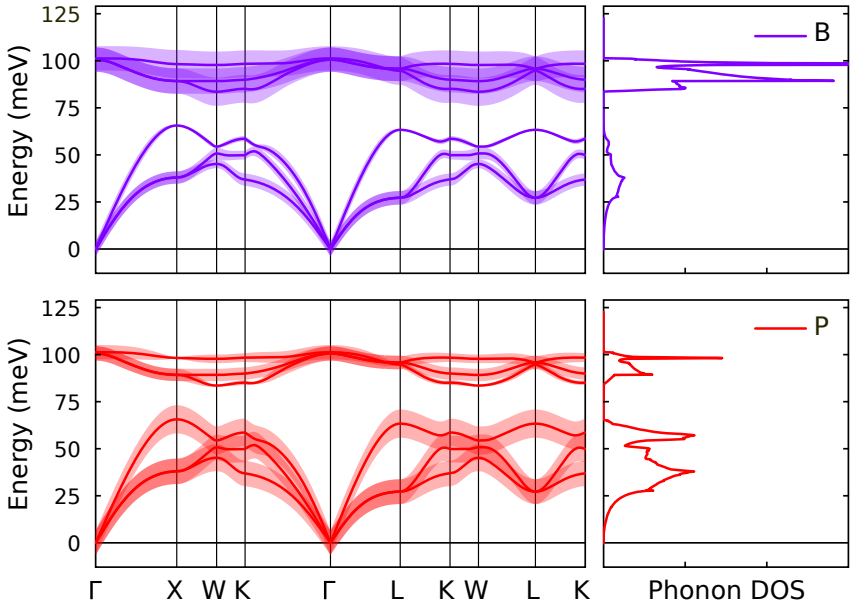

Figure 4.9: Phonon dispersions with fat bands representing atomic displacements associated with lattice vibrations. The width of fat bands gives qualitative understanding of the vibrational modes such as what are the atomic types involved in the vibrations at a given energy, their direction of oscillation and the amplitude (related to the displacement). The projected DOS of phonons on each type of atom are correspondingly shown next to the phonon dispersion.

with phonons, while carrier scattering might also depend on other mechanisms like (neutral and ionized) impurities or grain boundaries. This means that our calculated results represent the intrinsic upper limit for the mobility. In Tab. 4.2, the hole mobilities measured for samples experimentally synthesized by different methods vary in a very wide range. This repeatedly confirms for the complexity (as seen through Tab. 1.1 and Tab. 1.2 in Chp. 1) that carrier mobility is managed by many factors such as quality of the samples (crystalline, polycrystalline or even amorphous morphology), impurities, (neutral or charged) point defects,...

4.4.3 Calcium monotelluride and trilithium antimony

The conventional cells of CaTe and Li_3Sb are shown in Fig. 4.12 (a) and (b). Ca atoms in CaTe are surrounded by six Te atoms forming an octahedral local environment. In Li_3Sb, the cation fills tetrahedral and octahedral sites. Both CaTe and Li_3Sb are cubic phases with high symmetry, which explains their isotropic hole effective masses ($m_1 = m_2 = m_3$). CaTe and Li_3Sb exhibit very low hole effective masses with eigenvalues being 0.60 and 0.25 m_o (m_o-mass

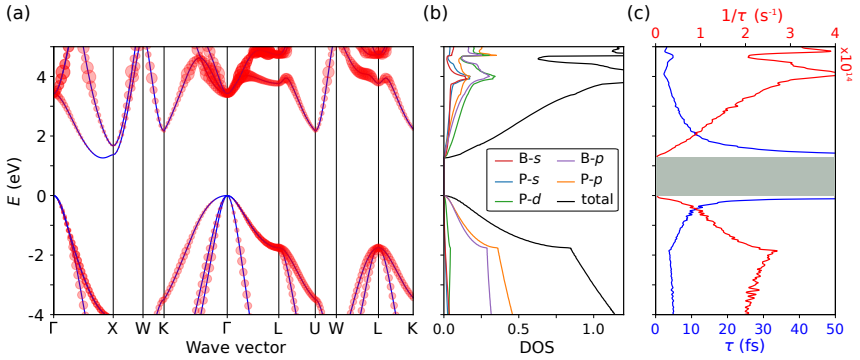

Figure 4.10: From left to right, DFT electronic band structure, projected DOS and relaxation time and scattering rate. Each DFT electronic state is marked with red dots representing its scattering rate with phonons at a temperature of 300 K (the intensity of scattering is proportional to the size of the dots). The projected DOS are computed using DFT. The relaxation time τ (in femtosecond) and its inverse, the scattering rate, $1/\tau$ (in 1/second) are shown as functions of energy.

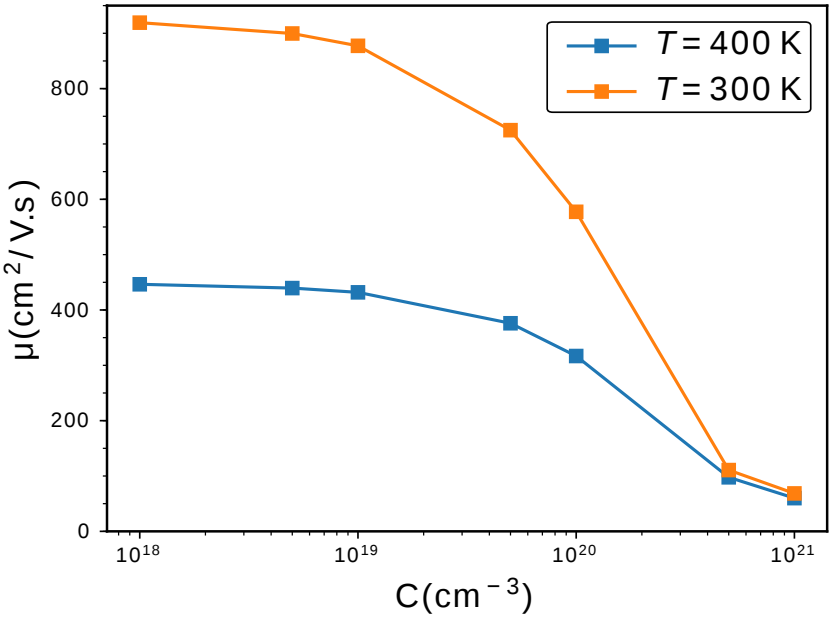

Figure 4.11: Hole mobilities of BP computed as as a function of carrier concentration at temperatures of 300 K and 400 K.

of free electron), respectively. It is worth noting that the lowest hole effective masses found so far in a computational database for a p-type conducting oxides

Table 4.2: The fabrication methods (abbreviations of some methods are at the bottom of this table), hole-carrier concentrations C (in cm^{-3}) and mobilities μ (in cm^2/Vs) of cubic BP. These values are extracted from experimental measurements (as cited references) at room temperature. The values of mobility depend on morphologies of fabricated-samples such as single crystal, polycrystalline, amorphous, thin-film,...

Processing	C (cm^{-3})	μ (cm^2/Vs)	Remarks
Solution (of Ni/Fe) growth	10^{18}	500 [307, 308]	+ 0.01% solvent
Epitaxial growth	8×10^{19}	285 [296]	Si substrate
Epitaxial growth	5×10^{19}	350 [296]	Si substrate
Hetero-Epitaxial growth	4.9×10^{19}	75.5 [297]	Si substrate
Hetero-Epitaxial growth	2.2×10^{19}	100.6 [297]	Si substrate
Chemical transport	1.67×10^{18}	1.77 [309]	+ A little B_6P
CVD + thermal neutron	1.1×10^{17}	100.3 [298, 300]	Si substrate
Photo-thermal CVD	10^{17}	82 [310]	Si substrate

$K_2Sn_2O_3$ [45, 311] is 0.27 m_o. Current Cu-based p-type TCOs show effective masses around 2 m_o [45]. The direct gaps of CaTe and Li_3Sb calculated using HSE hybrid functional are 3.5 and 3.06 eV respectively (see Tab. 4.1). Next to hybrid functional computations, we performed G_0W_0 calculations to confirm the value of these band gaps.

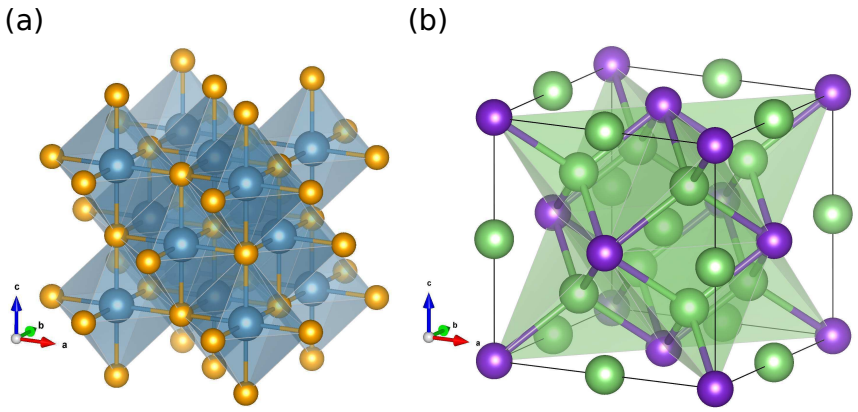

Figure 4.12: The conventional cells with polyhedra showing local environments around cations of (a) CaTe (Ca-blue and Te-orange) and (b) Li_3Sb (Li-green and Sb-violet). CaTe shows octahedra while Li_3Sb is composed of tetrahedra and octahedra environments.

Fig. 4.13 (a) shows the DFT band structure computed by G_0W_0 of CaTe. The G_0W_0 fundamental gap ($\Gamma - X$) is 2.95 eV while the direct gap is located at X-point and has a value of 4.14 eV. The G_0W_0 direct gap is consistent with the value of 4.1 eV measured in an optical experiment [312]. We expect such a

large direct band gap to lead to transparency in the visible region. The G_0W_0 fundamental gap here is wide enough to guarantee the high transparency even in a thick-film form or single crystal of CaTe. Li_3Sb is also a semiconductor with an indirect gap and the VBM locates at a point in Γ-K line. This VBM is slightly higher than the eigenvalue at Γ, which represents for a huge warping effect. In the same way, the DFT and G_0W_0 electronic band structures are presented in Fig. 4.13 (b). The G_0W_0 fundamental (indirect) band gap and direct gap are 1.37 and 3.17 eV, respectively. This is consistent with an experimental value of 3.1 eV measured recently [313] but much lower than another of 3.9 eV reported earlier [314]. The indirect band gap is narrow and will lead to some absorption in the visible range. However, the indirect nature of the absorption makes it phonon-assisted and is expected to lead to weak absorption.

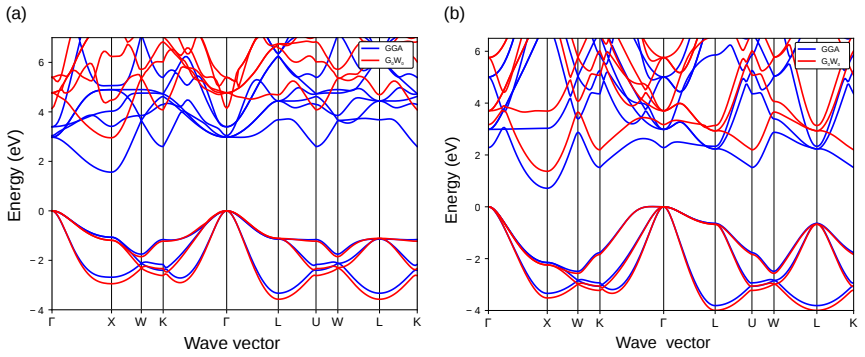

Figure 4.13: The band structure of (a) CaTe and (b) Li_3Sb computed by DFT (blue) and G_0W_0 (red).

To quantify this absorption, we computed the optical absorption including phonon-assisted processes using EPW [273, 274]. The result in Fig. 4.14 shows quite weak absorption in the visible range with the average intensity about 5×10^3 cm^{-1}. Similar to the case of BP, we also assess the loss of visible light energy caused by indirect transitions. For 100-nm Li_3Sb film, around 10 % of visible light energy is absorbed. This is suitable for applications and devices using thin-film form of Li_3Sb. The weak indirect optical absorption computed here is similar to that of other p-type TCMs such as SnO [230] and BP [228].

To verify p-type dopability of these candidates, we performed defect calculations using a HSE following the procedure described in section 4.3. Fig. 4.15 (a) presents the defect formation energy for both intrinsic and extrinsic defects for each sort of defect in CaTe. The chemical potentials are chosen in conditions which lead to the most favorable p-type doping tendency for this material. The chemical potentials corresponding to different conditions in the phase diagrams are available in Apd. C. Focusing first on intrinsic defects only including vacancies, anti-site defects (replacement of Te on Ca-sites and vice versa) and interstitial atoms, defect formation energies of these are plotted in Fig. 4.15 (a) with chemical potentials extracted in Te-rich condition of the phase diagram. Intrinsically, CaTe is unlikely to present p-type doping as no intrinsic defect acts as a low lying acceptor. The vacancy of Ca will be in

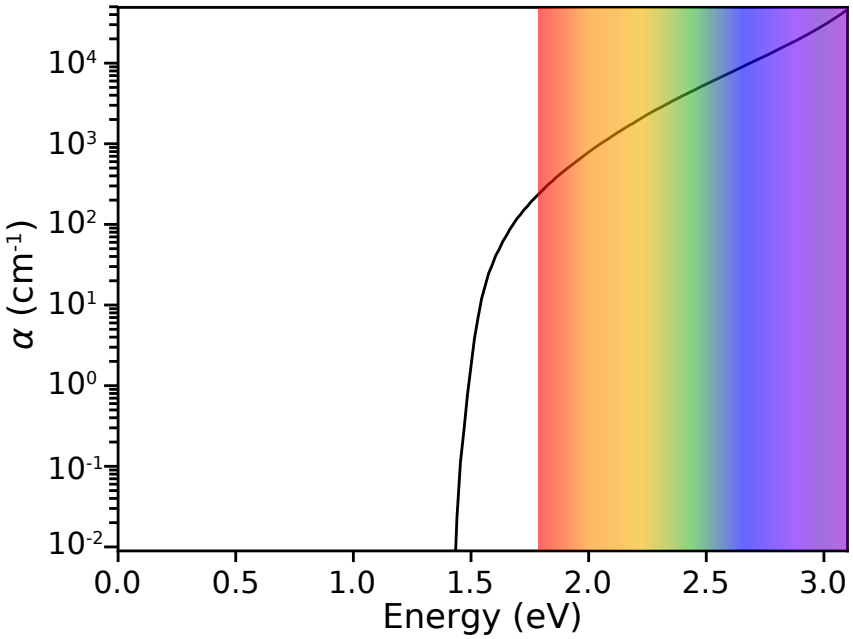

Figure 4.14: The indirect optical absorption of Li_3Sb due to phonon-assisted transitions.

competition with the hole killing vacancy of Te leading to a fermi level far from the valence band. However, the Te vacancy is not low enough in energy that it would prevent extrinsic p-type doping. When extrinsic defects with Na, K and Li substituting onto Ca-sites are considered, we find that all these substitutions offer shallow acceptors competitively compared to the Te vacancy. The Ca by Na substitution is the lowest in energy. Extrinsic doping by Na might therefore lead to p-type doping in CaTe. The plots of formation energies of K_{Ca}, Na_{Ca} and Li_{Ca} in Fig. 4.15 (a) were achieved with chemical potentials extracted from KTe−CaTe−K_2Te_3, $NaTe_3$−CaTe−Na_2Te and Li_2Te−CaTe−Te facets of the three-element phase diagrams (see Apd. C). For Li_3Sb, Fig. 4.15 (b) shows an intrinsic tendency for hole doping with the lithium vacancy (Vac_{Li}) acting as a shallow acceptor with a very low formation energy and no competing hole-killer. This plot is produced with chemical potentials computed in Li_3Sb−Li_2Sb facet of the phase diagram (see Apd. C).

Our final assessment focuses on the mobility of CaTe and Li_3Sb. CaTe and Li_3Sb show very low hole effective mass (0.60 and 0.24 m_o within DFT). In similar to BP, both materials have threefold degeneracy at VBM (Γ point), therefore, the transport of holes occurs in three bands with some lighter and some heavier. The change of effective mass in G_0W_0 calculations is not considered and DFT band structures were used in transport simulation. Fig. 4.17 shows projected DOS for (c) CaTe and (g) Li_3Sb. For both compounds, the top of valence band is mainly of anionic p-orbital characters (Sb^{3-} or Te^{2-})

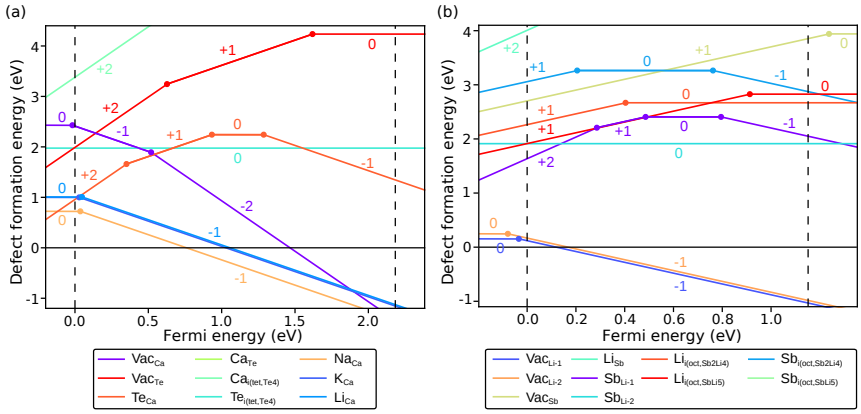

Figure 4.15: The defect formation energy as a function of Fermi level of intrinsic and extrinsic defects for (a) CaTe and (b) Li_3Sb. For CaTe, the intrinsic defects include vacancies (Vac_{Ca} and Vac_{Te}), anti-sites (Te_{Ca} and Ca_{Te}) and interstitial atoms inserted into the tetrahedral hollows formed by 4 Te atoms ($Ca_{i(tet,Te4)}$ and $Te_{i(tet,Te4)}$) while Na, K and Li are used as the extrinsic defects substituting Ca atoms (Na_{Ca}, K_{Ca} and Li_{Ca}). For Li_3Sb, the intrinsic defects include vacancies ($Vac_{Li\text{-}1}$, $Vac_{Li\text{-}2}$ and Vac_{Sb}), anti-sites (Li_{Sb}, $Sb_{Li\text{-}1}$ and $Sb_{Li\text{-}2}$) and interstitial atoms inserted into the octahedral hollows formed by Sb and Li atoms ($Li_{i(oct,\ Sb2Li4)}$, $Li_{i(oct,\ SbLi5)}$, $Sb_{i(oct,\ Sb2Li4)}$ and $Sb_{i(oct,\ SbLi5)}$). In both cases, the VBM is set to zero.

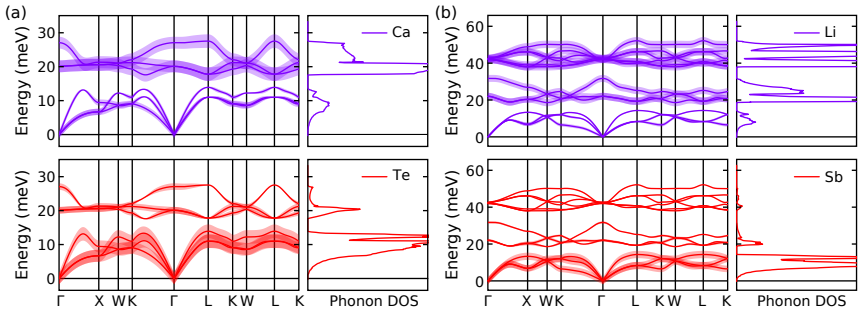

Figure 4.16: Phonon band structures with fat bands representing displacements of atomic vibrations. The width of fat bands gives qualitative understanding of the vibrational modes such as what are the atomic types involved in the vibrations at a given energy, their direction of oscillation and the amplitude (related to the displacement). The projected DOS of phonons on each type of atom are correspondingly shown next to the band structures. (a) CaTe and (b) Li_3Sb.

with some mixing from the cations. The effective masses are directly related to overlap and energy difference between orbitals [161]. The lower value of hole effective masses obtained in these non-oxide compounds can be associated to

both a better alignment between the anionic and cationic states than in oxides and larger anionic p-orbitals ($5p$ versus $2p$ for oxides).

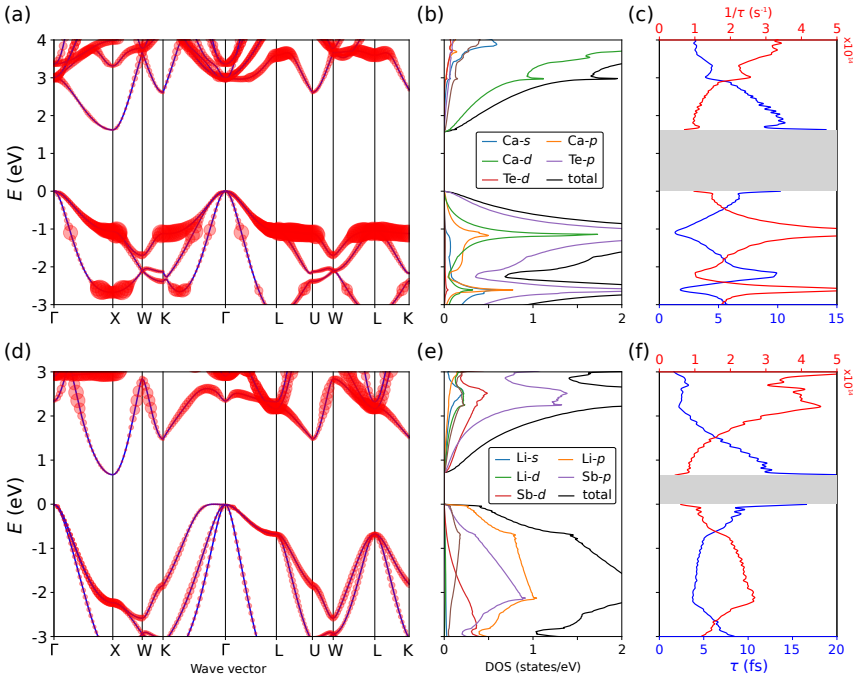

Figure 4.17: From the left to the right, the band structures, projected DOS and relaxation time and scattering rate. Sub-figures (a)-(c) and (e)-(f) show data of CaTe and Li_3Sb respectively. (a) and (d) plot DFT band structures with red dots representing its scattering rate with phonons at a temperature of 300 K (the intensity of scattering is proportional to the size of the dots). (c) and (f) show relaxation time τ (in femto-second) and scattering rate $1/\tau$ (in 1/second) as functions of energy at temperature 300 K. The projected DOS in (b) and (e) are computed by DFT.

Fig. 4.16 shows phonon band structures (fat bands) and projected DOS of phonons for (a) CaTe and (b) Li_3Sb. The fat bands represent qualitatively characteristics of vibrational modes including what type of atoms participates in the phonon modes at a given energy, their direction and amplitude. The absence of modes with negative (purely imaginary) frequencies show that these materials are dynamically stable at 0 K. The lighter atoms (Ca and Li) mainly contribute to the optical modes at high frequencies (3 and 9 modes in CaTe and Li_3Sb, respectively) while the heavier elements (Te and Sb) play an important role in the three acoustic modes at low frequencies.

Using the DFPT phonon computations and EPW, we can extract el-ph coupling matrices and the relaxation time $\tau_{n\mathbf{k}}$ on a dense $\boldsymbol{k}$-point grid. Fig. 4.17 (c) and (f) show the scattering rate and lifetime (inverse of scattering rate) as a function of energy at 300 K for CaTe and Li_3Sb, respectively. As commonly

observed, the scattering rate is proportional to the DOS. A higher DOS offers more states available for the scattered electrons. At the doping hole concentration of 10^{18} cm^{-3}, the Fermi levels are 90.5 and 120.8 meV above the VBMs for CaTe and Li_3Sb, respectively. For the highest doping of 10^{21} cm^{-3}, the Fermi levels lie below VBMs of 264.5 and 168.5 meV for CaTe and Li_3Sb, respectively. The transport of holes, therefore, takes place around VBMs (Γ-points). The DOS at Γ-point of Li_3Sb is larger than that of CaTe but the scattering rate of Li_3Sb are fairly similar (see Fig. 4.17 (c) and (f)) indicating that a weaker el-ph coupling is present in Li_3Sb.

We computed scattering rates at temperatures of 300 and 400 K. Fig. 4.18 shows the hole mobilities as a function of hole concentrations at 300 and 400 K for both CaTe and Li_3Sb. The mobilities decreases with hole concentrations. As the Fermi levels shifts deeper below the VBMs, the DOS increases as well as the scattering rate (see Fig. 4.17 (c) and (f)). CaTe shows values of hole mobility around 20 cm^2/Vs that is comparable with the mobility of Ba_2BiTaO_6, a recently reported *p*-type TCO [47], and larger than mobilities of the traditional *p*-type TCOs such as $CuAlO_2$ [79] and SnO [43]. Li_3Sb exhibits an exceptional hole mobility up to about 70 cm^2/Vs at room temperature. This value nearly reaches the values of the electron mobilities of the best current *n*-TCOs such as SnO_2, ZnO, In_2O_3 and Ga_2O_3 which are around 100 cm^2/Vs (see Tab. 1.2 in Chp. 1). It is worth noting that the mobility measured experimentally takes into account other scattering processes. Our computed mobilities as they only take into account phonon scattering can be seen as an upper bound.

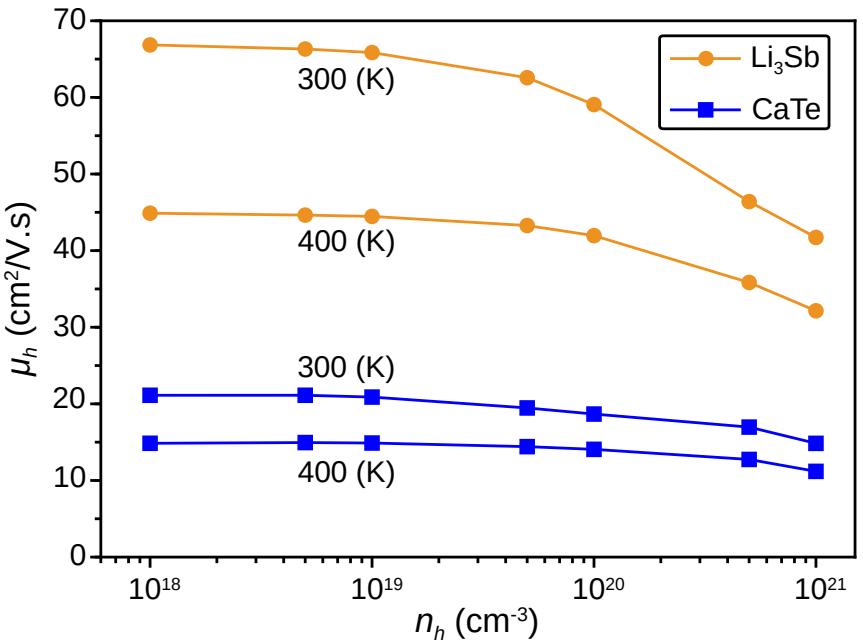

Figure 4.18: Hole mobilities as a function of hole concentrations of CaTe and Li_3Sb at temperatures 300 and 400 K.

4.5 Discussions and conclusions

Many efforts are directed toward the discovery and development of new p-type transparent conducting materials for various kinds of devices and applications. Computationally driven materials design has an important role to play in this challenging process. Targeting the identification of non-oxide p-type TCMs, we data mined a database of thousands of materials obtained from HT *ab initio* computations. Our analysis indicated that non-oxide chemistries such as nitrides, sulfides, phosphides, tellurides, antimonides, *et cetera* indeed offer much more opportunities for low hole effective mass materials. However, we also found that these alternative chemistries lead to lower band gap materials, which would compromise transparency. To bypass this fundamental correlation between effective mass and band gap, we proposed to search for materials with a small indirect, fundamental gap but a large direct band gap. We used a series of advanced *ab initio* techniques to identify several compounds with adequate band gap, hole effective mass, and defect behavior. BP, CaTe and Li_3Sb emerged from this search as a very promising candidate with exceptional properties.

In fact, BP had been widely investigated experimentally. In comparison with previous experimental studies, our computational predictions show very good agreement in fundamental band gap, direct gap and doping-tendency and fairly good trend in indirect optical absorption and hole mobility. Our work strongly motivates a reinvestigation of this fascinating compound and future experimental research in its growth, characterization, and device integration. On a more general note, we also demonstrated how decoupling electronic and optical properties by using the difference between direct and indirect absorption could lead to a new generation of p-type TCMs.

The discovery of the quite unanticipated Li_3Sb with a potential for very high hole mobility demonstrates the interest of our HT screening strategy. Li_3Sb is an unexpected compound for TCM applications and would have been difficult to intuitively identify. Among other A_3B compounds (A = Li, Na, K and Rb; and B = N, P, As and Sb), Li_3Sb is exceptional because of its very low hole effective masses (see Tab. C.7 of Apd. C). We suggest that the energy difference between A-ns^1 ($n = 2, 3, 4, 5$ for Li, Na, K and Rb, respectively) and B-np^3 ($n = 2, 3, 4, 5$ for N, P, As and Sb, respectively) orbitals of valence electrons (A and B) might play important role here. In fact, the energy difference between Li-$2s^1$ and Sb-$5p^3$ is about 1.954 (eV) [263] and is the smallest value among many other ones of A-ns^1/B-np^3 pairs. This leads to a small orbital-energy difference and strong s/p (anti-)bonding, which results in low hole effective mass. While we only focus on CaTe and Li_3Sb as they are likely the most potential candidates, there are other interesting materials with hole effective masses from 0.6 to 1.0 m_o and high direct gaps (see Tab. 4.1) such as CaS, SrSe, SrTe, $LiCa_4B_3N_6$, $LiSr_4B_3N_6$, $NaSr_4B_3N_6$... Defects calculations for these materials have not been performed in this work and we, therefore, cannot judge their p-type doping-tendency.

By going beyond oxides, we identified compounds with very high hole mobility. However, several other issues also arise and need to be considered.

The processing of phosphides, antimonides or tellurides might be more difficult than oxides. They are, however, very common chemistries in other applications such as thermoelectrics with several exemplary compounds such as PbTe, Bi_2Te_3 [315], or more recently Mg_3Sb_2 [316, 317, 318]. The band gaps in non-oxide compounds are narrower, which lowers in average their transparency in the visible light. As we already discussed [228], this can be overcome by exploiting the indirect gaps and weak phonon-assisted optical transitions. Lower band gaps are useful for p-dopability though as lower band gap materials tend to be easier to dope [1].

We note that the defect chemistry of non-oxide can be different than in traditional TCOs. For oxides, the cation-anion anti-site defects (replacement of anions on cations' sites and vice versa) are unlikely to be favorable energetically because of the large electronegativity difference between cations and anions. In non-oxide compounds, *e.g.* BP and CaTe, the cation-anion anti-sites are more likely to be present leading to potentially different hole-killing defects. While the anion (oxygen) vacancy is the most common hole-killer in oxides, we see our non-oxide materials presenting anti-sites cation-anion defects lower in energy than the anion vacancy such as in BP and CaTe. We also identify that the hydride chemistry while offering attractive electronic structures presents dopability issues (*i.e.* a low lying hydrogen vacancy acting as hole killer) preventing them for further consideration in p-type TCMs.

Using a large database and appropriate filtering strategies, we report on a HT search for non-oxide p-type TCMs. We identified three materials to be of interest: BP, CaTe and Li_3Sb. We performed extensive follow-up computational investigation of these candidates, evaluating their band structure using beyond DFT techniques, their transport and phonon-assisted optical properties using el-ph computations as well as their defect chemistry. BP, CaTe and Li_3Sb present very attractive properties for p-type TCM applications. BP shows extremely high upper limit of hole mobility of around 900 cm^2/Vs and this is consistent with experimental literature review. This behavior can be associated to its low polarization as the different electronegativity between B and P is not so high. BP also exhibits very weak indirect optical absorption, which allows it to keep high transparency when working in thin-film form. However, from the picture of defect formation energy, BP might not be the material doped with highly hole concentrations as the defect formation energy is not so low and the competition from intrinsic (defects) hole-killers is significantly. BP, therefore, is good for some applications like transparent transistor. Li_3Sb shows quite high upper limit of hole mobility of around 70 cm^2/Vs, which is close to electron mobility in the best n-type TCMs. The very low defect formation energy of intrinsic defects (Li-vacancies) is an advantage of this material leading to highly doped hole concentrations. This is suitable with some applications requiring high conductivity such as transparent electrodes.

Chapter 5

Summary and perspectives

In this chapter, the previous chapters will be briefly summarized. We will review what we have done and how these contributions potentially help to motivate later works in the field of transparent conducting materials, especially in high-mobility p-type. In addition, the remaining problems and open questions will also be raised. The further outlook and perspectives are presented in our points of view as well.

5.1 Short statements of main points

This thesis dedicates important and novel studies to the field of transparent conducting materials which is one of crucial topics in materials sciences and high technology. We focused mainly on high mobility p-type TCMs which are the need of many modern technologies like transparent transistors and solar cells. Nonetheless, they are still out of the commercial markets as performing poorly in carrier mobility. Here, we desire to accelerate progress in this issue by considering two research topics. First we developed novel design principles which can aid in finding higher performance TCMs. Second we explored the non-oxide space where there is still plenty of room for low hole effective mass p-type TCMs.

Design principles for higher performance TCMs: In Chp. 2, "second gap" in doped-TCMs is our consideration. The introduced free carriers might cause relevant effects such as plasmon reflection or additional optical transitions which can be harmful to transparent property of TCMs. In fact, plasmon effect was studied and the results show that this is minor even in very highly doped regime with carrier concentration of 10^{22} cm^{-3} [319]. The additional optical transitions had also been considered as an important criterion but not quantitatively investigated. People working in TCMs field believed that a wide "second gap" of ideally > 3 eV as fundamental band gap is needed. In this thesis, we studied this problem by selecting a diverse set of current TCMs including both n-type (In_2O_3, ZnO, SnO_2 and $BaSnO_3$) and p-type ($CuAlO_2$, LaCuOS, $ZnRh_2O_4$ and SnO). We used state-of-the-art hybrid functional HSE

to improve electronic band structures leading to better optical absorption. Our results show that the "second gap" transitions do not impact on transparency on current n-type TCMs as their "second gaps" > 3 eV. On the other hand, the "second gaps" are smaller leading to more absorption in visible light. These lower transparency of p-type TCMs but the magnitude is only significant if highly doped at level of 10^{21} cm^{-3}. The fraction of energy lost in the visible range was quantitatively estimated for thin films (100-nm thickness) about 10 % for the worst case of $CuAlO_2$. The value of 10 % energy lost for a 100-nm thin-film is acceptable. We, therefore, suggest that while it is always better for a TCM to have a wide "second gap" (ideally > 3 eV), this should not be applied as a stringent criteria in design of novel TCMs. The difference in "second gap" between current n and p-type TCMs is associated with chemical composition and interactions.

In the next chapter (Chp. 3), we concentrate on s-based oxides, in particular Sn^{2+} cation. This cation was identified through the previous HT work [45] as a promising chemistry which can give s-electrons to interact with p-electrons of oxygens in top valence bands leading to lower hole effective mass [311]. However, in this thesis, we proved that the presence of Sn^{2+} cation in oxides does not guarantee curvy shapes of valence band. Using DFT computations in combination with analysis of electronic band structures, we linked the evolution of chemical interaction between Sn and O with their local geometric environments. In a set of more than 50 Sn-based oxides collected from ICSD [168], we only select the ones in which there exists connecting-networks between Sn and O and the top of valence bands must mainly contain Sn-s and O-p characters. I found that ideally, a Sn$-$O$-$Sn angle of 180° induces the strongest overlap between Sn-s and O-p orbitals and thus the lowest hole effective mass. This is an important clue for people working on the design of novel Sn-based p-type oxides.

Stepping out of oxide space: Until now, the community of TCMs have mostly been working on oxides and achieved a slow progress in searching for high mobility p-type TCOs, *e.g.* Ba_2BiTaO_6, B_6O. There have been several works trying to go further with other rooms of sulfides, selenides, fluorides,... Here, we are also motivated by this trend and systematically approached through data mining of hole effective masses for non-oxide materials. From the statistical analysis, we saw a good potential for digging out novel high mobility p-type TCMs, in comparison with oxides. However, it turns out that these compounds can exhibit smaller band gaps which is detrimental to their transparency. We proposed a mechanism based on indirect band gap semiconductors to overcome this obstacle. Indeed, this is nothing strange as it is employed in one of current p-type TCMs, SnO.

By establishing a strategic HT screening, we identified BP, CaTe and Li_3Sb as the most promising candidates. We employed state-of-the-art computational methods such as hybrid functional HSE, G_0W_0, electron-phonon interaction,... to calculate and verify transparency and transport properties of these materials. We demonstrated that they meet all demands for a high hole mobility TCM when working in thin-film samples. They can be p-doped using extrinsic (BP

and CaTe) or intrinsic (Li_3Sb) defects. The calculated mobilities show that these materials perform exceptionally in comparison with traditional p-TCMs, *e.g.* $CuAlO_2$, SnO, $LaCrO_3$, *etc.* In particular, BP even surpasses the best current n-type TCMs (In_2O_3, ZnO, SnO_2) in mobility. This is explained as the weak polarization in BP leading to weaker electron-phonon interaction and lower scattering. Li_3Sb is another candidate potentially showing high hole mobility (comparable with the best current n-type TCMs). Although showing lower hole effective mass (0.24) in comparison with BP (0.34), Li_3Sb exhibits lower hole mobility. It is understandable as Li_3Sb is a more ionic material and its polarization, therefore, is stronger. As a result, the electron-phonon interaction in this material is significantly larger. Moreover, the high dopability of Li_3Sb (lower defect formation energy of Li vacancies) might be an its advantage. We also would like to note that our results obtained from HT screening are limited to the ICSD database. The splitting of bands at VBM caused by spin-orbit effect has not been considered in this thesis.

5.2 Outlook

In the forthcoming scenario, the advantageous development of DFT/DFT-based methods, machine learning techniques/algorithms and power of computational resources will open doors and move computational "inverse design" of materials forward. In this field, to investigate and understand fundamental principles which govern properties of materials should be one of primary steps because it can be used as constraints limiting chemical/crystalline space we need to mine and therefore, guiding us to target on potential zooms. We hope that the principles proposed in this thesis can contribute something to the future "inverse design" of high mobility p-type TCMs. Sn-based p-type oxides might attract the attention of people in the TCM community because Sn is an fairly earth-abundant element. As discussed in Chp. 3 preferred local environment of Sn^{2+}-based oxides is non-centrosymmetric, mainly trigonal non-coplanar [250]. This might indicate the fact that it is more difficult to design novel Sn^{2+}-based oxides with large Sn−O−Sn angles. However, the existence of cubic and rhombohedral $K_2Sn_2O_3$ and rhombohedral $Rb_2Sn_2O_3$ phases is a proof of possible practice. Besides Sn^{2+}, other cations sharing the similar electronic configuration of (n-1)$d^{10}ns^2$ such as Pb^{2+}, Bi^{3+}, Sb^{3+} [45, 47] should be considered as well.

In the time we are waiting for the novel p-type oxides inversely designed, we tried to mine non-oxide space and found out several interesting materials such as BP, CaTe and Li_3Sb. Our theoretical predictions will motivate later experimental works which can further assess both advantages and disadvantages of these materials. These candidates show exceptional high hole mobility which has been searched for in a long time. To achieve this, we also pay price for transparency due to indirect optical absorptions. However, thin films of these materials can still perform excellently if the thickness is not over 200 nm which is not problematic with the current manufacturing methods, *e.g.* epitaxial growth. Moreover, the isotropic hole effective mass tensors can help these materials to operate in polycrystalline (or in a further expectation, amorphous)

solid-state but to be able to keep adequate transport properties. This might be a significant advancement since fabrication of polycrystalline (or amorphous) morphology is less complicated and cheaper.

Among three promising compounds we suggest for applications in high mobility p-type TCMs, BP is the most well studied one. BP was experimentally manufactured in both thin-film and crystalline forms by different methods such as vapor phase reaction [294], high pressure melting solution [320], CVD [321, 322], epitaxy [308, 323], *etc.* As dicussed in section 4.4.2, BP was proved that it can be doped with both n- and p-type, thus it might be used for fabrication of a homojunction bipolar transistor. The hole concentrations (around 10^{19} cm^{-3}) reported in different experimental works (see Tab. 4.2) are not significantly high in comparison with the highest electron concentrations obtained in the best n-type TCMs (see Tab. 1.2 of Chp. 1). The mechanisms of acceptor levels have not been clarified experimentally. Our defect calculations (see Fig. 4.8) might explain for this observation as the anti-site defects actively work as hole killers around the VBM. We hope that the future experimental studies will improve p-type doping, thus, hole concentrations. This is very important for applications which require high conductivity property, *e.g.* transparent electrodes. However, the current hole doping levels (see Tab. 4.2) are suitable for transparent electronic applications. In fact, p-type Si/n-type BP heterojunctions was designed [324, 325]. BP was also proposed for other applications of neutron detectors, infrared coatings and thermoelectric devices [322]. Recently, other allotropes of BP including nanotube [326, 327] and monolayer [328, 329] have been theoretically investigated. Although there are still several practical limitations, *e.g.* not high hole doping concentrations, high temperature of synthesis ($\geq$ 1000 K), BP still has a great potential for high mobility p-type TCMs if the future researches consider and overcome the current difficulties.

CaTe, on the other hand, has not been abroad considered for practical applications. There have been a handful number of experimental works reporting on optical property [312], structural phase transition [330] or synthesis [331]. The high temperature of fabrication of CaTe is a problem. For instance, the temperature is 1073 K for vacuum evaporation method (from precursors calcium and tellurium) used in Ref. [312]. The reactions in solution method at temperature 1173 K was used in Ref. [331]. We hope that our results for CaTe shown in this thesis will conduct further investigations targeting on TCM applications. For Li_3Sb, this materials had been rather widely investigated because recently, antimony has been theoretically predicted to be high capacity anode of Li-ion batteries [332, 333]. However, this advantage for battery technology might be an obstacle to other applications because Li-ions can diffuse easily inside Li_3Sb [332]. Different fabrication methods including high temperature alloying, electrochemical deposition techniques and microwave-assisted solid-state method [334] had been utilized in manufacture of Li_3Sb. Recently, this material is theoretically proposed for thermoelectric applications [335]. Regarding to p-type TCM applications, we think that the solutions for restriction on Li-diffusion need to be studied and developed.

Appendix A

Density Functional Theory

In this appendix, I shortly rewrite fundamental theory and methods for Density Functional Theory. I mainly consulted references: the textbook "Electronic Structure: Basic theory and practical methods" by Richard M. Martin [177] and the lectures delivered by Xavier Gonze (2009) and Gian-Marco Rignanese (2015) in the Centre Européen de Calcul Atomique et Moléculaire (CECAM) workshops and Paolo Giannozzi in the ICTP/Psi-k/CECAM School (2018).

A.1 The many-body problem

By definition, a system that includes many particles (at least two) is called a many-body system. While Newtonian mechanics and statistical methods are used to treat the classical systems, quantum mechanics must be the core for treatment of the systems in which quantum effects are essentially important and cannot be ignored. In particular, many physical and chemical properties of materials can be computed and predicted using quantum mechanics to describe many-body systems including electrons and nuclei of atoms. The basic interaction in these ensembles is electrostatic Coulomb interaction (the gravitational, weak and strong interactions can be neglected) between electron-nucleus, electron-electron and nucleus-nucleus. The wave function of a systems including n electrons and N nuclei is

$$\Psi = \Psi(\mathbf{r}_1, \mathbf{r}_2, ..., \mathbf{r}_n, \mathbf{R}_1, \mathbf{R}_2, ..., \mathbf{R}_N), \tag{A.1}$$

where $\mathbf{r}_i$ $(i = 1, 2, ..., n)$ and $\mathbf{R}_\mu$ $(\mu = 1, 2, ..., N)$ are coordinates of electrons and nuclei, respectively. Here, the coordinates ($\mathbf{r}_i$ or $\mathbf{R}_\mu$) imply three components of space (x, y, z) and momentum (p_x, p_y, p_z) and one component of spin $(\sigma\uparrow/\sigma\downarrow)$.

Based on the fact that the nuclei are significantly heavier than the electrons (at least 1000 times), Born and Oppenheimer [336] proposed an approximation upon which the dynamic movement of nuclei is decoupled with that of electrons. The wave function in (A.1) can be split as its electronic and nuclear components

$$\Psi = \psi(\mathbf{r}_1, \mathbf{r}_2, ..., \mathbf{r}_n; \mathbf{R}_1, \mathbf{R}_2, ..., \mathbf{R}_N)\Phi(\mathbf{R}_1, \mathbf{R}_2, ..., \mathbf{R}_N). \tag{A.2}$$

This approach is a famous approximation and named after the pioneers Born-Oppenheimer. In practice, we can assume that the positions of nuclei are fixed when considering electronic dynamics. The system of n interacting electrons now can see Coulomb potential generated by nuclei as an external potential $V_{ext}(\mathbf{r})$ and their wave function $\psi(\mathbf{r}_1, \mathbf{r}_2, ..., \mathbf{r}_n; \mathbf{R}_1, \mathbf{R}_2, ..., \mathbf{R}_N)$ (from now on, we will simply denote as $\psi(\mathbf{r}_1, \mathbf{r}_2, ..., \mathbf{r}_n)$) is the root of Schrödinger equation:

$$\hat{H}\psi = \Big(\frac{-\hbar^2}{2m}\sum_i \nabla_i^2 + \sum_i V_{ext}(\mathbf{r}_i) + \frac{1}{2}\sum_i\sum_{j\neq i}\frac{e^2}{4\pi\epsilon_0|\mathbf{r}_i - \mathbf{r}_j|}\Big)\psi = E\psi, \quad \text{(A.3)}$$

where $\hbar$, m, e and ϵ_0 are reduced Planck constant, mass of electron, elementary charge and vacuum permittivity, respectively. E is total energy of the system. The first, second and third terms of Hamiltonian operator stand for kinetic, external and electron-electron potentials, respectively. The external potential $V_{ext}(\mathbf{r}_i)$ is produced by nuclei

$$V_{ext}(\mathbf{r}_i) = -\sum_\mu \frac{Z_\mu e^2}{4\pi\epsilon_0|\mathbf{r}_i - \mathbf{R}_\mu|}, \quad \text{(A.4)}$$

where Z_μ is atomic number of μ^{th} nucleus. When total energy $E \equiv E(\mathbf{R})$ for a given set of $\mathbf{R} \equiv \mathbf{R}_\mu$ ($\mu = 1, 2, ..., N$) is obtained by solving (A.3), the motion of nuclei can be treated. In fact, the number of particles is gigantic (Avogadro's number) and interaction between them is complicated leading to impossible analytic solutions. In practice, numerical methods have been developed to solve (A.3).

A.2 Methods for solving Schrödinger equation

A.2.1 Variational Quantum Monte Carlo

This is the first numerical method which was used to approximate the ground state of a quantum system $|\psi_0\rangle$ (ket-vector notation). The variational principle is applied to minimize the total energy

$$E = \frac{\langle\psi|\hat{H}|\psi\rangle}{\langle\psi|\psi\rangle}. \quad \text{(A.5)}$$

The wave function $|\psi\rangle$ is initially chosen as a trial function which depends on some parameters a, $|\psi(a)\rangle$. The energy

$$E_a = \frac{\langle\psi(a)|\hat{H}|\psi(a)\rangle}{\langle\psi(a)|\psi(a)\rangle} \geq E_0, \quad \text{(A.6)}$$

where E_0 is energy of ground-state. This is achieved if $\delta E_a/\delta a = 0$. By varying a, we can find a set of parameters, a_0, for the ground-state. The choice of the trial wave function is definitely very critical. In addition, n-electron wave function is very complicated to deal with.

A.2.2 Hartree and Hartree-Fock approximation

In fact, the electron-electron interactions are complex and the biggest issue. The simplest assumption is to skip these interactions, so (A.3) becomes

$$\hat{H}\psi = \sum_i \Big(\frac{-\hbar^2}{2m}\nabla_i^2 + V_{ext}(\mathbf{r}_i)\Big)\psi = E\psi. \tag{A.7}$$

We can separate n-electron wave function into the product of n one-electron wave function

$$\psi(\mathbf{r}_1, \mathbf{r}_2, ..., \mathbf{r}_n) = \phi_1(\mathbf{r}_1)\phi_1(\mathbf{r}_2)...\phi_1(\mathbf{r}_n). \tag{A.8}$$

Each wave function $\phi_1(\mathbf{r}_i)$ is the solution of one-electron Schrödinger equation

$$\Big(\frac{-\hbar^2}{2m}\nabla_i^2 + V_{ext}(\mathbf{r}_i)\Big)\phi_i(\mathbf{r}) = \epsilon_i\phi_i(\mathbf{r}), \tag{A.9}$$

and the total energy simply is the sum of ϵ_i, $E = \sum \epsilon_i$. This is called separation variable technique and is the base for the later approximations and solving methods.

Hartree approximation: This proposes that n-electron wave function of the interacting system still can be described by the product of n one-electron wave functions. Thus, we need to find a set of one-electron wave function $\{|\phi_i\rangle\}$ $(i = 1, 2, ...n)$ which can minimize the total energy

$$E = \frac{\langle\psi|\hat{H}|\psi\rangle}{\langle\psi|\psi\rangle}, \tag{A.10}$$

under normalization constraint $\langle\phi_i|\phi_i\rangle = 1$. The variational principle is applied here to find $\{|\phi_i\rangle\}$, so

$$\frac{\delta}{\delta|\psi\rangle}[\langle\psi|\hat{H}|\psi\rangle - E\langle\psi|\psi\rangle] \equiv \frac{\delta\langle\hat{H} - E\rangle}{\delta|\psi\rangle} = 0. \tag{A.11}$$

The Hamiltonian can be rewritten into two parts

$$\hat{H} = \sum_i \hat{H}_i + \frac{1}{2}\sum_i\sum_{j\neq i} V_{ij}, \tag{A.12}$$

where $\hat{H}_i$ is (non-interaction) Hamiltonian in (A.7) and V_{ij} is electron-electron Coulomb interaction. The wave function is written as the idea of Hartree approximation $|\psi\rangle = \prod_i |\phi_i\rangle$. We can use these expressions to represent $\langle\hat{H} - E\rangle$ and mind that $\hat{H}_i$ only operates on the i^{th} particle while V_{ij} only operates on the i^{th} and j^{th} particles, then

$$\langle\hat{H} - E\rangle = \sum_i \langle\phi_i|\hat{H}_i|\phi_i\rangle + \frac{1}{2}\sum_i\sum_{j\neq i}\langle\phi_i|\langle\phi_j|V_{ij}|\phi_i\rangle|\phi_j\rangle - E\prod_i\langle\phi_i|\phi_i\rangle. \tag{A.13}$$

We apply the functional derivative both two sides of this equation with respect to $\langle\phi_k|$ for the k^{th} particle and use (A.11), then

$$\Big(\frac{-\hbar^2}{2m}\nabla_k^2 + V_{ext}(\mathbf{r}_k) + \sum_{j\neq k}\langle\phi_j|V_{kj}|\phi_j\rangle\Big)|\phi_k\rangle = \epsilon_k^H|\phi_k\rangle. \tag{A.14}$$

(A.14) is a one-particle Schrödinger equation called "Hartree equation". The third term in the Hamiltonian operator that describes the Coulomb interaction between k^{th} particle with others is called *Coulomb operator*

$$J_j(\mathbf{r}) = \langle\phi_j|V_{kj}|\phi_j\rangle = \int \phi_j^*(\mathbf{r}')\frac{e^2}{4\pi\epsilon_0|\mathbf{r}-\mathbf{r}'|}\phi_j(\mathbf{r}')d\mathbf{r}'. \tag{A.15}$$

The eigenvalue of (A.14) can be written as

$$\epsilon_k^H = \Big\langle\phi_k\Big|\frac{-\hbar^2}{2m}\nabla_k^2 + V_{ext}(\mathbf{r}_k)\Big|\phi_k\Big\rangle + \sum_{j\neq k}J_{kj}, \tag{A.16}$$

where

$$J_{kj} = \int \phi_k^*(\mathbf{r})\phi_j^*(\mathbf{r}')\frac{e^2}{4\pi\epsilon_0|\mathbf{r}-\mathbf{r}'|}\phi_j(\mathbf{r}')\phi_k(\mathbf{r})d\mathbf{r}'d\mathbf{r}. \tag{A.17}$$

The total energy of the system is

$$\begin{aligned} E &= \sum_k\Big(\Big\langle\phi_k\Big|\frac{-\hbar^2}{2m}\nabla_k^2 + V_{ext}(\mathbf{r}_k)\Big|\phi_k\Big\rangle + \frac{1}{2}\sum_{j\neq k}J_{kj}\Big) \\ &= \sum_k\Big(\epsilon_k^H - \frac{1}{2}\sum_{j\neq k}J_{kj}\Big). \end{aligned} \tag{A.18}$$

We can identify the Coulomb potential in (A.14) with a so-called "Hartree potential"

$$\sum_{j\neq k}J_j(\mathbf{r}) \equiv V_H(\mathbf{r}) = \int\frac{e^2\rho(\mathbf{r}')}{4\pi\epsilon_0|\mathbf{r}-\mathbf{r}'|}d\mathbf{r}', \tag{A.19}$$

where $\rho(\mathbf{r}) = \sum_k\langle\phi_k|\phi_k\rangle$ is the electronic density. In this approach, the total energy is

$$E = \sum_k\epsilon_k^H - E_H, \tag{A.20}$$

where

$$E_H = \frac{1}{2}\int\frac{e^2\rho(\mathbf{r}')\rho(\mathbf{r})}{4\pi\epsilon_0|\mathbf{r}-\mathbf{r}'|}d\mathbf{r}'d\mathbf{r}. \tag{A.21}$$

Equation (A.14) is rewritten in new form as

$$\Big(\frac{-\hbar^2}{2m}\nabla^2 + V_{ext}(\mathbf{r}) + V_H(\mathbf{r})\Big)\phi_k(\mathbf{r}) = \epsilon_k^H\phi_k(\mathbf{r}). \tag{A.22}$$

We can see that instead of solving n-particle problem, we simply work with n one-particle problems. However, the difficulty in solving equation (A.22)

is that Hartree potential requires the knowledge of the one-particle states. In turn of states, they are defined through known Hartree potential. Thus, we regularly solve (A.22) in a scheme so-called "self-consistency" as shown in Fig. A.1. One can choose a trial electronic density and perform an iteration until the convergence achieved in which the difference in electronic density between two consecutive iteration times is smaller than an arbitrary tolerance, $\Delta\rho = |\rho_i - \rho_{i-1}| < \delta$.

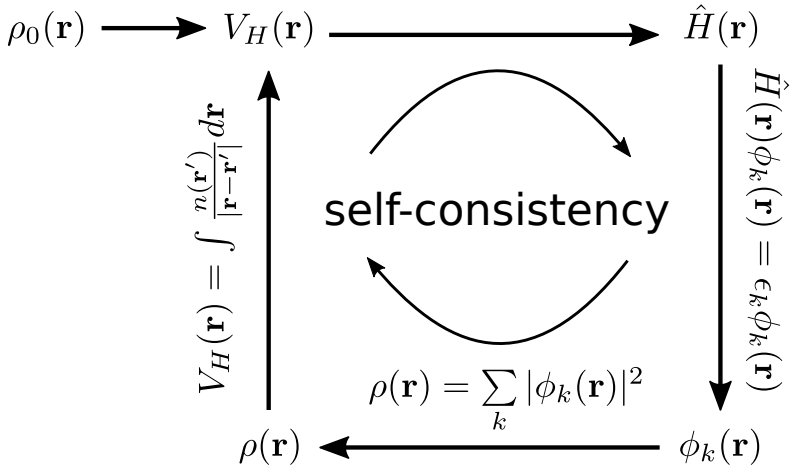

Figure A.1: The self-consistent scheme for solving Hartree equation.

Hartree-Fock approximation: This approximation follows the same idea from Hartree approximation but with taking into account the Pauli exclusion principle for the Fermion systems. The wave function $|\psi\rangle$ is written as a Slater determinant

$$\psi(\mathbf{r}_1, \mathbf{r}_2, ..., \mathbf{r}_n) = \frac{1}{\sqrt{n!}} \begin{vmatrix} \phi_1(\mathbf{r}_1) & \phi_2(\mathbf{r}_1) & \dots & \phi_n(\mathbf{r}_1) \\ \phi_1(\mathbf{r}_2) & \phi_2(\mathbf{r}_2) & \dots & \phi_n(\mathbf{r}_2) \\ \vdots & \vdots & \ddots & \vdots \\ \phi_1(\mathbf{r}_n) & \phi_2(\mathbf{r}_n) & \dots & \phi_n(\mathbf{r}_n) \end{vmatrix}. \tag{A.23}$$

Similar to Hartree approximation, we can show that the n-particle problem can be transformed to n one-particle problem, Hartree-Fock (HF) equation

$$\Big(\frac{-\hbar^2}{2m}\nabla_k^2 + V_{ext}(\mathbf{r}_k) + \sum_{j\neq k}(J_j - K_j)\Big)|\phi_k\rangle = \epsilon_k^{HF}|\phi_k\rangle, \tag{A.24}$$

where J_j is the Coulomb operator defined in (A.15) and K_j is the so-called *exchange operator* defined as

$$K_j\phi_k(\mathbf{r}) = \Big[\int \phi_j^*(\mathbf{r}')\frac{e^2}{4\pi\epsilon_0|\mathbf{r}-\mathbf{r}'|}\phi_k(\mathbf{r}')d\mathbf{r}'\Big]\phi_j(\mathbf{r}). \tag{A.25}$$

This is "non-local operator" standing for "non-local interaction" deriving from Pauli exclusion principle on Fermions, that the particles "avoid" each other leading to an exchange energy depending on the state in the entire space.

The total energy is

$$E = \langle\phi_k|\hat{H}|\phi_k\rangle = \sum_k \Big(\epsilon_k^{HF} - \frac{1}{2}\sum_{j\neq k}(J_{kj} - K_{kj})\Big), \tag{A.26}$$

where J_{kj} is the Hartree energy (see (A.17)) and K_{kj} is the exchange energy

$$K_{kj} = \int \phi_k^*(\mathbf{r})\phi_j^*(\mathbf{r}')\frac{e^2}{4\pi\epsilon_0|\mathbf{r}-\mathbf{r}'|}\phi_k(\mathbf{r}')\phi_j(\mathbf{r})d\mathbf{r}'d\mathbf{r}. \tag{A.27}$$

In the same way, we can identify (A.24) with

$$\Big(\frac{-\hbar^2}{2m}\nabla^2 + V_{ext}(\mathbf{r}) + V_H(\mathbf{r}) + V_x\Big)\phi_k(\mathbf{r}) = \epsilon_k^{HF}\phi_k(\mathbf{r}), \tag{A.28}$$

where V_x is the "non-local" *exchange* (Fock) potential operator, defined as

$$V_x\phi_k(\mathbf{r}) = \sum_j \Big[\int \phi_j^*(\mathbf{r}')\frac{e^2}{4\pi\epsilon_0|\mathbf{r}-\mathbf{r}'|}\phi_k(\mathbf{r}')d\mathbf{r}'\Big]\phi_j(\mathbf{r}). \tag{A.29}$$

The HF method calculates ionization energy of elements with rather accuracy but overestimate band gap of semiconductors and insulators. After HF method, there are other ones such as Configuration Interaction, Coupled Cluster, Møller-Plasset...

A.2.3 Density functional theory

Tracing back to Schrödinger equation (A.3) of a n-electron system in an external potential $V_{ext}(\mathbf{r})$, we can introduce the ground state charge density for n-electrons

$$\rho(\mathbf{r}) = n\int |\psi(\mathbf{r}_1, \mathbf{r}_2, ..., \mathbf{r}_n)|^2 d\mathbf{r}_1 d\mathbf{r}_2 ... d\mathbf{r}_n. \tag{A.30}$$

Hohenberg-Kohn theorem: "The ground state density $\rho(\mathbf{r})$ of a many-electron system determines uniquely the external potential $V(\mathbf{r})$, modulo one global constant." [337]

The proof: A lemma - Consider two local potentials $V_1(\mathbf{r})$ and $V_2(\mathbf{r})$. Their ground-state wave functions may or may not be degenerate, but one wave function ψ cannot be common to both, except if the potentials differ only by a shift or are identical everywhere (except at points of zero density). The difference between the corresponding Schrödinger equations would imply

$$\Big(\sum_i [V_1(\mathbf{r}_i) - V_2(\mathbf{r}_i)] + \Delta E\Big)\psi(\mathbf{r}_1, \mathbf{r}_2, ..., \mathbf{r}_n) \tag{A.31}$$

for each configuration of electrons. Fixing the positions corresponding to the indices from 2 to n, one obtains that the difference between $V_1(\mathbf{r}_1)$ and $V_2(\mathbf{r}_1)$ must be a constant in space.

So, we define ψ_1 as the ground-state wave function of $\hat{H}_{V_1}$ with associated charge density $\rho_1(\mathbf{r})$ and ψ_2 as the ground-state wave function of $\hat{H}_{V_2}$ with associated charge density $\rho_2(\mathbf{r})$. We have

$$E_1 = \langle\psi_1|\hat{H}_{V_1}|\psi_1\rangle, \tag{A.32}$$

$$E_2 = \langle\psi_2|\hat{H}_{V_2}|\psi_2\rangle, \tag{A.33}$$

and

$$E_1 = \langle\psi_1|\hat{H}_{V_1}|\psi_1\rangle < \langle\psi_2|\hat{H}_{V_1}|\psi_2\rangle, \tag{A.34}$$

due to the variational principle. Moreover,

$$\langle\psi_2|\hat{H}_{V_1}|\psi_2\rangle = \langle\psi_2|\hat{H}_{V_2}|\psi_2\rangle + \langle\psi_2|\hat{H}_{V_1} - \hat{H}_{V_2}|\psi_2\rangle, \tag{A.35}$$

with $\hat{H}_{V_1} - \hat{H}_{V_2} = V_1(\mathbf{r}) - V_2(\mathbf{r})$. Finally,

$$E_1 < E_2 + \int [V_1(\mathbf{r}) - V_2(\mathbf{r})]\rho_2(\mathbf{r})d\mathbf{r}. \tag{A.36}$$

Similarly, interchanging 1 and 2, we also have

$$E_2 < E_1 + \int [V_2(\mathbf{r}) - V_1(\mathbf{r})]\rho_1(\mathbf{r})d\mathbf{r}. \tag{A.37}$$

Summing the two inequalities (A.36) and (A.37), we get

$$0 < \int [V_2(\mathbf{r}) - V_1(\mathbf{r})][\rho_1(\mathbf{r}) - \rho_2(\mathbf{r})]. \tag{A.38}$$

Postulating $\rho_1(\mathbf{r})$ equal to $\rho_2(\mathbf{r})$ everywhere leads to $0 < 0$, which is obviously wrong.

The Hohenberg-Kohn (HK) theorem shows that the knowledge of the ground-state density defines the external potential up to a constant. The external potential is, therefore, a functional of the ground-state density followed by other quantities which are defined if the potential is fixed modulo a global constant (*e.g.* ground-state wave function followed by ground-state density). If one fixes the shift in the potential through a simple condition (*e.g.* $\lim_{\mathbf{r}\to\infty} V_{ext}(\mathbf{r}) = 0$), the electronic energy is also a functional of the density (Hamiltonian is uniquely defined with a given external potential). Using variational principle, we can write

$$\begin{aligned} E &= \min_{\psi}\left\{\langle\psi|\hat{H}|\psi\rangle\right\} = \min_{\rho}\Big\{\min_{\psi\mapsto\rho}\left\{\langle\psi|\hat{H}|\psi\rangle\right\}\Big\} \\ &= \min_{\rho}\Big\{\min_{\psi\mapsto\rho}\left\{\langle\psi|\hat{T} + V_{int} + \sum_i V_{ext}(\mathbf{r_i})|\psi\rangle\right\}\Big\} \\ &= \min_{\rho}\Big\{\min_{\psi\mapsto\rho}\left\{\langle\psi|\hat{T} + V_{int}|\psi\rangle\right\} + \int \rho(\mathbf{r})V_{ext}(\mathbf{r})d\mathbf{r}\Big\} \\ &= \min_{\rho}\Big\{F[\rho(\mathbf{r})] + \int \rho(\mathbf{r})V_{ext}(\mathbf{r})d\mathbf{r}\Big\}, \end{aligned} \tag{A.39}$$

where $\hat{T} = -\hbar^2\nabla^2/2m$ and V_{int} are kinetic and interaction operators of electrons, respectively, and $F[\rho(\mathbf{r})] = \min_{\psi\mapsto\rho}\left\{\langle\psi|\hat{T} + V_{int}|\psi\rangle\right\}$ is an universal functional of the density, but it is *not known explicitly.*

Kohn-Sham equation: Functional $F[\rho]$ in (A.39) is a large part of the total energy but hard to approximate. In 1965, Kohn and Sham [338] proposed an

approximation which connects it with a non-interacting system. This leads to an assumption in which kinetic energy is a functional of electronic density

$$T_s[\rho(\mathbf{r})] = \min_{\psi \mapsto \rho} \left\{ \langle \psi | \hat{T} | \psi \rangle \right\}, \tag{A.40}$$

and electron-electron interaction energy part is expressed through a functional of density

$$\min_{\psi \mapsto \rho} \left\{ \langle \psi | V_{int} | \psi \rangle \right\} \equiv E_H[\rho(\mathbf{r})] + E_{xc}[\rho(\mathbf{r})], \tag{A.41}$$

where, $E_H[\rho(\mathbf{r})]$ is Hartree (Coulomb) energy part (see (A.21)) and $E_{xc}[\rho(\mathbf{r})]$ is called the *exchange-correlation* energy of an interacting system. This should contain an *exchange* term as mentioned in HF approximation (see (A.27)) and a *correlation* term. However, it also contains the difference in the kinetic energies between the interacting and non-interacting (electron) systems. We assume that $E_{xc}[\rho(\mathbf{r})]$ can be approximated (known) explicitly, so, we need to minimize total energy in (A.39) in the representation of density

$$\begin{aligned} E[\rho(\mathbf{r})] = T[\rho(\mathbf{r})] + \int \rho(\mathbf{r}) V_{ext}(\mathbf{r}) d\mathbf{r} + \frac{1}{2} \int \frac{e^2 \rho(\mathbf{r}) \rho(\mathbf{r}')}{4\pi\epsilon_0 |\mathbf{r} - \mathbf{r}'|} d\mathbf{r} d\mathbf{r}' \\ + E_{xc}[\rho(\mathbf{r})], \end{aligned} \tag{A.42}$$

under the constraint $\int \rho(\mathbf{r}) d\mathbf{r} = n$. By introducing Lagrange multipliers and using variational principle, we need to solve

$$\frac{\delta(E[\rho(\mathbf{r})] - \lambda[\int \rho(\mathbf{r}) d\mathbf{r} - n])}{\delta \rho(\mathbf{r})} = 0. \tag{A.43}$$

Remembering that Kohn and Sham approximate n-electron interacting system as the non-interacting one, thus $\rho(\mathbf{r}) = \sum_k |\phi_k(\mathbf{r})|^2$. We can apply variational principle for (A.43) with respect to $\rho(\mathbf{r})$. We have

$$\frac{\delta T_s[\rho(\mathbf{r})]}{\delta \rho(\mathbf{r})} + V_{ext}(\mathbf{r}) + \int \frac{e^2 \rho(\mathbf{r}')}{4\pi\epsilon_0 |\mathbf{r} - \mathbf{r}'|} d\mathbf{r}' + \frac{\delta E_{xc}[\rho(\mathbf{r})]}{\delta \rho(\mathbf{r})} = \lambda. \tag{A.44}$$

This is completely equivalent to the Hamiltonian of the non-interacting system with the effective external field

$$\begin{aligned} V_{KS}(\mathbf{r}) &= V_{ext}(\mathbf{r}) + \int \frac{e^2 \rho(\mathbf{r}')}{4\pi\epsilon_0 |\mathbf{r} - \mathbf{r}'|} d\mathbf{r}' + \frac{\delta E_{xc}[\rho]}{\delta \rho(\mathbf{r})} \\ &= V_{ext}(\mathbf{r}) + V_H(\mathbf{r}) + V_{xc}(\mathbf{r}), \end{aligned} \tag{A.45}$$

where $V_{xc}(\mathbf{r})$ is *exchange-correlation* potential and $V_{KS}(\mathbf{r})$ is called Kohn-Sham (KS) potential. It, therefore, is equivalent to solve the one-electron Schrödinger equation self-consistently

$$\left(\frac{-\hbar^2}{2m} \nabla^2 + V_{KS}(\mathbf{r}) \right) \phi_k^{KS}(\mathbf{r}) = \epsilon_k^{KS} \phi_k^{KS}(\mathbf{r}). \tag{A.46}$$

The self-consistent scheme for solving n one-particle KS equations (A.46) can be summarized in Fig. A.2. The constraints of orthonormalization $\langle \phi_i | \phi_j \rangle = \delta_{ij}$ must be applied.

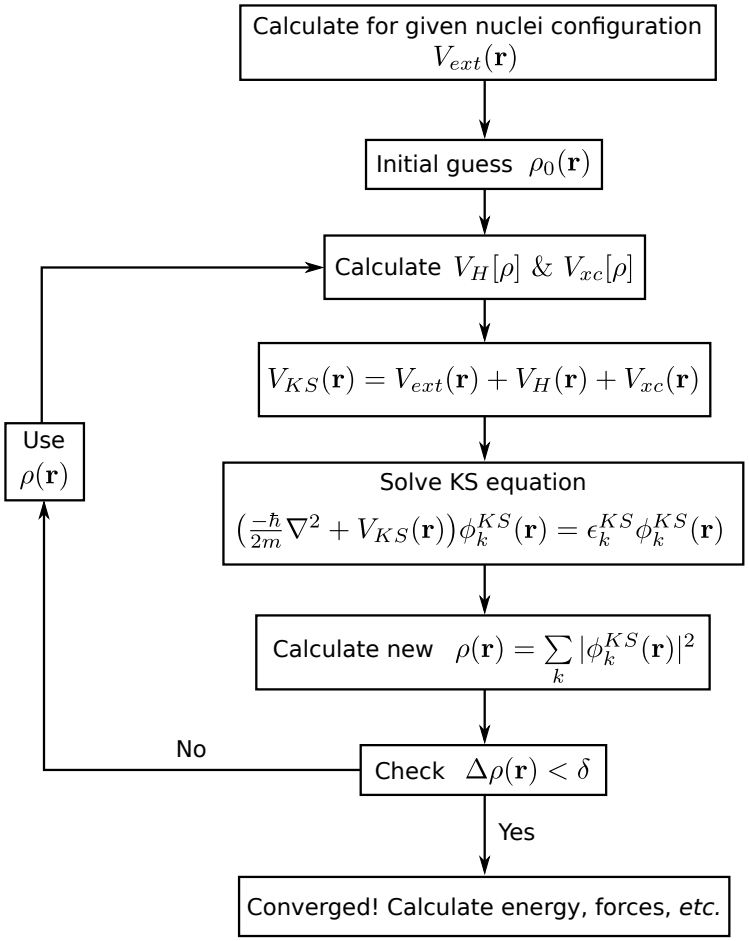

Figure A.2: The self-consistent scheme for solving KS equation.

A.3 Approximation for exchange-correlation energy

The *exchange-correlation* (XC) energy is a functional of density and can be computed by integral over the entire space

$$E_{xc}[\rho(\mathbf{r})] = \int \rho(\mathbf{r})\epsilon_{xc}[\mathbf{r};\rho(\mathbf{r})]d\mathbf{r}', \tag{A.47}$$

where $\epsilon_{xc}[\mathbf{r};\rho(\mathbf{r})]$ is the local exchange-correlation energy per particle. The development for approximation of this functional is an important issue in DFT.

Local density approximation (LDA): Here, the local XC energy per particle is assumed that it depends only on the local density and is equal to the

local XC energy per particle of an homogeneous electron gas of same density.

$$\epsilon_{xc}^{LDA}[\mathbf{r};\rho(\mathbf{r})] = \epsilon_{xc}^{homo}[\mathbf{r};\rho(\mathbf{r})]. \tag{A.48}$$

In fact, ϵ_{xc}^{homo} is split into exchange (ϵ_x^{homo}) and correlation (ϵ_c^{homo}) terms. While

$$\epsilon_x[\mathbf{r},\rho(\mathbf{r})] = \frac{-3}{4\pi}(3\pi^2)^{1/3}\rho(\mathbf{r})^{1/3}, \tag{A.49}$$

the correlation part is obtained from accurate numerical simulations, *e.g.* Quantum Monte Carlo and fitted with some analytic forms. The more general case in which the system is magnetically polarized leading to split of density into two parts corresponding to spin up and down $\rho(\mathbf{r}) \equiv (\rho(\mathbf{r})\uparrow, \rho(\mathbf{r})\downarrow)$. The approximation is still similar and called local spin density approximation (LSDA). This approximation is very coarse but in fact working excellently.

Generalized Gradient Approximation (GGA): The LDA gives very good prediction of different properties, *e.g.* bond lengths with error of 2-3%. However, it shows limits some particular cases, *e.g.* hydrogen bond. Beyond LDA should be considered. The next approximation is called GGA in which the XC energy is represented through not only local density (as in LDA) but also the local gradient of density $|\nabla\rho(\mathbf{r})|$

$$E_{xc}^{GGA}[\rho(\mathbf{r})] = \int \rho(\mathbf{r})\epsilon_{xc}^{GGA}\big(\rho(\mathbf{r}),|\nabla\rho(\mathbf{r})|\big)d\mathbf{r}. \tag{A.50}$$

In this case, no model system like the homogeneous electron gas is employed here. There are many proposals for ϵ_{xc}^{GGA} including PW86 [339], PW91 [340], PBE [235], LYP [341],... In between these, PBE is the simplest and most popular functional currently. The next step goes beyond GGA (meta-GGA) [342] by introducing non-interacting kinetic energy density $\tau(\mathbf{r})$ more into XC functional

$$E_{xc}^{meta-GGA}[\rho(\mathbf{r})] = \int \rho(\mathbf{r})\epsilon_{xc}^{meta-GGA}\big(\rho(\mathbf{r}),|\nabla\rho(\mathbf{r})|,\tau(\mathbf{r})\big)d\mathbf{r}, \tag{A.51}$$

where

$$\tau(\mathbf{r}) = \frac{1}{2}\sum_{occupied\ states}|\nabla\phi_k(\mathbf{r})|^2. \tag{A.52}$$

Meta-GGA functionals are more complicated than GGA in terms of computational cost, stability but give very accurate results.

The DFT band gap problem: DFT is constructed for many-body systems in ground-states and thus in principle can be used to compute exactly all ground-sate properties by solving Kohn-Sham equation (A.46). There is no direct interpretation of KS eigenenergies $\{\epsilon_k\}$ but they can be similar to quasi-particle band structure. LDA or GGA produces very good valence electronic band structures in comparison with experimental data but underestimates band gap in semiconductors and insulators.

Let us consider n-electron system. Its electronic excitations can be classified in two types: the number of electrons is unchanged or the number of electrons

is changed by adding or removing one electron. The former excitations relate to the specific heat, optical characteristics, *etc.* while the latter relates to the electronic structure of the system (probed by photoemission/inverse photoemission). The *band gap* (also named fundamental gap) is determined as the difference between the adding energy and the removing energy

$$E_g = E_c - E_v = \min\{(E_{n+1} - E_n) - (E_n - E_{n-1})\} = E_{n+1} + E_{n-1} - 2E_n, \quad \text{(A.53)}$$

where E_n is total energy of n-electron system. E_c and E_v are the conduction band minimum and the valence band maximum, respectively. In DFT-LDA/GGA, the XC potential is a continuous functional of the density, therefore, of the number of electrons. In fact, the XC potential might be discontinous with the number of electrons. This leads to a KS band gap defined as $E_g^{KS} = \epsilon_c - \epsilon_v$ is regularly wrong. LDA/GGA often underestimates 30-50% (or even 100%) band gap.

Hybrid functionals: The HF method is known to overestimate band gap in semiconductor/insulator while DFT-LDA/GGA underestimates it. Thus, the idea of hybrid functional is to mix some amount of exact exchange computed by HF theory. The non-local (Fock) *exchange* energy is

$$E_x^{HF} = -\frac{1}{2}\sum_{i,j}\int \phi_i^*(\mathbf{r})\phi_j^*(\mathbf{r}')\frac{e^2}{4\pi\epsilon_0|\mathbf{r}-\mathbf{r}'|}\phi_i(\mathbf{r}')\phi_j(\mathbf{r})d\mathbf{r}'d\mathbf{r}. \quad \text{(A.54)}$$

So, in DFT using hybrid-functionals, the total energy

$$\begin{aligned} E[\rho(\mathbf{r})] = T_s[\rho(\mathbf{r})] + \int \rho(\mathbf{r})V_{ext}(\mathbf{r})d\mathbf{r} + E_H[\rho(\mathbf{r})] + \alpha E_x^{HF} \\ + (1-\alpha)E_x^{DFT}[\rho(\mathbf{r})] + E_c^{DFT}[\rho(\mathbf{r})], \end{aligned} \quad \text{(A.55)}$$

where $\alpha = 0.2 \div 0.3$ is an adjustable (empirical) parameter. Several sorts of hybrid functionals have been proposed.

- PBE0 [343]:

$$E_{xc}^{PBE0} = \frac{1}{4}E_x^{HF} + \frac{3}{4}E_x^{PBE} + E_c^{PBE}, \quad \text{(A.56)}$$

  where E_x^{PBE} and E_c^{PBE} are the exchange and correlation parts of the GGA-PBE density functional.

- B3LYP [344, 345]:

$$\begin{aligned} E_x^{B3LYP} &= 0.2E_x^{HF} + 0.8E_x^{LDA} + 0.72\Delta E_x^{B88}, \\ E_c^{B3LYP} &= 0.19E_c^{VWN3} + 0.81E_c^{LYP}, \end{aligned} \quad \text{(A.57)}$$

  where E_x^{B3LYP} and E_c^{B3LYP} are exchange and correlation parts of B3LYP, respectively. ΔE_x^{B88} is the gradient corrections of the Becke88 exchange functional [234]. E_c^{LYP} is correlation energy of LYP functional [341]. E_c^{VWN3} is the (local) Vosko-Wilk-Nusair correlation functional III [346]. This is the most famous hybrid functional in quantum chemistry.

- HSE [198, 199]: In this approximation, HF exchange interaction is separated into short (S) and long range (L) parts. The slowly decaying long-ranged part is replaced by the corresponding part of GGA-PBE density functional

$$E_{xc}^{HSE} = \frac{1}{4}E_x^{HF,S}(\eta) + E_x^{PBE,L}(\eta) + \frac{3}{4}E_x^{PBE,S}(\eta) + E_c^{PBE}. \quad \text{(A.58)}$$

The Coulomb kernel in (A.54) is decomposed as

$$\begin{aligned}\frac{1}{|\mathbf{r}-\mathbf{r}'|} &= S_\eta(|\mathbf{r}-\mathbf{r}'|) + L_\eta(|\mathbf{r}-\mathbf{r}'|) \\ &= \frac{\mathrm{erfc}(\eta|\mathbf{r}-\mathbf{r}'|)}{|\mathbf{r}-\mathbf{r}'|} + \frac{\mathrm{erf}(\eta|\mathbf{r}-\mathbf{r}'|)}{|\mathbf{r}-\mathbf{r}'|}\end{aligned} \quad \text{(A.59)}$$

where η is the parameter that defines the range-separation. At the distance of $2/\eta$, short-range interactions can be negligible. The optimum η is approximately about 0.2-0.3 Å^{-1}. Here, $\mathrm{erf}(x)$ and $\mathrm{erfc}(x)$ are called the error function and complementary error function, respectively. By definition,

$$\begin{aligned}\mathrm{erf}(x) &= \frac{2}{\sqrt{\pi}}\int_0^x e^{-t^2}dt, \\ \mathrm{erfc}(x) &= 1 - \mathrm{erf}(x) = \frac{2}{\sqrt{\pi}}\int_x^\infty e^{-t^2}dt.\end{aligned} \quad \text{(A.60)}$$

The hybrid functionals are known to outperform DFT-LDA/GGA in different aspects such as energy, bond length, band gap, *etc.* However, computational cost is a problem.

A.4 Hellmann-Feynman force and structural relaxation

So far, we have used Born-Oppenheimer approximation which decouples motion of electrons and nuclei and these two parts are treated separately. As shown above, DFT helps one to find the electronic ground state in the potential generated by the nuclei at a given configuration $\{R_\mu\}$ $(\mu = 1, 2, ..., N)$. The initial nuclei configuration is usually not the equilibrium geometry, thus the force applying on these nuclei is non-zero. In order to handle the motion of nuclei, one must compute force in electronic ground state. The force conjugate to positions of nuclei and is calculated as

$$\mathbf{F}_\mu = -\frac{\partial\tilde{E}}{\partial\mathbf{R}_\mu}, \quad \text{(A.61)}$$

where $\tilde{E}$ is the total energy with taking into account nucleus-nucleus interactions as

$$E_{nn} = \frac{e^2}{2}\sum_{\mu\neq\nu}\frac{Z_\mu Z_\nu}{4\pi\epsilon_0|\mathbf{R}_\mu - \mathbf{R}_\nu|}. \quad \text{(A.62)}$$

Thus, $\tilde{E} = E + E_{nn}$ with E is the total electronic energy at ground state (see (A.42)). We have,

$$\begin{aligned} -\frac{\partial \tilde{E}}{\partial \mathbf{R}_\mu} &= -\frac{\partial E}{\partial \mathbf{R}_\mu} - \frac{\partial E_{nn}}{\partial \mathbf{R}_\mu} \\ &= -\langle \frac{\partial \psi}{\partial \mathbf{R}_\mu} | \hat{H} | \psi \rangle - \langle \psi | \frac{\partial \hat{H}}{\partial \mathbf{R}_\mu} | \psi \rangle - \langle \psi | \hat{H} | \frac{\partial \psi}{\partial \mathbf{R}_\mu} \rangle - \mathbf{F}_{nn}. \end{aligned} \tag{A.63}$$

Because the electrons are in exact ground state with respect to all possible variations of wave functions, the first and third terms vanish. Thus,

$$\mathbf{F}_\mu = -\langle \psi | \frac{\partial \hat{H}}{\partial \mathbf{R}_\mu} | \psi \rangle - \mathbf{F}_{nn} = -\int \frac{\partial V_{ext}(\mathbf{r})}{\partial \mathbf{R}_\mu} \rho(\mathbf{r}) d\mathbf{r} - \mathbf{F}_{nn}. \tag{A.64}$$

This expression is called "Hellmann-Feynman" force and has been proven independently by many authors: Paul Güttinger (1932) [347], Wolfgang Pauli (1933) [348], Hans Hellmann (1937) [349] and Richard Feynman (1939) [350]. From (A.4), we have

$$-\int \frac{\partial V_{ext}(\mathbf{r})}{\partial \mathbf{R}_\mu} \rho(\mathbf{r}) d\mathbf{r} = -\int \frac{Z_\mu e^2}{4\pi\epsilon_0 |r - \mathbf{R}_\mu|^3} (\mathbf{r} - \mathbf{R}_\mu) \rho(\mathbf{r}) d\mathbf{r}, \tag{A.65}$$

and we, therefore, can compute all forces $\mathbf{F}_\mu$ directly from the density $\rho(\mathbf{r})$.

When the force is calculated for all nuclei, one can use $\{\mathbf{F}_\mu\}$ ($\mu = 1, 2, ..., N$) to perform structural optimization by moving these nuclei to a new configuration $\{\mathbf{R}'_\mu\}$. All the processes will be iterated until we can find a nuclei configuration for which $\{\mathbf{F}_\mu\}$ ($\mu = 1, 2, ..., N$) vanishes and the structure is completely relaxed (minimum energy). In practice, there are different algorithms to move nuclei to $\{\mathbf{R}'_\mu\}$ and thus reach to the optimized structure. If a classical treatment of nuclei is assumed, one can do classical molecular dynamics simulation (Car-Parrinello method) with force calculated from DFT.

A.5 Plane wave basis sets

The solution of KS equation $\hat{H}_{KS}\phi^{KS} = \epsilon^{KS}\phi^{KS}$ is a hard problem. One can represent KS wave function into some suitable basis set $\{\varphi_i\}$

$$\phi(\mathbf{r}) = \sum_j c_j \varphi_j(\mathbf{r}), \tag{A.66}$$

under normalization condition $\sum_{j,k} \int c_k^* \varphi_k^*(\mathbf{r}) c_j \varphi_j(\mathbf{r}) d\mathbf{r} = 1$. If $\{\varphi_j\}$ is orthonormal, solving KS equation turns to solve the following secular equation

$$\sum_j (H_{jk} + \epsilon \delta_{jk}) c_k = 0, \tag{A.67}$$

where $H_{jk} = \langle \varphi_j | \hat{H}_{KS} | \varphi_k \rangle$ are elements of Hamiltonian matrix. In the case $\{\varphi_j\}$ is not orthonormal, the following matrix equation must be solved.

$$\sum_j (H_{jk} + \epsilon S_{jk}) c_k = 0, \tag{A.68}$$

where $S_{jk} = \langle\varphi_j|\varphi_k\rangle$ are elements of the overlap matrix. In fact, there are many types of basis set developed but can be grouped as

- Localized basis sets: Linear Combinations of Atomic Orbitals (LCAO), Gaussian-type Orbitals (GTO), Linearized Muffin-Tin Orbitals (LMTO)
- Delocalized basis sets: Plane Waves (PW)
- Mixed basis sets: The Linearized Augmented Plane Waves (LAPW)

Each type of basis set has some advantages and disadvantages. For localized basis set:

- Pros: Fast convergence with respect to number of basis sets because each atom need a handful of functions and working in both finite and periodic systems.
- Cons: Difficulty in evaluation of convergence quality, difficulty in usage and difficulty in force calculation.

And for plane waves (have infinite spatial extent):

- Pros: Simple evaluation of convergence quality (control by the energy cutoff), easy usage (Fourier transform) and easy force calculation.
- Cons: Slow convergence with respect to basis set size (a large number of functions), requirement of periodicity.

Here we focus on describing PW method more clearly as it is widely used in many popular DFT packages such as VASP, ABINIT, Quantum Espresso... For periodic systems defined by lattice translation vectors $\mathbf{R} = n_1\mathbf{R}_1+n_2\mathbf{R}_2+n_3\mathbf{R}_3$ via three primitive vectors $\mathbf{R}_1, \mathbf{R}_2, \mathbf{R}_3$ and three integer numbers n_1, n_2, n_3, Bloch theorem allows to represent a wave function

$$\varphi_{j\mathbf{k}}(\mathbf{r}) = e^{i\mathbf{k}.\mathbf{r}}u_{j\mathbf{k}}(\mathbf{r}), \tag{A.69}$$

where $\mathbf{k}$ is the crystal wave number, i is imaginary unit and $u_{j\mathbf{k}}(\mathbf{r})$ is a periodic function satisfying $u_{j\mathbf{k}}(\mathbf{r}+\mathbf{R}) = u_{j\mathbf{k}}(\mathbf{r})$. This leads to

$$\varphi_{j\mathbf{k}}(\mathbf{r}+\mathbf{R}) = e^{i\mathbf{k}.\mathbf{R}}\varphi_{j\mathbf{k}}(\mathbf{r}). \tag{A.70}$$

If we define the *reciprocal lattice* with translation vector $\mathbf{G}$ satisfying $\mathbf{G}.\mathbf{R} = 2\pi l$ with l is an integer. Thus the periodic part $u_{j\mathbf{k}}(\mathbf{r})$ can be written as

$$u_{j\mathbf{k}}(\mathbf{r}) = \sum_{\mathbf{G}} u_{j\mathbf{k}}(\mathbf{G})e^{i\mathbf{G}\mathbf{r}}, \tag{A.71}$$

where the coefficients $u_{j\mathbf{k}}(\mathbf{G})$ is defined by Fourier transform

$$u_{j\mathbf{k}}(\mathbf{G}) = \frac{1}{\Omega_0}\int_{\Omega_0} e^{-i\mathbf{G}\mathbf{r}}u_{j\mathbf{k}}(\mathbf{r})d\mathbf{r}, \tag{A.72}$$

with Ω_0 is volume of the primitive cell. Finally,

$$\varphi_{j\mathbf{k}}(\mathbf{r}) = \sum_{\mathbf{G}} u_{j\mathbf{k}}(\mathbf{G})e^{i(\mathbf{k}+\mathbf{G})\mathbf{r}}. \tag{A.73}$$

We can see that plane wave basis sets $|\mathbf{k}+\mathbf{G}\rangle = e^{i(\mathbf{k}+\mathbf{G})\mathbf{r}}$ are orthonormal because $\langle \mathbf{k}+\mathbf{G}'|\mathbf{k}+\mathbf{G}\rangle = \delta_{\mathbf{G}',\mathbf{G}}$. In addition, the usage of plane wave basis sets requires the periodicity. This condition is obviously satisfied in crystalline solids but dissatisfied in other finite systems such as molecule, surfaces, defects, amorphous solid... The supercell technique is proposed in order to keep periodic boundary condition and therefore, one still can use plane waves basis sets. Fig. A.3 shows the idea for construction of primitive cell of perfect crystal and supercells for other systems. The supercells must be large enough to minimize their interactions with the image-supercells (as the results of periodicity).

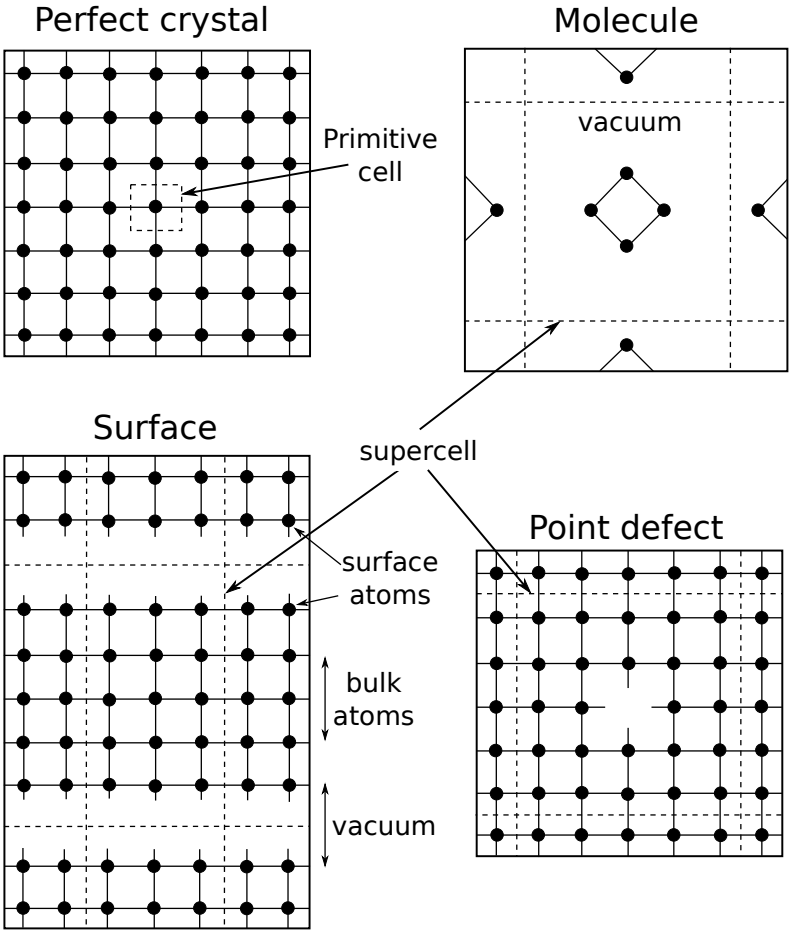

Figure A.3: The primitive cell and supercells allow to use periodic boundary condition.

The coefficients $u_{j\mathbf{k}}(\mathbf{G})$ in (A.73) (in DFT, this is obtained by solving KS equation in self-consistency method), decrease exponentially with the kinetic energy as

$$\hat{T}\varphi_{j\mathbf{k}}(\mathbf{r}) = \frac{-\hbar^2}{2m}\nabla^2\varphi_{j\mathbf{k}}(\mathbf{r}) \sim e^{-|\mathbf{k}+\mathbf{G}|^2}. \tag{A.74}$$

We, therefore, can determine number of plane waves by a cut-off energy E_{cut}

$$\frac{\hbar^2|\mathbf{k}+\mathbf{G}|^2}{2m} < E_{cut}. \tag{A.75}$$

Indeed, E_{cut} must be tested to obtain computational convergence. The number of PWs (the number of lattice points $\{\mathbf{G}\}$ in the *reciprocal space*) corresponding to a chosen E_{cut} is estimated

$$N_{PW} = \frac{1}{2\pi^2}\Omega_0 E_{cut}^{3/2}. \tag{A.76}$$

Fast Fourier Transform: As indicated above, we can represent wave function through PW basis sets which is defined through vectors of the *reciprocal lattice*. Consequently, the charge density for a given state can also be expanded through PW basis sets

$$\begin{aligned}\rho_{j\mathbf{k}}(\mathbf{r}) &= \langle\varphi_{j\mathbf{k}}(\mathbf{r})|\varphi_{j\mathbf{k}}(\mathbf{r})\rangle = \langle u_{j\mathbf{k}}(\mathbf{r})|u_{j\mathbf{k}}(\mathbf{r})\rangle \\ &= \sum_{\mathbf{G}\mathbf{G}'}[u^*_{j\mathbf{k}}(\mathbf{G})|u_{j\mathbf{k}}(\mathbf{G}')]e^{i(\mathbf{G}'-\mathbf{G})\mathbf{r}},\end{aligned} \tag{A.77}$$

with coefficients $u^*_{j\mathbf{k}}(\mathbf{G})$ and $u_{j\mathbf{k}}(\mathbf{G}')$ are only non-zero if $\mathbf{k}+\mathbf{G}$ and $\mathbf{k}+\mathbf{G}'$ are inside the region of the *reciprocal space* limited by E_{cut}. One knows that a periodic function can be Fourier-transformed forward and backward between two space as

$$\begin{aligned}f(\mathbf{G}) &= \frac{1}{\Omega_0}\int_{\Omega_0} e^{-i\mathbf{G}\mathbf{r}} f(\mathbf{r})d\mathbf{r} \\ f(\mathbf{r}) &= \sum_{\mathbf{G}} e^{i\mathbf{G}\mathbf{r}} f(\mathbf{G}).\end{aligned} \tag{A.78}$$

Equation (A.77) shows that $\rho_{j\mathbf{k}}(\mathbf{r})$ is computed on a double-grid and we can apply Fourier transform between *real* and *reciprocal* space by using a discrete mesh in *real* space

$$\begin{aligned}\rho_{j\mathbf{k}}(\mathbf{r}) &= \sum_{\mathbf{G}} \rho_{j\mathbf{k}}(\mathbf{G})e^{i\mathbf{G}\mathbf{r}} \\ \rho_{j\mathbf{k}}(\mathbf{G}) &= \frac{1}{N_{\mathbf{r}}}\sum_{\mathbf{r}_m} \rho_{j\mathbf{k}}(\mathbf{r}_m)e^{-i\mathbf{G}\mathbf{r}_m},\end{aligned} \tag{A.79}$$

where N_r is the number of points in the *real*-space mesh (indicated by index notation m above). The idea can be simply presented as in Fig. A.4. In fact, this transform is performed by Fast Fourier Transform (FFT) algorithm. The density $\rho(\mathbf{G})$ can be used for representation of Hartree part (the XC part is computed directly through the density) in KS potential (see (A.45)). It is rewritten here

$$V_H(\mathbf{r}) = \frac{e^2}{4\pi\epsilon_0}\int \frac{\rho(\mathbf{r}')}{|\mathbf{r}-\mathbf{r}'|}d\mathbf{r}'. \tag{A.80}$$

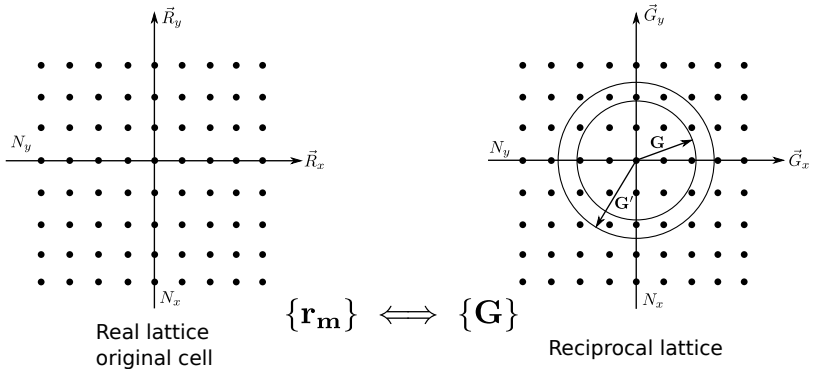

Figure A.4: The Fourier transform between *real* and *reciprocal* space.

The $V_H(\mathbf{G})$ is able to link directly to $\rho(\mathbf{G})$. Indeed, using Poisson's equation, we have

$$\nabla^2 V_H(\mathbf{r}) = -4\pi\rho(\mathbf{r}). \tag{A.81}$$

The Fourier transform is applied into both two sides of (A.81), leading to

$$\mathbf{G}^2 V_H(\mathbf{G}) = 4\pi\rho(\mathbf{G}) \implies V_H(\mathbf{G}) = \frac{4\pi}{\mathbf{G}^2}\rho(\mathbf{G}). \tag{A.82}$$

Thus,

$$V_H(\mathbf{r}) = \sum_{\mathbf{G}} e^{i\mathbf{G}\mathbf{r}} V_H(\mathbf{G}). \tag{A.83}$$

Numerical integration in Brillouin zone: As the periodicity, the evaluation of many quantities (after having KS wave functions) require an integration over (only) the BZ (over all states). For example: charge density

$$\rho(\mathbf{r}) = \sum_j \frac{1}{\Omega_0} \int_{\Omega_0} f(\epsilon_F - \epsilon_{j\mathbf{k}}), \psi^*_{j\mathbf{k}}(\mathbf{r})\psi_{j\mathbf{k}}(\mathbf{r}) d\mathbf{k}, \tag{A.84}$$

with f is Fermi-Dirac distribution (occupation). In numerical calculation, one works on discrete mesh of $\mathbf{k}$ in the BZ. Thus, the chosen of $\mathbf{k}$-mesh is very important for the convergence. There are several techniques developed for dealing with this issue, which can be grouped into two types. First, one employs smearing methods using normalized functions such as Fermi-Dirac, Gaussian, Gauss-Hermite,... These make numerical functions smearing locally around points in the discrete mesh, which helps numerical functions to be smoother and consequently the integral converges faster. Another approach named tetrahedron method, divides BZ into tetrahedra, as these triangular pyramids can fill an arbitrary-shape zone without overlap between them. The integration, thus, is performed on every tetrahedron. The latter gives faster convergence over number of $\mathbf{k}$-points but it is more complex in implementation. To reduce the calculations, all the symmetries of BZ are also exploited leading to an integration over a smaller number of $\mathbf{k}$-points. The smaller zone containing these reduced $\mathbf{k}$-points is called irreducible BZ.

A.6 Pseudopotentials

As mentioned above, PW basis sets are simple and easy to implement. However, a rough analysis of Fourier transform (see (A.71)) shows that the number of Fourier components need to be used for the convergence in a given point (with a tolerance δ) is inversely proportional to its length scale ($\sim 1/|\mathbf{r}|^N$ for N-dimensional space). As a consequence, the representation of core states, oscillations of other orbitals close to the nucleus of atoms need a huge number of PW basis sets. Based on the fact that core electrons occupying orbitals that are 'inert' in atomic, molecular and solid environments, we can separate core and valence orbitals. The density

$$\begin{aligned}\rho(\mathbf{r}) &= \sum_{i}^{n} \psi_i^*(\mathbf{r})\psi_i(\mathbf{r}) \\ &= \sum_{i\in core} \psi_i^*(\mathbf{r})\psi_i(\mathbf{r}) + \sum_{i\in val} \psi_i^*(\mathbf{r})\psi_i(\mathbf{r}) = \rho_{core}(\mathbf{r}) + \rho_{val}(\mathbf{r}),\end{aligned} \tag{A.85}$$

so we can freeze core electrons and see that these are tightly bound to their nucleus. It depends on the level of accuracy considered in specific calculations, the collection of core and valence states needs to be taken into account carefully for each type of atoms. For some elements, the core states are obvious, *e.g.* in F it is $1s^2$. The situation is more complicated in some cases especially transition metals. For instance Ti, its core states can be $1s^2\ 2s^2\ 2p^6$ or $1s^2\ 2s^2\ 2p^6\ 3s^2\ 3p^6$. The total energy E_{KS}

$$\begin{aligned}E^{KS} = \sum_{i}^{n} \langle\psi_i| \frac{-\hbar^2}{2m}\nabla^2 |\psi_i\rangle + \int V_{ext}(\mathbf{r})\rho(\mathbf{r})d\mathbf{r} \\ + \frac{1}{2}\int \frac{e^2\rho(\mathbf{r})\rho(\mathbf{r}')}{4\pi\epsilon_0|\mathbf{r}-\mathbf{r}'|}d\mathbf{r}d\mathbf{r}' + E_{xc}[\rho]\end{aligned} \tag{A.86}$$

is now split as

$$\begin{aligned}E^{KS} = &\sum_{i\in core} \langle\psi_i| \frac{-\hbar^2}{2m}\nabla^2 |\psi_i\rangle + \int V_{ext}(\mathbf{r})\rho_{core}(\mathbf{r})d\mathbf{r} + \frac{1}{2}\int \frac{e^2\rho_{core}(\mathbf{r})\rho_{core}(\mathbf{r}')}{4\pi\epsilon_0|\mathbf{r}-\mathbf{r}'|}d\mathbf{r}d\mathbf{r}' \\ &+ \sum_{i\in val} \langle\psi_i| \frac{-\hbar^2}{2m}\nabla^2 |\psi_i\rangle + \int V_{ext}(\mathbf{r})\rho_{val}(\mathbf{r})d\mathbf{r} + \frac{1}{2}\int \frac{e^2\rho_{val}(\mathbf{r})\rho_{val}(\mathbf{r}')}{4\pi\epsilon_0|\mathbf{r}-\mathbf{r}'|}d\mathbf{r}d\mathbf{r}' \\ &+ \int \frac{e^2\rho_{core}(\mathbf{r})\rho_{val}(\mathbf{r}')}{4\pi\epsilon_0|\mathbf{r}-\mathbf{r}'|}d\mathbf{r}d\mathbf{r}' + E_{xc}[\rho_{core}+\rho_{val}].\end{aligned} \tag{A.87}$$

The potential of the nucleus μ is screened by the core electrons, so on average

$$\begin{aligned}V_\mu(\mathbf{r}) &= \frac{-Z_\mu e}{4\pi\epsilon_0|\mathbf{r}_i-\mathbf{R}_\mu|} + \int \frac{e\rho_{core}(\mathbf{r}')}{4\pi\epsilon_0|\mathbf{r}-\mathbf{r}'|}d\mathbf{r}' \\ &= \frac{-Z_{\mu,val}e}{4\pi\epsilon_0|\mathbf{r}_i-\mathbf{R}_\mu|} + \Big(\frac{-Z_{\mu,core}e}{4\pi\epsilon_0|\mathbf{r}_i-\mathbf{R}_\mu|} + \int \frac{e\rho_{core}(\mathbf{r}')}{4\pi\epsilon_0|\mathbf{r}-\mathbf{r}'|}d\mathbf{r}'\Big).\end{aligned} \tag{A.88}$$

With $V_{ext}(\mathbf{r}) = \sum_\mu V_\mu(\mathbf{r})$, combining with equation (A.87), the total energy is

$$E^{KS} = E^{KS}_{val} + E^{KS}_{core} + \frac{1}{2}\sum_{\mu\neq\nu}\frac{e^2 Z_{\mu,val}Z_{\nu,val}}{4\pi\epsilon_0|\mathbf{R}_\mu-\mathbf{R}_\nu|}, \tag{A.89}$$

where

$$\begin{aligned} E_{val}^{KS} = & \sum_{i\in val} \langle\psi_i|\frac{-\hbar^2}{2m}\nabla^2|\psi_i\rangle + \int \Big(\sum_{\mu} V_\mu(\mathbf{r})\Big)\rho_{val}(\mathbf{r})d\mathbf{r} \\ & + \frac{1}{2}\int \frac{e^2\rho_{val}(\mathbf{r})\rho_{val}(\mathbf{r}')}{4\pi\epsilon_0|\mathbf{r}-\mathbf{r}'|}d\mathbf{r}d\mathbf{r}' + E_{xc}[\rho_{core}+\rho_{val}], \end{aligned} \tag{A.90}$$

and E_{core}^{KS} contains all terms relating to core electrons. However, in (A.90) the non-linear term $E_{xc}[\rho_{core}+\rho_{val}]$ cannot be separated into parts represented through ρ_{core} and ρ_{val} independently. We, therefore, still need to generate (ion)-pseudopotentials (PP) which remove completely core electrons, so there are only valence electrons considered in calculations. The requirements for PP are strict in which PP must produce pseudo-orbitals being smooth as possible (to simplify plane wave expansion) but close the true orbitals (all-electron) as possible. To do this, a cut-off radius r_{cut} is introduced and for a specific orbital in an isolated atom, we have

$$\begin{aligned} \Big(\frac{\hbar^2}{2m}\nabla^2 + V\Big)|\psi_i\rangle &= \epsilon_i|\psi_i\rangle, \\ \Big(\frac{\hbar^2}{2m}\nabla^2 + V_{ps}\Big)|\psi_i^{ps}\rangle &= \epsilon_i^{ps}|\psi_i^{ps}\rangle, \end{aligned} \tag{A.91}$$

and need the PP to meet the following conditions

- $V_{ps}(\mathbf{r})$ is smooth for $r < r_{cut}$ and $V_{ps}(\mathbf{r}) = V_\mu(\mathbf{r})$ for $r \geq r_{cut}$,
- $\psi_i^{ps}(\mathbf{r})$ is smooth for $r < r_{cut}$ and $\psi_i^{ps}(\mathbf{r}) = \psi_i(\mathbf{r})$ for $r \geq r_{cut}$,
- $\frac{d\psi_i^{ps}(\mathbf{r})}{d\mathbf{r}} = \frac{d\psi_i(\mathbf{r})}{d\mathbf{r}}$ for $r = r_{cut}$, and
- $\epsilon_i^{ps} = \epsilon_i$.

The operator V_{ps} must be linear and Hermitian. It acts on wave function as follows

$$V_{ps}\psi(\mathbf{r}) = \int V_{ps}^{kernel}(\mathbf{r},\mathbf{r}')\psi(\mathbf{r}')d\mathbf{r}', \tag{A.92}$$

where V_{ps}^{kernel} is written in 'local' and 'non-local' parts

$$V_{ps}^{kernel}(\mathbf{r},\mathbf{r}') = V_{loc}(\mathbf{r})\delta(\mathbf{r}-\mathbf{r}') + V_{nloc}(\mathbf{r},\mathbf{r}'), \tag{A.93}$$

with

$$V_{nloc}(\mathbf{r},\mathbf{r}') = \sum_{l,m} Y_{l,m}^*(\eta,\phi)V_l(r,r')Y_{l,m}(\eta',\phi'). \tag{A.94}$$

The most widely-used pseudopotentials are grouped as two classes

- Semi-local PP which represents $V_l(r,r') = V_l(r)\delta(r-r')$,
- Separable PP which represents $V_l(r,r') = \zeta_l^*(r)f_l\zeta_l(r')$.

There are additional conditions can be applied for generating PP, for example norm-conservation

$$\int_{r<r_{cut}} |\psi_i^{ps}(\mathbf{r})|^2 d\mathbf{r} = \int_{r<r_{cut}} |\psi_i(\mathbf{r})|^2 d\mathbf{r}. \tag{A.95}$$

The PP in this case is called Norm-Conserving PP (NCPP) which is easy to generate and therefore widely used. The examples for pseudo wave function and (norm-conserving) pseudopotential of Silicon is presented in Fig. A.5. If the norm-conservation condition is skipped, we have Ultra-Soft PP (USPP) which produces much softer PP in region $r < r_{cut}$. It, therefore, requires less number of plane wave basis sets in wave function expansion (smaller E_{cut}), however, this PP is not easy to generate and the

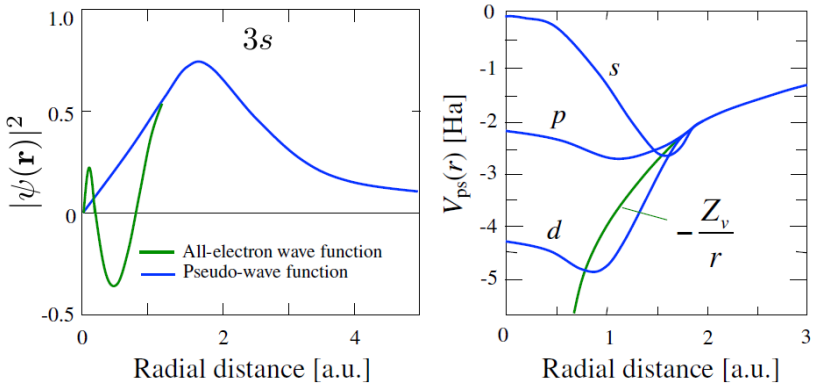

Figure A.5: Examples of pseudo wave function and pseudopotential for Silicon.

total charge is not conserved. In fact, the PP is produced for isolated atoms, then used in more complex environments such as molecule, solid structures,...

Projector Augmented Wave (PAW) method: This is another method developed for *ab initio* computations besides PP. Basically, PAW also employs frozen core states approximation and use fictitious pseudo wave function for valence electrons as PP does. The difference is that the true wave function so-called 'all-electron' is reconstructed from pseudo wave function.

$$\psi_i(\mathbf{r}) = T\psi_i^{ps}(\mathbf{r}). \tag{A.96}$$

Here, T is a transformation operator. It is worth noting that the 'all-electron' wave function refers one-electron Kohn-Sham orbital, and it differs with the many-body wave function. In the region $r > r_{cut}$, $\psi_i(\mathbf{r}) = \psi_i^{ps}(\mathbf{r})$, thus T has a form

$$T = 1 + \sum_{\mathbf{R}} T_{\mathbf{R}}, \tag{A.97}$$

where $T_{\mathbf{R}}$ is non-zero only within some spherical augmentation region $r < r_{cut}$. It is useful to expand $\psi_i^{ps}(\mathbf{r})$ into pseudo partial waves (*e.g.* orbitals at a given energy, not necessarily bound states)

$$|\psi_i^{ps}\rangle = \sum_i c_i |\phi_i^{ps}\rangle, \tag{A.98}$$

where $|\phi_i^{ps}\rangle = |\phi_i\rangle$ if $r > r_{cut}$ and $|\phi_i^{ps}\rangle$ is smooth functions if $r < r_{cut}$ (augmentation region). The 'all-electron' wave function is

$$\begin{aligned} |\psi_i\rangle &= T|\psi_i^{ps}\rangle = |\psi_i^{ps}\rangle + T_{\mathbf{R}}|\psi_i^{ps}\rangle \\ &= |\psi_i^{ps}\rangle + \sum_j (\phi_j - \phi_j^{ps})\langle p_j|\psi_i^{ps}\rangle, \end{aligned} \tag{A.99}$$

thus, $T = 1 + \sum_j (\phi_j - \phi_j^{ps})\langle p_j|$.

The 'projector' $\langle p_j|$ are atomic functions localized within its own augmentation region ($= 0$ if $r > r_{cut}$) and comply with orthonormal condition $\langle p_j|\psi_i\rangle = \delta_{ij}$. The finding of three sets $\{\phi_i\}$, $\{\phi_i^{ps}\}$ and $\{\langle p_i|\}$ is the main task in generating PAW. In fact, $\psi_i^{ps}(\mathbf{r})$ can be a linear combination of polynomials, Bessel functions or other smooth

functions in the region $r < r_{cut}$. For $r > r_{cut}$, it is equal to the 'all-electron' wave function and expanded in a plane wave basis set. PAW has several advantages such an accuracy comparable to all-electron techniques, information about the orbital close to the nucleus (as the all-electron wave function is reconstructed), lower E_{cut} and some disadvantages like complex generation, more additional terms. Recently, systematic comparisons between different pseudopotentials and 'all-electron' have been performed for many DFT codes [351].

Appendix B

Other computational methods

B.1 Dielectric response function

This part is rewritten with referring to different documents including textbooks [154, 177, 171] and lectures delivered by Francesco Sottile and Valérie Véniard in the Centre Européen de Calcul Atomique et Moléculaire (CECAM) workshops (2015).

In general, to discover properties of matters, people always have to use external action applied on them (excitation) and then measure their response. In particular, electronic exciation spectroscopy is a strong toolkit to investigate many electronic properties in materials. As briefly mentioned in Apd. A, electronic excitation spectra can be divided into two types: the number of electrons in the system is changed (by removing or adding one electron) or unchanged. The former one, in fact, is an interacting many-body system. In the picture described by HF or DFT, these excitation states are simply seen as eigenenergies ($\epsilon_{i\mathbf{k}}$) of the (effective) independent-particle Hamiltonians. This leads to broadening effects observed in experimental measurements which is only treated in the many-body framework (often defined through Green's response functions). The later one relates to different phenomena, for example, the optical absorption in semiconductors/insulators or light reflection in metals under the action of alternative current (AC) electric field. The dielectric function is one of the most important response function because photons are the most popular and important probe in experiments. This concept, indeed, is also utilized in description of screening from perturbative charged impurities, defects, *etc.* in solid. In theoretical side, if the external field is weak, we can assume the response of materials is linear and vice versa. Here we only focus on linear response for optical absorptions.

Let us consider a weak external potential $\delta V_{ext}(\mathbf{r}', t')$ applied to a systems of electrons. The response of the system to external field can be seen as a linear behavior (can be obtained from perturbation theory with considering only the first term).

$$\delta V(\mathbf{r}, t) = \int \epsilon^{-1}(\mathbf{r}, \mathbf{r}', t - t')\delta V_{ext}(\mathbf{r}', t')d\mathbf{r}'dt', \tag{B.1}$$

where $\delta V(\mathbf{r}, t)$ is the change of total potential in the system, ϵ^{-1} is called the inverse

dielectric function. Thus, we can rewrite V_{ext} as

$$\delta V_{ext}(\mathbf{r},t) = \int \epsilon(\mathbf{r},\mathbf{r}',t-t')\delta V(\mathbf{r}',t')d\mathbf{r}'dt'. \tag{B.2}$$

In general, ϵ is a two-point function because of the inhomogeneous characteristics of space while the dependence on $t-t'$ is the result of time translation symmetry.
The equation (B.2) can be Fourier-transformed with respect to both time ($t-t'$ to frequency ω) and space ($\mathbf{r},\mathbf{r}'$ to reciprocal space $\mathbf{q},\mathbf{q}'$)

$$\delta V_{ext}(\mathbf{q},\omega) = \int \epsilon(\mathbf{q},\mathbf{q}',\omega)\delta V(\mathbf{q}',\omega)d\mathbf{q}'. \tag{B.3}$$

It is worth noting that in the periodic crystal with translation vectors $\mathbf{R}$, thus

$$\epsilon(\mathbf{r},\mathbf{r}',\omega) = \epsilon(\mathbf{r}+\mathbf{R},\mathbf{r}'+\mathbf{R},\omega), \tag{B.4}$$

and in combination with backward Fourier transform

$$\begin{aligned}\epsilon(\mathbf{q},\mathbf{q}',\omega) &= \Omega\int e^{-i\mathbf{q}'.\mathbf{r}'}V_{ext}(\mathbf{r},\mathbf{r}',\omega)e^{i\mathbf{q}.\mathbf{r}}d\mathbf{r}'d\mathbf{r}\\ &= \Omega\int e^{-i\mathbf{q}'.\mathbf{r}'}V_{ext}(\mathbf{r},\mathbf{r}',\omega)e^{i\mathbf{q}.\mathbf{r}}e^{(\mathbf{q}'-\mathbf{q})\mathbf{R}}d\mathbf{r}'d\mathbf{r}.\end{aligned} \tag{B.5}$$

We infer that $\mathbf{q}'-\mathbf{q}=\mathbf{G}$, where $\mathbf{G}$ is a lattice vector of the reciprocal crystal. Here, Ω is volume of reciprocal space. We can now express δV_{ext} in momentum-frequency (energy) space

$$\begin{aligned}\delta V_{ext}(\mathbf{q}+\mathbf{G},\omega) &= \sum_{\mathbf{G}'}\epsilon(\mathbf{q}+\mathbf{G},\mathbf{q}+\mathbf{G}',\omega)\delta V(\mathbf{q}+\mathbf{G}',\omega)\\ &= \sum_{\mathbf{G}'}\epsilon_{\mathbf{G}\mathbf{G}'}(\mathbf{q},\omega)\delta V(\mathbf{q}+\mathbf{G}',\omega),\end{aligned} \tag{B.6}$$

with $\mathbf{q}$ being in the first BZ of the crystal and $\epsilon_{\mathbf{G}\mathbf{G}'}(\mathbf{q},\omega)$ is the matrix representation of ϵ with respect to $\mathbf{G},\mathbf{G}'$.
In fact, ϵ is a matrix with off-diagonal in $\mathbf{G},\mathbf{G}'$ represents inhomogenous charge in the crystal. The reason is that around each ion in crystal, its behavior is influenced and driven by the field around it (created by surrounding electrons and other ions). When an external field applied into crystals, it induces change in local field because

$$\delta V(\mathbf{q}+\mathbf{G},\omega) = \sum_{\mathbf{G}'}\epsilon^{-1}_{\mathbf{G}\mathbf{G}'}\delta V_{ext}(\mathbf{q}+\mathbf{G}',\omega). \tag{B.7}$$

The effect of local field is, therefore, represented through off-diagonal elements of the dielectric matrix.

Polarizability in self-consistent field framework: In the same idea of response function ϵ, the polarizability is defined to determine the change of the charge (electron) density under an action of the external field

$$\delta\rho(\mathbf{r},t) = \int \chi(\mathbf{r},\mathbf{r}',t-t')\delta V_{ext}(\mathbf{r}',t')d\mathbf{r}'dt'. \tag{B.8}$$

For simplicity

$$\delta\rho = \chi\delta V_{ext}. \tag{B.9}$$

In the framework of self-consistent field (see Apd. A for KS equation), we can define polarizability χ_0 for an independent-electron in response to total perturbative potential, so

$$\delta\rho = \chi_0\delta V, \tag{B.10}$$

where δV is the change of self-consistent potential seen by the electrons (see Apd. A). We have,

$$\delta V = \delta V_{ext} + \delta V_H + \delta V_{xc} = \delta V_{ext} + K_c \delta\rho + K_{xc}\delta\rho, \tag{B.11}$$

where K_c and K_{xc} are bare Coulomb interaction (the first derivative of Hartree potential V_H) and the first derivative of exchange-correlation potential V_{xc}. Combining (B.9), (B.10) and (B.11), we can write

$$\chi = (1 - \chi_0 K_c - \chi_0 K_{xc})^{-1}\chi_0. \tag{B.12}$$

Moreover, $\delta V = \epsilon^{-1}\delta V_{ext}$ and we can use (B.9) and (B.11) then easily obtain

$$\epsilon^{-1} = 1 + (K_c + K_{xc})\chi = 1 + \frac{K_c + K_{xc}}{1 - (K_c + K_{xc})\chi_0}\chi_0. \tag{B.13}$$

A popular approximation so-called 'random phase approximation' (RPA) which neglects exchange-correlation contribution leads to

$$\begin{aligned} \epsilon_{RPA}^{-1} &= 1 + K_c(1 - \chi_0 K_c)^{-1}\chi_0 = (1 - K_c\chi_0)^{-1}, \\ \epsilon_{RPA} &= 1 - K_c\chi_0. \end{aligned} \tag{B.14}$$

In momentum-frequency space, ϵ_{RPA} can be written as (Fourier transform)

$$\epsilon_{\mathbf{GG'}}(\mathbf{q},\omega) = \delta_{\mathbf{GG'}} - \frac{4\pi e^2}{|\mathbf{q}+\mathbf{G}||\mathbf{q}+\mathbf{G'}|}\chi^0_{\mathbf{GG'}}, \tag{B.15}$$

where $\chi^0_{\mathbf{GG'}}$ is the representation of χ_0 in momentum-frequency space. In the context of self-consistent field [186, 187]

$$\begin{aligned} \chi^0_{\mathbf{GG'}}(\mathbf{q},\omega) = \frac{1}{\Omega}\sum_{n,n',\mathbf{k}} &(f_{n,\mathbf{k}} - f_{n',\mathbf{k}+\mathbf{q}}) \\ &\times \frac{\langle n,\mathbf{k}|e^{-i(\mathbf{q}+\mathbf{G})\mathbf{r}}|n',\mathbf{k}+\mathbf{q}\rangle\langle n',\mathbf{k}+\mathbf{q}|e^{-i(\mathbf{q}+\mathbf{G'})\mathbf{r}}|n,\mathbf{k}\rangle}{\epsilon_{n,\mathbf{k}} - \epsilon_{n',\mathbf{k}+\mathbf{q}} + \hbar\omega + i\eta}, \end{aligned} \tag{B.16}$$

where n and $\mathbf{k}$ is band index and wave-vector in Bloch representation. In real space, $|n,\mathbf{k}\rangle = e^{i\mathbf{kr}}u_{n\mathbf{k}}(\mathbf{r})$, thus

$$\begin{aligned} \langle n,\mathbf{k}|e^{-i(\mathbf{q}+\mathbf{G})\mathbf{r}}|n',\mathbf{k}+\mathbf{q}\rangle &= \int_\Omega u^*_{n,\mathbf{k}}(\mathbf{r})e^{-i\mathbf{Gr}}u_{n',\mathbf{k}+\mathbf{q}}(\mathbf{r})d\mathbf{r} \\ &\equiv \langle u_{n,\mathbf{k}}|e^{-i\mathbf{Gr}}|u_{n',\mathbf{k}+\mathbf{q}}\rangle. \end{aligned} \tag{B.17}$$

In the atomic (micro) scale, dielectric tensor $\epsilon_{\mathbf{GG'}}(\mathbf{q},\omega)$ varies rapidly reflecting local field effect. However, many properties (optical absorption) are measured on samples with large (macro) scale of external field. Thus, it is useful to work with macro dielectric tensor

$$\epsilon(\omega) = \epsilon_1(\omega) + i\epsilon_2(\omega). \tag{B.18}$$

For infrared, visible and ultraviolet photons, $\mathbf{q}_{ph} << \mathbf{q}_{BZ}$, the macro dielectric tensor, therefore, can be obtained by averaging $\epsilon_{\mathbf{GG'}}(\mathbf{q},\omega)$ on large scale ($\mathbf{G} = \mathbf{G'} = 0$)

$$\epsilon(\omega) = \lim_{\mathbf{q}\to 0}\epsilon_{\mathbf{00}}(\mathbf{q},\omega). \tag{B.19}$$

The limits written above depends on directions of $\mathbf{q}$, so we define dielectric tensor $\epsilon_{\alpha\beta}(\omega)$ with α and β are Cartesian components. Using (B.15), (B.16), (B.17) and (B.19), we have the imaginary part

$$\begin{aligned}\epsilon^{(2)}_{\alpha\beta}(\omega) = \frac{4\pi^2 e^2}{\Omega} \lim_{|\mathbf{q}|\to 0} \frac{1}{q^2} \sum_{n,n',\mathbf{k}} \big[f(\epsilon_{n,\mathbf{k}}) - f(\epsilon_{n',\mathbf{k}+\mathbf{q}})\big] \\ \times \delta(\epsilon_{n,\mathbf{k}} - \epsilon_{n',\mathbf{k}+\mathbf{q}} + \hbar\omega) \langle u_{n\mathbf{k}+\mathbf{q}_\alpha} | u_{n'\mathbf{k}} \rangle \langle u_{n\mathbf{k}+\mathbf{q}_\beta} | u_{n'\mathbf{k}} \rangle^*.\end{aligned} \tag{B.20}$$

In fact, the calculation is performed in irreducible BZ and without taking into account spin polarization leading to

$$\begin{aligned}\epsilon^{(2)}_{\alpha\beta}(\omega) = \frac{4\pi^2 e^2}{\Omega} \lim_{|\mathbf{q}|\to 0} \frac{1}{q^2} \sum_{n,n',\mathbf{k}} 2w_{\mathbf{k}} \big[f(\epsilon_{n,\mathbf{k}}) - f(\epsilon_{n',\mathbf{k}+\mathbf{q}})\big] \\ \times \delta(\epsilon_{n,\mathbf{k}} - \epsilon_{n',\mathbf{k}+\mathbf{q}} + \hbar\omega) \langle u_{n\mathbf{k}+\mathbf{q}_\alpha} | u_{n'\mathbf{k}} \rangle \langle u_{n\mathbf{k}+\mathbf{q}_\beta} | u_{n'\mathbf{k}} \rangle^*.\end{aligned} \tag{B.21}$$

The real part of the dielectric tensor can be found through the Kramers-Kronig relation:

$$\varepsilon^{(1)}_{\alpha\beta}(\omega) = 1 + \frac{2}{\pi} \mathcal{P} \int_0^\infty \frac{\varepsilon^{(2)}_{\alpha\beta}(\omega')\omega'}{\omega'^2 - \omega^2} d\omega', \tag{B.22}$$

where $\mathcal{P}$ denotes the Cauchy principal value [193].

B.2 Crystal Orbital Hamilton Populations

This part is based on several scientific articles [216, 217, 218, 352].

Chemical bonding analysis is very important as it indicates bonding, non-bonding and anti-bonding between orbitals in atoms. This, therefore, helps to understand more deeply how chemical interactions associate with electrical, chemical properties in molecule and solid materials. In many DFT packages, Kohn-Sham (KS) wave functions are expanded into PW basis sets and thus, it is hard to interpret local information between atoms. On the other hand, if one expands wave functions into a linear combination of atomic orbitals (LCAO), the local information can be easily retrieved. Thus, it is useful to expand KS one-electron wave function ψ_i into LCAOs

$$|\psi_i\rangle = \sum_{\mathbf{R}L} C_{\mathbf{R}Li} |\chi_{\mathbf{R}L}\rangle, \tag{B.23}$$

where $|\chi_{RL}\rangle$ is atomic centered orbitals at atomic site $\mathbf{R}$ and corresponding to angular azimuthal momentum quantum number $L = \{l, m\}$, i stands for band index and $C_{\mathbf{R}Li}$ are expansion coefficients. Here, $\sum_{\mathbf{R}L}$ stands for sum over all atoms $\mathbf{R}$ in the unit cell and over all atomic orbitals L on site $\mathbf{R}$. Because of orthogonal condition of KS wave functions

$$\langle \psi_j | \psi_i \rangle = \sum_{\mathbf{R}'L'} \sum_{\mathbf{R}L} C^*_{\mathbf{R}'L'j} S_{\mathbf{R}'L',\mathbf{R}L} C_{\mathbf{R}Li} = \delta_{ij}, \tag{B.24}$$

where $S_{\mathbf{R}'L',\mathbf{R}L} = \langle\chi_{\mathbf{R}'L'}|\chi_{\mathbf{R}L}\rangle$ is the overlap matrix. To quantify strength of chemical bonding, there have been different quantities proposed.
For instance, a quantity so-called local DOS (LDOS) can be defined as

$$\mathrm{LDOS}_{\mathbf{R}L,L'}(\epsilon) = \sum_{i,\mathbf{k}} C^*_{\mathbf{R}Li} C_{\mathbf{R}L'i} \delta(\epsilon_{i\mathbf{k}} - \epsilon), \tag{B.25}$$

where ϵ is energy and $\epsilon_{i\mathbf{k}}$ is eigenenergy of Bloch state at band i^{th} and wave vector $\mathbf{k}$. The name LDOS is used for calculations directly using LCAO and it is changed to projected DOS (pDOS) in computations using other basis sets then projecting on specific sets of $|\chi_{RL}\rangle$.
If we look at off-site atoms, equation (B.25) is rewritten as

$$\mathrm{COOP}_{\mathbf{R}L,\mathbf{R}'L'}(\epsilon) = S_{\mathbf{R}L,\mathbf{R}'L'} \sum_{i,\mathbf{k}} C^*_{\mathbf{R}Li} C_{\mathbf{R}'L'i} \delta(\epsilon_{i\mathbf{k}} - \epsilon). \tag{B.26}$$

This is known as "crystal orbital overlap population" (COOP). The same framework was also used to define another quantity named "crystal orbital Hamilton population" (COHP).
Using equation (B.23), one-electron KS equation $\hat{H}|\psi_i\rangle = \epsilon_i|\psi_i\rangle$ can be rewritten in the matrix form as

$$\sum_{\mathbf{R}L} (H_{\mathbf{R}'L',\mathbf{R}L} - \epsilon_i S_{\mathbf{R}'L',\mathbf{R}L}) C_{\mathbf{R}Li} = 0, \tag{B.27}$$

where

$$H_{\mathbf{R}'L',\mathbf{R}L} = \langle\chi_{\mathbf{R}'L'}|\hat{H}|\chi_{\mathbf{R}L}\rangle. \tag{B.28}$$

The so-called band structure energy E^b is defined

$$E^b = \int^{\epsilon_F} d\epsilon \sum_i f_i \epsilon_i \delta(\epsilon_i - \epsilon), \tag{B.29}$$

with $0 < f_i < 2$ being occupation numbers. If we multilply (B.27) from the left by the conjugate complex eigenvectors, we have

$$\sum_{\mathbf{R}L} C^*_{\mathbf{R}'L'j} (H_{\mathbf{R}'L',\mathbf{R}L} - \epsilon_i S_{\mathbf{R}'L',\mathbf{R}L}) C_{\mathbf{R}Li} = 0. \tag{B.30}$$

We can repeat (B.30) for $\{\mathbf{R}', L'\}$ and use condition in (B.24) and obtain

$$\sum_{\mathbf{R}'L'} \sum_{\mathbf{R}L} C^*_{\mathbf{R}'L'j} H_{\mathbf{R}'L',\mathbf{R}L} C_{\mathbf{R}Li} = \epsilon_i \delta_{ij}. \tag{B.31}$$

Next,

$$\begin{aligned}
\sum_i f_i \epsilon_i \delta(\epsilon_i - \epsilon) &= \sum_i f_i \sum_{\mathbf{R}'L'} \sum_{\mathbf{R}L} C^*_{\mathbf{R}'L'i} H_{\mathbf{R}'L',\mathbf{R}L} C_{\mathbf{R}Li} \delta(\epsilon_i - \epsilon) \\
&= \sum_{\mathbf{R}'L'} \sum_{\mathbf{R}L} H_{\mathbf{R}'L',\mathbf{R}L} \sum_i f_i C^*_{\mathbf{R}'L'i} C_{\mathbf{R}Li} \delta(\epsilon_i - \epsilon) \\
&= \sum_{\mathbf{R}'L'} \sum_{\mathbf{R}L} H_{\mathbf{R}'L',\mathbf{R}L} N_{\mathbf{R}'L',\mathbf{R}L}(\epsilon) \\
&= \sum_{\mathbf{R}'L'} \sum_{\mathbf{R}L} \mathrm{COHP}_{\mathbf{R}'L',\mathbf{R}L}(\epsilon).
\end{aligned} \tag{B.32}$$

We can see that distribution of all one-particle energies is now represented through a sum of all pair contributions which is called "crystal orbital Hamilton population". The band structure in (B.29) can be represented as

$$E^b = \sum_{\mathbf{R}'L'} \sum_{\mathbf{R}L} H_{\mathbf{R}'L',\mathbf{R}L} M_{\mathbf{R}'L',\mathbf{R}L}(\epsilon), \tag{B.33}$$

where

$$M_{\mathbf{R}'L',\mathbf{R}L}(\epsilon) = \int^{\epsilon_F} N_{\mathbf{R}'L',\mathbf{R}L}(\epsilon) d\epsilon. \tag{B.34}$$

We can separate (B.32) into two parts including on-site COHP ($\mathbf{R}' \equiv \mathbf{R}$) which is $n \times n$ matrix with n is the number of orbitals per site (all possible L) and off-site COHP ($\mathbf{R}' \neq \mathbf{R}$)

$$\sum_i f_i \epsilon_i \delta(\epsilon_i - \epsilon) = \sum_{\mathbf{R}LL'} H_{\mathbf{R}L',\mathbf{R}L} N_{\mathbf{R}L',\mathbf{R}L}(\epsilon) + \sum_{\mathbf{R}'L'} \sum_{\mathbf{R}L} H_{\mathbf{R}'L',\mathbf{R}L} N_{\mathbf{R}'L',\mathbf{R}L}(\epsilon). \tag{B.35}$$

The second term represent *covalent* contribution to the bonds. If there are bonding contribution, COHP shows negative values as the system is in lowering energy and *vice versa*. This principle of COHP is contrary to that of COOP. In transformation from PW basis sets (*e.g.* KS wave functions computed by VASP, ABINIT, Quantum Espresso), the choice of LCAOs is in a constraint so that the retrieved total charge must not be much different (ideally $< 1\%$).

B.3 Phase diagram

This part is based on several scientific articles [353, 354] and an online tutorial of MP [209]

Phase diagram is used to represent the thermodynamic phase stability of multi-element compounds. This is a very helpful tool for experimentalists to navigate processing and synthesis of materials as it shows the tendency of reactions between phases from the view of formation energy. However, the experimental investigation of a phase diagram for a given set of elements is extremely difficult and costly. People, therefore, have tried to approach this issue using computational method, especially DFT calculations.

Compositional Phase Diagram: To establish a phase diagram of given set of elements, we need to compare relative thermodynamic stability of many phases composed of elements in the set. For an isothermal (T = constant), isobaric (P = constant) and closed system (the number of particles are fixed), the appropriate thermodynamic function to be used is the Gibbs free energy

$$\begin{aligned} G(T,P,N_1,N_2,..,N_n) &= H(T,P,N_1,N_2,..,N_n) - TS(T,P,N_1,N_2,..,N_n) \\ &= E(T,P,N_1,N_2,..,N_n) + PV(T,P,N_1,N_2,..,N_n) \\ &\quad - TS(T,P,N_1,N_2,..,N_n), \end{aligned} \tag{B.36}$$

where T, S, P and V are temperature, entropy, pressure and volume of the system. $N = \{N_1, N_2, .., N_n\}$ is number of atoms of species in the system. For systems including condensed phases, PV = constant is assumed. In the simple approach of DFT, calculations are done at 0 K. Thus, $G(T,P,N_1,N_2,..,N_n) = E(0,P,N_1,N_2,..,N_n)$.

One can normalize E with respect to the total number of particles in the system, we have

$$\tilde{E}(0, P, N_1, N_2, .., N_n) \equiv \tilde{E}(0, P, x_1, x_2, .., x_n), \quad \text{with} \quad x_i = \frac{N_i}{\sum_i N_i}. \tag{B.37}$$

Here, x_i is ratio of i^{th} element in the system, and $\sum_i x_i = 1$. By taking the convex hull of $\tilde{E}$ for all possible phases of n-element system and projecting the stable nodes into $(n-1)$-dimensional composition space, we can obtain phase diagram for the system at 0 K. In fact, DFT calculations are regularly performed at pressure 0 atm. We would like to emphasize that there is not a direct physical meaning for the thermodynamic stability at 0 K. However, in this approximation the phase diagram captures effectively the thermodynamic properties of materials. The efficiency of this approach was proved through a good agreement with the available experimental data [353]. Fig. B.1 shows an example of calculated phase diagram for a two-component system. We can quickly interpret stability of all phases in phase diagram by energy above hull E_{hull}.

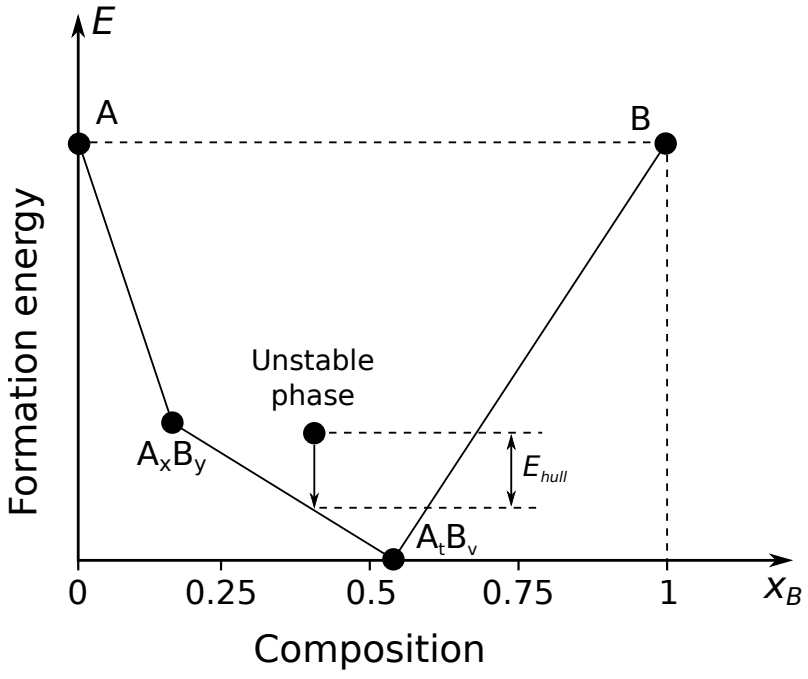

Figure B.1: Schematic phase diagram of a two-element (A and B) system.

Grand potential Phase Diagram: In many contexts, the considered system is not closed. For example, the synthesis process might be taken place in air, thus the system is open to oxygen, nitrogen,... In this case, the thermodynamic

function for a grand canonical ensemble must be used

$$\begin{aligned} G(T,P,N_1,N_2,..,N_n,\mu_j) &= H(T,P,N_1,N_2,..,N_n,\mu_j) \\ &- TS(T,P,N_1,N_2,..,N_n,\mu_j) \\ &- \mu_j N_j(T,P,N_1,N_2,..,N_n,\mu_j) \\ &= E(T,P,N_1,N_2,..,N_n,\mu_j) \\ &- TS(T,P,N_1,N_2,..,N_n,\mu_j) \\ &- \mu_j N_j(T,P,N_1,N_2,..,N_n,\mu_j). \end{aligned} \tag{B.38}$$

Here, PV term is ignored again. μ_j and N_j are chemical potential and number of atoms type j the system exchanges with a reservoir. In the same way, we can normalize with respect to total number of particles $\sum_i N_i$ and have

$$\tilde{G}(T,P,x_1,x_2,..,x_n,\mu_j) = \frac{E - TS - \mu_j N_j}{\sum_i N_i}, \tag{B.39}$$

where $x_i = \frac{N_i}{\sum_i N_i}$ is ratio of i^{th} element in the system. The introduction of temperature dependence into calculated phase diagram needs to take into account many relevant excitations such as vibrations (phonons), configurations and electrons because $S = S_{vib} + S_{con} + S_{el} + ...$ This would yield complicated and expensive calculations. However, in the system which is composed of solid phases we can assume the entropy of solid phases is small in comparison with that of gas, and

$$\tilde{G}(T,P,x_1,x_2,..,x_n,\mu_j) = \frac{E - \mu_j N_j}{\sum_i N_i}. \tag{B.40}$$

Thus, with equation (B.40), we can describe the effect of temperature and partial pressure (of the environment around) using a single chemical potential variable. This is smaller if the temperature increases and partial pressure decreases. For given condition corresponding to a chemical potential μ_j, the grand phase diagram can be obtained by taking the convex hull of $\tilde{G}(T,P,x_1,x_2,..,x_n,\mu_j)$ for all phases in the system and projecting the stable nodes into $(n-1)$-dimensional composition space.

Estimation of chemical potentials: The chemical potentials are needed for different purposes, *e.g* calculations of defects (see B.4). In fact, this is energy cost we have to pay for exchanging atoms between the defect and a thermodynamic reservoir. The chemical potential of each atom depends on the composition of the materials, for instance, A_tB_v in Fig. B.1. There are two approaches to compute individual chemical potentials in which one can use canonical or grand-canonical thermodynamic phase diagrams. Here, we present a later as it is used in our calculation. For simplicity, we show computation of chemical potentials for elements A and B (μ_A and μ_B) in A_tB_v (see Fig. B.1). We have,

$$E_{A_tB_v} = t\mu_A + v\mu_B, \tag{B.41}$$

where $E_{A_tB_v}$ is the bulk energy per formula unit. In B-rich condition, the value of μ_B is constrained by stability of the compound in the excess of B. This is constrained as $\mu_B < \mu_B^0$ with μ_B^0 is energy per atom in bulk B phase. In the extreme (limit) condition, one can select $\mu_B = \mu_B^0$ and thus

$$\mu_A = \frac{E_{A_tB_v} - v\mu_B^0}{t}. \tag{B.42}$$

If we consider A-rich condition, instead of defining μ_A directly through μ_A^0 (energy per atom in bulk B phase), we combine A_xB_y with A_tB_v and obtain

$$\begin{aligned} E_{A_xB_y} &> x\mu_A + y\mu_B, \\ E_{A_tB_v} &= t\mu_A + v\mu_B. \end{aligned} \tag{B.43}$$

In the limit condition,

$$\mu_A = \frac{vE_{A_xB_y} - yE_{A_tB_v}}{xv - yt} \quad \text{and} \quad \mu_B = \frac{tE_{A_xB_y} - xE_{A_tB_v}}{yt - xv}. \tag{B.44}$$

B.4 Dopability of a material and defects

In doped semiconductors, their carrier concentration is set by the amount and type of defects in the crystal. The intrinsic (or native) point defects consist of vacancies, self-interstitials and antisites (cations on sites of anions, for example). The extrinsic point defects (impurities or dopants) are substitutional and interstitial foreign atoms.
Point defects strongly influence the carrier concentration and hence the conductivity of semiconductors and TCMs. Indeed, charged defects in semiconductors can generate free electrons or holes. The intrinsic or extrinsic doping of a material can be assessed by computing defect formation energies as functions of the Fermi level. This defect formation energy (E_f) can be written as [266]:

$$E_f[D^q] = E[D^q] - E[\text{bulk}] - \sum_i n_i\mu_i + qE_F + E_{\text{corr}}[D^q], \tag{B.45}$$

where the defect D is in the charge state q, $E[D^q]$ and $E[\text{bulk}]$ are the total energies of the crystal with the defect D^q and without any defects, respectively, n_i is the number of atoms of type i that have been removed ($n_i < 0$) or added ($n_i > 0$) by the formation of the defect and μ_i is their chemical potential which is set by growth conditions and phase stability, E_F is the Fermi level referenced with respect to the VBM, and $E_{\text{corr}}[D^q]$ is a correction term introduced to take care of the spurious image charge interactions and the alignment of the potential for charged defects (see the Computational approach for defects studies section). Figure B.2 shows a typical defect formation energy versus Fermi level plot. In Fig. B.2 (a), each defect (D_1, D_2, D_3, D_4) has charged (positive or negative slope depending on the sign of the charge) and uncharged (horizontal lines) states. The defect D_1 has a rather low formation energy and easily exists in charge-state -1, making it a shallow acceptor. The defect D_2 is on the contrary a shallow donor. The defect D_3 is another shallow donor but it

is less stable as it has a larger formation energy. The defect D_4 is a deep defect because it displays charge-state transitions $(0/-1)$ and $(-1/-2)$ in the middle of the gap. Different defects always compete with each other in a material and it is the result of these competition that sets the Fermi level. For instance, Fig. B.2 (b) presents a n-type tendency: the donor defect D_2 has a much lower formation energy than the others and therefore easily exists in charge-sate $+1$ around the CBM and releases a free electron into the crystal. In the same way, Fig. B.2 (c) shows a p-type tendency. The case of undopability (neither n- or p-type) is shown in Fig. B.2 (d). The "hole-killers" defects D_2 and D_4, in charge-state $+1$, are very active around the VBM, completely dominating the acceptor defect D_1. Around the CBM, D_1 and D_4 have lower formation energies than the donor D_2 and are working as "electron-killers". Of course, this picture might be different in different chemical potential conditions. It is in practice not always very clear how certain chemical potential conditions could be reached experimentally. Chemical potential of elements and thus synthesis conditions will affect the defect formation energies and therefore their behavior in the material. In our approach, chemical potentials are usually extracted in limit conditions from phase diagram (more details in B.3).

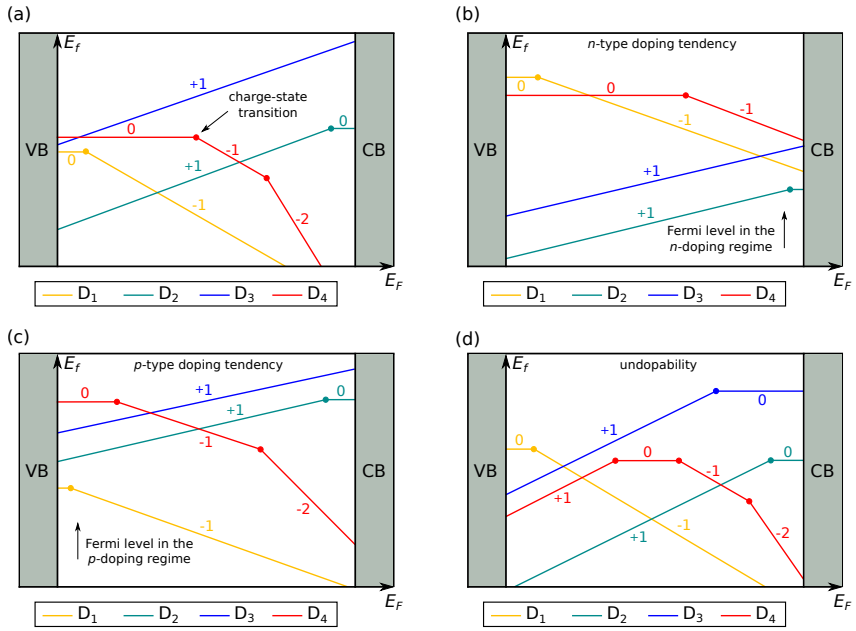

Figure B.2: (a) Schematic illustration of defect formation energies E_f as a function of the Fermi level E_F of four defects D_i in different charge states. (b), (c), (d) Defect formation energies for n-, p-type dopings and the case of undopability, respectively.

There are two natural ways to compute charged defects in solids: the use of clusters and supercells. In these approaches, ionized states of defects in semiconductors are investigated by using clusters or supercells containing de-

fects in the corresponding charge states. While using clusters leads to problems with the dangling bonds on their surfaces that are difficult to eliminate, using supercells with periodic boundary conditions induces spurious Coulomb interactions between image charges ($E_{\text{corr}}[D^q]$ in equation (B.45)) [355, 356, 357]. Nowadays, thanks to the advances of DFT-based calculations and hardware, large supercells can easily be treated for which the image charge interactions are minimized. Furthermore, corrections methods have been developed (see below) making supercell calculations a tool of choice.

Supercell computations are used to evaluate equation (B.45). DFT with semi-local functionals provides fairly good defect formation energies and general doping tendencies [358]. However, it is well-known that DFT relying on semi-local exchange-correlation functional drastically underestimates the band gap. Empirical corrections to the band edges to fit to experimental data (scissor operator) have been used to correct this underestimation with much controversies in the literature on the right method to perform this. When working with $3d$ transition metals, a Hubbard U correction has also been used. The current method of choice is to use hybrid functionals which add a fraction of exact exchange to the DFT functional and provide good energetics in addition to much improved band gaps. The HSE hybrid functional is especially powerful in solids [198, 199, 267]. Another way to obtain a correct evaluation of the band gap is to use many-body perturbation theory within the GW approximation, [359]. This approach is however problematic as it does not provide forces and cannot be used for atomic relaxation around the defect (contrary to hybrid functionals).

Charged defects computations are intrinsically difficult to perform in periodic boundary condition codes. Indeed, potential alignment (due to the background charge always present in charged defect computations) as well as spurious image charge Coulomb interactions have been known to affect the accuracy of the supercell computations. Different techniques have been suggested to correct these errors with a recent popularity for the methods developed by Freysoldt and Kumagai [360, 361, 270, 271]. Although defects calculations for supercells containing around 200 atoms are doable, they are challenging to perform HT both for computational and automation reasons. Recent tools such as PyCDT, PyDEF or other Python frameworks have been developed to handle such calculations as automatically as possible [272, 362, 363].

B.5 GW method

This method was originally proposed by Hedin [359] in 1965 with a successful application for the electron-gas system. The author showed a better approach to describe interacting many-particle systems. The complex many-body problem is also shifted to one-particle problem. A particular particle's interactions with other ones is screened by the surrounding 'cloud of particles'. This screening effect is described using dielectric function (as mentioned in B.1). Thus, the behavior of the one-particle can be represented as a propagator function (propagate in space and time), particular a Green's function, which carries information about its effective interactions with other particles. This is named

as "quasi-particle". Because the establishment of a series of coupled equations requires a lengthy detour, we concisely rewrite the final Schrödinger-equation for the quasi-particle

$$\Big[-\frac{\hbar^2\nabla^2}{2m}+V_{ext}(\mathbf{r})+V_H(\mathbf{r})\Big]\psi_i(\mathbf{r})+\int d\mathbf{r}', \Sigma(\mathbf{r},\mathbf{r}',E_i)\psi_i(\mathbf{r}')=E_i\psi_i(\mathbf{r}), \quad \text{(B.46)}$$

where $V_{ext}(\mathbf{r})$ is the nuclear-electron interaction potential, $V_H(\mathbf{r})$ in the Hartree potential, and Σ is the self-energy operator, which in so-called GW approximation has form

$$\Sigma(\mathbf{r},\mathbf{r}',\omega)=\frac{i}{4\pi}\int_{-\infty}^{\infty} e^{i\omega'\delta}G(\mathbf{r},\mathbf{r},\omega+\omega')W(\mathbf{r},\mathbf{r},\omega')d\omega', \quad \text{(B.47)}$$

where G is the one-particle Green's function, W is the screened Coulomb interaction which is regularly computed through polarizability in random phase approximation. The polarizability in turn of itself is calculated through Green function. Thus, equation (B.46) is solved in self-consistent loop. In fact, one often uses Kohn-Sham wave functions as a starting point to compute G and then other following operators. However, because this sort of computation is very heavy, the calculation is usually stopped after the first cycle of the self-consistency. This is known as G_0W_0 calculation. More details can be referred to the thesis of Giantomassi [277].

B.6 Electron-phonon interaction

This part is based on several scientific articles [304, 364, 274, 365] and textbooks [177, 171].

Lattice vibrations (phonons): The atoms in materials always vibrate around their equilibrium positions because of temperature and external field. Even at zero temperature, the lattice still vibrates as quantum effect. The vibrational characteristics of the lattice originate many properties and phenomena in materials such as electric resistance, superconductivity, indirect optical absorption, thermal expansion,... In theoretical approach, one regularly begins with *harmonic* (vibration) approximation and see displacement of atoms as small perturbation. The total energy of the lattice system can be expanded through Taylor series

$$E_{tot}(\{\Delta\tau\})=E^0_{tot}+\frac{1}{2}\sum_{a,\kappa,\alpha}\sum_{b,\kappa',\beta}\frac{\partial^2 E_{tot}}{\partial\tau^a_{\kappa,\alpha}\tau^b_{\kappa',\beta}}\Delta\tau^a_{\kappa,\alpha}\Delta\tau^b_{\kappa',\beta}+...., \quad \text{(B.48)}$$

where E^0_{tot} is the total energy of the equilibrium state and $\Delta\tau^a_{\kappa,\alpha}$ is the displacement along direction α of the atom κ in the cell labeled by a (with lattice vector $\mathbf{R}_a$) from its equilibrium position $\tau^a_{\kappa,\alpha}$. Here, because we approximate lattice vibrations are harmonic, the higher orders in (B.48) are truncated. Thus,

$$E_{tot}(\{\Delta\tau\})=E^0_{tot}+\frac{1}{2}\sum_{a,\kappa,\alpha}\sum_{b,\kappa',\beta}C_{\kappa\alpha,\kappa'\beta}(a,b)\Delta\tau^a_{\kappa,\alpha}\Delta\tau^b_{\kappa',\beta}, \quad \text{(B.49)}$$

where

$$C_{\kappa\alpha,\kappa'\beta}(a,b) = \frac{\partial^2 E_{tot}}{\partial\tau^a_{\kappa,\alpha}\tau^b_{\kappa',\beta}} \tag{B.50}$$

is called atomic force constant matrix which represents force on atom κ in cell a along direction α if atom κ' in cell b is displaced along direction β. Let us consider vibration of atom κ in cell a along direction α (in classical mechanics)

$$M_\kappa \frac{\partial^2 \Delta\tau^a_{\kappa,\alpha}}{\partial^2 t} = -\frac{\partial E_{tot}}{\partial \Delta\tau^a_{\kappa,\alpha}} = -\sum_{b,\kappa',\beta} C_{\kappa\alpha,\kappa'\beta}(a,b)\Delta\tau^b_{\kappa',\beta}. \tag{B.51}$$

To solve (B.51) for the normal modes, we find solution for each atom $[\kappa, a, \alpha]$ vibrating in periodic crystal at frequency ω in form

$$\Delta\tau^a_{\kappa,\alpha}(t) = A^a_{\kappa,\alpha}\frac{1}{\sqrt{M_\kappa}}e^{-i\omega t}, \tag{B.52}$$

where $A^a_{\kappa,\alpha}$ is the amplitude of vibration. Substitute this form of $\Delta\tau^a_{\kappa,\alpha}$ back into (B.51), we have

$$\omega^2 A^a_{\kappa,\alpha} = \sum_{b,\kappa',\beta} \frac{C_{\kappa\alpha,\kappa'\beta}(a,b)}{\sqrt{M_\kappa M_{\kappa'}}} A^b_{\kappa',\beta}. \tag{B.53}$$

Because of periodicity, $C_{\kappa\alpha,\kappa'\beta}(a,b)$ depends only on $\mathbf{R}_a - \mathbf{R}_b$. Thus, we note

$$D_{\kappa\alpha,\kappa'\beta}(\mathbf{R}_a - \mathbf{R}_b) = \frac{C_{\kappa\alpha,\kappa'\beta}(a,b)}{\sqrt{M_\kappa M_{\kappa'}}} \tag{B.54}$$

is a real $d \times n \times N$ symmetric matrix with d being degrees of freedom ($d = 3$ in 3-dimensional system), n being number of atoms in a units cell and N being number of unit cells in the lattice. In similar to the electron case in periodic crystals, we can also express $A^a_{\kappa,\alpha}$ in Bloch form. At given wave number of phonon $\mathbf{q}$ ($\mathbf{q}$ in BZ)

$$A^a_{\kappa,\alpha}(\mathbf{r} + \mathbf{R}_a, \mathbf{q}) = e^{i\mathbf{q}\mathbf{R}_a} A_{\kappa,\alpha}(\mathbf{r}, \mathbf{q}), \tag{B.55}$$

where $\mathbf{r}$ is position of atoms in original unit cell (can choose at origin). Equation (B.53) becomes

$$\omega^2 A_{\kappa,\alpha}(\mathbf{r},\mathbf{q}) = \sum_{\kappa',\beta}\Big[\sum_b D_{\kappa\alpha,\kappa'\beta}(\mathbf{R}_a - \mathbf{R}_b)e^{-i\mathbf{q}(\mathbf{R}_a - \mathbf{R}_b)}\Big]A_{\kappa',\beta}(\mathbf{r},\mathbf{q}). \tag{B.56}$$

The matrix

$$D_{\kappa\alpha,\kappa'\beta}(\mathbf{q}) = \sum_b D_{\kappa\alpha,\kappa'\beta}(\mathbf{R}_a - \mathbf{R}_b) \tag{B.57}$$

is called 'dynamical matrix'. Finally,

$$\omega^2 A_{\kappa,\alpha}(\mathbf{r},\mathbf{q}) = \sum_{\kappa',\beta} D_{\kappa\alpha,\kappa'\beta}(\mathbf{q}) A_{\kappa',\beta}(\mathbf{r},\mathbf{q}) \tag{B.58}$$

is a $d \times n$ matrix eigenvalue problem. If the dynamical matrix is known, we can obtain solutions $\omega_i(\mathbf{q})$ ($i = 1, 2, ..., nd$) are frequencies of $d \times n$ vibration modes. There are two approaches to compute dynamical matrix

- Direct calculation of total energy as a function of positions of atoms. This is called "frozen phonon". This, therefore, requires calculations with big supercells.
- Explicit calculations of derivative of energy at any order. This is called response function. In self-consistent field approach, density functional perturbation theory has been developed widely used today.

In quantum mechanics, lattice vibrations are quantized into quasi-particles so-called phonons which is very popular in solid physics.

Electron-phonon interaction: This concept has a long history as long as the quantum theory of solids. In the language of second-quantized formalism, we can write Hamiltonian of a el-ph system as

$$\begin{aligned}\hat{H} =& \sum_{n\mathbf{k}} \epsilon_{n\mathbf{k}} \hat{c}^{\dagger}_{n\mathbf{k}} \hat{c}_{n\mathbf{k}} + \sum_{\mathbf{q}\nu} (\hat{a}^{\dagger}_{\mathbf{q}\nu} \hat{a}_{\mathbf{q}\nu} + 1/2) \\ &+ \frac{1}{\sqrt{N}} \sum_{mn\nu} \sum_{\mathbf{kq}} g_{mn\nu}(\mathbf{k},\mathbf{q}) \hat{c}^{\dagger}_{m\mathbf{k}+\mathbf{q}} \hat{c}_{n\mathbf{k}} (\hat{a}_{\mathbf{q}\nu} - \hat{a}^{\dagger}_{-\mathbf{q}\nu}) \\ &+ \frac{1}{N} \sum_{mn\nu\nu'} \sum_{\mathbf{kqq}'} g^{DW}_{mn\nu\nu'}(\mathbf{k},\mathbf{q},\mathbf{q}') \hat{c}^{\dagger}_{m\mathbf{k}+\mathbf{q}+\mathbf{q}'} \hat{c}_{n\mathbf{k}} (\hat{a}_{\mathbf{q}\nu} - \hat{a}^{\dagger}_{-\mathbf{q}\nu})(\hat{a}_{\mathbf{q}'\nu'} - \hat{a}^{\dagger}_{-\mathbf{q}'\nu'}),\end{aligned} \tag{B.59}$$

where $\epsilon_{n\mathbf{k}}$ is the band energies of electron at band index n and wave vector $\mathbf{k}$, ν and $\mathbf{q}$ stand for mode (branch) index and wave vector of phonon, respectively, $\hat{c}^{\dagger}_{n\mathbf{k}}$ and $\hat{c}_{n\mathbf{k}}$ ($\hat{a}^{\dagger}_{\mathbf{q}\nu}$ and $\hat{a}_{\mathbf{q}\nu}$) are creation and annihilation operators of electrons (phonons), N is number of unit cells. The matrix elements $g_{mn\nu}(\mathbf{k},\mathbf{q})$ and $g^{DW}_{mn\nu\nu'}(\mathbf{k},\mathbf{q},\mathbf{q}')$ represent for strength of the el-ph interactions in one- and two-phonon process, respectively (in unit of energy, 'DW' is named after Debye-Waller). The theoretical calculations of these matrix has a long history which is represented clearly in Ref. [365]. Here, we shortly rewrite the formula constructed in *ab initio* DFT technique for the one-phonon process

$$g_{mn\nu}(\mathbf{k},\mathbf{q}) = \Big(\frac{\hbar}{2m\omega_{\mathbf{q}\nu}}\Big)^{1/2} \langle \psi_{m\mathbf{k}+\mathbf{q}} | \partial_{\mathbf{q}\nu} V^{KS} | \psi_{m\mathbf{k}} \rangle, \tag{B.60}$$

where $\hbar$ and m is reduced Planck constant and mass of free electron, $\omega_{\mathbf{q}\nu}$ is phonon frequency, $\psi_{n\mathbf{k}}$ is the electronic wave function and V^{KS} is self-consistent Kohn-Sham potential. The advantage of DFT-based method is that band energy $\epsilon_{n\mathbf{k}}$, wave functions $\psi_{m\mathbf{k}}$ and their derivatives and phonons $\omega_{\mathbf{q}\nu}$ can be all computed.
The imaginary part of electron self-energy in association with el-ph interactions is computed as

$$\begin{aligned}\mathrm{Im}\Sigma_{n\mathbf{k}}(T) =& \pi \sum_{m\nu} \int \frac{d\mathbf{q}}{\Omega_{BZ}} |g_{nm\nu}(\mathbf{k},\mathbf{q})|^2 \\ &\times [(1 - f_{m\mathbf{k}+\mathbf{q}} + n_{\mathbf{q}\nu}) \delta(\epsilon_{n\mathbf{k}} - \hbar\omega_{\mathbf{q}\nu} - \epsilon_{m\mathbf{k}+\mathbf{q}}) \\ &+ (f_{m\mathbf{k}+\mathbf{q}} + n_{\mathbf{q}\nu}) \delta(\epsilon_{n\mathbf{k}} + \hbar\omega_{\mathbf{q}\nu} - \epsilon_{m\mathbf{k}+\mathbf{q}})],\end{aligned} \tag{B.61}$$

where Ω_{BZ} is volume of BZ, $f_{m\mathbf{k}+\mathbf{q}} = [\exp((\epsilon_{n\mathbf{k}+\mathbf{q}} - \epsilon_F)/k_BT) + 1]^{-1}$ is Fermi-Dirac distribution of carriers at Fermi energy ϵ_F and temperature T, $n_{\mathbf{q}\nu} = [\exp(\hbar\omega_{\mathbf{q}\nu}/k_BT) - 1]^{-1}$ is Bose-Einstein distribution of phonons with frequencies $\omega_{\mathbf{q}\nu}$ at temperature T. The scattering rates of electron with phonons (inverse of relaxation/life time) at given temperature can be calculated through el-ph self-energy as (Heisenberg uncertainty principle)

$$\frac{1}{\tau_{n\mathbf{k}}}(T) = \frac{2\mathrm{Im}\Sigma_{n\mathbf{k}}(T)}{\hbar}, \tag{B.62}$$

where $\tau_{n\mathbf{k}}$ is relaxation time of carriers at band n and wave-vector $\mathbf{k}$, $\hbar$ is reduced Planck constant.
The scattering rates (inverse of relaxation time) as a function of energy is computed by averaging all states (in a discrete $\mathbf{k}$-mesh) as

$$\frac{1}{\tau(\epsilon)} = \frac{1}{N(\epsilon)} \sum_{n\mathbf{k}} \frac{1}{\tau_{n\mathbf{k}}} \delta(\epsilon_{n\mathbf{k}} - \epsilon), \tag{B.63}$$

where $N(\epsilon) = \sum_{n\mathbf{k}} \delta(\epsilon_{n\mathbf{k}} - \epsilon)$. We can see that $N(\epsilon)/N_{\mathbf{k}} \times S$ is DOS (in unit of states/energy-unit/cell), where, $N_{\mathbf{k}}$ is the number of $\mathbf{k}$-points and $S = 1$ or 2 for spin polarization or non-polarization calculation, respectively.
The el-ph coupling strength of a specific phonon mode ν and wave-vector $\mathbf{q}$ is defined

$$\lambda_{\mathbf{q}\nu} = \frac{1}{N(\epsilon_F)\hbar\omega_{\mathbf{q}\nu}} \sum_{nm} \int \frac{d\mathbf{k}}{\Omega_{BZ}} \left|g_{nm\nu}(\mathbf{k},\mathbf{q})\right|^2 \delta(\epsilon_{n\mathbf{k}} - \epsilon_F)\delta(\epsilon_{m\mathbf{k}+\mathbf{q}} - \epsilon_F), \tag{B.64}$$

where $N(\epsilon_F)$ is the density of state at Fermi level. We kept our materials intrinsic by setting the Fermi level at the mid-gap and in the very general approach of EPW, all phonon modes, both inter-band and intra-band scattering mechanisms are taken into account in the computation of scattering rates.

Phonon-assisted optical absorption: This quantity can be computed if the g-matrix in (B.60) is defined. By definition [295, 278]

$$\begin{aligned}\alpha(\omega) = {} & \frac{\pi e^2}{\epsilon_0 c \Omega_{cell}} \frac{1}{\omega n_r(\omega)} \int \frac{d\mathbf{k} d\mathbf{q}}{\Omega^2} \sum_{mn\nu} \sum_{s=\pm 1} (f_{n\mathbf{k}} - f_{m\mathbf{k}+\mathbf{q}}) \\ & \times \left| \mathbf{e}. \sum_p \left[\frac{\mathbf{v}_{np}(\mathbf{k}) g_{pm\nu}(\mathbf{k},\mathbf{q})}{\epsilon_{p\mathbf{k}} - \epsilon_{n\mathbf{k}} - \hbar\omega} + \frac{g_{np\nu}(\mathbf{k},\mathbf{q}) \mathbf{v}_{pm}(\mathbf{k}+\mathbf{q})}{\epsilon_{p\mathbf{k}} - \epsilon_{n\mathbf{k}} + s\hbar\omega_{\mathbf{q}\nu}} \right] \right|^2 \\ & \times (n_{\mathbf{q}\nu} + 1/2 + s/2) \delta(\epsilon_{m\mathbf{k}+\mathbf{q}} - \epsilon_{n\mathbf{k}} - \hbar\omega + s\hbar\omega_{\mathbf{q}\nu}),\end{aligned} \tag{B.65}$$

where $\alpha(\omega)$ is the absorption coefficient for visible light, e is the photon polarization, $\mathbf{v}_{mn}$ are matrix elements of the electron velocity operator, and $n_r(\omega)$ is the real part of the refractive index. The two denominators in second line of (B.65) corresponds to paths of indirect absorption. In the first one, the electron absorbs a *photon* and then absorbs or emits a *phonon*. In the second one, the electron absorbs or emits a *phonon* and then absorbs a *photon*. This is based on electric dipole approximation and thus valid for photon with energy of a few electron-volts. More details can be found in Refs. [278, 365].

B.7 Boltzmann transport equation

This part is rewritten with referring to several scientific articles [172, 366], textbooks [367, 154] and the lecture delivered by Samuel Poncé in the ICTP/Psik/CECAM School (2018).

Transport of carriers is an essential phenomenal in materials. The theoretical treatment of transport is developed from very simple approximation with

classical mechanics (Drude's model) to more complicated formalism with quantum mechanics (for quantum systems like nano-structures,...). This part will rewrites a semi-classical treatment using BTE. At equilibrium condition, carriers (*e.g.* electrons, holes) in materials (metals, semiconductors/insulators) occupy states obeying Fermi-Dirac distribution. However, if external actions such as electromagnetic field or temperature gradients, carriers are applied into the system, the carriers are accelerated and force to move. The carriers normally are scattered with phonons, defects, impurities... as materials are not perfect and always intrinsically exist lattice vibrations. Thus, the system will reach to a "steady state" in which the scattering balances with actions of external field. The equilibrium distribution of carriers $f_0(\mathbf{r}, \mathbf{k}, t)$ is now shifted to a new mode $f(\mathbf{r}, \mathbf{k}, t)$ that is stable in time. We have,

$$\frac{df}{dt} = \frac{\partial f}{\partial t} + \frac{\partial f}{\partial \mathbf{r}}\frac{\partial \mathbf{r}}{\partial t} + \frac{\partial f}{\partial \mathbf{k}}\frac{\partial \mathbf{k}}{\partial t} + \frac{\partial f}{\partial T}\frac{\partial T}{\partial t} + \Big(\frac{\partial f}{\partial t}\Big)_{coll} = 0, \tag{B.66}$$

where $\mathbf{r}$ and $\mathbf{k}$ are position and wave number of carriers (corresponding to occupied states), T is the temperature, $(\partial f/\partial t)_{coll}$ stands for scattering-dependence. If only direct-current and homogeneous electromagnetic field ($\partial f/\partial t = 0$), constant temperature ($\partial f/\partial T = 0$) and homogeneous materials ($\partial f/\partial \mathbf{r} = 0$) are assumed, we have

$$\frac{\partial \mathbf{k}}{\partial t}\nabla_{\mathbf{k}} f + \Big(\frac{\partial f}{\partial t}\Big)_{coll} = 0. \tag{B.67}$$

In solid with classical approach (for electron),

$$\hbar\frac{\partial \mathbf{k}}{\partial t} = -e\mathbf{E} - \frac{e}{c}\mathbf{v} \times \mathbf{H}. \tag{B.68}$$

If magnetic field is off ($\mathbf{H} = 0$), so that

$$\frac{e\mathbf{E}}{\hbar}\nabla_{\mathbf{k}} f(\mathbf{k}) = \Big(\frac{\partial f}{\partial t}\Big)_{coll}. \tag{B.69}$$

In *relaxation time approximation* context, the collision term can be represented as

$$\Big(\frac{\partial f}{\partial t}\Big)_{coll} = -\frac{f(\mathbf{k}) - f_0(\mathbf{k})}{\tau(\mathbf{k})}. \tag{B.70}$$

This implies that the carriers have tendency to go back the equilibrium state after scattered. We can write

$$f(\mathbf{k}) = f_0(\mathbf{k}) - e\tau(\mathbf{k})\mathbf{E}\nabla_{\mathbf{k}} f(\mathbf{k})/\hbar. \tag{B.71}$$

If the electric field is weak, we can assume that $f(\mathbf{k}) \approx f_0(\mathbf{k})$ and take into account the contribution of different bands in materials, so

$$\begin{aligned} f(n, \mathbf{k}) &= f_0(n, \mathbf{k}) - e\tau(n, \mathbf{k})\mathbf{E}\nabla_{\mathbf{k}} f_0(n, \mathbf{k})/\hbar, \\ f(n, \mathbf{k}) - f_0(n, \mathbf{k}) &= -e\tau(n, \mathbf{k})\mathbf{E}\frac{1}{\hbar}\frac{\partial \epsilon(n, \mathbf{k})}{\partial \mathbf{k}}\frac{\partial f_0(n, \mathbf{k})}{\partial \epsilon(n, \mathbf{k})}, \end{aligned} \tag{B.72}$$

where n is band index and $\epsilon(n, \mathbf{k})$ is band-energies. We can see that $\Delta f = f - f_0$ is the change of carrier distribution caused by external field $\mathbf{E}$, which

contributes to the electric current in materials. We define a density of electric current

$$\mathbf{J} = \sum_{n,\mathbf{k}} -\Delta f.e\mathbf{v}(n,\mathbf{k}) = \sum_{n,\mathbf{k}} e^2\tau(n,\mathbf{k})\mathbf{v}(n,\mathbf{k})\frac{1}{\hbar}\frac{\partial\epsilon(n,\mathbf{k})}{\partial\mathbf{k}}\frac{\partial f_0(n,\mathbf{k})}{\partial\epsilon(n,\mathbf{k})}\mathbf{E}, \quad \text{(B.73)}$$

where $\mathbf{v}(n,\mathbf{k}) = \frac{1}{\hbar}\frac{\partial\epsilon(n,\mathbf{k})}{\partial\mathbf{k}}$ is group velocity of carrier. Density of electric current can be written through the conductivity tensor

$$\mathbf{J} \equiv \sum_{n,\mathbf{k}} \begin{pmatrix} J_x \\ J_y \\ J_z \end{pmatrix} = \sum_{n,\mathbf{k}} \begin{pmatrix} \sigma_{xx} & \sigma_{xy} & \sigma_{xz} \\ \sigma_{yx} & \sigma_{yy} & \sigma_{yz} \\ \sigma_{zx} & \sigma_{zy} & \sigma_{zz} \end{pmatrix} \begin{pmatrix} E_x \\ E_y \\ E_z \end{pmatrix}, \quad \text{(B.74)}$$

where

$$\sigma_{\alpha\beta}(n,\mathbf{k}) = e^2\tau(n,\mathbf{k})\mathbf{v}_\alpha(n,\mathbf{k})\mathbf{v}_\beta(n,\mathbf{k})\frac{\partial f_0(n,\mathbf{k})}{\partial\epsilon(n,\mathbf{k})} \quad \text{(B.75)}$$

is called conductivity tensor. The term $\frac{\partial f_0(n,\mathbf{k})}{\partial\epsilon(n,\mathbf{k})}$ depends only on (scalar) energy ϵ. Thus, ones usually write

$$\sigma_{\alpha\beta}(n,\mathbf{k}) = e^2\tau(n,\mathbf{k})\mathbf{v}_\alpha(n,\mathbf{k})\mathbf{v}_\beta(n,\mathbf{k}). \quad \text{(B.76)}$$

The conductivity tensor can be expressed as a function of energy using (B.76) then summing over all bands and $\mathbf{k}$-points in the BZ as

$$\sigma_{\alpha\beta}(\epsilon) = \frac{1}{N}\sum_{n,\mathbf{k}} \sigma_{\alpha\beta}(n,\mathbf{k})\delta(\epsilon - \epsilon_{n,\mathbf{k}}), \quad \text{(B.77)}$$

where N is the number of $\mathbf{k}$-points. Finally, the conductivity tensor as a function of temperature T and Fermi level μ (electronic chemical potential) is computed through $\sigma_{\alpha\beta}(\epsilon)$ as

$$\sigma_{\alpha\beta}(T;\mu) = \frac{1}{\Omega}\int \sigma_{\alpha\beta}(\epsilon)\left[\frac{\partial f_\mu(T;\epsilon)}{\partial\epsilon}\right]d\epsilon, \quad \text{(B.78)}$$

where f_μ is the Fermi-Dirac distribution and Ω is the volume of the unit cell. The Fermi level μ is defined correspondingly to a given doping carrier concentration. In Chp. 4, we performed BTE to estimate mobility with taking into account only scattering with phonons. The relaxation time $\tau(n,\mathbf{k})$ is estimated from el-ph interactions as mentioned in section B.6. We used the BoltzTrap package [172] to solve BTE. In practice, BoltzTrap interpolates the DFT band-energies (computed on a finite number of $\mathbf{k}$-points) using star functions (see section 1.3 of Chp. 1). Hence, the group velocities can be easily obtained on a much denser $\mathbf{k}$-point grid thus facilitating the numerical convergence of the final results. In constant relaxation-time approximation, the calculations based on the interpolation of band-energies can produce many transport quantities such as conductivity, mobility, Seebeck coefficient, *etc.* as long as the relaxation-time is known. In this work, we go beyond this approximation using $\tau_{n,\mathbf{k}}$ computed by EPW. We implement an interpolation for relaxation time in BoltzTrap on the same very dense $\mathbf{k}$-point grid used for band-energies. The physical principle for this implementation is that the symmetries of the self-energy are the same as those of band-energies [277] ($\tau_{n,\mathbf{k}}$ can be calculated from the imaginary part of the electron self-energy in interaction with phonons as shown in B.6).

Appendix C

Supplementary materials

C.1 For chapter 3

Tab. C.1 shows information for Sn-based oxides that are included in our model (section 3.3 of Chp. 3).

Table C.1: Formula, space group (Spg), materials project [208, 209] identification number (MP-id), band gap E_g (in unit eV), three principal hole effective masses m_1, m_2 and m_3 (m_o-free electron mass), components of VBM including Sn-s, O-p, Sn-s and others (in %). All the oxides listed here have the Sn-O networks developing in at least one direction.

Formula	Spg	MP-id	E_g	m_1	m_2	m_3	Sn-s	O-p	Sn-p	Others
$K_2Sn_2O_3$	$R\bar{3}m$	7502	1.2	0.23	0.23	0.43	24.0	42.4	30.4	Sn-d, 2.1
$K_2Sn_2O_3$	$I2_13$	8624	1.3	0.27	0.27	0.27	24.9	42.1	31.4	Sn-d, 1.2
$Rb_2Sn_2O_3$	$R\bar{3}m$	7863	1.2	0.27	0.27	0.37	22.0	47.2	28.0	Sn-d, 2.1
Rb_2SnO_2	$P2_12_12_1$	27931	2.2	1.80	2.23	2.49	12.5	62.1	20.4	Sn-d, 2.2
SnO	$Pmn2_1$	545552	1.4	0.56	0.62	7.85	26.9	52.1	19.3	Sn-d, 1.6
SnO	$P4/nmm$	2097	0.5	0.59	2.82	2.82	51.9	43.1	1.59	Sn-d, 3.4
$Nb_2Sn_2O_7$	$Fd\bar{3}m$	556524	0.9	4.74	4.74	4.74	30.7	56.0	0.9	Nb-d, 8.8
Nb_2SnO_6	$C2/c$	3324	1.7	0.43	2.13	5.63	38.4	43.9	8.4	Nb-d, 8.6
$Sn_3(PO_4)_2$	$P2_1/c$	27493	3.4	1.0	2.0	3.16	33.6	49.6	14.8	O-s, 1.3
$Sn_4P_2O_9$	$P2_1/c$	561545	3.2	2.43	2.63	5.77	32.8	51.5	14.4	O-s, 0.6
$SnWO_4$	$Pnna$	19654	0.9	1.03	2.23	2.42	38.1	45.8	9.2	W-d, 4.6
$Ta_2Sn_2O_7$	$Fd\bar{3}m$	3593	1.5	6.92	6.92	6.92	32.2	57.9	1.0	Ta-d, 5.0
Ta_2SnO_6	Cc	556489	2.3	1.22	3.5	5.09	40.7	43.1	8.6	Ta-d, 7.0
$TiSn_2O_4$	$P4_2/mbc$	18288	1.1	0.96	0.96	1.43	32.6	51.1	13.5	Ti-d, 1.7
$BaSn_2H_2O_4$	$P2_1$	696946	2.1	1.47	2.27	5.26	30.9	46.4	16.6	Ba-d,3.0
$SnPHO_4$	$P2_1/c$	690702	3.4	0.96	1.09	4.52	35.9	53.2	9.0	P-p, 1.1
$Cs_2Sn_2O_3$	$Pnma$	540796	2.5	2.68	3.58	9.54	15.2	62.9	16.3	Cs-p, 2.8
$Sn(CO_2)_2$	$C2/c$	542769	2.6	0.77	10.21	12.23	17.2	66.7	7.2	C-p, 6.3

Tab. C.2 shows information for Sn-based oxides that are not included in our model because of several reasons (section 3.3 of Chp. 3).

Table C.2: Formula, space group (Spg), inorganic crystal structure data base [168] identification number (ICSD-id), materials project [208, 209] identification number (MP-id), DFT band gap E_g (in unit eV), three principal hole effective masses m_1, m_2 and m_3 (m_o-free electron mass), components of valence band maximum (VBM) Sn-s, O-p and Sn-s (in %) and remarks (RM) for all materials not matching with our model including $\times$: No Sn−O networks, C: Clusters of Sn−O and others noted at the bottom of the table.

Formula	Spg	ICSD-id	MP-id	E_g	m_1	m_2	m_3	Sn-s	O-p	Sn-p	RM
$NaSn_4(PO_4)_3$	$R3c$	409786	6226	3.7	4.7	4.7	4.7	26.2	59.9	12.8	$\times$
$SnMo_5O_8$	$P2_1/c$	68511	19524	1.0	2.2	2.3	12.7	0.0	2.4	6.0	†
$Sn_{15}Os_3O_{14}$	Cm	59312	28456	1.5	2.1	2.7	22.4	10.2	18.0	34.4	‖
$Na_2Sn(CO_2)_4$	$C2/c$	388	554823	2.8	1.6	9.9	24.5	20.8	62.6	7.6	$\times$
$Na_4Sn_4H_{10}O_{11}$	$P2_1/c$	35420	772039	2.7	8.0	12.0	13.1	28.4	51.8	17.0	$\times$
$Sn_3H_4N_2O_{10}$	$P2_1/c$	80019	705520	2.7	4.5	11.8	21.0	31.1	56.5	11.0	$\times$
$K_2SnP_2O_7$	$P2_1/c$	419264	554825	4.2	17.9	20.3	20.49	27.1	62.1	7.0	$\times$
$SnP_2H_2O_8$	$C2/c$	200364	-	2.6	8.2	16.0	31.9	0.0	96.8	0.0	⊥
$Sn_7S_2O_{20}$	$Pbca$	32673	-	1.5	32.2	38.4	112.9	0.3	96.0	0.6	⊥
K_4SnO_3	$Pbca$	79101	14988	2.1	1.0	2.8	9.6	0.0	0.0	0.0	⊢
$KSn_4(PO_4)_3$	$R3c$	59857	6755	3.8	4.1	4.1	7.4	28.0	58.1	12.1	$\times$
Na_4SnO_3	Cc	49624	28261	1.9	1.4	2.4	7.0	12.0	64.6	19.5	$\times$
$Sn(SO_2)_2$	$P2_1/c$	32684	31004	2.7	1.4	2.5	11.3	9.0	39.9	31.0	$\times$
$VSnPO_5$	$P\bar{1}$	415455	566025	1.2	0.8	4.6	18.5	28.4	40.5	5.8	⊣
$SnPO_3$	Cc	25034	-	0.5	1.0	4.2	13.4	0.0	46.7	6.5	±
SnB_4O_7	$Pmn2_1$	249206	13252	3.6	1.6	2.1	2.2	31.4	64.3	2.9	$\times$
$SnSO_4$	$P\bar{1}$	2748	645774	4.1	2.3	4.7	8.2	24.6	68.9	5.4	$\times$
$SnSO_4$	$Pnma$	2748	542967	4.1	1.3	3.8	5.2	27.4	63.6	8.5	$\times$
$Sn_2P_2O_7$	$P2_1/c$	170847	556031	3.6	0.9	1.3	4.8	33.0	54.0	11.0	C
$Sn_2P_2O_7$	$P\bar{1}$	170845	554022	3.5	1.9	5.1	8.5	38.3	49.5	8.5	C
Sn_2PCO_6	$P2_1/c$	50969	559291	2.3	1.9	3.0	3.8	39.2	46.8	12.3	C
Sn_2SO_5	$P\bar{4}2_1c$	35101	28025	3.5	4.3	7.6	7.6	32.1	52.7	13.6	C
$Na_2Sn_2H_4O_5$	$P2_12_12_1$	35421	707767	2.3	0.7	1.8	4.3	34.1	48.8	14.2	C
$SnHC_2O_3$	$C2/m$	96547	697873	2.1	0.7	0.8	5.0	18.4	58.4	3.6	C
$SiSn_6O_8$	$P6_3mc$	156236	556100	1.9	3.4	3.9	3.9	39.4	38.9	20	C
Sn_3O_4	$P2/c$	174299	-	0.9	0.4	1.9	11.3	41.6	49.4	17.1	∓
$SnWO_4$	$P2_13$	2840	19608	3.8	4.5	4.6	4.6	37.8	40.1	10.0	$\times$
$Sn_5(PO_5)_2$	$P\bar{1}$	418458	560715	2.7	0.8	4.8	9.3	37.8	45.0	15.9	$\times$
$Sn_3H_2O_4$	$P-42_1c$	203206	625541	2.3	1.1	2.1	10.3	43.0	36.6	19.2	$\times$

Continued on next page

Table C.2 – continued from previous page

Formula	Spg	ICSD-id	MP-id	E_g	m_1	m_2	m_3	Sn-s	O-p	Sn-p	RM
											†: 75.8% Mo-d in VBM
											‖: Little Sn-s in VBM
											⊥: No Sn-s in VBM
											⊢: 100% K-s in VBM
											⊣: 34.2% V-d in VBM
											±: 28% P-p in VBM
											∓: Mixture of both Sn^{2+} & Sn^{4+}

C.2 For chapter 4

Tab. C.3 shows 107 materials passing through the first two filters and then computed with HSE to obtain more accurate band gaps and direct gaps (section 4.4 of Chp. 4).

Table C.3: Formula, space group (Spg), Materials Project [208, 209] identification number (MP-id), three principal hole effective masses m_1, m_2 and m_3 (in m_o-free electron mass) (the data of effective masses is reported in the previous work [256]), stability measured by the energy above hull E_{hull} in the phase diagram (in meV/atom), fundamental E_g and direct gaps E_g^d (in unit eV) computed using PBE and HSE [198, 199].

							E_g		E_g^d	
Formula	Spg	MP-id	m_1	m_2	m_3	E_{hull}	PBE	HSE	PBE	HSE
BeS	$F\bar{4}3m$	422	0.65	0.65	0.65	0.0	3.14	4.05	5.62	6.89
$KMgH_3$	$Pm\bar{3}m$	23737	0.75	0.75	0.75	0.0	2.46	3.58	4.51	5.76
SiC	$F\bar{4}3m$	8062	0.58	0.58	0.58	0.7	1.39	2.25	4.53	5.75
BeSe	$F\bar{4}3m$	1541	0.55	0.55	0.55	0.0	2.69	3.36	4.22	5.27
$BeCN_2$	$I\bar{4}2d$	15703	0.75	0.75	0.78	0.0	3.85	5.21	3.85	5.21
$RbPbF_3$	Cc	674508	0.71	0.83	0.95	0.0	3.81	4.84	4.10	5.20
MgS	$Fm\bar{3}m$	1315	0.98	0.98	0.98	0.0	2.79	3.84	3.61	4.95
$RbHgF_3$	$Pm\bar{3}m$	7482	0.93	0.93	0.93	0.0	0.65	2.11	2.70	4.90
AgCl	$Fm\bar{3}m$	22922	0.83	0.83	0.83	0.0	0.95	2.28	2.89	4.81
$CsHgF_3$	$Pm\bar{3}m$	561947	0.89	0.89	0.89	0.0	0.76	2.20	2.43	4.59
Be_2C	$Fm\bar{3}m$	1569	0.37	0.37	0.37	0.0	1.19	1.63	4.12	4.56
$SrMgH_4$	$Cmc2_1$	643009	0.84	0.90	0.95	0.0	2.74	3.78	3.27	4.52
Li_2Se	$Fm\bar{3}m$	2286	0.95	0.95	0.95	0.0	3.00	3.70	3.36	4.36
BP	$F\bar{4}3m$	1479	0.34	0.34	0.34	0.0	1.24	2.26	3.39	4.35
CaS	$Fm\bar{3}m$	1672	0.88	0.88	0.88	0.0	2.39	3.34	3.18	4.28
$LiCa_4B_3N_6$	$Im\bar{3}m$	6799	0.86	0.86	0.86	0.0	2.21	3.38	2.98	4.25
$BaSrI_4$	$R\bar{3}m$	754852	0.73	0.73	0.80	21.8	3.37	4.22	3.35	4.22

Continued on next page

Table C.3 – continued from previous page

							E_g		E_g^d	
Formula	Spg	MP-id	m_1	m_2	m_3	E_{hull}	PBE	HSE	PBE	HSE
$LiSr_4B_3N_6$	$Im\bar{3}m$	9723	0.89	0.89	0.89	0.0	2.09	3.22	2.95	4.18
$NaSr_4B_3N_6$	$Im\bar{3}m$	10811	0.92	0.92	0.92	0.0	1.99	3.14	2.78	4.08
K_2LiAlH_6	$Fm\bar{3}m$	24411	0.65	0.65	0.65	9.1	2.45	3.70	2.93	4.04
BeTe	$F\bar{4}3m$	252	0.42	0.42	0.42	0.0	2.02	2.45	3.62	4.04
Ba_3SrI_8	$I4/mmm$	756235	0.70	0.81	0.81	7.5	3.23	4.02	3.23	4.02
CaSe	$Fm\bar{3}m$	1415	0.77	0.77	0.77	0.0	2.09	2.95	2.99	4.01
LiH	$Fm\bar{3}m$	23703	0.46	0.46	0.46	0.0	3.02	3.97	2.97	3.97
AlP	$F\bar{4}3m$	1550	0.56	0.56	0.56	0.0	1.63	2.50	3.09	3.90
YbS	$Fm\bar{3}m$	1820	0.76	0.76	0.76	0.0	2.22	2.96	2.91	3.76
Na_2LiAlH_6	$Fm\bar{3}m$	644092	0.66	0.66	0.66	3.9	2.64	3.75	2.89	3.75
SrSe	$Fm\bar{3}m$	2758	0.83	0.83	0.83	0.0	2.23	3.03	2.80	3.68
$BaLiH_3$	$Pm\bar{3}m$	23818	0.36	0.36	0.36	0.0	2.27	3.26	2.55	3.62
$CsPbF_3$	$Pm\bar{3}m$	5811	0.39	0.39	0.39	4.6	3.05	3.59	2.92	3.59
Cs_3ZnH_5	$I4/mcm$	643702	0.69	0.93	0.93	0.0	2.75	3.58	2.79	3.58
Al_2CdS_4	$Fd\bar{3}m$	9993	0.78	0.78	0.78	20.0	2.47	3.55	2.47	3.56
K_2LiAlH_6	$R\bar{3}m$	23774	0.68	0.84	0.84	0.0	2.58	3.52	2.90	3.52
$BaMgH_4$	$Cmcm$	643718	0.48	0.55	0.70	4.8	2.32	3.26	2.58	3.51
CaTe	$Fm\bar{3}m$	1519	0.60	0.60	0.60	0.0	1.55	2.18	2.62	3.50
Cs_3MgH_5	$P4/ncc$	23947	0.88	0.93	0.93	0.3	2.61	3.49	2.63	3.49
Cs_3MgH_5	$I4/mcm$	643895	0.83	0.94	0.94	0.0	2.59	3.49	2.61	3.49
YbSe	$Fm\bar{3}m$	286	0.67	0.67	0.67	0.0	1.97	2.43	2.77	3.48
ZnS	$F\bar{4}3m$	10695	0.81	0.81	0.81	0.0	2.02	3.46	2.02	3.46
$TaCu_3S_4$	$P\bar{4}3m$	10748	0.98	0.98	0.98	0.0	1.95	2.95	2.34	3.46
Al_2ZnS_4	$Fd\bar{3}m$	4842	0.66	0.66	0.66	0.0	2.49	3.43	2.52	3.46
Li_2ThN_2	$P\bar{3}m1$	27487	0.85	0.95	0.95	0.0	2.18	3.33	2.34	3.46
$Mg_2B_{24}C$	$P\bar{4}n2$	568556	0.77	0.93	0.93	0.0	2.63	3.41	2.62	3.42
Li_2GePbS_4	$I\bar{4}2m$	19896	0.61	0.61	0.98	0.0	2.25	3.20	2.31	3.33
Cs_3H_5Pd	$P4/mbm$	643006	0.79	0.83	0.83	0.0	2.28	3.09	2.38	3.32
SrTe	$Fm\bar{3}m$	1958	0.67	0.67	0.67	0.0	1.77	2.39	2.48	3.24
MgTe	$F\bar{4}3m$	13033	0.95	0.95	0.95	0.9	2.32	3.24	2.32	3.24
$CsTaN_2$	$I\bar{4}2d$	34293	0.71	0.71	0.92	0.0	2.15	3.22	2.21	3.22
Cs_3MnH_5	$I4/mcm$	643706	0.82	0.96	0.96	0.0	1.65	3.18	1.66	3.21
LiMgP	$F\bar{4}3m$	36111	0.65	0.65	0.65	0.0	1.56	2.00	2.39	3.18
BaS	$Fm\bar{3}m$	1500	0.85	0.85	0.85	0.0	2.16	3.02	2.30	3.17
$LiAlTe_2$	$I\bar{4}2d$	4586	0.52	0.83	0.83	0.0	2.44	3.11	2.44	3.11
YbTe	$Fm\bar{3}m$	1779	0.54	0.54	0.54	0.0	1.47	1.76	2.46	3.09
Li_3Sb	$Fm\bar{3}m$	2074	0.24	0.24	0.24	0.0	0.72	1.15	2.28	3.06
$SrAl_2Te_4$	$I422$	37091	0.42	0.79	0.80	0.0	1.50	2.66	1.55	3.06
$TaCu_3Te_4$	$P\bar{4}3m$	9295	0.63	0.63	0.63	0.0	1.14	2.50	1.59	3.05
$CsPbCl_3$	$Amm2$	675524	0.30	0.32	0.33	0.0	2.46	2.99	2.41	2.99
$TaCu_3Se_4$	$P\bar{4}3m$	4081	0.82	0.82	0.82	0.0	1.63	2.43	2.03	2.98
BaSe	$Fm\bar{3}m$	1253	0.76	0.76	0.76	0.0	1.96	2.59	2.19	2.95
KAg_2PS_4	$I\bar{4}2m$	12532	0.67	0.82	0.82	0.0	1.27	2.53	2.05	2.87

Continued on next page

Table C.3 – continued from previous page

							E_g		E_g^d	
Formula	Spg	MP-id	m_1	m_2	m_3	E_{hull}	PBE	HSE	PBE	HSE
AlAs	$F\bar{4}3m$	2172	0.50	0.50	0.50	0.0	1.52	2.12	1.77	2.84
$LiErS_2$	$I4_1/amd$	35591	0.62	0.99	0.99	10.4	1.99	2.80	1.99	2.80
GaN	$F\bar{4}3m$	830	0.94	0.94	0.94	5.2	1.57	2.80	1.56	2.80
$CsPbCl_3$	$Pm\bar{3}m$	23037	0.26	0.26	0.26	5.5	2.40	2.75	2.19	2.75
GaP	$F\bar{4}3m$	2490	0.45	0.45	0.45	0.0	1.59	1.97	1.59	2.69
$LiSmS_2$	$I4_1/amd$	34477	0.93	0.93	0.99	0.0	1.92	2.69	1.92	2.69
$LiGaTe_2$	$I\bar{4}2d$	5048	0.37	0.70	0.70	0.0	1.59	2.69	1.59	2.69
$ThSnI_6$	$P\bar{3}1c$	28815	0.55	0.57	0.57	20.8	1.99	2.32	2.23	2.66
BaTe	$Fm\bar{3}m$	1000	0.64	0.64	0.64	0.0	1.59	2.22	1.97	2.65
CuI	$F\bar{4}3m$	22895	0.86	0.86	0.86	6.0	1.14	2.65	1.13	2.65
$NbCu_3Se_4$	$P\bar{4}3m$	4043	0.82	0.82	0.82	0.0	1.40	2.12	1.79	2.64
TaSbRu	$F\bar{4}3m$	31454	0.73	0.73	0.73	0.0	0.71	1.30	1.84	2.63
Nd_2TeS_2	$P\bar{3}m1$	10933	0.45	0.72	0.72	0.0	1.62	2.23	1.95	2.63
Zr_2SN_2	$P6_3/mmc$	11583	0.40	0.54	0.54	0.0	0.56	1.38	1.62	2.62
Ca_3PCl_3	$Pm\bar{3}m$	29342	0.63	0.63	0.63	0.0	1.84	2.60	1.84	2.60
$BaMg_2P_2$	$P\bar{3}m1$	8278	0.62	0.62	0.88	0.0	1.15	1.69	1.75	2.60
WS_2	$R3m$	9813	0.79	0.91	0.91	3.8	1.34	2.12	1.84	2.60
Ca_3AsCl_3	$Pm\bar{3}m$	28069	0.58	0.58	0.58	0.0	1.84	2.57	1.84	2.57
$BaSnS_2$	$P2_1/c$	12181	0.44	0.57	0.85	0.0	1.62	2.40	1.69	2.54
LiZnP	$F\bar{4}3m$	10182	0.40	0.40	0.40	0.0	1.36	1.69	1.50	2.51
$ScCuS_2$	$P3m1$	6980	0.75	0.75	0.87	0.0	0.88	1.77	1.50	2.50
IrSbS	$Pca2_1$	9270	0.50	0.52	0.89	4.5	1.04	1.76	1.54	2.43
Cd_2P_3Cl	Cc	29246	0.41	0.76	0.80	9.1	1.12	2.06	1.58	2.42
$CsPbBr_3$	$Pnma$	567629	0.25	0.28	0.29	0.0	2.01	2.39	2.01	2.39
Hg_2P_3Cl	$C2/c$	28875	0.40	0.82	0.99	2.3	1.13	1.89	1.56	2.38
Cd_2P_3Br	$C2/c$	29245	0.44	0.78	0.87	6.8	1.05	2.01	1.57	2.37
$CsNbN_2$	$Fd\bar{3}m$	8978	0.53	0.53	0.53	8.2	1.53	2.36	1.53	2.36
$RbGeBr_3$	$Pna2_1$	28558	0.32	0.42	0.47	0.0	1.99	2.34	1.99	2.34
IrSbS	$P2_13$	8630	0.39	0.39	0.39	0.0	1.42	2.18	1.56	2.34
Ca_3AsBr_3	$Pm\bar{3}m$	27294	0.57	0.57	0.57	0.0	1.67	2.34	1.67	2.34
$LiYSe_2$	$I4_1/amd$	37879	0.55	0.83	0.83	17.6	1.55	2.33	1.55	2.33
ZrCoBi	$F\bar{4}3m$	31451	0.80	0.80	0.80	0.0	1.15	1.28	1.66	2.31
$NaLi_2Sb$	$Fm\bar{3}m$	5077	0.41	0.41	0.41	0.0	0.71	1.04	1.61	2.27
ZnP_2	$P4_12_12$	2782	0.37	0.65	0.65	0.0	1.47	2.14	1.59	2.27
$KHgF_3$	$Pm\bar{3}m$	7483	0.87	0.87	0.87	0.0	0.64	2.26	2.82	2.26
$LiHoSe_2$	$I4_1/amd$	33322	0.52	0.83	0.83	16.8	1.58	2.25	1.58	2.25
$LiDySe_2$	$I4_1/amd$	35717	0.55	0.81	0.82	16.0	1.56	2.23	1.56	2.23
P_2Pt	$Pa\bar{3}$	730	0.25	0.25	0.25	0.0	1.06	1.79	1.51	2.22
$TbLiSe_2$	$I4_1/amd$	38695	0.61	0.78	0.78	15.4	1.54	2.20	1.54	2.20
$MgGeP_2$	$I\bar{4}2d$	34903	0.26	0.61	0.61	13.0	1.51	2.16	1.54	2.16
$LiSmSe_2$	$I4_1/amd$	35388	0.72	0.72	0.75	0.0	1.51	2.15	1.51	2.15
$LiNdSe_2$	$I4_1/amd$	37605	0.72	0.72	0.84	7.6	1.52	2.15	1.52	2.15
$SrMg_2Sb_2$	$P\bar{3}m1$	9566	0.53	0.55	0.55	0.0	0.98	1.42	1.51	2.06

Continued on next page

Table C.3 – continued from previous page

							E_g		E_g^d	
Formula	Spg	MP-id	m_1	m_2	m_3	E_{hull}	PBE	HSE	PBE	HSE
RbAu	$Pm\bar{3}m$	30373	0.24	0.24	0.24	0.0	0.57	0.49	1.80	2.02
CsAu	$Pm\bar{3}m$	2667	0.25	0.25	0.25	0.0	1.02	1.25	1.73	1.99
$LiNbS_2$	$P6_3/mmc$	7936	0.61	0.61	0.68	0.0	0.73	1.06	1.56	1.95
Ag_3SbS_3	$R3c$	4515	0.49	0.49	1.00	2.3	1.00	1.30	1.54	1.94

Fig. C.1 presents scattering rate of BP as a functions of energy at room temperature (VBMs are set to zeros). The specific contributions of acoustic (the first three modes) and optical (the remaining ones) phonon-modes are also shown. We can see that the optical modes are the main source of scattering in valence band.

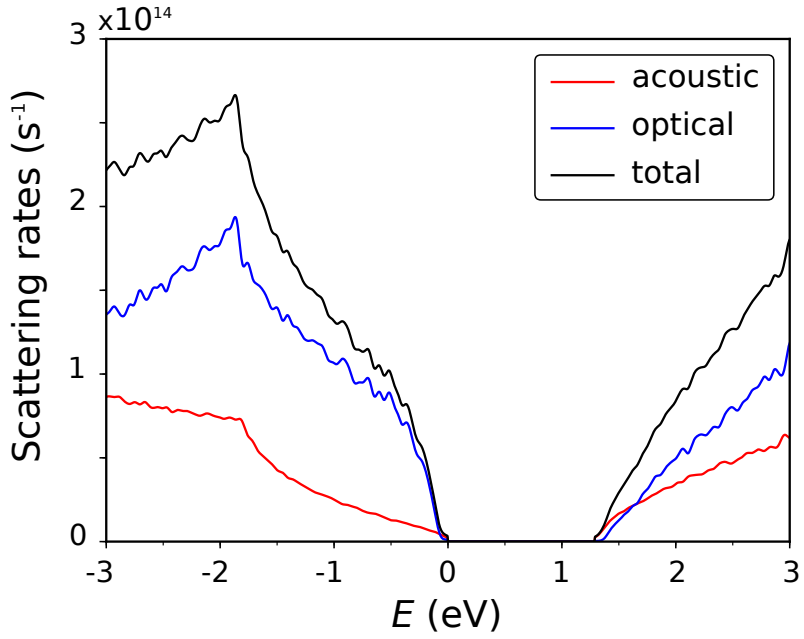

Figure C.1: Scattering rates of BP at temperature of 300 K. The contributions of acoustic and optical phonon-modes are shown as well.

Fig. C.2 presents scattering rate of both CaTe and Li_3Sb as a functions of energy at room temperature (VBMs are set to zeros). The specific contributions of acoustic (the first three modes) and optical (the remaining ones) phonon-modes are also shown. We can see that the optical modes are the main source of scattering in both cases.

We performed convergence tests for G_0W_0 calculations over the number of bands (N_b) and the kinetic energy cut-off for dielectric tensor (E_c). These

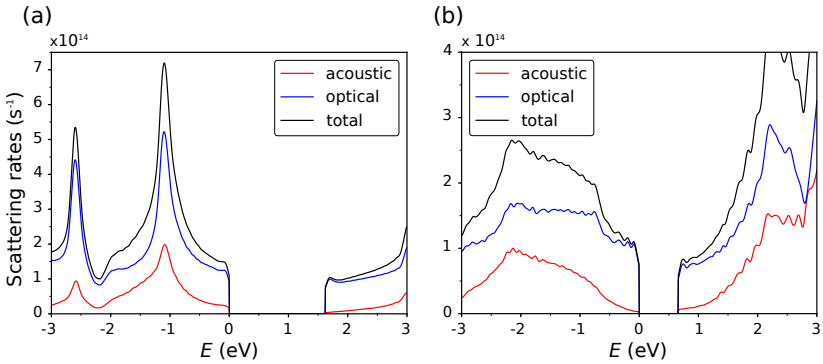

Figure C.2: Scattering rates of (a) CaTe and (b) Li_3Sb at temperature of 300 K. The contributions of acoustic and optical phonon-modes are shown as well.

two parameters will be simultaneously investigated in specific ranges, then we can choose appropriate values those give acceptable convergence of band gap. Fig. C.3 and Tab. C.4 show how band gap at Γ point of BP evolves with the change of N_b and E_c. Here, $N_b = [30, 60, 90, 120]$ and $E_c = [4, 6, 8, 10, 12]$ Ha. In the same way, Fig. C.4 and Tab. C.5 show band gap at Γ point of CaTe with the change of $N_b = [75, 150, 300, 450]$ and $E_c = [6, 8, 10, 12, 14]$. Fig. C.5 and Tab. C.6 present how band gap at Γ point of Li_3Sb converges with the change of number of band and energy cut-off for the dielectric tensor. In the case, $N_b = [80, 160, 240, 320]$ and $E_c = [4, 6, 8, 10, 12]$ Ha.

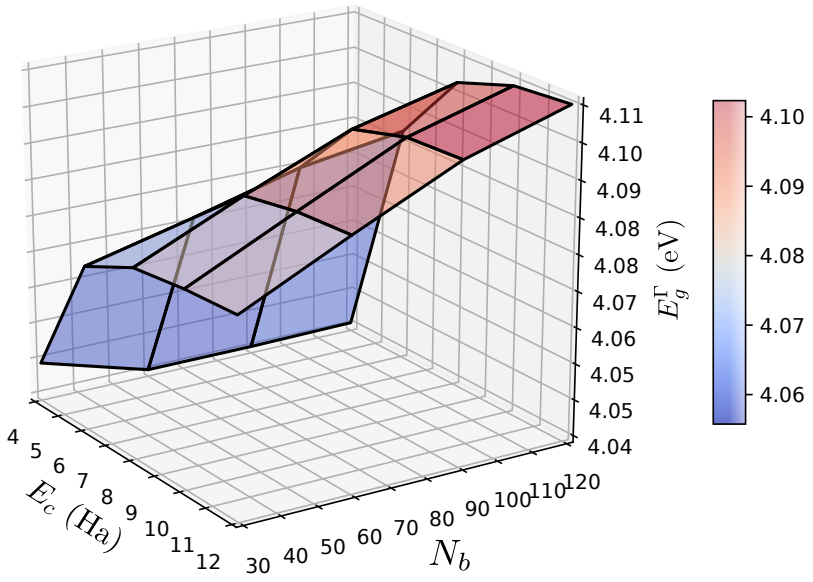

Figure C.3: The convergence test for the gap at Γ point of BP in G_0W_0 computation.

Table C.4: The evolution of the gap at Γ point of BP E_g^Γ (in eV) with the change of number of bands N_b and kinetic energy cut-off for dielectric tensor E_c (in Ha).

N_b	30	30	30	30	30
E_c	4.0	6.0	8.0	10.0	12.0
E_g^Γ	4.04594	4.07201	4.07725	4.07858	4.07917
N_b	60	60	60	60	60
E_c	4.0	6.0	8.0	10.0	12.0
E_g^Γ	4.03933	4.07742	4.08716	4.08918	4.08988
N_b	90	90	90	90	90
E_c	4.0	6.0	8.0	10.0	12.0
E_g^Γ	4.03932	4.08337	4.09629	4.09954	4.10009
N_b	120	120	120	120	120
E_c	4.0	6.0	8.0	10.0	12.0
E_g^Γ	4.03963	4.08678	4.10168	4.10571	4.10674

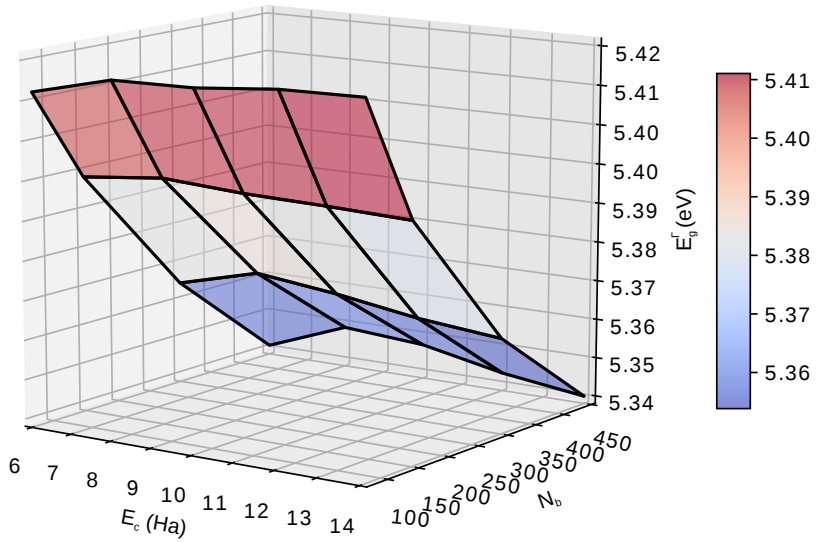

Figure C.4: The convergence test for the gap at Γ point of CaTe in G_0W_0 computation.

Table C.5: The evolution of the gap at Γ point of CaTe E_g^Γ (in eV) with the change of number of bands N_b and kinetic energy cut-off for dielectric tensor E_c (in Ha).

N_b	75	75	75	75	75
E_c	6.0	8.0	10.0	12.0	14.0
E_g^Γ	5.41558	5.42030	5.42063	5.42239	5.42275
N_b	150	150	150	150	150
E_c	6.0	8.0	10.0	12.0	14.0
E_g^Γ	5.39362	5.39570	5.39460	5.39418	5.39352
N_b	300	300	300	300	300
E_c	6.0	8.0	10.0	12.0	14.0
E_g^Γ	5.36266	5.36771	5.36552	5.36260	5.36077
N_b	450	450	450	450	450
E_c	6.0	8.0	10.0	12.0	14.0
E_g^Γ	5.34078	5.34818	5.34680	5.34287	5.34034

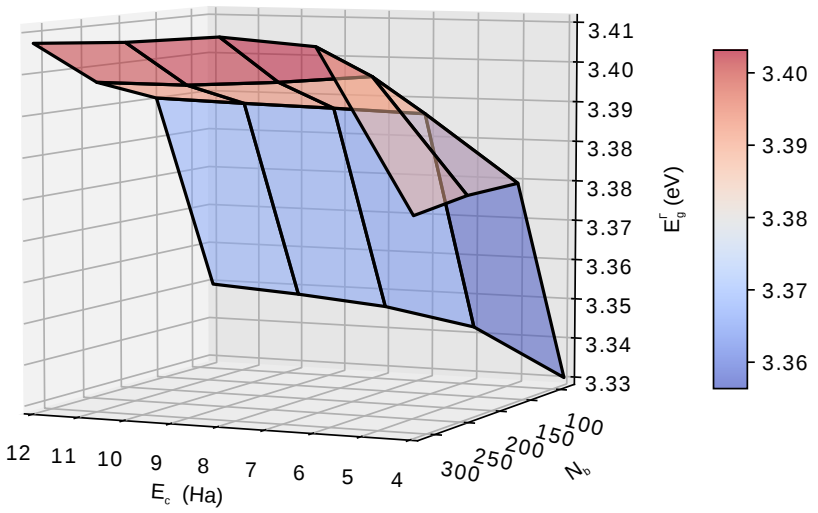

Figure C.5: The convergence test for the gap at Γ point of Li_3Sb in G_0W_0 computation.

Fig. C.8, Fig. C.9, Fig. C.10, Fig. C.11 and Fig. C.12 show defect for-

Table C.6: The evolution of the gap at Γ point of Li_3Sb E_g^Γ (in eV) with the change of number of bands N_b and kinetic energy cut-off for dielectric tensor E_c (in Ha).

N_b	80	80	80	80	80
E_c	4.0	6.0	8.0	10.0	12.0
E_g^Γ	3.33445	3.34410	3.34744	3.34911	3.35034
N_b	160	160	160	160	160
E_c	4.0	6.0	8.0	10.0	12.0
E_g^Γ	3.37762	3.39112	3.39166	3.39208	3.39262
N_b	240	240	240	240	240
E_c	4.0	6.0	8.0	10.0	12.0
E_g^Γ	3.37743	3.40028	3.39860	3.39749	3.39752
N_b	320	320	320	320	320
E_c	4.0	6.0	8.0	10.0	12.0
E_g^Γ	3.37587	3.40757	3.40897	3.40748	3.40683

mation energies and phase diagrams of AlP, $BaLiH_3$, LiH, SrTe and Al_2ZnS_4 (computed by DFT), correspondingly. The facets of phase diagrams in which the chemical potentials of elements were estimated are marked to corresponding defect formation energies. It worth noting that although DFT calculations using GGA underestimate band gap, the defect formation energy computed with it is still reliable [358]. In HSE computations, the VBM shifts down while the CBM shifts up, therefore, the general trend of defect formation energy is similar to that in DFT-GGA computations. The change of formation energy is small as well [358].

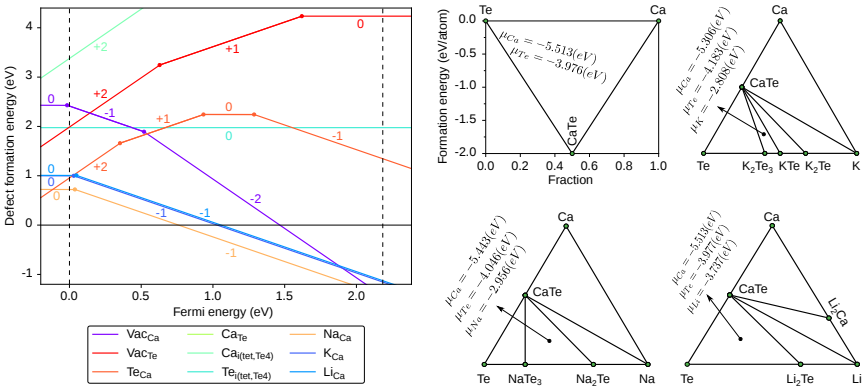

Figure C.6: The defect formation energy as a function of Fermi level of intrinsic and extrinsic defects for CaTe (left) and the phase diagrams with chemical potentials of each element in specific facets (right). The intrinsic defects include vacancies (Vac_{Ca} and Vac_{Te}), anti-sites (Te_{Ca} and Ca_{Te}) and interstitial atoms inserting into the tetrahedral hollows formed by 4 Te atoms ($Ca_{i(tet,Te4)}$ and $Te_{i(tet,Te4)}$) while Na, K and Li are used as the extrinsic defects substituting onto Ca-sites (Na_{Ca}, K_{Ca} and Li_{Ca}). The chemical potential of elements are obtained from phase diagrams of Ca-Te and Ca-Te-X (X=Na, K and Li) for intrinsic and extrinsic defects, respectively. The VBM is set to zero.

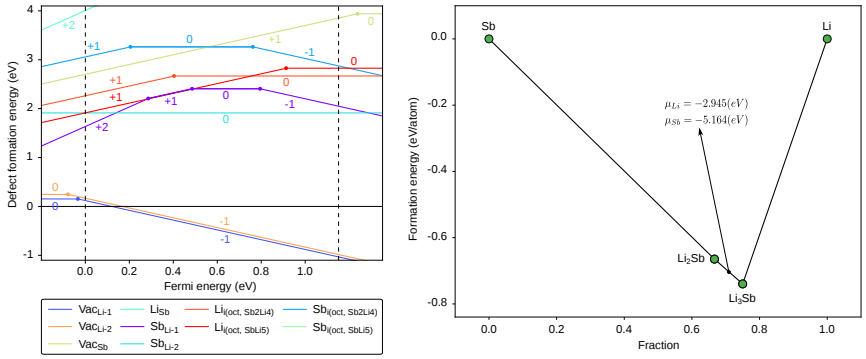

Figure C.7: The defect formation energy as a function of Fermi level of intrinsic defects for Li_3Sb (left) and the phase diagram with chemical potentials of each element in a specific facet (right). The intrinsic defects include vacancies ($Vac_{Li\text{-}1}$, $Vac_{Li\text{-}2}$ and Vac_{Sb}), anti-sites (Li_{Sb}, $Sb_{Li\text{-}1}$ and $Sb_{Li\text{-}2}$) and interstitial atoms inserting into the octahedron hallows formed by Sb and Li atoms ($Li_{i(oct,\ Sb2Li4)}$, $Li_{i(oct,\ SbLi5)}$, $Sb_{i(oct,\ Sb2Li4)}$ and $Sb_{i(oct,\ SbLi5)}$). The chemical potentials of Li and Sb are obtained from their phase diagram. The VBM is set to zero.

Tab. C.7 shows information for different A_3B compounds (A = Li, Na, K, Rb and Cs; and B = N, P, As and Sb). The very unstable compounds are not considered here. The data of compounds with narrow gap $E_g < 0.4\ eV$ is not

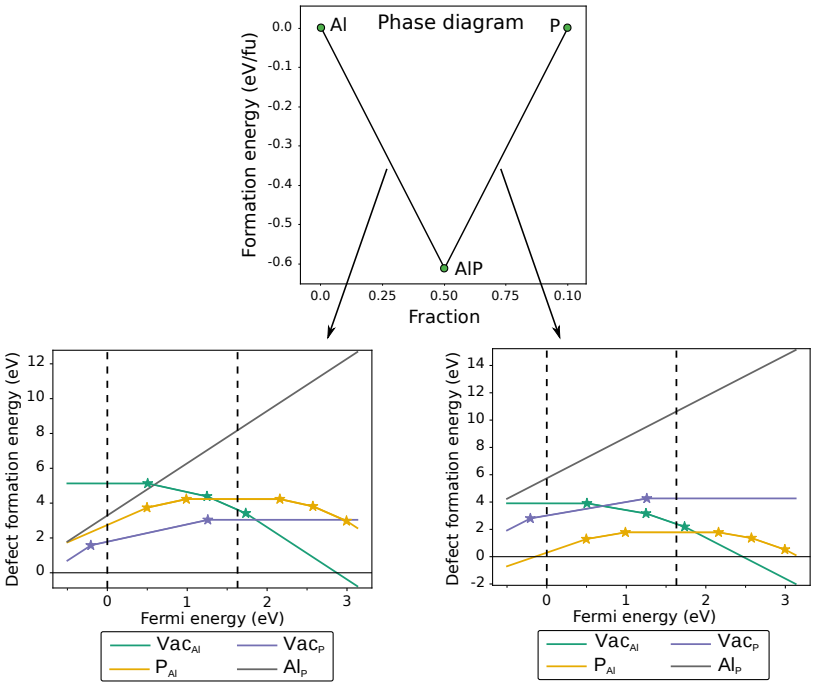

Figure C.8: The phase diagram and defect formation energies of AlP in Al-rich and P-rich conditions.

presented because the values of effective masses are not reliable.

Table C.7: Formula, space group (Spg), Materials Project [208, 209] identification number (MP-id), fundamental E_g computed with DFT (in eV), three principal hole effective masses m_1, m_2 and m_3 (m_o-free electron mass) and stability measured by energy above hull E_{hull} in the phase diagram (in meV/atom).

Formula	Spg	MP-id	E_g	m_1	m_2	m_3	E_{hull}
Li_3N	$P6/mmm$	2251	0.98	1.09	1.09	5.30	0.0
Li_3N	$P6_3/mmc$	2341	1.22	1.60	1.60	3.66	10.0
Li_3P	$P6_3/mmc$	736	0.70	0.84	0.84	2.41	0.0
Li_3As	$P6_3/mmc$	757	0.64	0.74	0.74	2.10	0.0
Li_3Sb	$P6_3/mmc$	7955	0.48	0.61	0.61	1.75	3.0
Li_3Sb	$Fm\bar{3}m$	2074	0.85	**0.24**	**0.24**	**0.24**	0.0
Na_3P	$P6_3/mmc$	1598	0.41	1.61	1.61	6.52	0.0
Na_3Sb	$P6_3/mmc$	7956	0.40	1.10	1.10	3.85	0.0
K_3Sb	$Fm\bar{3}m$	10159	0.68	5.22	5.22	5.22	29.0
Rb_3Sb	$Fm\bar{3}m$	33018	0.43	1.71	1.71	1.71	34.0
Cs_3Sb	$Fm\bar{3}m$	10378	0.61	1.03	1.03	1.03	0.0

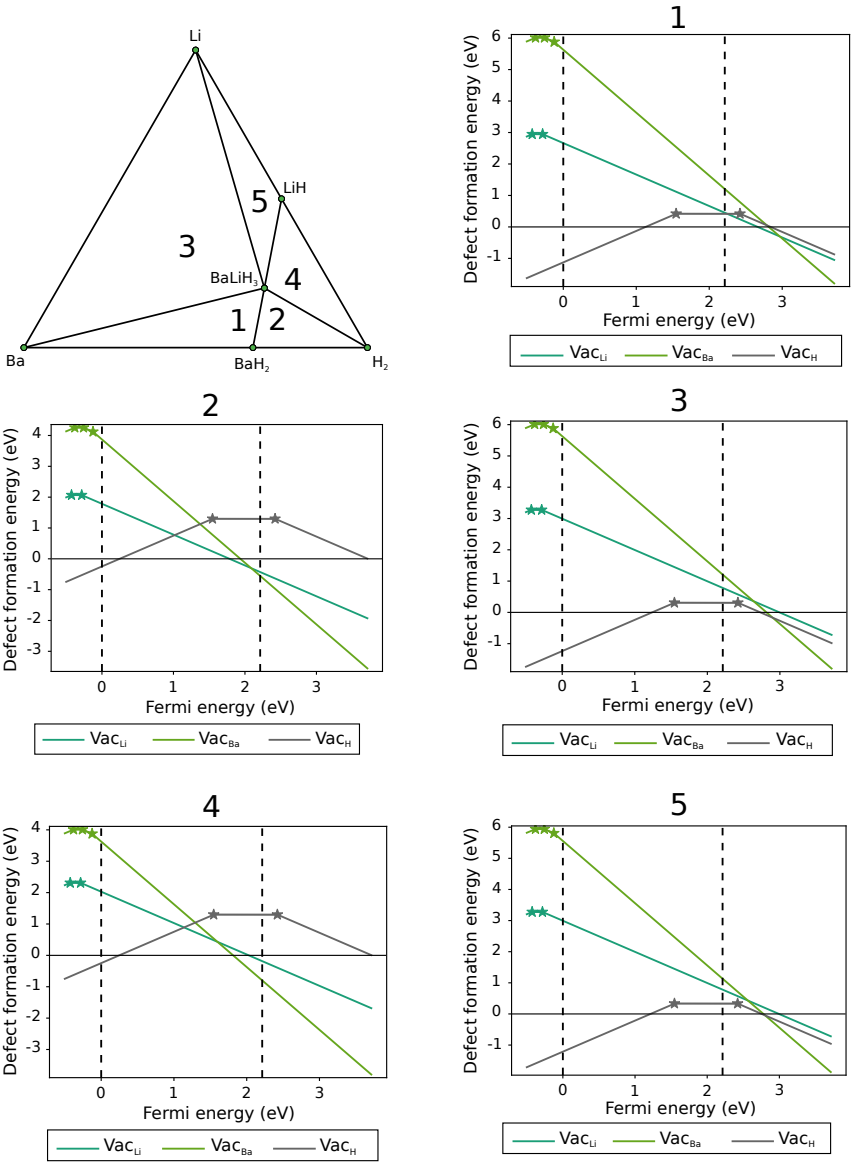

Figure C.9: The phase diagram and defect formation energies of $BaLiH_3$ in different conditions corresponding to the numbers marked in different facets.

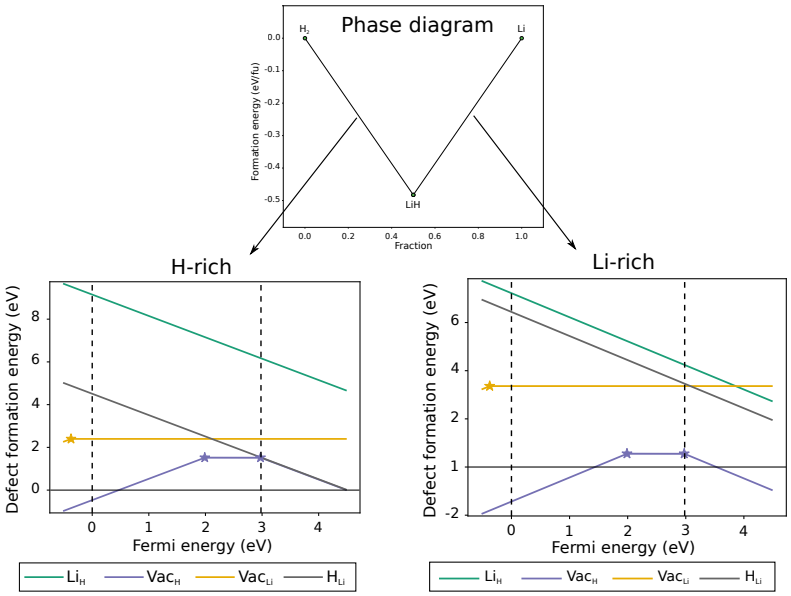

Figure C.10: The phase diagram and defect formation energies of LiH in H-rich and Li-rich conditions.

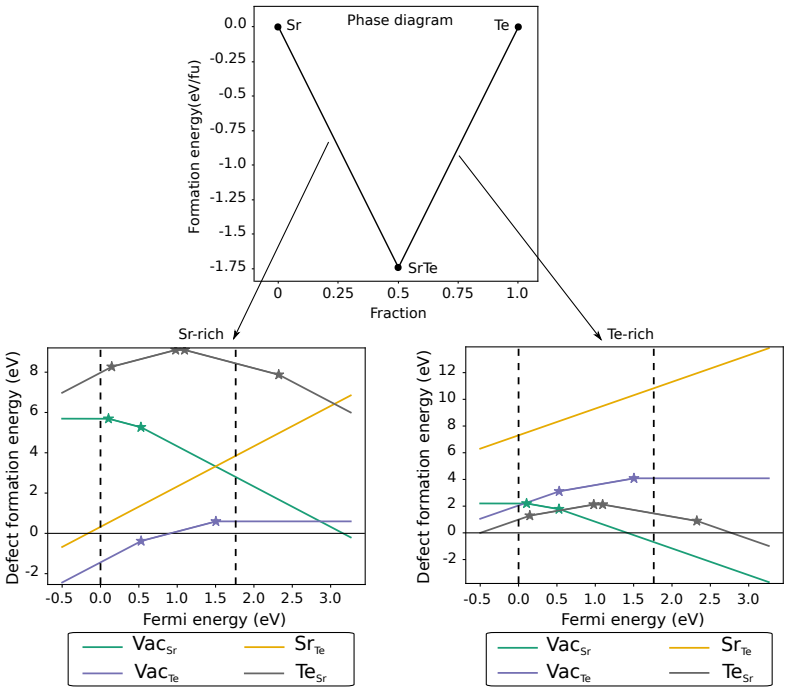

Figure C.11: The phase diagram and defect formation energies of SrTe in Sr-rich and Te-rich conditions.

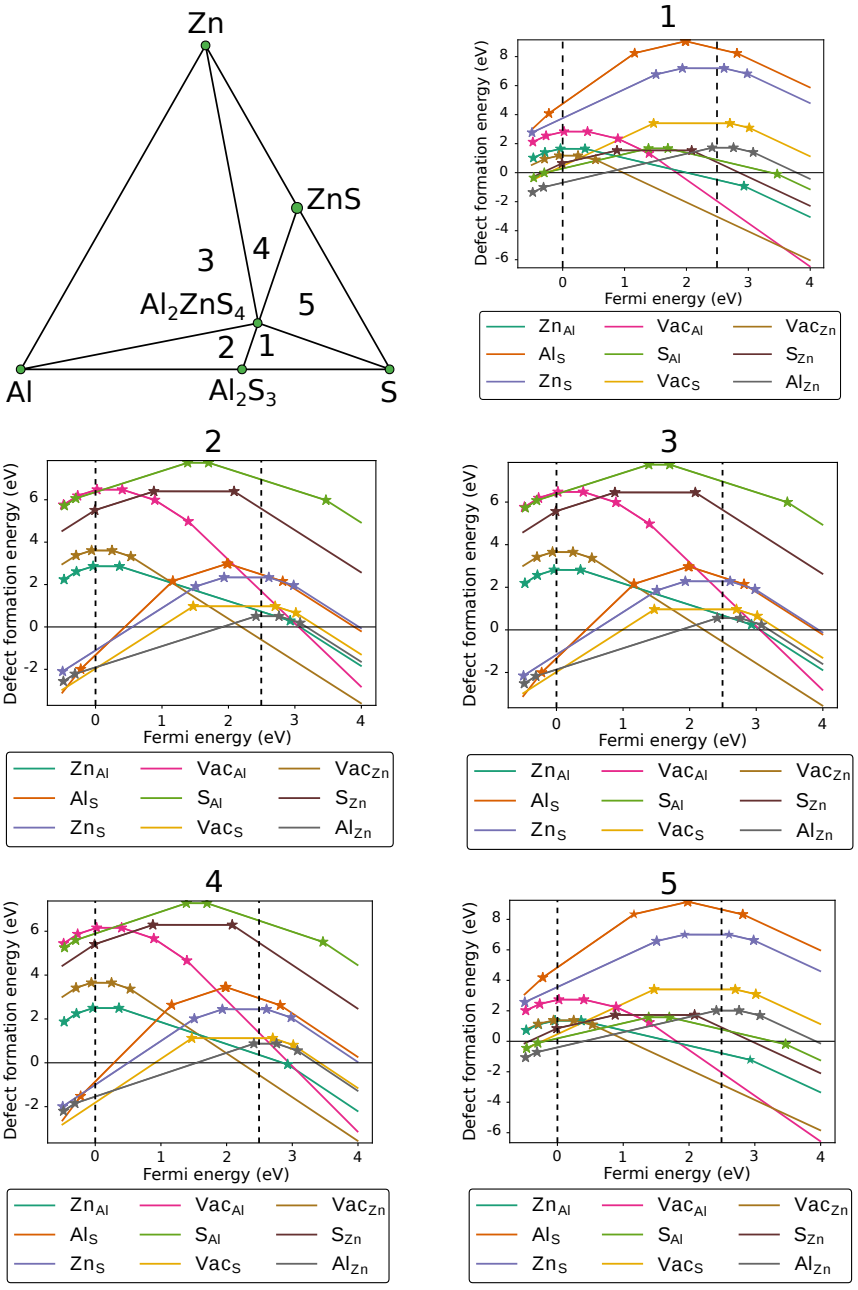

Figure C.12: The phase diagram and defect formation energies of Al_2ZnS_4 in different conditions corresponding to the numbers marked in different facets.

Appendix D

Publications and contributions

Journal articles

7. V.-A. Ha, G. Yu, F. Ricci, D. Dahliah, M. J. van Setten, M. Giantomassi, G.-M. Rignanese, and G. Hautier, 'Computationally-driven high throughput identification of CaTe and Li_3Sb as promising candidates for high mobility p-type transparent conducting materials', Phys. Rev. Materials **3**, 034601 (2019).

6. S. Maier, S. Ohno, G. Yu, S. D. Kang, T. C. Chasapis, V. A. Ha, S. A. Miller, D. Berthebaud, M. G. Kanatzidis, G.-M. Rignaness, G. Hautier, G. J. Snyder, and F. Gascoin, 'Resonant bonding, multiband thermoelectric transport, and native defects in n-type $BaBiTe_{3-x}Se_x$ (x = 0, 0.05, and 0.1)', Chem. Mater. **30**, 174 (2018).

5. V.-A. Ha, F. Ricci, G.-M. Rignanese and G. Hautier, 'Structural design principles for low hole effective mass s-orbital-based p-type oxides', J. Mater. Chem. C **5**, 5772 (2017).

4. J. B. Varley, A. Miglio, V.-A. Ha, M. J. van Setten, G.-M. Rignanese, and G. Hautier, 'High-throughput design of non-oxide p-type transparent conducting materials: data mining, search strategy and identification of boron phosphide', Chem. Mater. **29**, 2568 (2017).

3. Ha V.-A., Nguyen H.-C., Nguyen T., Luong M.-T., Duong X.-N., Nguyen D.-D., Nguyen D.-T.-K., Pham T.-H. and Dao X.-V., 'Understanding ferromagnetism in C-doped CdS: Monte Carlo simulation', J. Alloys Compd. **695**, 1624 (2017).

2. V.-A. Ha, D. Waroquiers, G.-M. Rignanese and G. Hautier, 'Influence of the "second gap" on the transparency of transparent conducting oxides: An

ab initio study', Appl. Phys. Lett. **108**, 201902 (2016).

1. Ha V.-A., Dao X.-V., Nguyen D.-T.-K. and Pham T.-H., 'Monte Carlo study of the room-temperature ferromagnetism in C-doped ZnO', IEEE Trans. Magn. **50**, 2400704 (2014).

Contributed talks

5. 'Computationally-driven high throughput identification of CaTe and Li_3Sb as promising candidates for high mobility *p*-type transparent conducting materials', E-MRS Spring Meeting, Jun. 2018, Strasbourg, France.

4. 'Structural design principles for low hole effective mass *s*-orbital-based *p*-type oxides', TCO 2017 - Transparent Conductive Oxides - Fundamentals and Applications, Sep. 2017, Leipzig, Germany.

3. 'Structural design principles for low hole effective mass *s*-orbital-based *p*-type oxides', E-MRS Spring Meeting, May 2017, Strasbourg, France.

2. 'Influence of the "second gap" on the transparency of transparent conducting oxides: An *ab initio* study', E-MRS Spring Meeting, May 2016, Lille, France.

1. 'Influence of the "second gap" on the transparency of transparent conducting oxides: An *ab initio* study', APS March Meeting, Mar. 2016, Baltimore, Maryland, USA.

Conference poster presentations

5. 'Influence of the "second gap" on the transparency of transparent conducting oxides: An *ab initio* study', Psi-k 2015 Conference, Sep. 2015, Donostia/Sansebastian, Spain.

4. 'Monte Carlo study of the room-temperature ferromagnetism in C-doped CdS', JSPS Core-to-Core Program, Chulalongkorn University, Dec. 2013, Bangkok, Thailand.

3. 'Monte Carlo study of the room-temperature ferromagnetism in C-doped ZnO', the 3^{rd} International Symposium on Frontiers in Materials Science (FMS), Nov. 2013, Hanoi, Vietnam.

2. 'Monte Carlo study of the room-temperature ferromagnetism in C-doped CdS', the 1^{st} International Workshop on Theoretical and Computational

Physics, Jul. 2013, Da Nang City, Vietnam.

1. 'Monte Carlo study of the room-temperature ferromagnetism in C-doped ZnO', the 6^{th} International Workshop on Advanced Materials Science and NanoTechnology, Oct. 2012, Ha Long City, Vietnam.

Conference proceedings

1. Nguyen T.-T., Vuong X.-A., Ha V.-A., Nguyen D.-C., Nguyen H.-L., 'Silicon nanowire fabrication by thermal CVD and sputtering methods', the 3^{rd} International Workshop on Nanotechnology and Application, Nov. 2011, Vung Tau, Vietnam , pp. 576-579.

Acronyms

GW *GW* approximation. 7, 31, 56–61, 68, 117, 118

***G*$_0$*W*$_0$** one-shot *GW* calculation. vi, vii, 31, 60, 66, 68, 69, 73–75, 82, 118, 130–133

BTE Boltzmann Transport Equation. 55, 62, 68, 122, 123

BZ Brillouin Zone. v, 19, 20, 39, 44, 59, 101

CB Conduction Band. 26, 27, 33, 38

CBM Conduction Band Minimum. 2, 15, 16, 38, 48, 66, 116, 134

COHP Crystal Orbital Hamilton Populations. iv, v, 32, 37, 38, 111, 112

COOP Crystal Orbital Overlap Population. 44–49, 51, 111, 112

DFPT Density Functional Perturbation Theory. 21, 62, 69, 77

DFT Density Functional Theory. iv–vi, x, 5, 7, 21, 23, 24, 28, 29, 31, 37, 38, 43–50, 56–60, 63, 64, 66, 68, 69, 72–75, 77, 80, 82, 83, 93–99, 105, 107, 110, 112, 113, 117, 120, 123, 126, 134, 136

DOS Density Of States. vi, 15, 16, 28, 33, 68–72, 75–78, 111, 121

el-ph electron-phonon. 7, 16, 20, 22, 23, 55, 57, 59, 62, 63, 66, 68–70, 77, 78, 80, 120, 121, 123

GGA General Gradient Approximation. 24, 43, 59, 60, 94–96, 134

HF Hartree-Fock. 89, 90, 92, 95, 96, 107

HK Hohenberg-Kohn. 91

HSE Heyd-Scuseria-Ernzherof. ix, 29–31, 33, 58, 60, 62, 64, 73, 74, 81, 82, 96, 117, 127–130, 134

HT High Throughput. vi, 16–19, 23, 24, 41, 42, 46, 55–61, 79, 80, 82, 83, 117

IBZ Irreducible Brillouin Zone. 28

ICSD Inorganic Crystal Structure Database. 18, 42, 43, 49, 58, 59, 82, 83

ICSD-id Inorganic Crystal Structure Database identification number. ix, x, 51, 52, 126, 127

ITO Indium-doped Tin Oxide. iv, 4–7, 12

KS Kohn-Sham. vii, 92–95, 97, 99–101

LCAO Linear Combination of Atomic Orbitals. 45, 98, 110–112

LDA Local Density Approximation. 24, 94–96

MP Materials Project. ix, 31, 43, 58–60

MP-id Materials Project identification number. ix, x, 31, 64–66, 125–130, 136

NC Norm-Conserving. 60, 62

ONCVPSP Optimized Norm-Conservinng Vanderbilt PSeudopotential. 61

PAW Projector Augmented Wave. 31, 43, 104, 105

PBE Perdew-Burke-Ernzerhof. 43, 59–61, 68, 94–96, 127–130

PP PseudoPotentials. 103, 104

PW Plane Waves. 98, 100, 102

RPA Random Phase Approximation. 28, 109

Spg Space group. ix, x, 31, 51, 52, 64–66, 125–130, 136

TCM Transparent Conducting Material. 2, 5–7, 12, 13, 18, 26, 27, 31, 36, 48, 56, 57, 63, 79, 80, 82–84

TCMs Transparent Conducting Materials. iv–vi, ix, 2–4, 6–12, 14–18, 24–27, 30–33, 36–42, 55–60, 74, 79–84, 115

TCO Transparent Conducting Oxide. 42, 44

TCOs Transparent Conducting Oxides. iv, 27, 34, 35, 41–43, 46, 53, 54

VB Valence Band. 26, 27, 40

VBM Valence Band Maximum. 2, 7, 16, 38, 39, 45, 47, 49, 50, 53, 62, 66–70, 74–76, 83, 84, 115, 116, 125–127, 130, 134, 135

XC eXchange-Correlation. 43, 59–61

Bibliography

[1] A. Zunger. "Practical doping principles". In: *Appl. Phys. Lett.* **83** (2003), p. 57. DOI: 10.1063/1.1584074.

[2] K. Ellmer. "Past achievements and future challenges in the development of optically transparent electrodes". In: *Nat. Photonics* **6** (2012), p. 809. DOI: 10.1038/NPHOTON.2012.282.

[3] H. Ohta and H. Hosono. "Transparent oxide optoelectronics". In: *Mater. Today* **7** (2004), p. 42. DOI: 10.1016/S1369-7021(04)00288-3.

[4] M. Grundmann. "Karl Bädeker (1877-1914) and the discovery of transparent conductive materials". In: *Phys. Status Solidi* **212** (2015), p. 1409. DOI: 10.1002/pssa.201431921.

[5] K. Bädeker. "Über die elektrische Leitfähigkeit und die thermoelektrische Kraft einiger Schwermetallverbindungen". In: *Ann. Phys.* **327** (1907), p. 749. DOI: 10.1002/andp.19073270409.

[6] H. A. McMaster. "Conductive coating for glass and method of application". Patent 2429420 (U.S.). 1947.

[7] J. M. Mochel. "Coated resistance". Patent 2564706 (U.S.). 1947.

[8] W. O. Lytle and A. E. Junge. "Electrocondutive products and production thereof". Patent 2566346 (U.S.). 1951.

[9] J. M. Mochel. "Electrically conducting coating on glass and other ceramic bodies". Patent 2564707 (U.S.). 1951.

[10] M. J. Zunick. "Conductive coating on glass". Patent 2516663 (U.S.). 1950.

[11] G. Rupprecht. "Untersuchungen der elektrischen und lichtelektrischen Leitfähigkeit dünner Indiumoxydsehiehten". In: *Z. Phys.* **139** (1954), p. 504. DOI: 10.1007/BF01374559.

[12] R. Groth. "Untersuchungen an halbleitenden Indiumoxydschichten". In: *Phys. Status Solidi* **14** (1966), p. 69. DOI: 10.1002/pssb.19660140104.

[13] T. Hada. "Structures and electrical properties of zinc oxide films prepared by low pressure sputtering system". In: *Thin Solid Films* **7** (1971), p. 135. DOI: 10.1016/0040-6090(71)90032-0.

[14] T. Minami, H. Nanto, and S. Takata. "Highly conductive and transparent zinc oxide films prepared by rf magnetron sputtering under an applied external magnetic field". In: *Appl. Phys. Lett.* **41** (1982), p. 958. DOI: 10.1063/1.93355.

[15] C. W. Litton, D. C. Reynolds, and T. C. Collins. "Zinc oxide materials for electronic and optoelectronic device applications". In: Chichester, UK: Wiley, 2011. ISBN: 978-0470519714.

[16] "Transparent conductive zinc oxide: Basics and applications in thin film solar cells". In: ed. by K. Ellmer, A. Klein, and B. Rech. Berlin, Germany: Springer, 2008. ISBN: 978-3540736110.

[17] S. C. Dixon, D. O. Scanlon, C. J. Carmalt, and I. P. Parkin. "*n*-type doped transparent conducting binary oxides: an overview". In: *J. Mater. Chem. C* **4** (2016), p. 6946. DOI: 10.1039/c6tc01881e.

[18] H. Kawazoe, M. Yasukawa, H. Hyodo, M. Kurita, H. Yanagi, and H. Hosono. "*P*-type electrical conduction in transparent thin films of $CuAlO_2$". In: *Nature* **389** (1997), p. 939. DOI: 10.1038/40087.

[19] K. H. L. Zhang, K. Xi, M. G. Blamire, and R. G. Egdell. "*P*-type transparent conducting oxides". In: *J. Phys.: Condens. Matter* **28** (2016), p. 383002. DOI: 10.1088/0953-8984/28/38/383002.

[20] H. Yanagi, S. Inoue, K. Ueda, H. Kawazoe, H. Hosono, and N. Hamada. "Electronic structure and optoelectronic properties of transparent *p*-type conducting $CuAlO_2$". In: *J. Appl. Phys.* **88** (2000), p. 4159. DOI: 10.1063/1.1308103.

[21] R. Nagarajan, A. D. Draeseke, A. W. Sleight, and J. Tate. "*p*-type conductivity in $CuCr_{1-x}Mg_xO_2$ films and powders". In: *J. Appl. Phys.* **89** (2001), p. 8022. DOI: 10.1063/1.1372636.

[22] T. Arnold et al. "X-ray spectroscopic study of the electronic structure of $CuCrO_2$". In: *Phys. Rev. B* **79** (2009), p. 075102. DOI: 10.1103/PhysRevB.79.075102.

[23] H. Yanagi, T. Hase, S. Ibuki, K. Ueda, and H. Hosono. "Bipolarity in electrical conduction of transparent oxide semiconductor $CuInO_2$ with delafossite structure". In: *Appl. Phys. Lett.* **78** (2001), p. 1583. DOI: 10.1063/1.1355673.

[24] H. Yanagi, K. Ueda, H. Ohta, M. Orita, M. Hirano, and H. Hosono. "Fabrication of all oxide transparent *p*-*n* homojunction using bipolar $CuInO_2$ semiconducting oxide with delafossite structure". In: *Solid State Commun.* **121** (2002), p. 15. DOI: 10.1016/S0038-1098(01)00439-2.

[25] C. W. Teplin, T. Kaydanova, D. L. Young, J. D. Perkins, D. S. Ginley, A. Ode, and D. W. Readey. "A simple method for the preparation of transparent *p*-type Ca-doped $CuInO_2$ films: Pulsed-laser deposition from air-sintered Ca-doped $Cu_2In_2O_5$ targets". In: *Appl. Phys. Lett.* **85** (2004), p. 3789. DOI: 10.1063/1.1808498.

[26] N. Duan, A. W. Sleight, M. K. Jayaraj, and J. Tate. "Transparent *p*-type conducting $CuScO_{2+x}$ films". In: *Appl. Phys. Lett.* **77** (2000), p. 1325. DOI: 10.1063/1.1289906.

[27] M. K. Jayaraj, A. D. Draeseke, J. Tate, and A.W. Sleight. "*p*-type transparent thin films of $CuY_{1-x}Ca_xO_2$". In: *Thin Solid Films* **397** (2001), p. 244. DOI: 10.1016/S0040-6090(01)01362-1.

[28] K. Ueda, T. Hase, H. Yanagi, H. Kawazoe, H. Hosono, H. Ohta, M. Orita, and M. Hirano. "Epitaxial growth of transparent *p*-type conducting $CuGaO_2$ thin films on sapphire (001) substrates by pulsed laser deposition". In: *J. Appl. Phys.* **89** (2001), p. 1790. DOI: 10.1063/1.1337587.

[29] A. Kudo, H. Yanagi, H. Hosono, and H. Kawazoe. "$SrCu_2O_2$: A *p*-type conductive oxide with wide band gap". In: *Appl. Phys. Lett.* **73** (1998), p. 220. DOI: 10.1063/1.121761.

[30] H. Ohta, M. Orita, M. Hirano, I. Yagi, K. Ueda, and H. Hosono. "Electronic structure and optical properties of $SrCu_2O_2$". In: *J. Appl. Phys.* **91** (2002), p. 3074. DOI: 10.1063/1.1445498.

[31] K. Ueda, S. Inoue, S. Hirose, H. Kawazoe, and H. Hosono. "Transparent *p*-type semiconductor: LaCuOS layered oxysulfide". In: *Appl. Phys. Lett.* **77** (2000), p. 2701. DOI: 10.1063/1.1319507.

[32] K. Ueda, S. Inoue, H. Hosono, N. Sarukura, and M. Hirano. "Room-temperature excitons in wide-gap layered-oxysulfide semiconductor: LaCuOS". In: *Appl. Phys. Lett.* **78** (2001), p. 2333. DOI: 10.1063/1.1364656.

[33] H. Hiramatsu, K. Ueda, H. Ohta, M. Hirano, T. Kamiya, and H. Hosono. "Degenerate *p*-type conductivity in wide-gap $LaCuOS_{1-x}Se_x$ (x=0-1) epitaxial films". In: *Appl. Phys. Lett.* **82** (2003), p. 1048. DOI: 10.1063/1.1544643.

[34] J. Tate, P. F. Newhouse, R. Kykyneshi, P. A. Hersh, J. Kinney, D. H. McIntyre, and D. A. Keszler. "Chalcogen-based transparent conductors". In: *Thin Solid Films* **516** (2008), p. 5795. DOI: 10.1016/j.tsf.2007.10.073.

[35] A. Zakutayev, D. H. McIntyre, G. Schneider, R. Kykyneshi, D. A. Keszler, C.-H. Park, and J. Tate. "Tunable properties of wide-band gap *p*-type $BaCu(Ch_{1-x}Ch'_x)F$ (Ch = S,Se,Te) thin-film solid solutions". In: *Thin Solid Films* **518** (2010), p. 5494. DOI: 10.1016/j.tsf.2010.04.027.

[36] A. Zakutayev, J. Tate, and G. Schneider. "Defect physics of BaCuChF (Ch=S, Se, Te) *p*-type transparent conductors". In: *Phys. Rev. B* **82** (2010), p. 195204. DOI: 10.1103/PhysRevB.82.195204.

[37] M.-L. Liu, L.-B. Wu, F.-Q. Huang, L.-D. Chen, and I.-W. Chen. "A promising *p*-type transparent conducting material: Layered oxysulfide $[Cu_2S_2][Sr_3Sc_2O_5]$". In: *J. Appl. Phys.* **102** (2007), p. 1 16108. DOI: 10.1063/1.2817643.

[38] M. Dekkers, G. Rijnders, and D. H. A. Blank. "$ZnIr_2O_4$, a *p*-type transparent oxide semiconductor in the class of spinel zinc-d^6-transition metal oxide". In: *Appl. Phys. Lett.* **90** (2007), p. 021903. DOI: 10.1063/1.2431548.

[39] E. Arca, K. Fleischer, and I. V. Shvets. "Magnesium, nitrogen codoped Cr_2O_3: A *p*-type transparent conducting oxide". In: *Appl. Phys. Lett.* **99** (2011), p. 111910. DOI: 10.1063/1.3638461.

[40] H. Peng et al. "Li-doped Cr_2MnO_4: A new *p*-type transparent conducting oxide by computational materials design". In: *Adv. Funct. Mater.* **23** (2013), p. 5267. DOI: 10.1002/adfm.201300807.

[41] A. R. Nagaraja, K. H. Stone, M. F. Toney, H. Peng, S. Lany, and T. O. Mason. "Experimental characterization of a theoretically designed candidate *p*-type transparent conducting oxide: Li-doped Cr_2MnO_4". In: *Chem. Mater.* **26** (2014), p. 4598. DOI: 10.1021/cm501974t.

[42] K. H. L. Zhang, Y. Du, A. Papadogianni, O. Bierwagen, S. Sallis, L. F. J. Piper, M. E. Bowden, V. Shutthanandan, P. V. Sushko, and S. A. Chambers. "Perovskite Sr-doped $LaCrO_3$ as a new *p*-type transparent conducting oxide". In: *Adv. Mater.* **27** (2015), p. 5191. DOI: 10.1002/adma.201501959.

[43] Y. Ogo, H. Hiramatsu, K. Nomura, H. Yanagi, T. Kamiya, M. Hirano, and H. Hosono. "p-channel thin-film transistor using p-type oxide semiconductor, SnO". In: *Appl. Phys. Lett.* **93** (2008), p. 032113. DOI: 10.1063/1.2964197.

[44] H. Yabuta, N. Kaji, R. Hayashi, H. Kumomi, K. Nomura, T. Kamiya, M. Hirano, and H. Hosono. "Sputtering formation of p-type SnO thin-film transistors on glass toward oxide complimentary circuits". In: *Appl. Phys. Lett.* **97** (2010), p. 072111. DOI: 10.1063/1.3478213.

[45] G. Hautier, A. Miglio, G. Ceder, G.-M. Rignanese, and X. Gonze. "Identification and design principles of low hole effective mass p-type transparent conducting oxides". In: *Nat. Commun.* **4** (2013), p. 2292. DOI: 10.1038/ncomms3292.

[46] J. B. Varley, V. Lordi, A. Miglio, and G. Hautier. "Electronic structure and defect properties of B_6O from hybrid functional and many-body perturbation theory calculations: A possible ambipolar transparent conductor". In: *Phys. Rev. B* **90** (2014), p. 045205. DOI: 10.1103/PhysRevB.90.045205.

[47] A. Bhatia et al. "High-mobility Bismuth-based transparent p-type oxide from high-throughput material screening". In: *Chem. Mater.* **28** (2016), p. 30. DOI: 10.1021/acs.chemmater.5b03794.

[48] "Transparent electronics: From synthesis to applications". In: ed. by A. Facchetti and T. J. Marks. Chichester, UK: Wiley, 2010. ISBN: 978-0470990773.

[49] "Handbook of transparent conductors". In: ed. by D. S. Ginley, H. Hosono, and D. C. Paine. NY, USA: Springer, 2010. ISBN: 978-1441916372.

[50] C. Kittel. "Introduction to solid state physics". In: 8^{th}. Hoboken, NJ, USA: Wiley, 2005. ISBN: 978-0471415268.

[51] A. McEvoy, L. Castaner, and T. Markvart. "Solar cells: Materials, manufacture and operation". In: 2^{nd}. Oxford, UK: Elsevier, 2012. Chap. IA-1. ISBN: 978-0123869647.

[52] B. Comiskey, J. D. Albert, H. Yoshizawa, and J. Jacobson. "An electrophoretic ink for all-printed reflective electronic displays". In: *Nature* **394** (1998), p. 253. DOI: 10.1038/28349.

[53] R. Singh. *Transparent Conductive Films Market is Expected to Reach $ 5.86 Billion, Globally, by 2020.* 2014.

[54] J. F. Wager, D. A. Keszler, and R. E. Presley. "Transparent electronics". In: NY, USA: Springer, 2008. ISBN: 978-0387723419.

[55] P. Barquinha, R. Martins, L. Pereira, and E. Fortunato. "Transparent oxide electronics: From materials to devices". In: Chichester, UK: Wiley, 2012. ISBN: 978-0470683736.

[56] M. Orita, H. Ohta, M. Hirano, S. Narushima, and H. Hosono. "Amorphous transparent conductive oxide $InGa_{03}(ZnO)_m$, (m < 4): a Zn 4*s* conductor". In: *Philos. Mag. B* **81** (2001), p. 501. DOI: 10.1080/13642810110045923.

[57] N. L. Dehuff, E. S. Kettenring, D. Hong, H. Q. Chiang, J. F. Wager, R. L. Hoffman, C.-H. Park, and D. A. Keszler. "Transparent thin-film transistors with zinc indium oxide channel layer". In: *J. Appl. Phys.* **97** (2005), p. 064505. DOI: 10.1063/1.1862767.

[58] H. Q. Chiang, J. F. Wager, R. L. Hoffman, J. Jeong, and D. A. Keszler. "High mobility transparent thin-film transistors with amorphous zinc tin oxide channel layer". In: *Appl. Phys. Lett.* **86** (2005), p. 013503. DOI: 10.1063/1.1843286.

[59] A. J. Leenheer, J. D. Perkins, M. F. A. M. van Hest, J. J. Berry, R. P. O'Hayre, and D. S. Ginley. "General mobility and carrier concentration relationship in transparent amorphous indium zinc oxide films". In: *Phys. Rev. B* **77** (2008), p. 115215. DOI: 10.1103/PhysRevB.77.115215.

[60] S.-J. Seo, C. G. Choi, Y. H. Hwang, and B.-S. Bae. "High performance solution-processed amorphous zinc tin oxide thin film transistor". In: *J. Phys. D: Appl. Phys.* **42** (2009), p. 035106. DOI: 10.1088/0022-3727/42/3/035106.

[61] M. K. Jayaraj, K. J. Saji, K. Nomura, T. Kamiya, and H. Hosono. "Optical and electrical properties of amorphous zinc tin oxide thin films examined for thin film transistor application". In: *J. Vac. Sci. Technol. B* **26** (2008), p. 495. DOI: 10.1116/1.2839860.

[62] J. R. Bellingham, W. A. Phillips, and C. J. Adkins. "Electrical and optical properties of amorphous indium oxide". In: *J. Phys.: Condens. Matter* **2** (1990), p. 6207. DOI: 10.1088/0953-8984/2/28/011.

[63] K. Nomura, H. Ohta, K. Ueda, T. Kamiya, M. Hirano, and H. Hosono. "Thin-film transistor fabricated in single-crystalline transparent oxide semiconductor". In: *Science* **300** (2003), p. 1269. DOI: 10.1126/science.1083212.

[64] E. Fortunato, P. Barquinha, and R. Martins. "Oxide semiconductor thin-film transistors: A review of recent advances". In: *Adv. Mater.* **24** (2012), p. 2945. DOI: 10.1002/adma.201103228.

[65] X. Yu, T. J. Marks, and A. Facchetti. "Metal oxides for optoelectronic applications". In: *Nat. Mater.* **15** (2016), p. 383. DOI: 10.1038/NMAT4599.

[66] D. B. Buchholz, Q. Ma, D. Alducin, A. Ponce, M. Jose-Yacaman, R. Khanal, J. E. Medvedeva, and R. P. H. Chang. "The structure and properties of amorphous Indium oxide". In: *Chem. Mater.* **26** (2014), p. 5401. DOI: 10.1021/cm502689x.

[67] R. Khanal, D. B. Buchholz, R. P. H. Chang, and J. E. Medvedeva. "Composition-dependent structural and transport properties of amorphous transparent conducting oxides". In: *Phys. Rev. B* **91** (2015), p. 205203. DOI: 10.1103/PhysRevB.91.205203.

[68] J. E. Medvedeva, D. B. Buchholz, and R. P. H. Chang. "Recent advances in understanding the structure and properties of amorphous oxide semiconductors". In: *Adv. Electron. Mater.* **3** (2017), p. 1700082. DOI: 10.1002/aelm.201700082.

[69] M. Grundmann, F.-L. Schein, M. Lorenz, T. Böntgen, J. Lenzner, and H. von Wenckstern. "Cuprous iodide: A *p*-type transparent semiconductor, history, and novel applications". In: *Phys. Status Solidi A* **210** (2013), p. 1671. DOI: 10.1002/pssa.201329349.

[70] Y. Kokubun, H. Watanabe, and M. Wada. "Electrical Properties of CuI Thin Films". In: *Jpn. J. Appl. Phys.* **10** (1971), p. 864. DOI: 10.1143/jjap.10.864.

[71] D. Chen, Y. Wang, Z. Lin, J. Huang, X. Chen, D. Pan, and F. Huang. "Growth strategy and physical properties of the high mobility *p*-type CuI Crystal". In: *Cryst. Growth Des.* **10** (2010), p. 2057. DOI: 10.1021/cg100270d.

[72] M. Zi, J. Li, Z. Zhang, X. Wang, J. Han, X. Yang, Z. Qiu, H. Gong, Z. Ji, and B. Cao. "Effect of deposition temperature on transparent conductive properties of γ-CuI film prepared by vacuum thermal evaporation". In: *Phys. Status Solidi A* **212** (2015), p. 1466. DOI: 10.1002/pssa.201532015.

[73] N. Yamada, R. Ino, and Y. Ninomiya. "Truly transparent *p*-type γ-CuI thin films with high hole mobility". In: *Chem. Mater.* **28** (2016), p. 4971. DOI: 10.1021/acs.chemmater.6b01358.

[74] C. H. Cheng, J. Wang, G. T. Du, S. H. Shi, Z. J. Du, Z. Q. Fan, J. M. Bian, and M. S. Wang. "Organic solar cells with remarkable enhanced efficiency by using a CuI buffer to control the molecular orientation and modify the anode". In: *Appl. Phys. Lett.* **97** (2010), p. 083305. DOI: 10.1063/1.3483159.

[75] F.-L. Schein, H. von Wenckstern, and M. Grundmann. "Transparent p-CuI/n-ZnO heterojunction diodes". In: *Appl. Phys. Lett.* **102** (2013), p. 092109. DOI: 10.1063/1.4794532.

[76] M. Sun, J. Hu, C. Zhai, M. Zhu, and J. Pan. "CuI as hole-transport channel for enhancing photoelectrocatalytic activity by constructing CuI/BiOI heterojunction". In: *ACS Appl. Mater. Interfaces* **9** (2017), p. 13223. DOI: 10.1021/acsami.7b01840.

[77] T. Akashi, T. Itoh, I. Gunjishima, H. Masumoto, and T. Goto. "Thermoelectric properties of hot-pressed boron suboxide B_6O". In: *Mater. Trans.* **43** (2002), p. 1719. DOI: 10.2320/matertrans.43.1719.

[78] R.-S. Yu, S.-C. Liang, C.-J. Lu, D.-C. Tasi, and F.-S. Shieu. "Characterization and optoelectronic properties of p-type N-doped $CuAlO_2$ films". In: *Appl. Phys. Lett.* **90** (2007), p. 191117. DOI: 10.1063/1.2679233.

[79] J. Tate, H. L. Ju, J. C. Moon, A. Zakutayev, A. P. Richard, J. Russell, and D. H. McIntyre. "Origin of p-type conduction in single-crystal $CuAlO_2$". In: *Phys. Rev. B* **80** (2009), p. 165206. DOI: 10.1103/PhysRevB.80.165206.

[80] S. Mahapatra and S. A. Shivashankar. "Low-pressure metal-organic chemical vapor deposition of transparent and p-type conducting $CuCrO_2$ thin films with high conductivity". In: *Chem. Vap. Deposition* **9** (2003), p. 238. DOI: 10.1002/cvde.200304147.

[81] G. Dong, M. Zhang, X. Zhao, H. Yan, C. Tian, and Y. Ren. "Improving the electrical conductivity of $CuCrO_2$ thin film by N doping". In: *Appl. Surf. Sci.* **256** (2010), p. 4121. DOI: 10.1016/j.apsusc.2010.01.094.

[82] R.-S. Yu and C.-M. Wu. "Characteristics of p-type transparent conductive $CuCrO_2$ thin films". In: *Appl. Surf. Sci.* **282** (2013), p. 92. DOI: 10.1016/j.apsusc.2013.05.061.

[83] A. Barnabé, Y. Thimont, M. Lalanne, L. Presmanes, and P. Tailhades. "p-type conducting transparent characteristics of delafossite Mg-doped $CuCrO_2$ thin films prepared by RF-sputtering". In: *J. Mater. Chem. C* **3** (2015), p. 6012. DOI: 10.1039/C5TC01070E.

[84] L. Farrell, K. Fleischer, D. Caffrey, D. Mullarkey, E. Norton, and I. V. Shvets. "Conducting mechanism in the epitaxial p-type transparent conducting oxide Cr_2O_3:Mg". In: *Phys. Rev. B* **91** (2015), p. 125202. DOI: 10.1103/physrevb.91.125202.

[85] D. Muñoz-Rojas, M. Jordan, C. Yeoh, A. T. Marin, A. Kursumovic, L. A. Dunlop, D. C. Iza, A. Chen, H. Wang, and J. L. M. Driscoll. "Growth of 5 cm^2/Vs mobility, p-type Copper(I) oxide (Cu_2O) films by fast atmospheric atomic layer deposition (AALD) at 225°C and below". In: *AIP Adv.* **2** (2012), p. 042179. DOI: 10.1063/1.4771681.

[86] B. Yang, Y. He, A. Polity, and B. K. Meyer. "Structural, optical and electrical properties of transparent conducting $CuInO_2$ thin films prepared by RF sputtering". In: *Mater. Res. Soc. Symp. Proc.* **865** (2005), F14.7. DOI: 10.1557/PROC-865-F14.7.

[87] B. J. Ingram, B. J. Harder, N. W. Hrabe, T. O. Mason, and K. R. Poeppelmeier. "Transport and defect mechanisms in cuprous delafossites. 2. $CuScO_2$ and $CuYO_2$". In: *Chem. Mater.* **16** (2004), p. 5623. DOI: 10.1021/cm048982k.

[88] Y. Kakehi, K. Satoh, T. Yoshimura, A. Ashida, and N. Fujimura. "Effects of Mg doping on structural, optical, and electrical properties of $CuScO_2$ (0001) epitaxial films". In: *Vacuum* **84** (2010), p. 618. DOI: 10.1016/j.vacuum.2009.06.023.

[89] Y. Kakehi, K. Satoh, T. Yoshimura, A. Ashida, and N. Fujimura. "Control of carrier concentration of p-type transparent conducting $CuScO_2$ (0001) epitaxial films". In: *Thin Solid Films* **518** (2010), p. 3097. DOI: 10.1016/j.tsf.2009.07.204.

[90] R. L. Hoffman, J. F. Wager, M. K. Jayaraj, and J. Tate. "Electrical characterization of transparent $p-i-n$ heterojunction diodes". In: *J. Appl. Phys.* **90** (2001), p. 5763. DOI: 10.1063/1.1413710.

[91] T. Mine, H. Yanagi, K. Nomura, T. Kamiya, M. Hirano, and H. Hosono. "Control of carrier concentration and surface flattening of $CuGaO_2$ epitaxial films for a p-channel transparent transistor". In: *Thin Solid Films* **516** (2008), p. 5790. DOI: 10.1016/j.tsf.2007.10.072.

[92] C.-Y. Tsay and C.-L. Chen. "Improved electrical properties of p-type $CuGaO_2$ semiconductor thin films through Mg and Zn doping". In: *Ceram. Int.* **43** (2017), p. 2563. DOI: 10.1016/j.ceramint.2016.11.059.

[93] S. Sheng, G. Fang, C. Li, Z. Chen, S. Ma, L. Fang, and X. Zhao. "Oriented growth of p-type transparent conducting Ca-doped $SrCu_2O_2$ thin films by pulsed laser deposition". In: *Semicond. Sci. Technol.* **21** (2006), p. 586. DOI: 10.1088/0268-1242/21/5/002.

[94] E. L. Papadopoulou, Z. A. Viskadourakis, A. V. Pennos, G. Huyberechts, and E. Aperathitis. "The effect of deposition parameters on the properties of $SrCu_2O_2$ films fabricated by pulsed laser deposition". In: *Thin Solid Films* **516** (2008), p. 1449. DOI: 10.1016/j.tsf.2007.03.085.

[95] N. Mansourian-Hadavi, S. Wansom, N. H. Perry, A. R. Nagaraja, T. O. Mason, L.-H. Ye, and A. J. Freeman. "Transport and band structure studies of crystalline $ZnRh_2O_4$". In: *Phys. Rev. B* **81** (2010), p. 075112. DOI: 10.1103/PhysRevB.81.075112.

[96] H. J. Kim, I. C. Song, J. H. Sim, H. Kim, D. Kim, Y. E. Ihm, and W. K. Choo. "Structural and transport properties of cubic spinel $ZnCo_2O_4$ thin films grown by reactive magnetron sputtering". In: *Solid State Commun.* **129** (2004), p. 627. DOI: 10.1016/j.ssc.2003.12.025.

[97] H. Hiramatsu, K. Ueda, H. Ohta, M. Hirano, and H. Hosono. "Heteroepitaxial growth of a wide gap *p*-type oxysulfide, LaCuOS". In: *Mat. Res. Soc. Symp. Proc.* **747** (2003), V6.9. DOI: 10.1557/PROC-747-V6.9.

[98] H. Hiramatsu, K. Ueda, H. Ohta, M. Hirano, T. Kamiya, and H. Hosono. "Degenerate *p*-type conductivity in wide-gap $LaCuOS_{1-x}Se_x$ (x=0-1) epitaxial films". In: *Appl. Phys. Lett.* **82** (2003), p. 1048. DOI: 10.1063/1.1544643.

[99] T. Kamiya, K. Ueda, H. Hiramatsu, H. Kamioka, H. Ohta, M. Hirano, and H. Hosono. "Two-dimensional electronic structure and multiple excitonic states in layered oxychalcogenide semiconductors, LaCuOCh (Ch=S, Se, Te): Optical properties and relativistic *ab initio* study". In: *Thin Solid Films* **486** (2005), p. 98. DOI: 10.1016/j.tsf.2004.11.235.

[100] E. Fortunato, R. Barros, P. Barquinha, V. Figueiredo, S. H. K. Park, C. S. Hwang, and R. Martins. "Transparent *p*-type SnO_x thin film transistors produced by reactive rf magnetron sputtering followed by low temperature annealing". In: *Appl. Phys. Lett.* **97** (2010), p. 052105. DOI: 10.1063/1.3469939.

[101] W. Guo, L. Fu, Y. Zhang, K. Zhang, L. Y. Liang, Z. M. Liu, H. T. Cao, and X. Q. Pan. "Microstructure, optical, and electrical properties of *p*-type SnO thin films". In: *Appl. Phys. Lett.* **96** (2010), p. 042113. DOI: 10.1063/1.3277153.

[102] P.-C. Hsu, C.-C. Wu, H. Hiramatsu, T. Kamiya, and H. Hosono. "Film texture, hole transport and field-effect mobility in polycrystalline SnO thin films on glass". In: *ECS J. Solid State Sci. Technol.* **3** (2014), p. 3040. DOI: 10.1149/2.009409jss.

[103] H. Hosono, Y. Ogo, H. Yanagi, and T. Kamiya. "Bipolar conduction in SnO thin films". In: *Electrochem. Solid State Lett.* **14** (2011), p. 13. DOI: 10.1149/1.3505288.

[104] J. A. Caraveo-Frescas, P. K. Nayak, H. A. Al-Jawhari, D. B. Granato, U. Schwingenschlögl, and H. N. Alshareef. "Record mobility in transparent *p*-type tin monoxide films and devices by phase engineering". In: *ACS Nano* **77** (2013), p. 5160. DOI: 10.1021/nn400852r.

[105] A. J. Freeman, K. R. Poeppelmeier T. O. Mason, R. P. H. Chang, and T. J. Marks. "Chemical and thin-film strategies for new transparent conducting oxides". In: *MRS Bull.* **25** (2000), p. 45. DOI: 10.1557/mrs2000.150.

[106] F. P. Koffyberg. "Electron concentration and mobility in semimetallic CdO". In: *Can. J. Phys.* **49** (1971), p. 435. DOI: 10.1139/p71-055.

[107] M. Yan, M. Lane, C. R. Kannewurf, and R. P. H. Chang. "Highly conductive epitaxial CdO thin films prepared by pulsed laser deposition". In: *Appl. Phys. Lett.* **78** (2001), p. 2342. DOI: 10.1063/1.1365410.

[108] A. W. Metz et al. "Transparent conducting oxides: Texture and microstructure effects on charge carrier mobility in MOCVD-derived CdO thin films grown with a thermally stable, low-melting precursor". In: *J. Am. Chem. Soc.* **126** (2004), p. 8477. DOI: 10.1021/ja039232z.

[109] A. A. Dakhel. "Transparent conducting properties of samarium-doped CdO". In: *J. Alloys Compd.* **475** (2009), p. 51. DOI: 10.1016/j.jallcom.2008.08.008.

[110] C. G. Fonstad and R. H. Rediker. "Electrical properties of high-quality stannic oxide crystals". In: *J. Appl. Phys.* **42** (1971), p. 2911. DOI: 10.1063/1.1660648.

[111] S. Nakao, N. Yamada, T. Hitosugi, Y. Hirose, T. Shimada, and T. Hasegawa. "High mobility exceeding 80 $cm^2V^{-1}s^{-1}$ in polycrystalline Ta-doped SnO_2 thin films on glass using anatase TiO_2 seed layers". In: *Appl. Phys. Express* **3** (2010), p. 031102. DOI: 10.1143/APEX.3.031102.

[112] J. E. Dominguez, L. Fu, and X. Q. Pan. "Effect of crystal defects on the electrical properties in epitaxial tin dioxide thin films". In: *Appl. Phys. Lett.* **81** (2002), p. 5168. DOI: 10.1063/1.1530745.

[113] D. C. Look, D. C. Reynolds, J. R. Sizelove, R. L. Jones, C. W. Litton, G. Cantwell, and W. C. Harsch. "Electrical properties of bulk ZnO". In: *Solid State Commun.* **105** (1998), p. 399. DOI: 10.1016/S0038-1098(97)10145-4.

[114] E. M. Kaidashev, M. Lorenz, H. von Wenckstern, A. Rahm, H.-C. Semmelhack, K.-H. Han, G. Benndorf, C. Bundesmann, H. Hochmuth, and M. Grundmann. "High electron mobility of epitaxial ZnO thin films on *c*-plane sapphire grown by multistep pulsed-laser deposition". In: *Appl. Phys. Lett.* **82** (2003), p. 3901. DOI: 10.1063/1.1578694.

[115] C. Agashe, O. Kluth, J. Hüpkes, U. Zastrow, B. Rech, and M. Wuttig. "Efforts to improve carrier mobility in radio frequency sputtered aluminum doped zinc oxide films". In: *J. Appl. Phys.* **95** (2004), p. 1911. DOI: 10.1063/1.1641524.

[116] K. Ellmer, F. Kudella, R. Mientus, R. Schieck, and S. Fiechter. "Influence of discharge parameters on the layer properties of reactive magnetron sputtered ZnO:Al films". In: *Semicond. Sci. Technol.* **247** (1994), p. 15. DOI: 10.1016/0040-6090(94)90470-7.

[117] K. Ellmer. "Magnetron sputtering of transparent conductive zinc oxide: relation between the sputtering parameters and the electronic properties". In: *J. Phys. D: Appl. Phys.* **33** (2000), p. 17. DOI: 10.1088/0022-3727/33/4/201.

[118] R. L. Weiher. "Electrical properties of single crystals of indium oxide". In: *J. Appl. Phys.* **33** (1962), p. 2834. DOI: 10.1063/1.1702560.

[119] H. K. Müller. "Electrical and optical properties of sputtered In_2O_3 films". In: *Phys. Status Solidi* **27** (1968), p. 723. DOI: 10.1002/pssb.19680270229.

[120] S. Noguchi and H. Sakata. "Electrical properties of undoped In_2O_3 films prepared by reactive evaporation". In: *J. Phys. D : Appl. Phys.* **13** (1980), p. 1129. DOI: 10.1088/0022-3727/13/6/023.

[121] C. A. Pan and T. P. Ma. "Highly transparent conductive films of thermally evaporated In_2O_3". In: *J. Electron. Mater.* **10** (1981), p. 43. DOI: 10.1007/BF02654901.

[122] I. Hamberg and C. G. Granqvist. "Evaporated Sn-doped In_2O_3 films: Basic optical properties and applications to energy-efficient windows". In: *J. Appl. Phys.* **60** (1986), p. 123. DOI: 10.1063/1.337534.

[123] S. J. Wen, G. Couturier, J. P. Chaminade, E. Marquestaut, J. Claverie, and P. Hagenmuller. "Electrical properties of pure In_2O_3 and Sn-doped In_2O_3 single crystals and ceramics". In: *J. Solid State Chem.* **101** (1992), p. 203. DOI: 10.1016/0022-4596(92)90176-V.

[124] M. Sawada and M. Higuchi. "Electrical properties of ITO films prepared by tin ion implantation in In_2O_3 film". In: *Thin Solid Films* **317** (1998), p. 157. DOI: 10.1016/S0040-6090(97)00513-0.

[125] Y. Meng, X.-L Yang, H.-X. Chen, J. Shen, Y.-M. Jiang, Z.-J. Zhang, and Z.-Y. Hua. "A new transparent conductive thin film In_2O_3:Mo". In: *Thin Solid Films* **394** (2001), p. 219. DOI: 10.1016/S0040-6090(01)01142-7.

[126] C. Warmsingh, Y. Yoshida, D. W. Readey, C. W. Teplin, J. D. Perkins, P. A. Parilla, L. M. Gedvilas, B. M. Keyes, and D. S. Ginley. "High-mobility transparent conducting Mo-doped In_2O_3 thin films by pulsed laser deposition". In: *J. Appl. Phys.* **95** (2004), p. 3831. DOI: 10.1063/1.1646468.

[127] T. Koida, H. Fujiwara, and M. Kondo. "Hydrogen-doped In_2O_3 as high-mobility transparent conductive oxide". In: *Jpn. J. Appl. Phys.* **46** (2007), p. 685. DOI: 10.1143/JJAP.46.L685.

[128] T. Koida, H. Fujiwara, and M. Kondo. "High-mobility hydrogen-doped In_2O_3 transparent conductive oxide for a-Si:H/c-Si heterojunction solar cells". In: *Sol. Energy Mater. Sol. Cells* **93** (2009), p. 851. DOI: 10.1016/j.solmat.2008.09.047.

[129] N. Oka, Y. Kawase, and Y. Shigesato. "High-rate deposition of high-quality Sn-doped In_2O_3 films by reactive magnetron sputtering using alloy targets". In: *Thin Solid Films* **520** (2012), p. 4101. DOI: 10.1016/j.tsf.2011.06.063.

[130] M. R. Lorenz and J. F. Woods R. J. Gambino. "Some electrical properties of the semiconductor β-Ga_2O_3". In: *J. Phys. Chem. Solids* **28** (1967), p. 403. DOI: 10.1016/0022-3697(67)90305-8.

[131] N. Ueda, H. Hosono, R. Waseda, and H. Kawazoe. "Anisotropy of electrical and optical properties in β-Ga_2O_3 single crystals". In: *Appl. Phys. Lett.* **71** (1997), p. 933. DOI: 10.1063/1.119693.

[132] T. Oishi, Y. Koga, K. Harada, and M. Kasu. "High-mobility β-Ga_2O_3 (201) single crystals grown by edge-defined film-fed growth method and their Schottky barrier diodes with Ni contact". In: *Appl. Phys. Express* **8** (2015), p. 031101. DOI: 10.7567/APEX.8.031101.

[133] N. Ma, N. Tanen, A. Verma, Z. Guo, T. Luo, H. Xing, and D. Jena. "Intrinsic electron mobility limits in β-Ga_2O_3". In: *Appl. Phys. Lett.* **109** (2016), p. 212101. DOI: 10.1063/1.4968550.

[134] H. J. Kim et al. "High mobility in a stable transparent perovskite oxide". In: *Appl. Phys. Express* **5** (2012), p. 061102. DOI: 10.1143/APEX.5.061102.

[135] X. Luo, Y. S. Oh, A. Sirenko, P. Gao, T. A. Tyson, K. Char, and S.-W. Cheong. "High carrier mobility in transparent $Ba_{1-x}La_xSnO_3$ crystals with a wide band gap". In: *Appl. Phys. Lett.* **100** (2012), p. 172112. DOI: 10.1063/1.4709415.

[136] C. Park, U. Kim, C. J. Ju, J. S. Park, Y. M. Kim, and K. Char. "High mobility field effect transistor based on $BaSnO_3$ with Al_2O_3 gate oxide". In: *Appl. Phys. Lett.* **105** (2014), p. 203503. DOI: 10.1063/1.4901963.

[137] S. Raghavan, T. Schumann, H. Kim, J. Y. Zhang, T. A. Cain, and S. Stemmer. "High-mobility $BaSnO_3$ grown by oxide molecular beam epitaxy". In: *APL Mater.* **4** (2016), p. 016106. DOI: 10.1063/1.4939657.

[138] T. Minami, S. Takata, H. Sato, and H. Sonohara. "Properties of transparent zinc-stannate conducting films prepared by radio frequency magnetron sputtering". In: *J. Vac. Sci. Technol. A* **13** (1995), p. 1095. DOI: 10.1116/1.579592.

[139] J. H. Ko, I. H. Kim, D. Kim, K. S. Lee, T. S. Lee, B. Cheong, and W. M. Kim. "Transparent and conducting Zn-Sn-O thin films prepared by combinatorial approach". In: *Appl. Surf. Sci.* **253** (2007), p. 7298. DOI: 10.1016/j.apsusc.2007.03.036.

[140] Y.-Y. Choi, S. J. Kang, and H.-K. Kim. "Rapid thermal annealing effect on the characteristics of $ZnSnO_3$ films prepared by RF magnetron sputtering". In: *Curr. Appl. Phys.* **12** (2012), p. 104. DOI: 10.1016/j.cap.2012.05.014.

[141] M. Orita, H. Tanji, M. Mizuno, H. Adachi, and I. Tanaka. "Mechanism of electrical conductivity of transparent $InGaZnO_4$". In: *Phys. Rev. B* **61** (2000), p. 1811. DOI: 10.1103/PhysRevB.61.1811.

[142] W. Lim, E. A. Douglas, S.-H. Kim, D. P. Norton, S. J. Pearton, F. Ren, H. Shen, and W. H. Chang. "High mobility $InGaZnO_4$ thin-film transistors on paper". In: *Appl. Phys. Lett.* **94** (2009), p. 072103. DOI: 10.1063/1.3086394.

[143] A. Takagi, K. Nomura, H. Ohta, H. Yanagi, T. Kamiya, M. Hirano, and H. Hosono. "Carrier transport and electronic structure in amorphous oxide semiconductor, a-$InGaZnO_4$". In: *Thin Solid Films* **486** (2005), p. 38. DOI: 10.1016/j.tsf.2004.11.223.

[144] M. J. Gadre and T. L. Alford. "Highest transmittance and high-mobility amorphous indium gallium zinc oxide films on flexible substrate by room-temperature deposition and post-deposition anneals". In: *Appl. Phys. Lett.* **99** (2011), p. 051901. DOI: 10.1063/1.3619196.

[145] T. Minami, S. Takata, T. Kakumu, and H. Sonohara. "New transparent conducting $MgIn_2O_4$-$Zn_2In_2O_5$ thin films prepared by magnetron sputtering". In: *Thin Solid Films* **270** (1995), p. 22. DOI: 10.1016/0040-6090(95)06852-X.

[146] S. Muranaka and T. Shigematsu. "Influence of rf power on structure and physical properties of reactively evaporated $Zn_2In_2O_5$ films". In: *J. Jpn Soc. Powder Powder Metall.* **49** (2002), p. 570. DOI: 10.2497/jjspm.49.570.

[147] A. Takeoka et al. "Development and application of see-through a-Si solar cells". In: *Sol. Energy Mater. Sol. Cells* **29** (1993), p. 243. DOI: 10.1016/0927-0248(93)90039-6.

[148] T. Miyazaki, A. Akisawa, and T. Kashiwagi. "Energy savings of office buildings by the use of semi-transparent solar cells for windows". In: *Renew. Energy* **30** (2005), p. 281. DOI: 10.1016/j.renene.2004.05.010.

[149] J. P. Campbell, E. W. Galyean, and H. R. Spreckman. "Transparent solar cell and method of fabrication". Patent 6320117 B1 (U.S.). 2001.

[150] P.-H. Chang, H.-C. Lu, C.-T. Lee, L.-B. Chang, G.-M. Wu, N.-C. Chen, and A.-P. Chiu. "Transparent solar cell system". Patent 2008/0053518 A1 (U.S.). 2008.

[151] J. Lim, D. Suh, and S. J. Yun. "Transparent solar cell". Patent 2015/0287863 A1 (U.S.). 2015.

[152] E. Fortunato, D. Ginley, H. Hosono, and D. C. Paine. "Transparent conducting oxides for photovoltaics". In: *MRS Bull.* **32** (2007), p. 242. DOI: 10.1557/mrs2007.29.

[153] R. R. Lunt and V. Bulovic. "Transparent, near-infrared organic photovoltaic solar cells for window and energy-scavenging applications". In: *Appl. Phys. Lett.* **98** (2011), p. 113305. DOI: 10.1063/1.3567516.

[154] N. W. Ashsoft and N. Mermin. "Solid state physics". In: Harcourt College, Orlando, FL, USA: Harcourt College Publishers, 1976. ISBN: 0030839939.

[155] K. Nomura, T. Kamiya, and H. Hosono. "Ambipolar oxide thin-film transistor". In: *Adv. Mater.* **23** (2011), p. 3431. DOI: 10.1002/adma.201101410.

[156] C. Chiu, Y.-S. Li, M.-S. Tu, and C. Cheng. "Complementary oxide-semiconductor-based circuits with *n*-channel ZnO and *p*-channel SnO thin-film transistors". In: *IEEE Electr. Device Lett.* **35** (2014), p. 1263. DOI: 10.1109/LED.2014.2364578.

[157] Y.-S. Li, J.-C. He, S.-M. Hsu, C.-C. Lee, D.-Y. Su, F.-Y. Tsai, and C. Cheng. "Flexible complementary oxide-semiconductor-based circuits employing *n*-channel ZnO and *p*-channel SnO thin-film transistors". In: *IEEE Electr. Device Lett.* **37** (2016), p. 46. DOI: 10.1109/LED.2015.2501843.

[158] H. Ohta, K.-I Kawamura, M. Orita, M. Hirano, N. Sarukura, and H. Hosono. "Current injection emission from a transparent *p*-*n* junction composed of *p*-$SrCu_2O_2$/*n*-ZnO". In: *Appl. Phys. Lett.* **77** (2000), p. 475. DOI: 10.1063/1.127015.

[159] H. Ohta, H. Mizoguchi, M. Hirano, S. Narushima, T. Kamiya, and H. Hosono. "Fabrication and characterization of heteroepitaxial *p*-*n* junction diode composed of wide-gap oxide semiconductors *p*-$ZnRh_2O_4$/*n*-ZnO". In: *Appl. Phys. Lett.* **82** (2003), p. 823. DOI: 10.1063/1.1544436.

[160] H. A. Al-Jawhari, J. A. Caraveo-Frescas, M. N. Hedhili, and H. N. Alshareef. "P-type Cu_2O/SnO bilayer thin film transistors processed at low temperatures". In: *ACS Appl. Mater. Interfaces* **5** (2013), p. 9615. DOI: 10.1021/am402542j.

[161] G. Hautier, A. Miglio, D. Waroquiers, G.-M. Rignanese, and X. Gonze. "How Does Chemistry Influence Electron Effective Mass in Oxides? A High-Throughput Computational Analysis". In: *Chem. Mater.* **26** (2014), p. 5447. DOI: 10.1021/cm404079a.

[162] S. Lany and A. Zunger. "Dopability, intrinsic conductivity, and nonstoichiometry of transparent conducting oxides". In: *Phys. Phys. Lett.* **98** (2007), p. 045501. DOI: 10.1103/PhysRevLett.98.045501.

[163] J. Robertson and S. J. Clark. "Limits to doping in oxides". In: *Phys. Rev. B* **83** (2011), p. 075205. DOI: 10.1103/PhysRevB.83.075205.

[164] Y.-J. Zhao C. Persson, S. Lany, and A. Zunger. "n-type doping of $CuInSe_2$ and $CuGaSe_2$". In: *Phys. Rev. B* **72** (2005), p. 035211. DOI: 10.1103/PhysRevB.72.035211.

[165] K. Biswas, S. Lany, and A. Zunger. "The electronic consequences of multivalent elements in inorganic solar absorbers: Multivalency of Sn in Cu_2ZnSnS_4". In: *Appl. Phys. Lett.* **96** (2010), p. 201902. DOI: 10.1063/1.3427433.

[166] L. Bjerg, G. K. H. Madsen, and B. B. Iversen. "*Ab initio* calculations of intrinsic point defects in ZnSb". In: *Chem. Mater.* **24** (2012), p. 2111. DOI: 10.1021/cm300642t.

[167] H. Wang, E. Schechtel, Y. Pei, and G. J. Snyder. "High thermoelectric efficiency of n-type PbS". In: *Adv. Energy Mater.* **3** (2013), p. 488. DOI: 10.1002/aenm.201200683.

[168] *Inorganic Crystal Structure Database.* https://www.fiz-karlsruhe.de/de/leistungen/kristallographie/icsd.html. [FIZ Karlsruhe: Karlsruhe, Germany, 2013]. 2013.

[169] A. Walsh, D. J. Payne, R. G. Egdell, and G. W. Watson. "Stereochemistry of post-transition metal oxides: revision of the classical lone pair model". In: *Chem. Soc. Rev.* **40** (2011), p. 4455. DOI: 10.1039/c1cs15098g.

[170] J. M. Luttinger and W. Kohn. "Motion of electrons and holes in perturbed periodic fields". In: *Phys. Rev.* **97** (1955), p. 869. DOI: 10.1103/physrev.97.869.

[171] M. L. Cohen and S. G. Louie. "Fundamentals of condensed matter physics". In: Cambridge, UK: Cambridge University Press, 2016. ISBN: 978-0521513319.

[172] G. K. H. Madsen and D. J. Singh. "BoltzTraP. A code for calculating band-structure dependent quantities". In: *Comput. Phys. Commun.* **175** (2006), p. 67. DOI: 10.1016/j.cpc.2006.03.007.

[173] J. L. Janssen, Y. Gillet, S. Poncé, A. Martin, M. Torrent, and X. Gonze. "Precise effective masses from density functional perturbation theory". In: *Phys. Rev. B* **93** (2016), p. 205147. DOI: 10.1103/physrevb.93.205147.

[174] N. A. Mecholsky, L. Resca, I. L. Pegg, and M. Fornari. "Theory of band warping and its effects on thermoelectronic transport properties". In: *Phys. Rev. B* **89** (2014), p. 155131. DOI: 10.1103/physrevb.89.155131.

[175] L. D. Landau and S. I. Pekar. "Effective mass of a polaron". In: *Zh. Eksp. Teor. Fiz.* **18** (1948), p. 419.

[176] J. T. Devreese. "Polarons". In: *Encycl. Appl. Phys.* **14** (1996), p. 383. URL: http://cds.cern.ch/record/436143.

[177] R. M. Martin. "Electronic structure: Basic theory and practical methods". In: Cambride, UK: Cambridge University Press, 2004. ISBN: 0521782856.

[178] P. P. Edwards, A. Porch, M. O. Jones, D. V. Morgan, and R. M. Perks. "Basic materials physics of transparent conducting oxides". In: *Dalton Trans.* **19** (2004), p. 2995. DOI: 10.1039/B408864F.

[179] G. Trimarchi, H. Peng, J. Im, A. J. Freeman, V. Cloet, A. Raw, K. R. Poeppelmeier, K. Biswas, S. Lany, and A. Zunger. "Using design principles to systematically plan the synthesis of hole-conducting transparent oxides: Cu_3VO_4 and Ag_3VO_4 as a case study". In: *Phys. Rev. B* **84** (2011), p. 165116. DOI: 10.1103/PhysRevB.84.165116.

[180] D. O. Scanlon and G. W. Watson. "Conductivity limits in $CuAlO_2$ from screened-hybrid Density Functional Theory". In: *J. Phys. Chem. Lett.* **1** (2010), p. 3195. DOI: 10.1021/jz1011725.

[181] A. Walsh, J. L. F. Da Silva, Y. Yan, M. M. Al-Jassim, and S.-H. Wei. "Origin of electronic and optical trends in ternary $In_2O_3(ZnO)_n$ transparent conducting oxides (n=1,3,5): Hybrid density functional theory calculations". In: *Phys. Rev. B* **79** (2009), p. 073105. DOI: 10.1103/PhysRevB.79.073105.

[182] J. D. Perkins et al. "Inverse design approach to hole doping in ternary oxides: Enhancing *p*-type conductivity in cobalt oxide spinels". In: *Phys. Rev. B* **84** (2011), p. 205207. DOI: 10.1103/PhysRevB.84.205207.

[183] F. Yan, X. Zhang, Y. G. Yu, L. Yu, A. Nagaraja, T. O. Mason, and A. Zunger. "Design and discovery of a novel half-Heusler transparent hole conductor made of all-metallic heavy elements". In: *Nat. Commun.* **6** (2015), p. 7308. DOI: 10.1038/ncomms8308.

[184] T. F. T. Cerqueira, S. Lin, M. Amsler, S. Goedecker, S. Botti, and M. A. L. Marques. "Identification of novel Cu, Ag, and Au ternary oxides from global structural prediction". In: *Chem. Mater.* **27** (2015), p. 4562. DOI: 10.1021/acs.chemmater.5b00716.

[185] D. O. Scanlon, J. Buckeridge, C. R. A. Catlow, and G. W. Watson. "Understanding doping anomalies in degenerate *p*-type semiconductor LaCuOSe". In: *J. Mater. Chem. C* **2** (2014), p. 3429. DOI: 10.1039/c4tc00096j.

[186] S. L. Adler. "Quantum theory of the dielectric constant in real solids". In: *Phys. Rev.* **126** (1962), p. 413. DOI: 10.1103/PhysRev.126.413.

[187] N. Wiser. "Dielectric constatnt with local field effect included". In: *Phys. Rev.* **129** (1963), p. 62. DOI: 10.1103/PhysRev.129.62.

[188] S. Baroni and R. Resta. "*Ab initio* calculation of the macroscopic dielectric constant in silicon". In: *Phys. Rev. B* **33** (1986), p. 7017. DOI: 10.1103/PhysRevB.33.7017.

[189] M. S. Hybertsen and S. G. Louie. "*Ab initio* static dielectric matrices from the density-functional approach. I. Formulation and application to semiconductors and insulators". In: *Phys. Rev. B* **35** (1987), p. 5585. DOI: 10.1103/PhysRevB.35.5585.

[190] G. Kresse and J. Furthmüller. "Efficiency of *ab-initio* total energy calculations for metals and semiconductors using a plane-wave basis set". In: *Comput. Mater. Sci.* **6** (1996), p. 15. DOI: 10.1016/0927-0256(96)00008-0.

[191] G. Kresse and J. Furthmüller. "Efficient iterative schemes for *ab initio* total-energy calculations using a plane-wave basis set". In: *Phys. Rev. B* **54** (1996), p. 11169. DOI: 10.1103/PhysRevB.54.11169.

[192] M. Gajdos, K. Hummer, G. Kresse, J. Furthm̈uller, and F. Bechstedt. "Linear optical properties in the projector-augmented wave methodology". In: *Phys. Rev. B* **73** (2006), p. 045112. DOI: 10.1103/PhysRevB.73.045112.

[193] V. S. Vladimirov. "Equations of mathematical physics". In: NY, USA: Marcel Dekker, 1971. ISBN: 0824717139.

[194] S. P. Ong, W. D. Richards, A. Jain, G. Hautier, M. Kocher, and *et al.* "Python Materials Genomics (pymatgen): A robust, open-source python library for materials analysis". In: *Comput. Mater. Sci.* **68** (2013), p. 314. DOI: 10.1016/j.commatsci.2012.10.028.

[195] C. Ambrosch-Draxl and J. O. Sofo. "Linear optical properties of solids within the full-potential linearized augmented planewave method". In: *Comput. Phys. Commun.* **175** (2006), p. 1. DOI: 10.1016/j.cpc.2006.03.005.

[196] Y. Li, L. Zhang, Y. Ma, and D. J. Singh. "Tuning optical properties of transparent conducting barium stannate by dimensional reduction". In: *APL Mat.* **3** (2015), p. 011102. DOI: 10.1063/1.4906785.

[197] K. P. Ong, X. Fan, A. Subedi, M. B. Sullivan, and D. J. Singh. "Transparent conducting properties of $SrSnO_3$ and $ZnSnO_3$". In: *APL Mat.* **3** (2015), p. 062505. DOI: 10.1063/1.4919564.

[198] J. Heyd, G. E. Scuseria, and M. Ernzerhof. "Hybrid functionals based on a screened Coulomb potential". In: *J. Chem. Phys.* **118** (2003), p. 8207. DOI: 10.1063/1.1564060.

[199] E. N. Brothers, A. F. Izmaylov, J. O. Normand, V. Barone, and G. E. Scuseria. "Accurate solid-state band gaps via screened hybrid electronic structure calculations". In: *J. Chem. Phys.* **129** (2008), p. 011102. DOI: 10.1063/1.2955460.

[200] A. Walsh, J. L. F. Da Silva, S.-H. Wei, C. Körber, A. Klein, and *et al.* "Nature of the band gap of In_2O_3 revealed by first-principles calculations and X-Ray spectroscopy". In: *Phys. Rev. Lett.* **100** (2008), p. 167402. DOI: 10.1103/PhysRevLett.100.167402.

[201] P. Agoston, K. Albe, R. M. Nieminen, and M. J. Puska. "Intrinsic n-type behavior in transparent conducting oxides: A comparative hybrid-functional study of In_2O_3, SnO_2, and ZnO". In: *Phys. Rev. Lett.* **103** (2009), p. 245501. DOI: 10.1103/PhysRevLett.103.245501.

[202] H.-R. Liu, J.-H. Yang, H. J. Xiang, X. G. Gong, and S.-H. Wei. "Origin of the superior conductivity of perovskite $Ba(Sr)SnO_3$". In: *Appl. Phys. Lett.* **102** (2013), p. 112109. DOI: 10.1063/1.4798325.

[203] F. Trani, J. Vidal, S. Botti, and M. A. L. Marques. "Band structures of delafossite transparent conductive oxides from a self-consistent GW approach". In: *Phys. Rev. B* **82** (2010), p. 085115. DOI: 10.1103/PhysRevB.82.085115.

[204] D. O. Scanlon and G. W. Watson. "Band gap anomalies of the $ZnM_2^{III}O_4$ (M^{III} = Co, Rh, Ir) spinels". In: *Phys. Chem. Chem. Phys.* **13** (2011), p. 9667. DOI: 10.1039/C0CP02562C.

[205] J. B. Varley, A. Janotti, and C. G. Van de Walle. "Group-V impurities in SnO_2 from first-principles calculations". In: *Phys. Rev. B* **81** (2010), p. 245216. DOI: 10.1103/PhysRevB.81.245216.

[206] J. B. Varley, A. Schleife, A. Janotti, and C. G. Van de Walle. "Ambipolar doping in SnO". In: *Appl. Phys. Lett.* **103** (2013), p. 082118. DOI: 10.1063/1.4819068.

[207] F. Oba, M. Choi, A. Togo, and I. Tanaka. "Point defects in ZnO: an approach from first principles". In: *Sci. Technol. Adv. Mater.* **12** (2011), p. 034302. DOI: 10.1088/1468-6996/12/3/034302.

[208] A. Jain et al. "The Materials Project: A materials genome approach to accelerating materials innovation". In: *APL Mater.* **1** (2013), p. 011002. ISSN: 2166532X. DOI: 10.1063/1.4812323.

[209] *The Materials Project*. https://www.materialsproject.org/. [accessed September 1, 2013]. 2013.

[210] A. R. H. Preston, B. J. Ruck, L. F. J. Piper, A. DeMasi, K. E. Smith, A. Schleife, F. Fuchs, F. Bechstedt, J. Chai, and S. M. Durbin. "Band structure of ZnO from resonant X-ray emission spectroscopy". In: *Phys. Rev. B* **78** (2008), p. 155114. DOI: 10.1103/physrevb.78.155114.

[211] D. Waroquiers, A. Lherbier, A. Miglio, M. Stankovski, S. Poncé, M. J. T. Oliveira, M. Giantomassi, G.-M. Rignanese, and X. Gonze. "Band widths and gaps from the Tran-Blaha functional: Comparison with many-body perturbation theory". In: *Phys. Rev. B* **87** (2013), p. 075121. DOI: 10.1103/physrevb.87.075121.

[212] Ü. Özgür, Ya. I. Alivov, C. Liu, A. Teke, M. A. Reshchikov, S. Doğan, V. Avrutin, S.-J. Cho, and H. Morkoç. "A comprehensive review of ZnO materials and devices". In: *J. Appl. Phys.* **98** (2005), p. 041301. DOI: 10.1063/1.1992666.

[213] M. Nagasawa and S. Shionoya. "Exciton structure in optical absorption of SnO_2 crystals". In: *Phys. Lett.* **22** (1966), p. 409. DOI: 10.1016/0031-9163(66)91202-9.

[214] H. J. Kim et al. "Physical properties of transparent perovskite oxides (Ba,La)SnO_3 with high electrical mobility at room temperature". In: *Phys. Rev. B* **86** (2012), p. 165205. DOI: 10.1103/PhysRevB.86.165205.

[215] P. E. Blöchl. "Projector augmented-wave method". In: *Phys. Rev. B* **50** (1994), p. 17953. DOI: 10.1103/PhysRevB.50.17953.

[216] R. Dronskowski and P. E. Blöchl. "Crystal orbital Hamilton populations (COHP): energy-resolved visualization of chemical bonding in solids based on density-functional calculations". In: *J. Phys. Chem.* **97** (1993), p. 8617. DOI: 10.1021/j100135a014.

[217] V. L. Deringer, A. L. Tchougréeff, and R. Dronskowski. "Crystal orbital Hamilton population (COHP) analysis as projected from plane-wave basis sets". In: *J. Phys. Chem. A* **115** (2011), p. 5461. DOI: 10.1021/jp202489s.

[218] S. Maintz, V. L. Deringer, A. L. Tchougréeff, and R. Dronskowski. "Analytic projection from plane-wave and PAW wavefunctions and application to chemical-bonding analysis in solids". In: *J. Comput. Chem.* **34** (2013), p. 2557. DOI: 10.1002/jcc.23424.

[219] M. Grundmann. "The physics of semiconductors". In: Berlin, Germany: Springer, 2006. ISBN: 978-3540253709.

[220] Y. Ohhata, F. Shinoki, and S. Yoshida. "Optical properties of r.f. reactive sputtered tin-doped In_2O_3 films". In: *Thin Solid Films* **59** (1979), p. 255. DOI: 10.1016/0040-6090(79)90298-0.

[221] J.-C. Manifacier, L. Szepessy, J. F. Bresse, M. Perotin, and R. Stuck. "In_2O_3:(Sn) and SnO_2:(F) films - application to solar energy conversion part II - Electrical and optical properties". In: *Mater. Res. Bull.* **14** (1979), p. 163. DOI: 10.1016/0025-5408(79)90115-6.

[222] Z. Banyamin, P. Kelly, G. West, and J. Boardman. "Electrical and optical properties of fluorine doped tin oxide thin films prepared by magnetron sputtering". In: *Coatings* **4** (2014), p. 732. DOI: 10.3390/coatings4040732.

[223] K. H. Kim, K. C. Park, and D. Y. Ma. "Structural, electrical and optical properties of aluminum doped zinc oxide films prepared by radio frequency magnetron sputtering". In: *J. Appl. Phys.* **81** (1997), p. 7764. DOI: 10.1063/1.365556.

[224] Q. Liu, J. Dai, Z. Liu, X. Zhang, G. Zhu, and G. Ding. "Electrical and optical properties of Sb-doped $BaSnO_3$ epitaxial films grown by pulsed laser deposition". In: *J. Phys. D: Appl. Phys.* **43** (2010), p. 455401. DOI: 10.1088/0022-3727/43/45/455401.

[225] P. Dong, M. Zhang, G. Dong, X. Zhao, and H. Yan. "The optical and electrical properties of Zn-doped $CuAlO_2$ thin films deposited by RF magnetron sputtering". In: *J. Electrochem. Soc.* **155** (2008), H319. DOI: 10.1149/1.2884858.

[226] H. Peelaers, E. Kioupakis, and C. G. Van de Walle. "Fundamental limits on optical transparency of transparent conducting oxides: Free-carrier absorption in SnO_2". In: *Appl. Phys. Lett.* **100** (2012), p. 011914. DOI: 10.1063/1.3671162.

[227] A. Zunger. "Inverse design in search of materials with target functionalities". In: *Nat. Rev. Chem.* **2** (2018), p. 0121. DOI: 10.1038/s41570-018-0121.

[228] J. B. Varley, A. Miglio, V.-A. Ha, M. J. van Setten, G.-M. Rignanese, and G. Hautier. "High-throughput design of non-oxide *p*-type transparent conducting materials: Data mining, search strategy, and identification of boron phosphide". In: *Chem. Mater.* **29** (2017), p. 2568. DOI: 10.1021/acs.chemmater.6b04663.

[229] L. Farrell, E. Norton, C. M. Smith, D. Caffrey, I. V. Shvets, and K. Fleischer. "Synthesis of nanocrystalline Cu deficient $CuCrO_2$ - a high figure of merit *p*-type transparent semiconductor". In: *J. Mater. Chem. C* **4** (2016), p. 126. DOI: 10.1039/c5tc03161c.

[230] N. F. Quackenbush et al. "Origin of the bipolar doping behavior of SnO from X-ray spectroscopy and Density Functional Theory". In: *Chem. Mater.* **25** (2013), p. 3114. DOI: 10.1021/cm401343a.

[231] Y. Li, D. J. Singh, M.-H. Du, Q. Xu, L. Zhang, W. Zheng, and Y. Ma. "Design of ternary alkaline-earth metal Sn(II) oxides with potential good *p*-type conductivity". In: *J. Mater. Chem. C* **4** (2016), p. 4592. DOI: 10.1039/C6TC00996D.

[232] Q. Xu, Y. Li, L. Zhang, W. Zheng, D. J. Singh, and Y. Ma. "Sn(II)-containing phosphates as optoelectronic materials". In: *Chem. Mater.* **29** (2017), p. 2459. DOI: 10.1021/acs.chemmater.6b03669.

[233] D. C. Langreth and M. J. Mehl. "Beyond the local-density approximation in calculations of ground-state electronic properties". In: *Phys. Rev. B* **28** (1983), p. 1809. DOI: 10.1103/physrevb.28.1809.

[234] A. D. Becke. "Density-functional exchange-energy approximation with correct asymptotic behavior". In: *Phys. Rev. A* **38** (1988), p. 3098. DOI: 10.1103/physreva.38.3098.

[235] J. P. Perdew, K. Burke, and M. Ernzerhof. "Generalized gradient approximation made simple". In: *Phys. Rev. Lett.* **77** (1996), p. 3865. DOI: 10.1103/physrevlett.77.3865.

[236] J. F. Nye. "Physical properties of crystals: Their representation by tensors and matrices". In: Oxford, UK: Clarendon Press, 1985. Chap. I, p. 24. ISBN: 978-0198511656.

[237] W. Setyawan and S. Curtarolo. "High-throughput electronic band structure calculations: Challenges and tools". In: *Comput. Mater. Sci.* **49** (2010), p. 299. DOI: 10.1016/j.commatsci.2010.05.010.

[238] *Visualization for electronic and structural analysis*. http://jp-minerals.org/vesta/en/doc.html. version 3.3.9. 2016.

[239] Y. Ogo, H. Hiramatsu, K. Nomura, H. Yanagi, T. Kamiya, M. Kimura, M. Hirano, and H. Hosono. "Tin monoxide as an *s*-orbital-based *p*-type oxide semiconductor: Electronic structures and TFT application". In: *Phys. Status Solidi A* **206** (2009), p. 2187. DOI: 10.1002/pssa.200881792.

[240] A. Togo, F. Oba, I. Tanaka, and K. Tatsumi. "First-principles calculations of native defects in tin monoxide". In: *Phys. Rev. B* **74** (2006), p. 195128. DOI: 10.1103/PhysRevB.74.195128.

[241] Y. Pei, W. Liu, J. Shi, Z. Chen, and G. Wang. "Fabrication and characterization of *p*-type SnO thin film with high *c*-axis preferred orientation". In: *J. Electron. Mater.* **45** (2016), p. 5967. DOI: 10.1007/s11664-016-4816-7.

[242] J. K. Burdett. "Chemical bonding in solids". In: Oxford, UK: Oxford University Press, 1995. Chap. I, p. 9. ISBN: 978-0195089929.

[243] W. Zhou and N. Umezawa. "Band gap engineering of bulk and nanosheet SnO: an insight into the interlayer Sn-Sn lone pair interactions". In: *Phys. Chem. Chem. Phys.* **17** (2015), p. 17816. DOI: 10.1039/C5CP02255J.

[244] R. Hoppe and R. Nowitz. "Oxydationsprodukte intermetallischer Phasen. III. Tieftemperaturformen von $K_2Sn_2O_3$ und $Rb_2Sn_2O_3$ und eine Notiz über $K_2Ge_2O_3$". In: *Z. Anorg. Allg. Chem.* **609** (1984), p. 145. DOI: 10.1002/zaac.19845090215.

[245] R. M. Braun and R. Hoppe. "Das erste Oxostannat(II): $K_2Sn_2O_3$". In: *Angew. Chem.* **90** (1978), p. 475. DOI: 10.1002/ange.19780900614.

[246] Y. Kang, S. H. Jeon, Y.-W. Son, Y.-S. Lee, M. Ryu, S. Lee, and S. Han. "Microscopic origin of universal quasilinear band structures of Transparent Conducting Oxides". In: *Phys. Rev. Lett.* **108** (2012), p. 196404. DOI: 10.1103/PhysRevLett.108.196404.

[247] A. Walsh, J. L. F. D. Silva, and S.-H. Wei. "Interplay between order and disorder in the high performance of amorphous transparent conducting oxides". In: *Chem. Mater.* **21** (2009), p. 5119. DOI: 10.1021/cm9020113.

[248] M. J. Wahila et al. "Lone-pair stabilization in transparent amorphous tin oxides: A potential route to *p*-type conduction pathways". In: *Chem. Mater.* **28** (2016), p. 4706. DOI: 10.1021/acs.chemmater.6b01608.

[249] H. Mizoguchi, T. Kamiya, S. Matsuishi, and H. Hosono. "A germanate transparent conductive oxide". In: *Nat. Commun.* **2** (2011), p. 470. DOI: 10.1038/ncomms1484.

[250] D. Waroquiers et al. "Statistical analysis of coordination environments in oxides". In: *Chem. Mater.* **29** (2017), p. 8346. DOI: 10.1021/acs.chemmater.7b02766.

[251] H. Yanagi, J. Tate, S. Park, C.-H. Park, and D. Keszler. "*p*-type conductivity in wide-band-gap BaCuQF (Q=S,Se)". In: *Appl. Phys. Lett.* **82** (2003), p. 2814. DOI: 10.1063/1.1571224.

[252] S. Park, D. A. Keszler, M. M. Valencia, R. L. Hoffman, J. P. Bender, and J. F. Wager. "Transparent *p*-type conducting $BaCu_2S_2$ films". In: *Appl. Phys. Lett.* **80** (2002), p. 4393. DOI: 10.1063/1.1485133.

[253] R. Woods-Robinson, J. K. Cooper, X. Xu, L. T. Schelhas, V. L. Pool, A. Faghaninia, C. S. Lo, M. F. Toney, I. D. Sharp, and J. W. Ager. "*p*-type transparent Cu-alloyed ZnS deposited at room temperature". In: *Adv. Electron. Mater.* **2** (2016), p. 1500396. DOI: 10.1002/aelm.201500396.

[254] J. Perdew, K. Burke, and M. Ernzerhof. "Generalized gradient approximation made simple". In: *Phys. Rev. Lett.* **77** (1996), p. 3865. DOI: 10.1103/PhysRevLett.77.3865.

[255] A. Jain et al. "FireWorks: A dynamic workflow system designed for high-throughput applications". In: *Concurr. Comput. Pract. Exp.* **27** (2015), p. 5037. DOI: 10.1002/cpe.3505.

[256] F. Ricci, W. Chen, U. Aydemir, G. J. rey Snyder, G.-M. Rignanese, A. Jain, and G. Hautier. "An *ab initio* electronic transport database for inorganic materials". In: *Sci. Data* **4** (2017), p. 170085. DOI: 10.1038/sdata.2017.85.

[257] G. Hautier, S. P. Ong, A. Jain, C. J. Moore, and G. Ceder. "Accuracy of density functional theory in predicting formation energies of ternary oxides from binary oxides and its implication on phase stability". In: *Phys. Rev. B* **85** (2012), p. 155208. DOI: 10.1103/physrevb.85.155208.

[258] X. Gonze et al. "First-principles computation of material properties: the ABINIT software project". In: *Comput. Mater. Sci.* **25** (2002), p. 478. DOI: 10.1016/S0927-0256(02)00325-7.

[259] X. Gonze. "A brief introduction to the ABINIT software package". In: *Z. Kristallogr.* **202** (2005), p. 558. DOI: 10.1524/zkri.220.5.558.65066.

[260] X. Gonze et al. "ABINIT : First-principles approach of materials and nanosystem properties". In: *Comput. Phys. Commun.* **180** (2009), p. 2582. DOI: 10.1016/j.cpc.2009.07.007.

[261] X. Gonze et al. "Recent developments in the ABINIT software package". In: *Comput. Phys. Commun.* **205** (2016), p. 106. DOI: 10.1016/j.cpc.2016.04.003.

[262] D. R. Hamann. "Optimized norm-conserving Vanderbilt pseudopotentials". In: *Phys. Rev. B* **88** (2013), p. 085117. DOI: 10.1103/PhysRevB.88.085117.

[263] M. J. van Setten, M. Giantomassi, E. Bousquet, M. J. Verstraete, D. R. Hamann, X. Gonze, and G.-M. Rignanese. "The PseudoDojo: Training and grading a 85 element optimized norm-conserving pseudopotential table". In: *Comput. Phys. Commun.* **226** (2018), p. 39. DOI: 10.1016/j.cpc.2018.01.012.

[264] M. J. van Setten, M. Giantomassi, X. Gonze, G.-M. Rignanese, and G. Hautier. "Automation methodologies and large-scale validation for *GW*: Towards high-throughput *GW* calculations". In: *Phys. Rev. B* **96** (15 2017), p. 155207. DOI: 10.1103/PhysRevB.96.155207.

[265] M. Giantomassi and *et al. Open-source library for analyzing the results produced by ABINIT*. https://github.com/abinit/abipy. 2014.

[266] C. Freysoldt, B. Grabowski, T. Hickel, J. Neugebauer, G. Kresse, A. Janotti, and C. G. Van de Walle. "First-principles calculations for point defects in solids". In: *Rev. Mod. Phys.* **86** (2014), p. 253. DOI: 10.1103/RevModPhys.86.253.

[267] E. R. Batista, J. Heyd, R. G. Hennig, B. P. Uberuaga, R. L. Martin, G. E. Scuseria, C. J. Umrigar, and J. W. Wilkins. "Comparison of screened hybrid density functional theory to diffusion Monte Carlo in calculations of total energies of silicon phases and defects". In: *Phys. Rev. B* **74** (2006), p. 121102. DOI: 10.1103/physrevb.74.121102.

[268] H.-P. Komsa, T. T. Rantala, and A. Pasquarello. "Finite-size supercell correction schemes for charged defect calculations". In: *Phys. Rev. B* **86** (2012), p. 045112. DOI: 10.1103/PhysRevB.86.045112.

[269] S. B. Zhang and J. E. Northrup. "Chemical potential dependence of defect formation energies in GaAs: Application to Ga self-diffusion". In: *Phys. Rev. Lett.* **67** (1991), p. 2339. DOI: 10.1103/PhysRevLett.67.2339.

[270] C. Freysoldt, J. Neugebauer, and C. G. Van de Walle. "Electrostatic interactions between charged defects in supercells". In: *Phys. Status Solidi B* **248** (2011), p. 1067. DOI: 10.1002/pssb.201046289.

[271] Y. Kumagai and F. Oba. "Electrostatics-based finite-size corrections for first-principles point defect calculations". In: *Phys. Rev. B* **89** (2014), p. 195205. DOI: 10.1103/PhysRevB.89.195205.

[272] D. Broberg, B. Medasani, N. E. R. Zimmermann, G. Yu, A. Canning, M. Haranczyk, M. Asta, and G. Hautier. "PyCDT: A Python toolkit for modeling point defects in semiconductors and insulators". In: *Comput. Phys. Commun* **226** (2018), p. 165. DOI: 10.1016/j.cpc.2018.01.004.

[273] J. Noffsinger, F. Giustino, B. D. Malone, C.-H. Park, S. G. Louie, and M. L. Cohen. "EPW: A program for calculating the electron-phonon coupling using maximally localized Wannier functions". In: *Comput. Phys. Commun.* **181** (2010), p. 2140. DOI: 10.1016/j.cpc.2010.08.027.

[274] S. Poncé, E. R. Margine, C. Verdi, and F. Giustino. "EPW: Electron–phonon coupling, transport and superconducting properties using maximally localized Wannier functions". In: *Comput. Phys. Commun.* **209** (2016), p. 116. DOI: 10.1016/j.cpc.2016.07.028.

[275] P. Giannozzi and *et al.* "QUANTUM ESPRESSO: a modular and open-source software project for quantum simulations of materials". In: *J. Phys.: Condens. Matter* **21** (2009), p. 395502. DOI: 10.1088/0953-8984/21/39/395502.

[276] P. Giannozzi and *et al.* "Advanced capabilities for materials modelling with Quantum ESPRESSO". In: *J. Phys.: Condens. Matter* **29** (2017), p. 465901. DOI: 10.1088/1361-648X/aa8f79.

[277] M. Giantomassi. "Core-electrons and self-consistency in the *GW* approximation from a PAW perspective". PhD thesis. Université catholique de Louvain, 2009.

[278] J. Noffsinger, E. Kioupakis, C. G. Van de Walle, S. G. Louie, and M. L. Cohen. "Phonon-assisted optical absorption in Silicon from first principles". In: *Phys. Rev. Lett.* **108** (2012), p. 167402. DOI: 10.1103/PhysRevLett.108.167402.

[279] W. J. Choyke and G. Pensl. "Physical properties of SiC". In: *MRS Bull.* **22** (1997), p. 25. DOI: 10.1557/S0883769400032723.

[280] K. Furukawa, A. Uemoto, M. Shigeta, A. Suzuki, and S. Nakajima. "3C-SiC $p-n$ junction diodes". In: *Appl. Phys. Lett.* **48** (1986), p. 1536. DOI: 10.1063/1.96860.

[281] Y. Kondo, T. Takahashi, K. Ishii, Y. Hayashi, E. Sakuma, S . Misawa, H. Daimon, M. Yamanaka, and S . Yoshida. "Experimental 3C-SiC MOSFET". In: *IEEE Electr. Device Lett.* **7** (1986), p. 404. DOI: 10.1109/EDL.1986.26417.

[282] K. Shibahara, N. Kuroda, S. Nishino, and H. Matsunami. "Fabrication of p-n junction diodes using homoepitaxially grown 6H-SiC at low temperature by chemical vapor deposition". In: *Jpn. J. Appl. Phys.* **26** (1987), p. 1815. DOI: 10.1143/JJAP.26.L1815.

[283] R. Weingärtner, P. J. Wellmann, M. Bickermann, D. Hofmann, T. L. Straubinger, and A. Winnacker. "Determination of charge carrier concentration in n- and p-doped SiC based on optical absroption measurements". In: *Appl. Phys. Lett.* **80** (2002), p. 70. DOI: 10.1063/1.1430262.

[284] H. Morkoç, S. Strite, G. B. Gao, M. E. Lin, B. Sverdlov, and M. Burns. "Large-band-gap SiC, III-V nitride, and II-VI ZnSe-based semiconductor device technologies". In: *J. Appl. Phys.* **76** (1994), p. 1363. DOI: 10.1063/1.358463.

[285] H. R. Philipp. "Intrinsic optical absorption in single-crystal silicon carbide". In: *Phys. Rev.* **111** (1958), p. 440. DOI: 10.1103/PhysRev.111.440.

[286] M. Liu, M. B. Johnston, and H. J. Snaith. "Efficient planar heterojunction perovskite solar cells by vapour deposition". In: *Nature* **501** (2013), p. 395. DOI: 10.1038/nature12509.

[287] M. A. Green, A. Ho-Baillie, and H. J. Snaith. "The emergence of perovskite solar cells". In: *Nat. Photonics* **8** (2014), p. 506. DOI: 10.1038/nphoton.2014.134.

[288] R. J. Archer, R. Y. Koyama, E. E. Loebner, and R. C. Lucas. "Optical absorption, electroluminescence, and the band gap of BP". In: *Phys. Rev. Lett.* **12** (1964), p. 538. DOI: 10.1103/physrevlett.12.538.

[289] V. A. Fomichev, I. I. Zhukova, and I.K. Polushina. "Investigation of the energy band structure of boron phosphide by ultra-soft X-ray spectroscopy". In: *J. Phys. Chem. Solids* **29** (1968), p. 1025. DOI: 10.1016/0022-3697(68)90238-2.

[290] M. Iwami, T. Tohda, and K. Kawabe. "Crystal growth of boron mono-phosphide and its electrical and optical properties". In: *IEEJ Transactions on Fundamentals and Materials* **95** (1975), p. 216. DOI: 10.1541/ieejfms1972.95.216.

[291] M. Odawara, T. Udagawa, and G. Shimaoka. "Organometallic chemical vapor deposition growth of heterostructure of wide band gap and transparent boron phosphide on silicon". In: *Jpn. J. Appl. Phys.* **44** (2005), p. 681. DOI: 10.1143/jjap.44.681.

[292] S. Dalui, S. Hussain, S. Varma, D. Paramanik, and A. K. Pal. "Boron phosphide films prepared by co-evaporation technique: Synthesis and characterization". In: *Thin Solid Films* **516** (2008), p. 4958. DOI: 10.1016/j.tsf.2007.09.047.

[293] K. Woo, K. Lee, and K. Kovnir. "BP: synthesis and properties of boron phosphide". In: *Mater. Res. Express* **3** (2016), p. 074003. DOI: 10.1088/2053-1591/3/7/074003.

[294] B. Stone and D. Hill. "Semiconducting properties of cubic boron phosphide". In: *Phys. Rev. Lett.* **4** (1960), p. 282. DOI: 10.1103/physrevlett.4.282.

[295] F. Bassani and G. Pastori Parravicini. "Electronic states and optical transitions in solids". In: Oxford, UK: Pergamon Press, 1975. ISBN: 0080168469.

[296] K. Shohno, M. Takigawa, and T. Nakada. "Epitaxial growth of BP compounds on Si substrates using the B_2H_6-PH_3-H_2 system". In: *J. Cryst. Growth* **24-25** (1974), p. 193. DOI: 10.1016/0022-0248(74)90303-0.

[297] M. Takigawa, M. Hirayama, and K. Shohno. "Hetero-Epitaxial growth of boron monophosphide on Silicon substrate using B_2H_6-PH_3-H_2 system". In: *Jpn. J. Appl. Phys.* **13** (1974), p. 411. DOI: 10.1143/jjap.13.411.

[298] Y. Kumashiro, K. Kudo, K. Matsumoto, Y. Okada, and T. Koshiro. "Thermal neutron irradiation experiments on ^{10}BP single-crystal wafers". In: *Journal of the Less Common Metals* **143** (1988), p. 71. DOI: 10.1016/0022-5088(88)90031-8.

[299] Y. Kumashiro, M. Hirabayashi, and S. Takagi. "Boron phosphide as a refractory semiconductor". In: *MRS Proceedings* **162** (1989), p. 585. DOI: 10.1557/proc-162-585.

[300] Y. Kumashiro. "Refractory semiconductor of boron phosphide". In: *J. Mater. Res.* **5** (1990), p. 2933. DOI: 10.1557/jmr.1990.2933.

[301] Y. Kumashiro, K. Nakamura, T. Enomoto, and M. Tanaka. "Preparation and thermoelectric properties of BP films on SOI and sapphire substrates". In: *J. Mater. Sci. Mater. Electron.* **22** (2010), p. 966. DOI: 10.1007/s10854-010-0245-1.

[302] R. K. M. Raghupathy, T. D. Kühne, C. Felser, and H. Mirhosseini. "Rational design of transparent p-type conducting non-oxide materials from high-throughput calculations". In: *J. Mater. Chem. C* **6** (2018), p. 541. DOI: 10.1039/c7tc05311h.

[303] K. Kuhar, M. Pandey, K. S. Thygesen, and K. W. Jacobsen. "High-throughput computational assessment of previously synthesized semiconductors for photovoltaic and photoelectrochemical devices". In: *ACS Energy Lett.* **3** (2018), p. 436. DOI: 10.1021/acsenergylett.7b01312.

[304] X. Gonze and C. Lee. "Dynamical matrices, Born effective charges, dielectric permittivity tensors, and interatomic force constants from density-functional perturbation theory". In: *Phys. Rev. B* **55** (1997), p. 10355. DOI: 10.1103/physrevb.55.10355.

[305] G. Petretto, S. Dwaraknath, H. P. C. Miranda, D. Winston, M. Giantomassi, M. J. van Setten, X. Gonze, K. A. Persson, G. Hautier, and G.-M. Rignanese. "High-throughput density-functional perturbation theory phonons for inorganic materials". In: *Sci. Data* **5** (2018), p. 180065. DOI: 10.1038/sdata.2018.65.

[306] C. Verdi and F. Giustino. "Fröhlich electron-phonon vertex from first principles". In: *Phys. Rev. Lett.* **115** (2015), p. 176401. DOI: 10.1103/physrevlett.115.176401.

[307] C. C. Wang, M. Cordova, and A. G. Fischer. "Preparation, optical properties and band structure of boron monophosphide". In: *RCA Rev.* **25** (1964), p. 159.

[308] T. L. Chu, J. M. Jackson, A. E. Hyslop, and S. C. Chu. "Crystals and epitaxial layers of boron phosphide". In: *J. Appl. Phys.* **42** (1971), p. 420. DOI: 10.1063/1.1659614.

[309] Y. Kumashiro, T. Yao, and S. Gonda. "Crystal growth of boron phosphide by high pressure flux method". In: *J. Cryst. Growth* **70** (1984), p. 515. DOI: 10.1016/0022-0248(84)90310-5.

[310] Y. Kumashiro, K. Sato, S. Chiba, S. Yamada, D. Tanaka, K. Hyodo, T. Yokoyama, and K. Hirata. "Preparation of boron and boron phosphide films by photo- and thermal chemical vapor deposition processes". In: *J. Solid State Chem.* **154** (2000), p. 39. DOI: 10.1006/jssc.2000.8808.

[311] V.-A. Ha, F. Ricci, G.-M. Rignanese, and G. Hautier. "Structural design principles for low hole effective mass *s*-orbital-based *p*-type oxides". In: *J. Mater. Chem. C* **5** (2017), p. 5772. DOI: 10.1039/c7tc00528h.

[312] G. A. Saum and E. B. Hensley. "Fundamental optical absorption in the IIA-VIB compounds". In: *Phys. Rev.* **7** (1959), p. 1019. DOI: 10.1103/PhysRev.113.1019.

[313] T. J. Richardson. "New electrochromic mirror systems". In: *Solid State Ion.* **165** (2003), p. 305. DOI: 10.1016/j.ssi.2003.08.047.

[314] R. Gobrecht. "Photoelektrische eigenschaften von Lithiumantimonid". In: *Phys. Status Solidi* **13** (1966), p. 429. DOI: 10.1002/pssb.19660130215.

[315] E. Maciá-Barber. "Thermoelectric materials: Advances and applications". In: FL, USA: Pan Stanford, 2015. ISBN: 978-9814463539.

[316] T. Kajikawa, N. Kimura, and T. Yokoyama. "Thermoelectric properties of intermetallic compounds: Mg_3Bi_2 and Mg_3Sb_2 for medium temperature range thermoelectric elements". In: *Proceedings ICT' 03. 22nd International Conference on Thermoelectrics (IEEE Cat. No.03TH8726)*. IEEE, 2003. ISBN: 078038301X. DOI: 10.1109/ict.2003.1287510.

[317] C. L. Condron, S. M. Kauzlarich, F. Gascoin, and G. J. Snyder. "Thermoelectric properties and microstructure of Mg_3Sb_2". In: *J. Solid State Chem.* **179** (2006), p. 2252. DOI: 10.1016/j.jssc.2006.01.034.

[318] J. Zhang, L. Song, A. Mamakhel, M. R. V. Jørgensen, and B. B. Iversen. "High-performance low-cost n-type Se-doped Mg_3Sb_2-based zintl compounds for thermoelectric application". In: *Chem. Mater.* **29** (2017), p. 5371. DOI: 10.1021/acs.chemmater.7b01746.

[319] G. Brunin, G.-M. Rignanese, and G. Hautier. *Are small polarons always detrimental to transparent conducting oxides ?* 2018. eprint: arXiv:1810.04919.

[320] K.P. Ananthanarayanan, C. Mohanty, and P.J. Gielisse. "Synthesis of single crystal boron phosphide". In: *J. Cryst. Growth* **20** (1973), p. 63. DOI: 10.1016/0022-0248(73)90038-9.

[321] K. Kumashiro, K. Hirata, K. Sato, T. Yokoyama, T. Aisu, T. Ikeda, and M. Minaguchi. "Thermoelectric properties of boron and boron phosphide films". In: *J. Solid State Chem.* **154** (2000), p. 26. DOI: 10.1006/jssc.2000.8806.

[322] J. D. Brasfield. "Chemical vapor deposition of heteroepitaxial boron phosphide thin films". PhD thesis. University of Tennessee-Knoxville, 2013.

[323] B. Padavala, C. D. Frye, X. Wang, Z. Ding, R. Chen, M. Dudley, B. Raghothamachar, P. Lu, B. N. Flanders, and J. H. Edgar. "Epitaxy of boron phosphide on aluminum nitride(0001)/sapphire substrate". In: *Cryst. Growth Des.* **16** (2015), p. 981. DOI: 10.1021/acs.cgd.5b01525.

[324] A. Goossens, E. M. Kelder, R. J. M. Beeren, C. J. G. Bartels, and J. Schoonman. "Structural, optical, and electronic properties of silicon/boron phosphide heterojunction photoelectrodes". In: *Ber. Bunsenges. Phys. Chem.* **95** (1991), p. 503. DOI: 10.1002/bbpc.19910950410.

[325] A. Goossens and J. Schoonman. "Electrochemical investigations of silicon/boron phosphide heterojunction photoelectrodes". In: *Electrochim. Acta* **40** (1995), p. 1339. DOI: 10.1016/0013-4686(95)00069-q.

[326] M. Mirzaei and M. Giahi. "Computational studies on boron nitride and boron phosphide nanotubes: Density functional calculations of boron-11 electric field gradient tensors". In: *Physica E: Low Dimens. Syst. Nanostruct.* **42** (2010), p. 1667. DOI: 10.1016/j.physe.2010.01.022.

[327] M. D. Esrafili and H. Behzadi. "A comparative study on carbon, boron-nitride, boron-phosphide and silicon-carbide nanotubes based on surface electrostatic potentials and average local ionization energies". In: *J. Mol. Model.* **19** (2013), p. 2375. DOI: 10.1007/s00894-013-1787-y.

[328] D. Çakır, D. Kecik, H. Sahin, E. Durgun, and F. M. Peeters. "Realization of *p*-*n* junction in a single layer boron-phosphide". In: *Phys. Chem. Chem. Phys.* **17** (2015), p. 13013. DOI: 10.1039/c5cp00414d.

[329] H. R. Jiang, W. Shyy, M. Liu, L. Wei, M. C. Wu, and T. S. Zhao. "Boron phosphide monolayer as a potential anode material for alkali metal-based batteries". In: *J. Mater. Chem. A* **5** (2017), p. 672. DOI: 10.1039/c6ta09264k.

[330] H. Luo, R. G. Greene, K. Ghandehari, T. Li, and A. L. Ruoff. "Structural phase transformations and the equations of state of calcium chalcogenides at high pressure". In: *Phys. Rev. B* **50** (1994), p. 16232. DOI: 10.1103/physrevb.50.16232.

[331] P. C. Piña, H. Arriola, and F. Guzmán. "Synthesis of calcium telluride as a possible mössbauer source". In: *Hyperfine Interact.* **161** (2005), p. 123. DOI: 10.1007/s10751-005-9174-4.

[332] L. Baggetto, P. Ganesh, C.-N. Sun, R. A. Meisner, T. A. Zawodzinski, and G. M. Veith. "Intrinsic thermodynamic and kinetic properties of Sb electrodes for Li-ion and Na-ion batteries: experiment and theory". In: *J. Mater. Chem. A* **1** (2013), p. 7985. DOI: 10.1039/c3ta11568b.

[333] J. He, Y. Wei, T. Zhai, and H. Li. "Antimony-based materials as promising anodes for rechargeable lithium-ion and sodium-ion batteries". In: *Mater. Chem. Front.* **2** (2018), p. 437. DOI: 10.1039/c7qm00480j.

[334] G.-T. Zhou, O. Palchik, V. G. Pol, E. Sominski, Y. Koltypin, and A. Gedanken. "Microwave-assisted solid-state synthesis and characterization of intermetallic compounds of Li_3Bi and Li_3Sb". In: *J. Mater. Chem.* **13** (2003), p. 2607. DOI: 10.1039/b303163b.

[335] X. Yang, Z. Dai, Y. Zhao, J. Liu, and S. Meng. "Low lattice thermal conductivity and excellent thermoelectric behavior in Li_3Sb and Li_3Bi". In: *J. Phys.: Condens. Matter* **30** (2018), p. 425401. DOI: 10.1088/1361-648x/aade17.

[336] M. Born and R. Oppenheimer. "Zur quantentheorie der molekeln". In: *Ann. Phys.* **389** (1927), p. 457. DOI: 10.1002/andp.19273892002.

[337] P. Hohenberg and W. Kohn. "Inhomogeneous electron gas". In: *Phys. Rev.* **136** (1964), p. 864. DOI: 10.1103/physrev.136.b864.

[338] W. Kohn and L. J. Sham. "Self-consistent equations including exchange and correlation effects". In: *Phys. Rev.* **140** (1965), p. 1133. DOI: 10.1103/physrev.140.a1133.

[339] J. P. Perdew and Y. Wang. "Accurate and simple density functional for the electronic exchange energy: Generalized gradient approximation". In: *Phys. Rev. B* **33** (1986), p. 8800. DOI: 10.1103/physrevb.33.8800.

[340] J. P. Perdew, J. A. Chevary, S. H. Vosko, K. A. Jackson, M. R. Pederson, D. J. Singh, and C. Fiolhais. "Atoms, molecules, solids, and surfaces: Applications of the generalized gradient approximation for exchange and correlation". In: *Phys. Rev. B* **46** (1992), p. 6671. DOI: 10.1103/physrevb.46.6671.

[341] C. Lee, W. Yang, and R. G. Parr. "Development of the Colle-Salvetti correlation-energy formula into a functional of the electron density". In: *Phys. Rev. B* **37** (1988), p. 785. DOI: 10.1103/physrevb.37.785.

[342] J. Tao, J. P. Perdew, V. N. Staroverov, and G. E. Scuseria. "Climbing the density functional ladder: Nonempirical meta–generalized gradient approximation designed for molecules and solids". In: *Phys. Rev. Lett.* **91** (2003), p. 146401. DOI: 10.1103/physrevlett.91.146401.

[343] J. P. Perdew, M. Ernzerhof, and K. Burke. "Rationale for mixing exact exchange with density functional approximations". In: *J. Chem. Phys.* **105** (1996), p. 9982. DOI: 10.1063/1.472933.

[344] M. Reiher, O. Salomon, and B. A. Hess. "Reparameterization of hybrid functionals based on energy differences of states of different multiplicity". In: *Theor. Chem. Acc.* **107** (2001), p. 48. DOI: 10.1007/s00214-001-0300-3.

[345] O. Salomon, M. Reiher, and B. A. Hess. "Assertion and validation of the performance of the B3LYP* functional for the first transition metal row and the G2 test set". In: *J. Chem. Phys.* **117** (2002), p. 4729. DOI: 10.1063/1.1493179.

[346] S. H. Vosko, L. Wilk, and M. Nusair. "Accurate spin-dependent electron liquid correlation energies for local spin density calculations: a critical analysis". In: *Can. J. Phys.* **58** (1980), p. 1200. DOI: 10.1139/p80-159.

[347] P. Güttinger. "Das verhalten von atomen im magnetischen drehfeld". In: *Z. Phys.* **73** (1932), p. 169. DOI: 10.1007/BF01351211.

[348] W. Pauli. "Handbuch der physik". In: Berlin, Germany: Springer, 1933, pp. 82–272. ISBN: 978-3540519492.

[349] H. Hellmann. *Einfuhrung in die quantumchemie*. Franz Duetsche, Leipzig. 1937.

[350] R. P. Feynman. "Forces in molecules". In: *Phys. Rev.* **56** (1939), p. 340. DOI: 10.1103/physrev.56.340.

[351] K. Lejaeghere et al. "Reproducibility in density functional theory calculations of solids". In: *Science* **351** (2016), p. 3000. DOI: 10.1126/science.aad3000.

[352] S. Maintz, V. L. Deringer, A. L. Tchougréeff, and R. Dronskowski. "LOBSTER: A tool to extract chemical bonding from plane-wave based DFT". In: *J. Comput. Chem.* **37** (2016), p. 1030. DOI: 10.1002/jcc.24300.

[353] S. P. Ong, L. Wang, B. Kang, and G. Ceder. "Li-Fe-P-O_2 Phase diagram from first principles calculations". In: *Chem. Mater.* **20** (2008), p. 1798. DOI: 10.1021/cm702327g.

[354] S. P. Ong, A. Jain, G. Hautier, B. Kang, and G. Ceder. "Thermal stabilities of delithiated olivine MPO_4 (M=Fe, Mn) cathodes investigated using first principles calculations". In: *Electrochem. Commun.* **12** (2010), p. 427. DOI: 10.1016/j.elecom.2010.01.010.

[355] D. A. Drabold and S. Estreicher. "Theory of defects in semiconductors". In: Berlin, Germany: Springer, 2007. ISBN: 978-3540334002.

[356] A. Alkauskas, P. Deák, J. Neugebauer, A. Pasquarello, and C. G. Van de Walle. "Advanced calculations for defects in materials: Electronic structure methods". In: Weinheim, Germany: John Wiley & Sons, 2011. ISBN: 978-3527410248.

[357] S. K. Estreicher. "Hydrogen-related defects in crystalline semiconductors: a theorist's perspective". In: *Mater. Sci. Eng. R Rep.* **14** (1995), p. 319. DOI: 10.1016/0927-796x(95)00178-6.

[358] H. Peng, D. O. Scanlon, V. Stevanovic, J. Vidal, G. W. Watson, and S. Lany. "Convergence of density and hybrid functional defect calculations for compound semiconductors". In: *Phys. Rev. B* **88** (2013), p. 115201. DOI: 10.1103/physrevb.88.115201.

[359] L. Hedin. "New method for calculating the one-particle Green's function with application to the electron-gas problem". In: *Phys. Rev.* **139** (1965), p. 796. DOI: 10.1103/physrev.139.a796.

[360] G. Makov and M. C. Payne. "Periodic boundary conditions in *ab initio* calculations". In: *Phys. Rev. B* **51** (1995), p. 4014. DOI: 10.1103/physrevb.51.4014.

[361] C. Freysoldt, J. Neugebauer, and C. G. Van de Walle. "Fully *ab initio* finite-size corrections for charged-defect supercell calculations". In: *Phys. Rev. Lett.* **102** (2009), p. 016402. DOI: 10.1103/physrevlett.102.016402.

[362] E. Péan, J. Vidal, S. Jobic, and C. Latouche. "Presentation of the PyDEF post-treatment Python software to compute publishable charts for defect energy formation". In: *Chem. Phys. Lett.* **671** (2017), p. 124. DOI: 10.1016/j.cplett.2017.01.001.

[363] A. Goyal, P. Gorai, H. Peng, S. Lany, and V. Stevanović. "A computational framework for automation of point defect calculations". In: *Comput. Mater. Sci.* **130** (2017), p. 1. DOI: 10.1016/j.commatsci.2016.12.040.

[364] X. Gonze. "First-principles responses of solids to atomic displacements and homogeneous electric fields: Implementation of a conjugate-gradient algorithm". In: *Phys. Rev. B* **55** (1997), p. 10337. DOI: 10.1103/physrevb.55.10337.

[365] F. Giustino. "Electron-phonon interactions from first principles". In: *Rev. Mod. Phys.* **89** (2017), p. 015003. DOI: 10.1103/revmodphys.89.015003.

[366] A. Faghaninia, J. W. Ager, and C. S. Lo. "*Ab initio* electronic transport model with explicit solution to the linearized Boltzmann transport equation". In: *Phys. Rev. B* **91** (2015), p. 235123. DOI: 10.1103/physrevb.91.235123.

[367] D. L. Rode. "Semiconductors and semimetals: Transport phenomena". In: NY, USA: Academic Press, 1975. Chap. 1. ISBN: 0127521100.